Interfacial modification for carbon nanotubes enhanced magnesium alloys

Nur Syazana Natasha binti Hisham

Imperial College London

Department of Aeronautics

A thesis submitted for the degree of Doctor of Philosophy

April 2023

Declaration

I declare that this thesis has been entirely written on my own based on the work that I've carried out at the Department of Aeronautics, Department of Chemistry and Department of Materials of Imperial College London, and all other works have been appropriately referenced. This work has not been submitted elsewhere for a reward of a degree at this or any other university.

Nur Syazana Natasha binti Hisham

2022

The copyright of this thesis rests with the author. Unless otherwise indicated, its contents are licensed under a Creative Commons Attribution-Non Commercial 4.0 International Licence (CC BY-NC). Under this licence, you may copy and redistribute the material in any medium or format. You may also create and distribute modified versions of the work. This is on the condition that: you credit the author and do not use it, or any derivative works, for a commercial purpose. When reusing or sharing this work, ensure you make the licence terms clear to others by naming the licence and linking to the licence text. Where a work has been adapted, you should indicate that the work has been changed and describe those changes. Please seek permission from the copyright holder for uses of this work that are not included in this licence or permitted under UK Copyright Law.

Abstract

Magnesium (Mg) offers a tremendous weight saving potential as an advanced lightweight material in the automotive and aerospace industries. However, the application of Mg is limited by its low corrosion resistance and low mechanical properties especially at elevated temperature. To overcome the limitations of Mg, carbon nanotubes (CNTs) are considered to be ideal for the fabrication of Mg matrix composites due to their high aspect ratio and superior mechanical properties. However, the design of CNTs-reinforced Mg matrix composites requires a homogeneous dispersion of CNTs and a good interfacial bonding between the CNTs and the Mg matrix for an effective strengthening of the composites by CNTs. Consequently, the coating of CNTs is considered to be an effective strategy to improve the wettability of CNTs by Mg and promote the dispersion of CNTs in the metal matrix. In this work, a new technique was developed for the coating of CNTs with either SiOC or SiC using a polymethylhydrosiloxane (PMHS) precursor to enhance the properties of AZ91 composites. Initially, the transformation of PMHS to SiOC and SiC was established via a simple curing technique followed by pyrolysis in Ar at 900 and 1500 °C, respectively. Then, a preliminary application of PMHS as a coating precursor for CNTs found that SiOC can be coated on the individual CNTs as a discontinuous or continuous coating layer or precipitated densely on the CNTs agglomerates. The effect of coating concentration on the morphology and dispersibility of the CNTs were further studied through a more extensive production of SiOC and SiC coated CNTs. Intermediate coating concentration (i.e. 45-55 wt%) was found to be suitable for the wetting of CNTs by the AZ91. The addition of either SiOC coated CNTs or SiC coated CNTs had successfully led to a notable grain refinement by up to 66 % in grain size reduction, increase in hardness by up to 17 %, and increase in yield strength by up to 15 % in the AZ91 composites in comparison to the pure AZ91.

Table of contents

Declaration 2
Abstract 3
Table of contents 4
Acknowledgement 7
List of publications 9
List of figures 10
List of tables 19
List of abbreviations and symbols 22
Chapter 1 : Introduction 24
1.1 Background and motivation 24
1.2 Aim and objectives 25
1.3 Thesis structure 26
Chapter 2 : Literature Review 27
2.1 Magnesium (Mg) as a lightweight material 27
2.1.1 Properties of Mg and its alloys 29
2.2 Carbon nanotubes-reinforced Mg matrix composites 31
2.2.1 Strengthening mechanisms in metal composites 32
2.2.2 Carbon nanotubes (CNTs) 36
2.2.3 Composite design and fabrication: Challenges and strategies 38
2.3 Surface modification of CNTs 43
2.3.1 Properties of coated CNTs-reinforced Mg matrix composites 43
2.3.2 Silicon oxycarbide (SiOC) and silicon carbide (SiC) for CNTs coating 50
2.3.3 Polysiloxane conversion to SiOC and SiC 52
2.3.4 Polymethylhydrosiloxane (PMHS) as CNTs coating precursor 59
Chapter 3 : Experimental 61
3.1 Materials 61
3.2 Experimental methods 62
3.2.1 Production of SiOC and SiC coated CNTs 62
3.2.2 Stir casting 68
3.2.3 CNTs addition to AZ91 melt 70
3.2.4 Post-processing treatment 71
3.2.5 Metallographic sample preparation 73
3.3 Characterisation techniques 74

3.3.1 Infrared (IR) spectroscopy 75
3.3.2 Ultraviolet-visible (UV-Vis) spectroscopy 75
3.3.3 X-ray diffraction (XRD) 77
3.3.4 Thermogravimetric analysis (TGA) 77
3.3.5 Differential scanning calorimetry (DSC) 78
3.3.6 Optical microscopy (OM) 79
3.3.7 Scanning electron microscopy (SEM) 80
3.3.8 Transmission electron microscopy (TEM) 81
3.3.9 Density measurement 81
3.3.10 Grain size measurement 82
3.3.11 Hardness test 84
3.3.12 Tension test 86
3.3.13 Compression test 88
Chapter 4 : Development of CNTs coating process 90
4.1 Introduction 90
4.2 Transformation of polymethylhydrosiloxane (PMHS) to silicon oxycarbide (SiOC) and silicon carbide (SiC) 91
4.2.1 Crosslinking via thermal oxidation 91
4.2.2 Ceramisation via pyrolysis 99
4.3 PMHS as a coating precursor for CNTs 104
4.3.1 Wettability of carbon by PMHS 104
4.3.2 CNTs dispersion in organic solvents 105
4.3.3 Coating morphology of SiOC coated CNTs 108
4.3.4 Effect of CNTs on PMHS decomposition 115
4.4 Conclusions 123
Chapter 5 : AZ91-SiOC coated CNTs composites 125
5.1 Introduction 125
5.2 SiOC coated CNTs 127
5.2.1 Effect of starting PMHS concentration on SiOC concentration 127
5.2.2 Effect of SiOC concentration on coating morphology 130
5.2.3 Effect of SiOC coating on CNTs dispersibility 136
5.3 AZ91 composites 146
5.3.1 General microstructure of pure AZ91 146
5.3.2 Effect of SiOC coating on AZ91 composite properties 152
5.3.3 Effect of CNTs loading on AZ91 composite properties 162
5.4 Conclusions 179
Chapter 6 : AZ91-SiC coated CNTs composites 181

6.1 Introduction 181
6.2 SiC coated CNTs 181
6.2.1 Effect of starting PMHS concentration on SiC concentration 181
6.2.2 Effect of SiC concentration on coating morphology 184
6.2.3 Effect of SiC coating on CNTs dispersibility 194
6.3 AZ91 composites 201
6.3.1 Effect of SiC coating on AZ91 composite properties 201
6.3.2 Effect of CNTs loading on AZ91 composites properties 206
6.4 Conclusions 220
Chapter 7 : Conclusions and future work 222
Appendix 228
References 239

Acknowledgement

I would like to take this opportunity to express my deepest gratitude to many people who have helped and supported me throughout my PhD journey, and without whom this thesis would not have been possible.

First and foremost, to my supervisor, Dr. Qianqian Li, I would like to thank you for your endless support, motivation and guidance. Your constant kindness and empathy have always helped me to feel confident to grow as a researcher. Thank you for always creating a healthy and positive environment where we can always discuss regardless of scientific topics or personal matters.

To my second supervisor, Prof. Milo Shaffer, I would like to thank you for helping me to develop my skills and attitudes as a scientist. Your meticulous and insightful feedbacks and suggestions have always pushed me to think critically of my work. Thank you also for the opportunity to participate in the NanoHAC group activities as they had helped to broaden my PhD experience at Imperial.

To the present and past members in Dr Li's groups especially Zhuocheng, Xinyi, Zhenghao and Dan. I am honoured to be able to work with you as a team. I also treasure the meals and conversations that we've had outside of the lab. I wish you all the best in your endeavours.

I also would like to extend my gratitude to the Department of Aeronautics staff. To Frank Gommer, Joseph Meggyesi, Jon Cole, Gary Senior, Roland Hutchins and Ian James, thank you for providing me with a great technical assistance without which this work would not have

been possible. To Ela Sapinsky and Clodagh Li, thank you for always being kind while helping me with administrative tasks. Finally, to Amy Picton, thank you for helping me to overcome some challenging moments in my life.

To my colleagues in the NanoHAC group: Dave A., Noelia, Chris, Evgeny, Kalpana, Gabe, Tomasso, Peach, Yuhan, Alex, Joe, Maariyah and Shirley thank you for helping me with various tasks in my work and for always inspiring me with your works and wisdom. To the other members in CAGB 150 lab: Andre, Grace, Daniela, Yifang, Joanne and Dharu, thank you for always brightening up my days with our meals and conversations.

To my friends: Annie, Luqman, Darryl, Michelle and Zahid, thank you for enriching my life in the UK and providing me with many great moments that I will cherish forever. To my sparring buddies at the Imperial College Taekwondo club: I am grateful for all of you as you've made me grow so much as a person and in this sport which made my experience at Imperial so much more fulfilling.

To the Ministry of Higher Education of Malaysia, thank you for providing me with the opportunity to pursue this PhD degree at Imperial.

Most importantly, to my beloved family: Abah, Mama and Ajim, thank you for always being there for me, for always lifting up my spirits with your love and care, for always believing in me and for always supporting me no matter what kind of endeavour I'm pursuing. I pray that you are always granted with peace and health in this life, and goodness in the hereafter.

List of publications

In preparation

1. Designing interfaces for exogenous nanocarbon reinforced lightweight metal composites (review paper). N. S. N. Hisham, M. S. P. Shaffer, Q. Li
2. Polysiloxane-derived SiOC/SiC coated CNTs for enhanced Mg alloys. N. S. N. Hisham, M. S. P. Shaffer, Q. Li

Conferences

1. Development of nanocarbon coatings for the application in metal matrix composites (poster presentation). European Congress and Exhibition on Advanced Materials and Processes (EUROMAT) 2019, September 2019.
2. The application of coated carbon nanotubes in metal matrix composites (oral presentation). European Congress and Exhibition on Advanced Materials and Processes (EUROMAT) 2021, September 2019.
3. The application of coated carbon nanotubes in lightweight metal matrix composites (oral presentation). The 20th European Conference on Composite Materials (ECCM20), June 2022.

List of figures

Figure 2.1. Material composition of (a) a generic vehicle (Honda Accord, Internal combustion engine, 2011) and its principal part production process, and (b) a Boeing 787 aircraft. Images reproduced from [24, 27]. 28
Figure 2.2. Major crystallographic planes and directions in a hexagonal close-packed crystal lattice. Image reproduced from [31]. 29
Figure 2.3. Schematic illustration showing the Orowan looping mechanism in which dislocation must loop around the reinforcing particles (blue circles) to traverse through the matrix. Image reproduced from [54]. 32
Figure 2.4. Schematic illustrations showing the grain refinement mechanisms of reinforcement particles in a metal matrix via (a) heterogeneous nucleation and (b) Zener pinning effect. Images are reproduced from [60] [61]. 34
Figure 2.5. Single-walled CNTs (SWCNTs) can be visualised as a single layer of graphene rolled into a cylinder. Double-walled CNTs (DWCNTs) and multiwalled CNTs (MWCNTs) consist of two or more concentric SWCNTs. Image reproduced from [64]. 36
Figure 2.6. Plot showing the comparison between the theoretical calculations (excluding grain refinement which was not observed in the study) and experimental results (black rectangles) for the yield strength of pure Mg-As received CNTs composites over a range of CNTs volume fractions. Image reproduced from [76]. 38
Figure 2.7. Plots showing the variation of tensile properties of Mg-CNTs composites relative to the unreinforced Mg matrix as a function of CNTs loading based on the results reported in [77, 78, 83-86]: (a) increase in tensile yield strength, (b) increase in ultimate tensile strength and (c) increase in ductility. 40
Figure 2.8. SEM images showing the results from using several CNTs distribution techniques: (a) as-received CNTs dispersed on the surface of a metal flake after ball milling, (b) as-received CNTs dispersed on the surface of a Mg chip after pre-dispersion using block co-polymer and (c and d) homogeneous as-received CNTs dispersion in the as-cast Mg-Zn-CNTs composite following an ultrasonic vibration assisted mechanical stirring process. Images reproduced from [53, 92]. 42
Figure 2.9. Plots showing the variation of tensile properties of Mg matrix composites reinforced with as-received and coated CNTs relative to the unreinforced Mg matrix as a function of CNTs loading based on the results reported in [109, 113-118]: (a) increase in tensile yield strength, (b) increase in ultimate tensile strength and (c) increase in ductility. Each literature work is labelled with a different symbol and colour. Mg-as received CNTs composites are labelled with filled symbols meanwhile Mg-coated CNTs composites are labelled with unfilled symbols. 45

Figure 2.10. Variation in the CNTs coating material used in the fabrication of coated-CNTs reinforced Mg matrix composites as reported in the literature. 47
Figure 2.11. SEM images showing (a) as-received CNTs and (b) Ni-coated CNTs whereby the latter was produced using electroless deposition technique. Images reproduced from [117]. 47
Figure 2.12. TEM images showing (a) a discontinuous Mg_2Ni layer formed at the Ni-coated CNTs-Mg matrix interface and (b) a coherent interface formed between Mg_2Ni [1124] plane and Mg [1011] plane with a coherent relationship angle of 126.85 °. Images reproduced from [118]. 48
Figure 2.13. Reaction mechanism for Mg-Al/SiC system: (a) initial configuration, (b) formation of MgO and Al_2O_3, (c) dissolution of Si into Mg-Al and precipitation of C, and (d) precipitation of Mg_2Si and Al_4C_3. Figure redrawn from [125, 126]. 51
Figure 2.14. Crosslinking of polysiloxanes can be carried out via (a) hydrolysis and condensation reactions, and (b) platinum catalyst assisted hydrosilylation reaction. Images modified from [149, 150]. 54
Figure 2.15. Structural evolution of crosslinked polysiloxane precursor with increasing pyrolysis temperature. Image reproduced from [174]. 58
Figure 2.16. Molecular structure of polymethylhydrosiloxane (PMHS). 59
Figure 3.1. Photograph of Mg AZ91D chips. 61
Figure 3.2. Process flowchart for the production of SiOC and SiC coated CNTs. 62
Figure 3.3. Schematic diagram of the tube furnace set up showing the air and inert gas connections at the inlet, and the exhaust gas route at the outlet. 64
Figure 3.4. Photograph of the tube furnace set-up used for the heat treatment of samples in air or inert atmosphere. 64
Figure 3.5. Photograph of the automated vertical tube furnace used in the stir casting process. 69
Figure 3.6. Photographs showing (a) gravity casting of AZ91 melt into the mould and (b) as-cast sample obtained after cooling down to room temperature. 69
Figure 3.7. Photograph of an Al parcel containing the nanoparticle powder sample. 70
Figure 3.8. Photographs of the rolling slab produced (a) from the as-cast sample prior to rolling and (b) after the hot and cold rolling processes showing the parallel (left) and transverse (right) planes relative to the rolling direction. 72
Figure 3.9. Schematic diagram of a single hot rolling pass. 72
Figure 3.10. Correlation table for the assignment of absorption band to the specific functional group. Image reproduced from [183]. 75
Figure 3.11. Optical micrograph of the etched surface of Mg matrix sample showing six test lines (three horizontal and three vertical lines) drawn for the measurement of average grain size using the mean linear intercept method. 83
Figure 3.12. Optical micrograph showing a Vickers indentation made on a Mg matrix sample and the measurement of the mean indentation diagonal length (d) in the inset. 85

Figure 3.13. Minimum sample thickness required based on the indentation load and Vickers hardness value. Image reproduced from: https://www.tec-science.com/material-science/material-testing/vickers-hardness-test/ 85
Figure 3.14. Schematic diagram of (a) a uniaxial tensile loading which produces an elongation and a positive linear strain and (b) a uniaxial compressive loading which produces a contraction and a negative linear strain. Images reproduced from [62]. 87
Figure 3.15. Typical engineering stress-strain curve under tensile load. 87
Figure 4.1. Process flowchart for the conversion of polysiloxane precursor to SiOC and SiC ceramics. 91
Figure 4.2. (a) DSC and (b) TGA curves of as-received PMHS under heating in air and N_2. 92
Figure 4.3. DSC curves of as-received and crosslinked PMHS samples. The crosslinked PMHS samples had been subjected to various curing treatments as described in Table 4.1. 94
Figure 4.4. TGA-MS of as-received PMHS in air under the established curing procedure. 95
Figure 4.5. FT-IR spectra of as-received, partially cured and completely cured PMHS. 96
Figure 4.6. Possible mechanism for the crosslinking of PMHS via heat treatment in air by the oxidation of (a) Si-H and (b) Si-CH_3 groups which leads to the formation of Si-O-Si bonds and the evolution of water. 97
Figure 4.7. TGA of as-received, partially cured and completely cured PMHS in N_2. 98
Figure 4.8. DTG-MS of crosslinked PMHS in N_2. Inset showing a close-up for m/z = 2, 15, 30 and 44 between 300 to 500 °C. 99
Figure 4.9. Photographs of the as-received PMHS, the crosslinked PMHS and the pyrolysis products, PMHS-900 and PMHS-1500, contained in flat boat alumina boats. 101
Figure 4.10. XRD patterns of crosslinked PMHS and the pyrolysed products, PMHS-900 and PMHS-1500. 102
Figure 4.11. Photographs of (a) As-received PMHS and (b) water droplets on a carbon substrate. 104
Figure 4.12. SEM images of as-received NC7000 multiwalled CNTs at (a) low and (b) high magnifications. 105
Figure 4.13. TEM images of as-received NC7000 multiwalled CNTs at (a) low and (b) high magnifications. 105
Figure 4.14. Optical micrographs of CNTs dispersions in (a) acetone, (b) ethanol and (c) THF each at a concentration of 1 mg/mL after ultrasonication for 30 min. 106
Figure 4.15. Photographs of CNTs dispersions in (a) acetone, (b) ethanol and (c) THF at t=0, 1 hr and 2 days after 30 min ultrasonication. 107
Figure 4.16. TEM images and EDX spectra of (a) as received (i.e. uncoated) CNTs and SiOC coated CNTs produced from PMHS/CNT w/w of (b) 2/1, (c) 3/1 and (d) 6/1. The outer surface of CNTs and the outer layer of SiOC coating are highlighted with yellow and black dotted lines, respectively, to

outline the coating layer. The area of EDX measurement is outlined with white dotted circle. Cu detected in the EDX spectra is attributed to the TEM copper grid. 110
Figure 4.17. Variation in coating morphology found in the SiOC coated CNTs grouped according to (a) minimal to no apparent coating (b) thin and continuous layer and (d) discontinuous layer. The outer surface of CNTs and the outer layer of SiOC coating are highlighted with yellow and white dotted lines, respectively, to outline the coating layer. 111
Figure 4.18. TEM images and EDX spectra of CNTs agglomerates for (a) as-received CNTs and SiOC coated CNTs produced from PMHS/CNT w/w of (b) 2/1 and (c) 3/1. The area of EDX measurement is outlined with white dotted circle and labelled with letters A and B. Al detected in EDX is attributed to the residual alumina impurity in the as-received NC7000 CNTs. 112
Figure 4.19. (a) Expected and (b) actual SiOC coating behaviour of on the CNTs. SiOC is denoted in blue while the CNTs are represented as black lines. The outer surface of CNTs and the outer layer of SiOC coating are highlighted with yellow and white dotted lines, respectively..... 114
Figure 4.20. Comparison between the experimental and expected values for total curing, pyrolysis and ceramic yield and SiOC coating concentration of the SiOC coated CNTs produced from starting PMHS concentration of 2/1 and 6/1 PMHS/CNTs w/w. The expected values were calculated by assuming that the total curing, pyrolysis and ceramic yield of the polymer were equivalent to those of the pure PMHS as reported in Table 4.3 and that no mass loss occurred for the CNTs. 116
Figure 4.21. Comparison between the actual and expected TGA curves of crosslinked PMHS-CNTs produced from PMHS/CNTs w/w of 2/1 and 6/1 as performed in N_2. The expected TGA curves of the crosslinked PMHS-CNTs were determined by assuming that the pyrolytic behaviour of the polymer was equivalent to that of a completely cured pure PMHS as shown in Figure 4.7 and that no mass loss occurred for the CNTs during pyrolysis. 117
Figure 4.22. Effect of modified procedures on the total ceramic yield of PMHS-CNTs samples. 118
Figure 4.23. Total ceramic yield of PMHS-CNTs as a function of (a) CNTs loading and (b) starting PMHS volume..... 121
Figure 5.1. (a) TGA curves of as-received CNTs and SiOC coated CNTs as performed in air. (b) Scatter plot showing the relationship between the starting PMHS concentration in the PMHS-CNTs samples and the final SiOC coating concentration in the SiOC coated CNTs products. 128
Figure 5.2. SiOC coated CNTs (shown here for SiOC22CNT78) (a) before and (b) after TGA operation in Figure 5.1 (a)..... 129
Figure 5.3. SEM images and EDX spectra of (a) as-received CNTs and as produced SiOC coated CNTs: (b) SiOC22CNT78, (c and d) SiOC55CNT45, (e) SiOC67CNT33 and (f) SiOC77CNT23. Point EDX measurement was performed at the locations marked by the capital letters A-G in the SEM images. Note that the Al shown in the EDX spectra corresponds to the alumina impurities which were originally present in the as-received NC7000 CNTs. 132

Figure 5.4. TEM images and EDX spectra of the CNTs agglomerate and individual tubes in the as-produced SiOC coated CNTs: (a and b) SiOC22CNT78, (c and d) SiOC55CNT45, (e and f) SiOC67CNT33 and (g and h) SiOC77CNT23. The outer surface of the CNTs and the outer layer of the SiOC coating are highlighted with yellow and white dotted lines, respectively, to outline the coating layer. Point EDX measurement was performed at the areas marked with white dotted circles and labelled with capital letters A-D. Cu detected in the EDX spectra is attributed to the TEM copper grid. 134
Figure 5.5. Proposed model for the evolution of the SiOC coated CNTs morphology at a different SiOC concentration: (a) low, (b) intermediate and (c) high. 135
Figure 5.6. Photographs of as-received CNTs and SiOC coated CNTs in THF before and after ultrasonication, and after centrifugation. Each dispersion was prepared at a concentration of 1 mg equivalent of as-received CNTs per mL of THF. 137
Figure 5.7. Optical micrographs of (a) as-received CNTs, (b) SiOC22CNT78, (c) SiOC55CNT45 (d) SiOC67CNT33 and (e) SiOC77CNT23 dispersions in THF after 30 min ultrasonication. Each dispersion was prepared at a concentration of 1 mg equivalent of as-received CNTs per mL of THF. Some of the yellowish-brown particles are highlighted by the arrows. 139
Figure 5.8. SEM images of ultrasonically dispersed CNTs deposited on Al foil: (a) As-received CNTs, (b) SiOC22CNT78, (c and d) SiOC55CNT45, (e and f) SiOC67CNT33 and (g and h) SiOC77CNT23. Point EDX measurement was performed on the locations marked by the capital letters A-L. Some of the debundled individual CNTs are highlighted by the orange arrows. Al detected in the EDX is attributed to the Al foil. 142
Figure 5.9. (a) UV-Vis spectra of as-received CNTs and SiOC coated CNTs supernatant solutions. (b) Plot showing the absorbance value of the supernatant solutions at 260 nm as a function of SiC concentration in the CNTs sample. 143
Figure 5.10. Photograph showing the as-cast pure Mg AZ91 and the locations at which specimens are taken for microstructural characterisation. 146
Figure 5.11. Optical micrographs showing the polished cross sections of pure Mg AZ91 specimens taken from the top, middle and bottom locations of the cylindrical section of the casting. 147
Figure 5.12. Optical micrographs (left) and SEM images (right) showing the casting defects typically found in the as-cast pure Mg AZ91 sample: (a and b) at low magnification, (c and d) shrinkage porosity at a higher magnification and (e and f) gas porosity at a higher magnification. 148
Figure 5.13. Optical micrographs of polished (left) and etched (right) cross sections of pure Mg AZ91 alloys at different conditions: (a) as-cast, (b) after solution heat treatment and natural ageing (i.e. T4 treatment), and (c and d) after solution heat treatment and hot rolling. ND, TD and RD refer to the normal, transverse and rolling directions, respectively. The grain sizes are denoted in the grain structure images. 150

Figure 5.14. SEM images of pure Mg AZ91 alloys at different conditions: (a) as-cast and (b) after solution heat treatment and natural ageing (i.e. T4 treatment). (c) is a magnification of an area in (a). Point EDX measurement was carried out at the locations marked with the capital letters. 151
Figure 5.15. Photographs of (a) AZ91-As received CNTs, (b) AZ91-SiOC22CNT78 and (c) AZ91-SiOC45CNT55 castings. 153
Figure 5.16. Optical micrographs showing the cross sections of as-cast (a) pure AZ91 and AZ91 composites reinforced with (b) As-received CNTs, (c) SiOC22CNT78, (d) SiOC55CNT45, (e) SiOC67CNT33 and (f) SiOC77CNT23. Each cross section was taken from the middle location of the cylindrical part of the casting (see Figure 5.10). 154
Figure 5.17. Porosity comparison between the as-cast pure AZ91 and AZ91 composites (a) by average and (b) by specimen location (see Figure 5.10). A single measurement was performed for each specimen location. 155
Figure 5.18. Optical micrographs showing the porosity formation in the AZ91 composites reinforced with (a) as-received CNTs, (b) SiOC22CNT78, (c) SiOC55CNT45 and (d) SiOC67CNT33. 156
Figure 5.19. SEM images showing the cross-section of as-cast AZ91 composites reinforced with (a) as-received CNTs, (b) SiOC22CNT78, (c and d) SiOC55CNT45 and (f) SiOC67CNT33 along with their corresponding EDX spectra. Point EDX measurement was performed at the locations marked by the capital letters A-G in the SEM images. 158
Figure 5.20. Grain size comparison between the as-cast pure AZ91 and AZ91 composites (a) by average and (b) by specimen location. A single measurement was performed for each specimen location. ... 159
Figure 5.21. Relationship between the porosity and grain size of pure AZ91 and AZ91 composites reinforced with as-received and SiOC coated CNTs. 160
Figure 5.22. Hardness comparison between the as-cast pure AZ91 and AZ91 composites (a) by average and (b) by specimen location. 160
Figure 5.23. Photographs of as-cast (a) AZ91-1.0 wt% As received CNTs and (b) AZ91-2.22 wt% SiOC55CNT45 composites. 163
Figure 5.24. Optical micrographs showing the cross sections of solution treated-hot rolled (a) pure AZ91 and AZ91 composites reinforced with (b-e) As-received CNTs and (f-i) SiOC55CNT45 in a range of equivalent as received CNTs loading. 165
Figure 5.25. Optical micrographs showing the porosity formed in the solution treated-hot rolled AZ91 composites reinforced with (a) as-received CNTs and (b) SiOC55CNT45. 166
Figure 5.26. Scatter plot showing the porosity of pure AZ91 and AZ91 composites reinforced with as-received CNTs and SiOC55CNT45 for the solution treated-naturally aged and solution treated-hot rolled samples. 168
Figure 5.27. (a) Grain size and (b) hardness comparison the pure AZ91 and AZ91 composites reinforced with as-received CNTs and SiOC55CNT45. 169

Figure 5.28. Optical micrographs showing the grain structures of solution treated-hot rolled (a) pure AZ91 and AZ91 composites reinforced with (b-e) as received CNTs and (f-i) SiOC55CNT45 at various CNTs loadings. 170
Figure 5.29. (a) Stress-strain curves, (b) 0.2% tensile yield strength, (c) ultimate tensile strength and (d) ductility of solution treated-hot rolled pure AZ91 and AZ91 composites reinforced with as-received CNTs and SiOC55CNT45. 172
Figure 5.30. (a) Stress-strain curves, (b) 0.2% compressive yield strength, (c) ultimate compressive strength and (d) compression at failure of solution treated-naturally aged pure AZ91 and AZ91 composites reinforced with as-received CNTs and SiOC55CNT45. 174
Figure 5.31. Scatter plots showing the relationship between porosity and ultimate compressive strength of the solution treated-naturally aged (a) pure AZ91, (b) AZ91-As received CNTs and (c) AZ91-SiOC55CNT45..... 175
Figure 5.32. SEM images showing the fracture surface of AZ91 composites reinforced with (a-b) as-received CNTs and (c-e) SiOC55CNT45 after compression test. Point EDX measurement was performed at the locations marked by the letters A-H in the SEM images. Individual CNTs found on the fracture surface are denoted by the yellow arrows. 178
Figure 6.1. (a) TGA curves of as-received CNTs and SiC coated CNTs as performed in air. (b) Scatter plot showing the relationship between the starting PMHS concentration in the PMHS-CNTs samples and the final SiC coating concentration in the SiC coated CNTs products..... 183
Figure 6.2. SiC coated CNTs (shown here for SiC45CNT55) (a) before and (b) after TGA operation in Figure 6.1 (a)..... 183
Figure 6.3. SEM images and EDX spectra of as produced SiC coated CNTs: (a) as-received CNTs, (b) SiC25CNT75, (c and d) SiC45CNT55 and (e) SiC56CNT44. Point EDX measurement was performed at the locations marked by the capital letters A-G in the SEM images meanwhile EDX mapping was performed on the areas marked with 'ROI #'. Note that the Al shown in the EDX spectra is attributed to the alumina residue which was originally present in the starting NC7000 CNTs. 188
Figure 6.4. TEM images and EDX spectra of as-produced (a) SiC25CNT75, (b and c) SiC45CNT55, (d) SiC56CNT44 and (e) the SiC whisker found in some of the samples. The area of EDX measurement is outlined with white dotted circle and marked by capital letters A-G. Cu detected in the EDX spectra is attributed to the TEM copper grid. Dotted orange lines are used to outline the cylindrical SiC precipitate on SiC25CNT75 image. 190
Figure 6.5. XRD patterns of as-received CNTs and SiC coated CNTs: SiC25CNT75, SiC45CNT55, SiC53CNT47 and SiC56CNT44. 191
Figure 6.6. Proposed model for the evolution of the 'SiC coated CNTs' morphology at different coating concentrations: (a) low, (b) intermediate and (c) high. 192

Figure 6.7. Photographs of as-received CNTs and SiC coated CNTs in THF before and after ultrasonication, and after centrifugation. Each dispersion was prepared at a concentration of 1 mg equivalent of as-received CNTs per mL of THF. 195
Figure 6.8. Optical micrographs of (a) as-received CNTs, (b) SiC25CNT75, (c) SiC45CNT55 and (d) SiC56CNT47 dispersions in THF after 30 min ultrasonication. Each dispersion was at a concentration of 1 mg equivalent of as-received CNTs per mL of THF. 196
Figure 6.9. SEM images of ultrasonically dispersed CNTs deposited on Al foil: (a) as-received CNTs, (b) SiC25CNT75, (c) SiC45CNT55 and (d and e) SiC56CNT44. Point EDX measurement as performed at the locations marked by the capital letters. Al detected in the EDX is attributed to the Al foil. 198
Figure 6.10. (a) UV-Vis spectra of as-received CNTs and SiC coated CNTs supernatant solutions. (b) Plot showing the absorbance value of the supernatant solutions at 260 nm as a function of SiC concentration in the CNTs sample. 199
Figure 6.11. Photographs of (a and b) AZ91-SiC25CNT45 and (c) AZ91-SiC45CNT55 castings... 202
Figure 6.12. Optical micrographs showing the cross sections of as-cast AZ91 composites reinforced with (a) SiC25CNT75, (b) SiC45CNT55, (c) SiC53CNT47 and (d) SiC56CNT44. Each cross section was taken from the middle location of the cylindrical part of the casting (see Figure 5.10). 203
Figure 6.13. Porosity comparison between the as-cast pure AZ91 and AZ91 composites reinforced with as-received CNTs and SiC coated CNTs (a) by average and (b) by specimen location. A single measurement was performed for each specimen location. 205
Figure 6.14. Optical micrographs showing the cross-section of AZ91 composites reinforced with SiC56CNT44 at a higher magnification. 205
Figure 6.15. Optical micrographs showing the cross sections of solution treated-hot rolled AZ91 composites reinforced with SiC45CNT55 in a range of equivalent as received CNTs loading. 208
Figure 6.16. Scatter plot showing the porosity of pure AZ91 and AZ91 composites reinforced with as-received CNTs and SiC45CNT55 for the solution treated-naturally aged and solution treated-hot rolled samples. 209
Figure 6.17. Optical micrographs showing the grain structures of solution treated-hot rolled (a) pure AZ91 and AZ91 composites reinforced with (b-e) as received CNTs and (f-i) SiC45CNT55 at various CNTs loadings. 211
Figure 6.18. (a) Grain size and (b) hardness comparison between the pure AZ91 and AZ91 composites reinforced with as-received CNTs and SiC45CNT55. 212
Figure 6.19. (a) Stress-strain curves, (b) 0.2% tensile yield strength, (c) ultimate tensile strength and (d) ductility of solution treated-hot rolled pure AZ91 and AZ91 composites reinforced with as-received CNTs and SiC45CNT55. 212
Figure 6.20. (a) Stress-strain curves, (b) 0.2% compressive yield strength, (c) ultimate compressive strength and (d) compression at failure of solution treated-naturally aged pure AZ91 and AZ91 composites reinforced with as-received CNTs and SiOC55CNT45. 214

Figure 6.21. Scatter plot showing the relationship between porosity and ultimate compressive strength of the solution treated-naturally aged AZ91-SiC45CNT55. 215
Figure 6.22. SEM images showing the fracture surface of AZ91 composites reinforced SiOC45CNT55 after compression test. Point EDX measurement was performed at the locations marked by the letters A-E in the SEM images. Individual CNTs found on the fracture surface are denoted by the yellow arrows..... 219

Figure A.1. Temperature profile inside the work tube (with insulation plugs fitted) as measured by an external thermocouple showing the uniform hot zone relative to the length of the work tube. 228
Figure A.2. Design of the H13 tool steel crucible used in the stir casting process. 229
Figure A.3. Design of the S235 steel stirrer head used in the stir casting process. 230
Figure A.4. Design of the permanent steel mould used in the stir casting process. 231
Figure A.5. Al-Mg phase diagram. The dotted line indicates the Mg-Al composition of the Mg AZ91 alloy used in this work. A and B points mark the temperatures typically used for the ageing and solution heat treatments, respectively. Image reproduced from [256]. 232
Figure A.6. Configuration of tensile test specimen. 233
Figure A.7. DSC curves of PMHS samples which had been subjected to a heat treatment in air at 160 °C for t min. 234
Figure A.8. DSC curves of PMHS samples which had been subjected to a heat treatment in air at 160 °C for 45 min and 170 °C for t min. 235
Figure A.9. DSC curves of PMHS samples which had been subjected to a heat treatment in air at 160 °C for 45 min, 170 °C for 75 min and 190 °C for t min. 236
Figure A.10. DSC curves of PMHS samples which had been subjected to a heat treatment in air at 160 °C for 45 min, 170 °C for 75 min, 190 °C for 30 min and 210 °C for t min. 237

List of tables

Table 1. Mechanical properties comparison of cast Mg alloys with other materials. Data collected from [45-48]. 30
Table 2.2. Properties of Mg matrix composites reinforced with as-received CNTs and coated CNTs. 46
Table 2.3. Various types of polysiloxane precursors used in the literature for the production of SiOC and SiC ceramics, and their processing parameters. 55
Table 3.1. Elemental composition of the Mg AZ91D chips used in this study. 62
Table 3.2. Summary of the characterisation techniques used at different processes throughout this work. 74
Table 4.1. Degree of cure measurement of as-received and crosslinked PMHS samples based on the DSC measurement in Figure 4.3. 94
Table 4.2. Curing, pyrolysis and ceramic yield of as-received, partially cured and completely cured PMHS based on the TGA investigation in Figure 4.7. 98
Table 4.3. Curing, pyrolysis and ceramic yield of PMHS-900 and PMHS-1500. 102
Table 4.4. Expected SiOC coating concentration and coating thickness of the SiOC coated CNTs produced from a range of PMHS concentrations. 108
Table 4.5. Summary of the onset temperature and the total pyrolysis yield determined from the actual and expected TGA curves in Figure 4.21. 118
Table 4.6. Description of PMHS-CNTs samples prepared to investigate the chemical effect of CNTs on the total ceramic yield of PMHS-CNTs. 119
Table 5.1. Onset temperature, residual weight % at 800 °C and calculated SiOC concentration of the of the treated CNTs according to the TGA results in Figure 5.1. The starting PMHS-CNTs sample before the production of SiOC coated CNTs is denoted as PMHSxCNTy where x/y is the PMHS/CNTs w/w (i.e. weight to weight ratio). The final sample after the production of SiOC coated CNTs is labelled as SiOCmCNTn where m and y are the SiOC and CNTs wt% in the SiOC coated CNTs product, respectively. 128
Table 5.2. List of Mg AZ91 samples fabricated to investigate the effect of SiOC coating concentration in the CNTs on the properties of AZ91 composites. 152
Table 5.3. Density, porosity, grain size and hardness results of pure AZ91 and AZ91 composites reinforced with as-received and SiOC coated CNTs. A single measurement was performed for each specimen location. 159
Table 5.4. Mg AZ91 samples fabricated to investigate the effectiveness of SiOC coating on improving the wettability and distribution of CNTs in the Mg matrix while increasing the CNTs loading. 163

Table 5.5. Density and porosity results of pure AZ91 and AZ91 composites reinforced with as-received CNTs and SiOC55CNT45 for the solution treated-naturally aged and solution treated-hot rolled samples. The solution treated-hot rolled samples were used for all sample characterisations except for compression testing where the solution treated-naturally aged samples were used. 167
Table 5.6. Grain size, hardness and tensile properties of solution treated-hot rolled pure AZ91 and AZ91 composites reinforced with as-received CNTs and SiOC55CNT45. Individual data are presented for the tensile results since only a limited number of specimens were tested. 169
Table 5.7. Compressive properties of solution treated-naturally aged pure AZ91 and AZ91 composites reinforced with as-received CNTs and SiOC55CNT45. 173
Table 6.1. Onset temperature, residual weight % at 800 °C and calculated SiC coating concentration of the as-received and SiC coated CNTs according to the TGA results in Figure 6.1 (a). The starting PMHS-CNTs sample before the production of SiC coated CNTs is denoted as PMHSxCNTy where x/y is the PMHS/CNTs w/w (i.e. weight to weight ratio). On the other hand, the final product after the production of SiC coated CNTs is labelled as SiCmCNTn where m and y are the SiC and CNTs wt% in the SiC coated CNTs product, respectively. 182
Table 6.2. List of Mg AZ91 samples fabricated to investigate the effect of SiC coating concentration in the CNTs on the properties of AZ91 composites. 201
Table 6.3. Density and porosity of pure AZ91 and AZ91 composites reinforced with as-received and SiC coated CNTs. A single measurement was performed for each specimen location. 204
Table 6.4. Mg AZ91 samples fabricated to investigate the efficacy of SiC coating on improving the wettability and distribution of CNTs in the Mg matrix while increasing the CNTs loading. 207
Table 6.5. Density and porosity results of pure AZ91 and AZ91 composites reinforced with as-received CNTs and SiC45CNT55 for the solution treated-naturally aged and solution treated-hot rolled samples. The solution treated-hot rolled samples were used for all sample characterisations except for compression testing where the solution treated-naturally aged samples were used. 208
Table 6.6. Grain size, hardness and tensile properties of solution treated-hot rolled pure AZ91 and AZ91 composites reinforced with as-received CNTs and SiC45CNT55. 210
Table 6.7. Compressive properties of solution treated-naturally aged pure AZ91 and AZ91 composites reinforced with as-received CNTs and SiC45CNT55. 213

Table A.1. Degree of cure measurement of PMHS based on Figure A.7 after heat treatment in air at 160 °C for t min. The maximum curing time and the new onset temperature of the remaining exothermic peak are highlighted in bold. 234
Table A.2. Degree of cure measurement of PMHS based on Figure A.8 after heat treatment in air at 160 °C for 45 min and 170 °C for t min. The maximum curing time and the new onset temperature of the remaining exothermic peak are highlighted in bold. 235

Table A.3. Degree of cure measurement of PMHS based on Figure A.9 after heat treatment in air at 160 °C for 45 min, 170 °C for 75 min and 190 °C for t min. The maximum curing time and the new onset temperature of the remaining exothermic peak are highlighted in bold. 236
Table A.4. Degree of cure measurement of PMHS based on Figure A.10 after heat treatment in air at 160 °C for 45 min, 170 °C for 75 min, 190 °C for 30 min and 210 °C for t min The maximum curing time is highlighted in bold. 237
Table A.5. Modifications of established SiOC and SiC coated CNTs produced to improve the ceramic yield of PMHS-CNTs samples..... 238

List of abbreviations and symbols

Al	Aluminium
Al_2O_3	Aluminium oxide
Ar	Argon
C	Carbon
CNTs	Carbon nanotubes
CTE	Coefficient of thermal expansion
Cu	Copper
CVD	Chemical vapour deposition
DSC	Differential scanning calorimetry
DTG	Derivative thermogravimetry
EDX	Energy-dispersive X-ray spectroscopy
Fe	Iron
HEPA	High efficiency particulate air
HV	Vickers hardness
H_2O	Water
LEV	Local exhaust ventilation
Mg	Magnesium
Mn	Manganese
MS	Mass spectrometry
PMHS	Polymethylhydrosiloxane
PVD	Physical vapour deposition
ROI	Region of interest
SEM	Scanning electron microscopy
Si	Silicon
SiC	Silicon carbide
SiOC	Silicon oxycarbide
SiO_2	Silica
TEM	Transmission electron microscopy
TGA	Thermogravimetric analysis
THF	Tetrahydrofuran
Ti	Titanium
TiC	Titanium carbide
UV-Vis	Ultraviolet-visible
w/w	Weight-to-weight ratio
wt %	Weight percent
XRD	X-ray diffraction
Zn	Zinc

$\bar{d}$	Average grain size
ρ	Density
σ	Stress
ϵ	Strain
E	Young's modulus
H_T	Total heat of reaction
H_s	Heat of reaction
t	Time

Chapter 1 : Introduction

1.1 Background and motivation

Advanced lightweight materials are increasingly used in the automotive and aerospace industries to produce vehicles with high operating efficiency which are capable of reducing greenhouse gas emission (GHG) and energy consumption simultaneously fulfilling emission and fuel economy standards [1]. According to the report by the United Nations Intergovernmental Panel on Climate Change [2], lightweighting is considered among the highly potential mitigation measures for near-term GHG emission reduction especially during the next 10-20 years [3] through direct reduction of energy loads for vehicles ranging from passenger cars to aircrafts. It was also reported that between 2-20 tonnes life-time CO_2 savings can be achieved by a 100 kg weight reduction for light duty, heavy duty and rail vehicles [4]. Meanwhile, in aviation, lightweighting design is not only an effective way to reduce fuel consumption [5] but can also contribute to improvements in flight performance such as better acceleration, higher structural strength and stiffness, and better safety performance [6].

Magnesium (Mg) offers a tremendous weight saving potential for the substitution of conventional structural metals such as steel, titanium (Ti) and aluminium (Al) by 77%, 61% and 33% of weight reduction, respectively. However, the current application of Mg in the automotive and aerospace vehicles is very limited such that only less than 1% by weight is used in an average automobile [7]. Nevertheless, the interest in Mg alloys in the research field has continued to grow in the recent years such that they account for 20% of all alloy research [8, 9]. Mg and its alloys offer many desirable properties such as high specific stiffness and strength that are comparable to Al and steel [10, 11] and excellent castability [12]. Particularly, Mg

AZ91 is interesting for further development since it is used in a vast majority of Mg die casting applications due to its relatively high strength and good castability [13-15]. However, the application of Mg is mainly limited due to its low corrosion resistance and low mechanical properties at elevated temperature. Consequently, the fabrication of Mg matrix composites, is considered to be an effective strategy to improve the mechanical properties of Mg and to overcome their limitations [16-18]. An effective strengthening of metal matrix composite would require the reinforcements to have high strength, high aspect ratio, small size and a large difference in the coefficient of thermal expansion from the matrix. Carbon nanotubes (CNTs) are considered to be an ideal reinforcement for the strengthening of metal matrix due to their high aspect ratio [19], superior elastic modulus (of up to 1 TPa [20-25]) and extremely high strength (of up to 150 GPa [26]).

The fabrication of CNTs-reinforced Mg composites faces critical challenges due to the tendency of CNTs to agglomerate and the poor wettability of CNTs by Mg. Even though many strategies had been employed to effectively improve the dispersion and distribution of CNTs in the Mg matrix, the poor wettability of CNTs would eventually lead to the deterioration of the mechanical properties of the composites especially at a higher loading. An effective strategy to overcome this limitation would be by coating the CNTs with a suitable material that can be wetted by the Mg matrix.

1.2 Aim and objectives

The aim of this PhD project is to develop and investigate the surface modification of CNTs for enhancing magnesium alloys. The key objectives are:

- To develop a feasible and scalable technique for coating the CNTs with a suitable coating material that can enhance the wettability of CNTs by the Mg matrix.

- To understand the influence of coating concentration and morphology on the CNTs dispersion and wettability by the Mg matrix.
- To investigate the effect of CNTs coating on the microstructure and mechanical properties of Mg composites.

1.3 Thesis structure

This thesis consists of 6 chapters. Chapter 1 introduces the background, motivation, aim and objectives as well as the description of the thesis structure. Chapter 2 provides a literature review which covers the challenges and strategies in the fabrication of CNTs-reinforced Mg matrix composites and reviews the current literature works for the fabrication of coated CNTs-reinforced Mg matrix composites. Chapter 3 describes the materials, experimental methods and characterisation techniques used in this work. Chapter 4 explores the use of polymethylhydrosiloxane (PMHS) as a precursor for the coating of CNTs with either SiOC or SiC. In Chapter 5, the SiOC coated CNTs are studied more extensively to understand the effect of SiOC coating on the morphology and dispersibility of CNTs, and the properties of AZ91 composites. Chapter 6 focuses on the study of SiC coated CNTs and the types of morphologies formed as well as their effects on the dispersibility of CNTs and the properties of AZ91 composites. Chapter 7 summarises the findings in this work and provides suggestions for future works.

Chapter 2 : Literature Review

2.1 Magnesium (Mg) as a lightweight material

A key strategy for lightweighting is through the substitution of conventional materials such as mild steel and cast iron with lightweight materials such as high-strength steel and aluminium (Al) [27]. As shown in Figure 2.1 (a), a generic car is made from nearly 50% steel, 13% aluminium (Al) and 5% iron (Fe) [28]. Steel, despite of its high density of about 7.8 g/cm^3, is attractive due to its low cost, manufacturability and recyclability such that advanced high-strength steels (AHSS) have also been developed for the purpose of lightweighting which allow for thinner sheets and therefore vehicle weight reduction [29]. In the aerospace applications, high performance composites such as fibre reinforced polymer and fibre metal laminates are now replacing metals due to their lower density and higher specific strength and stiffness despite of their higher cost [30]. For example, more than 50% of the Boeing 787 fuselage is made of carbon-fibre reinforced polymer composite in comparison to 20%, 15% and 10% of Al, titanium (Ti) and steel, respectively (Figure 2.1 (b)) [31]. Nevertheless, metals have the advantages of manufacturability, much lower cost, lightning safety and easy detection of damage for repair which make them still extensively used in many aerospace applications [32].

In the longer term, magnesium (Mg) can provide a tremendous weight saving potential for structural metals by offering 77%, 61% and 33% weight reduction than steel, Ti and Al, respectively. Currently, the application of Mg was reported to be limited to only less than 1% of an average vehicle by weight [7] and the use of Mg in automotive vehicles is predicted to remain only at 4-5 kg per vehicle towards 2040 [29]. Considering the current Mg market, the main obstacles to the use of Mg in high-volume vehicle applications include manufacturing

and processing due to its low formability at typical automotive processing conditions, in-service performance such as low corrosion resistance when joint with other automotive materials, and higher cost in comparison to Al and steel [15]. Nevertheless, the interest in Mg has continued to grow in the recent years such that publications on Mg alloys in the past decade accounted for 20% of all alloy research [8, 9]. Despite of the technical and commercial barriers that must be overcome for significant Mg applications in the long-term, sustained effort in the reduction of primary metal cost and the development and deployment of corrosion protection technologies would help to unlock many potential applications for Mg in the automotive and aerospace industries [15, 33]. Furthermore, the improvement in the properties of Mg can also be achieved through various methodologies and technologies such as heat treatment, alloying, composite fabrication, surface treatment and deformation processes [34].

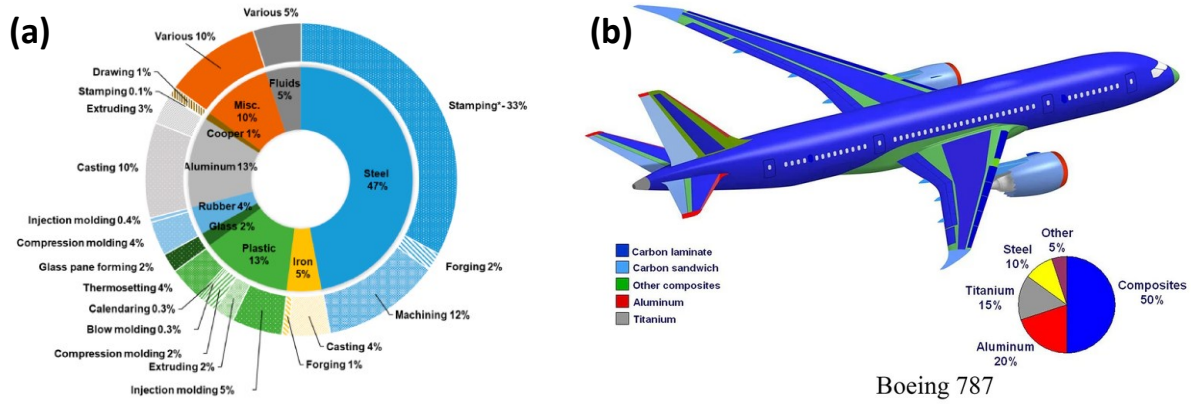


Figure 2.1. Material composition of (a) a generic vehicle (Honda Accord, Internal combustion engine, 2011) and its principal part production process, and (b) a Boeing 787 aircraft. Images reproduced from [28, 31].

2.1.1 Properties of Mg and its alloys

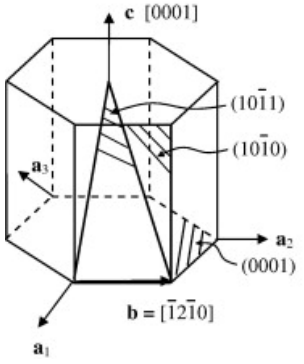


Figure 2.2. Major crystallographic planes and directions in a hexagonal close-packed crystal lattice. Image reproduced from [35].

Mg in its purest form has a density of 1.74 g/cm^3, but the density of its alloys can range from 1.3 to 1.87 g/cm^3 [36, 37]. Due to its hexagonal close-packed structure (Figure 2.2), the deformation of Mg at room temperature is restricted to only two independent slip systems occurring on the basal plane (0001) along the <11$\bar{2}$0> direction meanwhile the non-basal slips on prismatic or pyramidal planes are usually activated at elevated temperatures [35]. Therefore, Mg fails to satisfy the von Mises-Taylor criterion which requires a minimum of 5 independent slip systems to accommodate a homogeneous polycrystalline deformation [38]. As a result, Mg alloys exhibit poor formability at room temperatures and are much more workable at elevated temperatures [39].

Table 1 compares the mechanical properties of cast Mg alloys with other competing materials. Aside from being the lightest structural metal, Mg and its alloys offer many desirable properties such as high specific stiffness and strength which are comparable to those of Al and steel [10, 11], high machinability, high damping capacity, good electromagnetic shielding and biocompatibility [7, 40, 41]. In comparison to plastics, the elastic modulus of Mg is almost 20 times higher despite of being slightly heavier. Furthermore, due to its high fluidity and low

susceptibility to hydrogen, Mg is often considered to have better castability than other cast metals such as Al and copper (Cu) [12]. However, the application of Mg is limited mainly due to its low corrosion resistance and low mechanical properties at elevated temperature [11, 33]. The poor corrosion resistance of Mg can be attributed to its highly negative electrode potential which leads to galvanic corrosion when it is in contact with other structural metals [42-44].

Table 1. Mechanical properties comparison of cast Mg alloys with other materials. Data collected from [45-48].

Material	**Cast Mg**			**Steel**	**Cast Al**	**Plastics (polycarbonate/ acrylonitrile-butadiene-styrene blend)**
Alloy/Grade	AZ91	AM60	AE44	Galvanised	A380	Dow Pulse 2000
Density (g/cm^3)	1.81	1.80	1.82	7.80	2.68	1.13
Elastic modulus (GPa)	45	45	45	210	71	2.3
Yield strength (MPa)	160	115-130	100-135	200	159	53
Ultimate tensile strength (MPa)	240	205-225	185-240	320	324	55
Elongation (%)	3	6-8	6-12	40	3	5 at yield and 125 at break

Alloying is usually employed to enhance the material properties of Mg whereby the formation of intermetallic phases influences the microstructure and alters the material properties of the alloys. AZ91D, consisting of Mg, Al, zinc (Zn) and manganese (Mn), is the most commonly used alloy for commercial high-pressure die casting which exhibits good mechanical properties at room temperature, excellent castability and corrosion resistance [39]. While the addition of Al provides good fluidity to the alloy, the formation of β-$Mg_{17}Al_{12}$ intermetallic has an adverse effect on the creep resistance. AZ91 starts to creep at temperatures above 100 °C up to a maximum operating temperature of 125 °C therefore making it unsuitable for the manufacturing of power train and engine castings [14, 49]. Subsequently, the addition of rare earth (RE) elements such as in the WE43 (4 wt% RE), AE44 (4 wt% RE) and ZEK 100 (0.5

wt% neodymium (Nd)) alloys can help to significantly improve creep performance and mechanical properties in temperatures up to 300 °C [50-52]. However, the alloys are costly and not suitable for use in long-term, high volume applications [15].

2.2 Carbon nanotubes-reinforced Mg matrix composites

The enhancement of Mg alloys properties such as strength and creep resistance can be achieved via the fabrication of Mg matrix composites using various types and sizes of reinforcements such as silicon carbide (SiC), aluminium oxide (Al_2O_3), titanium carbide (TiC), boron carbide (B_4C) and boron nitride (BN) [16, 17]. In comparison to ceramic reinforcements, carbon materials such as carbon fibres and graphite particulates are particularly attractive to be used as reinforcements due to their high thermal conductivity, low coefficient of thermal expansion (COE), high damping capacity and good self-lubricant property [18, 53]. Furthermore, the strength, ductility and failure mode of the composite can also be strongly affected by the size of the reinforcement particles whereby the strength and ductility would be decreased with the increase in particle size [54]. Therefore, large particulates such as graphite particulates with sizes from several micrometres to few millimetres are susceptible to cracking and void formation at the particle-matrix interface which results in premature failure of the composites during the mechanical testing [18, 55].

2.2.1 Strengthening mechanisms in metal composites

The strengthening in metal matrix composites can be explained by a few possible reinforcing mechanisms, namely Orowan strengthening, load transfer, thermal mismatch strengthening and grain refinement. The mechanisms are briefly explained in this section.

1. Orowan strengthening

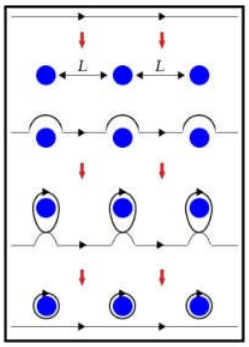


Figure 2.3. Schematic illustration showing the Orowan looping mechanism in which dislocation must loop around the reinforcing particles (blue circles) to traverse through the matrix. Image reproduced from [56].

Reinforcements can act as obstacles to impede the dislocation motion in a metal matrix. Gliding dislocation or dislocation pairs must bow or loop around the reinforcing particles in order to further traverse through the matrix (Figure 2.3). The looping mechanism involves a higher energy path which therefore requires a higher applied stress to drive the dislocations to bypass the particles. As a result, the yield strength of the matrix would be increased. The increase in yield strength due to Orowan looping is given by [57]:

$$\Delta\sigma_{Orowan} = \frac{0.8\, G_m b M}{L_p} \qquad \text{Equation 2.1}$$

where G_m is the shear modulus of the matrix, b is the Burgers vector of the matrix , M is the Taylor factor (assumed to be 3 [18, 58]) and L_p is the interparticle distance. From this equation,

it can be seen that the reinforcements should ideally be small in size and homogeneously dispersed in order to keep the interparticle spacing small.

2. Load transfer

According to the shear lag model [59], load can be transferred from the elastically softer metal matrix to the stronger and stiffer reinforcements by the generation of interfacial shear stress. Assuming that there is an ideal load transfer efficiency through an interface, the increase in yield strength due to load transfer in its simplest form [58] can be described as follows:

$$\Delta\sigma_{load} = \sigma_{re} v_{re}$$

Equation 2.2

where σ_{re} is the yield strength of the reinforcement and v_{re} is the volume fraction of the reinforcement. Variations to the shear lag model had also been made to consider the disorientation of the nanoparticle reinforcements with respect to the loading direction [60]. For an effective load transfer strengthening to occur, reinforcements should ideally have high aspect ratio and can also form a good interfacial bonding with the metal matrix.

3. Thermal mismatch strengthening

Next, a significant difference in the coefficient of thermal expansion (CTE) between the metal matrix and reinforcement can also result in the increase in prismatically punched geometrically necessary dislocations at the metal-reinforcement interface to accommodate the thermal strain and internal stress generated due to the thermal mismatch [61]. The increase in yield strength due to thermal mismatch strengthening is described as [62]:

$$\Delta\sigma_{thermal} = \alpha G_m b\sqrt{\rho}$$

Equation 2.3

where α is a geometric constant (1.25 for Mg [58]). ρ is the increase in dislocation density due to the difference in the CTE between the matrix and reinforcement, and is defined as [61, 63]:

$$\rho = \frac{Bv_{re}\Delta CTE\Delta T}{bd(1-v_{re})} \qquad \text{Equation 2.4}$$

where B is a geometric constant (theoretically [61]), ΔCTE is the difference in coefficient of thermal expansion between the matrix and reinforcement, ΔT is the difference between the process and test temperature. Based on this strengthening model, a large difference in the CTE between the reinforcement and the matrix is required.

4. Grain refinement

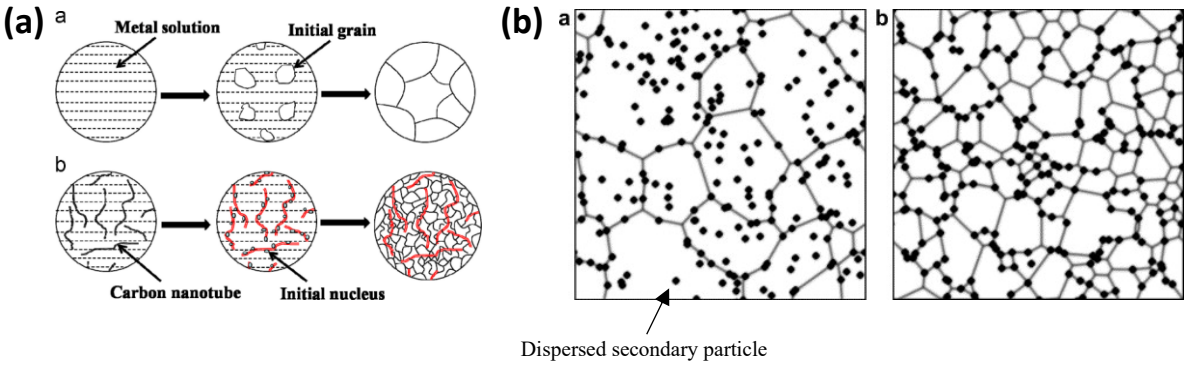


Figure 2.4. Schematic illustrations showing the grain refinement mechanisms of reinforcement particles in a metal matrix via (a) heterogeneous nucleation and (b) Zener pinning effect. Images are reproduced from [64] [65].

Grain refinement can also contribute to the strengthening of material via the Hall-Petch effect [66] as described by the following equation:

$$\sigma_{grain} = \sigma_o + kd^{-\frac{1}{2}} \qquad \text{Equation 2.5}$$

where σ_o is the frictional stress of the matrix, k is the strengthening coefficient and d is the grain size. Dislocation motions initiate within a single crystal pile-up at the grain boundaries; hence, decreasing the grain size increases the total grain boundary area which can impede the dislocation motions therefore resulting in the improvement of the mechanical properties of the material. The addition of secondary particles to a metal matrix can lead to grain refinement through nucleation and/or the Zener pinning effect. In the nucleation mechanism, the reinforcing particles can act as heterogeneous nucleus substrate to stimulate the generation of nuclei from which smaller grains could grow [64] (Figure 2.4 (a)). On the other hand, the Zener pinning effect results in the impedance of grain growth due to the pinning force exerted by dispersed secondary particles [67] (Figure 2.4 (b)). Therefore, for grain refinement to be achieved, the reinforcing particles should be homogeneously dispersed.

The strengthening contribution from each mechanism can be simply added linearly to predict the theoretical yield strength of the composite [58] as follows:

$$\sigma_c = \sigma_m + +\Delta\sigma_{load\ transfer} + \Delta\sigma_{thermal} + \Delta\sigma_{grain} \qquad \text{Equation 2.6}$$

Based on the strengthening mechanisms, the main requirements for the reinforcements include high strength, high aspect ratio, small size, large difference in the coefficient of thermal expansion than the metal matrix and a homogeneous dispersion in the metal matrix. Therefore, based on these criteria, carbon nanotubes (CNTs) are considered to be an ideal reinforcement for metal matrix composites due to their high aspect ratio and superior mechanical properties [18].

2.2.2 Carbon nanotubes (CNTs)

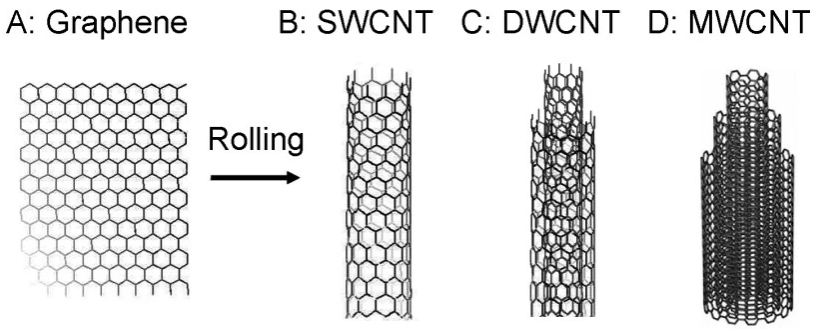


Figure 2.5. Single-walled CNTs (SWCNTs) can be visualised as a single layer of graphene rolled into a cylinder. Double-walled CNTs (DWCNTs) and multiwalled CNTs (MWCNTs) consist of two or more concentric SWCNTs. Image reproduced from [68].

Since the rediscovery of carbon nanotubes (CNTs) by Iijima in 1991 [69], the interest in CNTs in various different applications has increased rapidly due to their unique set of electrical and mechanical properties. CNTs can be distinguished as single-walled CNTs (SWCNT), double-walled CNTs (DWCNTs) or multiwalled CNTs (MWCNTs) (Figure 2.5). SWCNTs can be regarded as a single graphene layer rolled into a cylinder with a diameter of 1-2 nm meanwhile DWCNTs and MWCNTs consist of two or more concentric SWCNTs with diameters typically ranging from 4 to 50 nm [18, 70]. The tips of MWCNTs are usually capped by dome-shaped half-fullerene molecules. Similar to graphene, the carbon atoms in CNTs are densely organized in an sp^2-bonded honeycomb (hexagonal) lattice which provides CNTs with their unique strength [71]. Furthermore, based on the orientation of the tube axis relative to the carbon network, CNTs can also be further identified as either armchair, zigzag or chiral [72].

Generally, CNTs are produced by three main techniques namely arc discharge process, laser ablation method and chemical vapour deposition (CVD) [73]. While arc discharge technique is able to yield high-quality CNTs with more perfect crystalline lattice, CVD is the most preferred technique for large-scale production of CNTs whereby high purity material can be

obtained and the reaction course can be easily controlled at low temperature [74]. Alternatively, the laser ablation method is capable of producing CNTs with a higher purity (of up to 90%) and better graphitisation than those produced by the arc discharge process; however, the yield is relatively smaller [75].

The elastic modulus of MWCNTs was measured to be up to 0.027 TPa for CVD-grown [20], 1.25 TPa for laser ablation-grown [76] and in the range of 0.81-1.8 TPa for arc grown [21]. Due to their excellent elasticity, it has been shown that stresses imposed on the nanotubes led to the elastic buckling of the tubes which upon release of the stress can return to its original straight form [77]. This behaviour distinguishes CNTs from conventional carbon fibres and other known fibres which are more likely to fracture when applied with stress beyond the elastic limit. Furthermore, the tensile strength of MWCNTs had also been measured to be 0.15 TPa for arc-grown [26] and 0.11 TPa for CVD-grown [78]. CNTs are also known to be very good thermal conductors with thermal conductivity ranging from 500 to 2069 W/mK depending on the size of the tube [79].

2.2.3 Composite design and fabrication: Challenges and strategies

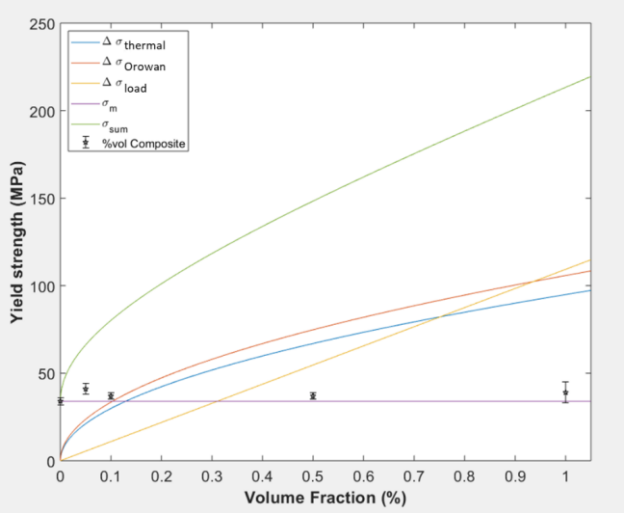


Figure 2.6. Plot showing the comparison between the theoretical calculations (excluding grain refinement which was not observed in the study) and experimental results (black rectangles) for the yield strength of pure Mg-As received CNTs composites over a range of CNTs volume fractions. Image reproduced from [80].

A study conducted previously by a student in our group [80] showed that the yield and ultimate compressive strength of pure Mg-0.05 vol% As-received CNTs composite could be improved by 21 and 8%, respectively, in comparison to the pure Mg alloy, but no improvement was measured in the yield strength, ultimate compressive strength and compression at failure as the CNTs loading was increased to 1.0 vol%. Furthermore, as shown in Figure 2.6, the theoretical yield strength calculated from the strengthening models discussed previously (except for grain refinement which was not observed in the study) showed a large discrepancy with the experimental results. These results highlight the huge potential that can be achieved with the fabrication of CNTs-reinforced Mg matrix composites, but further investigations are still required to improve the design and fabrication of the composites to meet the theoretical expectations.

The predicted increase in yield strength shown in Figure 2.6 assumes that the CNTs are perfectly aligned and individually dispersed while having an ideal interface with the Mg matrix. In reality, the fabrication of CNTs-reinforced Mg matrix composites faces the challenges to produce a homogeneous dispersion of CNTs in the metal matrix and to obtain a good interfacial bonding between the CNTs and the metal matrix.

The effect of CNTs agglomeration on the mechanical properties of Mg-CNTs composites could be observed in the literature works. As shown in Figure 2.7, at CNTs loading below 1.5 wt%, the yield strength, ultimate tensile strength and ductility could be increased with the increase in CNTs loading. However, at CNTs loading higher than 1.5 wt%, the mechanical properties were reduced as the CNTs loading was increased such that they could be worse than the mechanical properties of the pure Mg matrix alloy. The deterioration of the mechanical properties at high CNTs loading had been attributed to the increase in CNTs agglomeration or clustering in the metal matrix as the CNTs content became larger which had also led to the increase in the porosity of the composites thereby contributing to crack initiation during deformation [81, 82].

CNTs have a very large surface area of up to 1000 m^2/g [83] which can be very effective for load transfer via the interfacial shear stress [84]. However, due to the van der Waals forces between the CNTs surfaces, CNTs tend to tangle with each other which results in the formation of agglomerates with hundreds or thousands of CNTs [85]. This behaviour makes it challenging for the CNTs to be homogeneously dispersed in the metal matrix meanwhile the agglomeration of the tubes can significantly decrease the number of individual tubes distributed in the matrix. Furthermore, agglomeration is undesirable since the high axial strength and modulus of the nanotubes can be reduced due to sliding between the tubes [86].

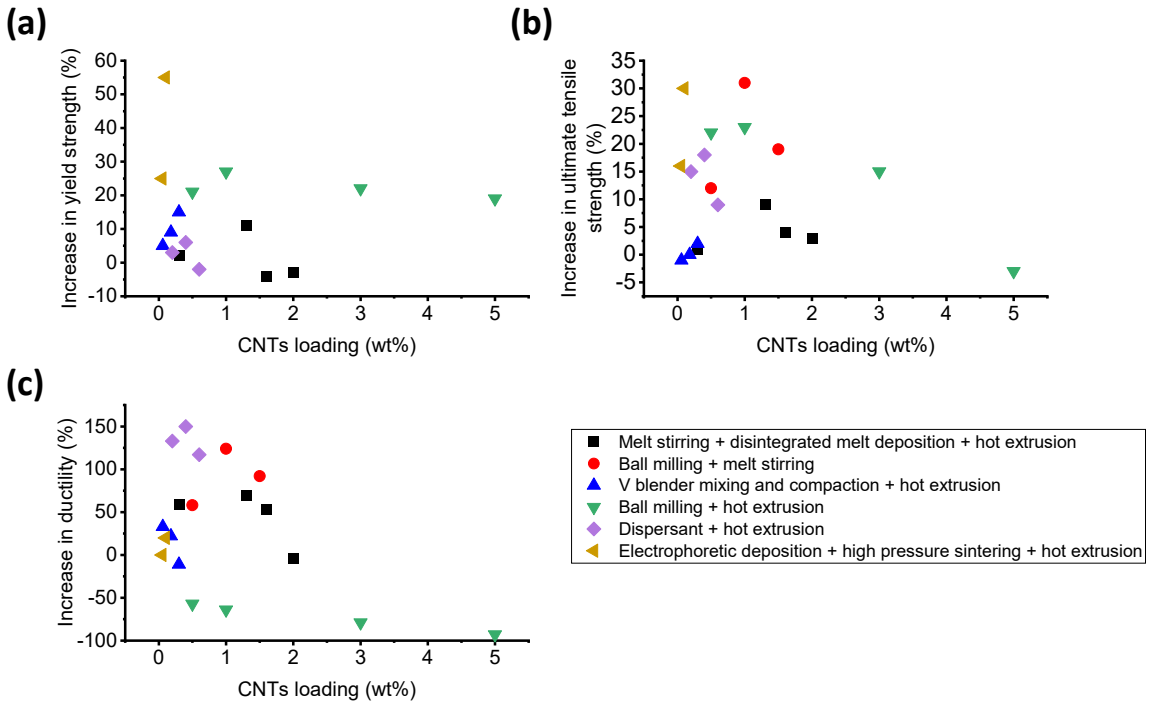


Figure 2.7. Plots showing the variation of tensile properties of Mg-CNTs composites relative to the unreinforced Mg matrix as a function of CNTs loading based on the results reported in [81, 82, 87-90]: (a) increase in tensile yield strength, (b) increase in ultimate tensile strength and (c) increase in ductility.

Several strategies had been employed in the literature to improve the CNTs dispersion and distribution in the Mg matrix such as:

1. Mechanical mixing of CNTs with metal powder

   CNTs can be effectively dispersed in the powder feedstock by mechanically mixing the CNTs with Mg metal powder using a few techniques such as roll mixing [91], ball milling [92-96] or V-blender mixing [82]. Shi et. al. [96] found that ball milling helped to break the entangled raw CNTs and led to the adherence and homogeneous dispersion of the CNTs on the metal flakes as shown in Figure 2.8 (a). However, the mixing techniques should also be applied carefully so as not to cause damage that can compromise the structural integrity of the CNTs [97-99].

2. Use of dispersants

   Generally, ultrasonication provides a more effective dispersion of CNTs whereby the local shear stress provided is much more sufficient than that generated from the mechanical mixing techniques [53]. The ultrasonication of CNTs in aqueous solutions can be assisted by the use of dispersants to promote the debundling of CNTs agglomerates and the dispersion of individual CNTs [58, 64, 100, 101]. For example, block copolymer which works by hindering the nanotubes aggregation via steric repulsion had been used by Li et. al. to pre-disperse the CNTs on the surface of Mg metal as shown in Figure 2.8 (b) prior to the melt stirring process [58].

3. Stir casting

   For the dispersion and distribution of CNTs during composite processing, mechanical stirring employed in the melt stirring technique can help to create and maintain a good distribution of the reinforcements in the metal melt prior to casting [18].

4. Ultrasonic melt processing

   Ultrasonication also be applied during the melt processing whereby the acoustic streaming and cavitation can help to promote a more homogeneous distribution of CNTs in the metal melt [99, 100, 102]. Shi et. al. [96] found that by combining the ball milling technique in the pre-dispersion step and ultrasonic vibration assisted mechanical stirring, a uniform dispersion of CNTs with a small amount of clustering could be observed in their as cast Mg-Zn-CNTs composite as shown in Figure 2.8 (c) and (d).

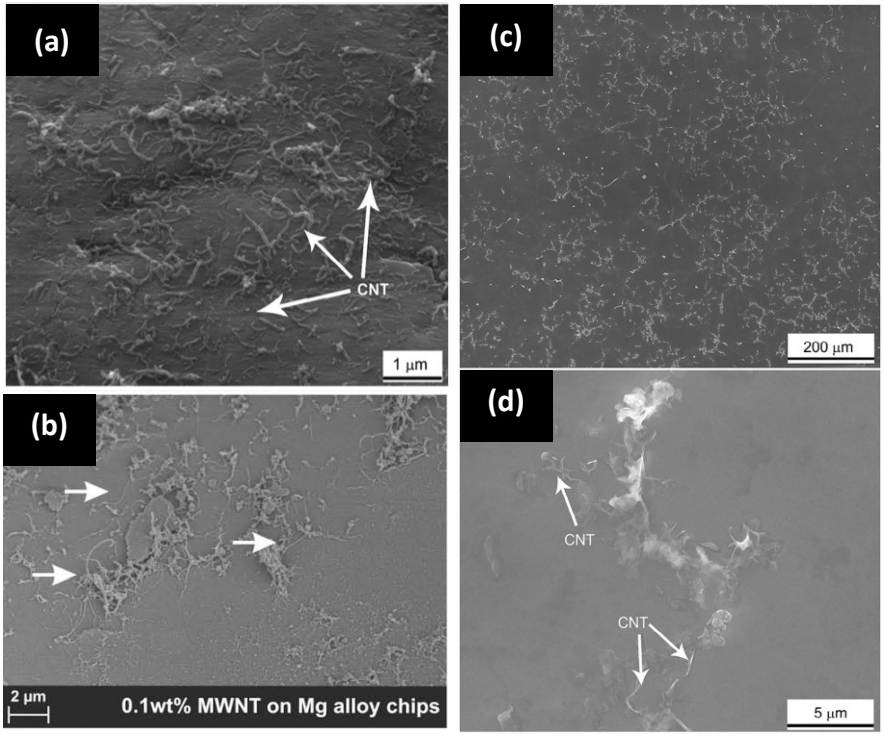


Figure 2.8. SEM images showing the results from using several CNTs distribution techniques: (a) as-received CNTs dispersed on the surface of a metal flake after ball milling, (b) as-received CNTs dispersed on the surface of a Mg chip after pre-dispersion using block co-polymer and (c and d) homogeneous as-received CNTs dispersion in the as-cast Mg-Zn-CNTs composite following an ultrasonic vibration assisted mechanical stirring process. Images reproduced from [58, 96].

While most of the techniques discussed were able to show successful results in the dispersion and distribution of CNTs, their effectiveness had mostly been demonstrated for low CNTs content and in some cases were found to be ineffective at higher CNTs content as shown in Figure 2.7 [81, 88]. Furthermore, based on our experience, despite of successfully producing homogeneously dispersed CNT on the surface of the metal matrix using an enhanced pre-dispersion step, no significant improvement was observed in the mechanical properties of the composite in comparison to the pure alloy due to a possible reagglomeration of the CNTs during melt stirring and the rejection of as-received CNTs from the melt [80].

Therefore, aside from the dispersion and distribution of CNTs, equal consideration should also be given to the wettability between CNTs and the Mg matrix which significantly influences the integrity of the CNTs/Mg interface. A strong adhesion at the CNTs/metal interface would lead to an effective stress transfer from the matrix to the CNTs allowing the stronger and stiffer CNTs to take a disproportionate share of the load [103]. Unfortunately, it is widely known that CNTs are poorly wetted by Mg. Based on the thermodynamic calculations, the formation of magnesium carbides, i.e., Mg_2C_3 and MgC_2 at the temperature range of 923-1150 K requires a really high positive free energy of formation ($\Delta G°$) where $\Delta G°_{Mg2C3} = 15.912 + 3.56T$ kJmol^{-1}K^{-1} and $\Delta G°_{MgC2} = 36.056 + 0.5T$ kJmol^{-1}K^{-1} [104]. The surface tension of liquid Mg (i.e., 560 mJ/m^2) also far exceeds the maximum surface tension required for the wetting of CNTs (i.e., around 200 mJ/m^2) as determined by Dujardin et. al. [105]. Furthermore, sessile drop experiments also showed that molten Mg droplet would form a non-wetting contact angle (i.e., 120-125 ° for the temperature range of 973-1189 K) on the basal plane of graphite [106, 107]. Given these points, further steps need to be done to improve on the wettability between CNTs and Mg. The coating of CNTs with a wettable coating material is an effective way to achieve this goal which became the main strategy explored in this PhD work.

2.3 Surface modification of CNTs

2.3.1 Properties of coated CNTs-reinforced Mg matrix composites

Table 2.2 presents the fabrication process and properties of the coated CNTs-reinforced Mg matrix composites from the literature works. A few CNTs coating materials had been considered for the fabrication of Mg matrix composites, namely MgO, Ni, NiO and Si, as also shown in Figure 2.10. Ni-coated CNTs were the most commonly used mainly due to the possible wetting of Ni by Mg [108, 109] and the feasibility of the coating technique using the

established electroless deposition technique [110-112]. Liang et. al. [113] found that the contact angle of AZ91 droplet was reduced from 84° on a carbon substrate to 51° on a Ni substrate indicating that Ni can be better wetted by Mg than CNTs. Furthermore, using the electroless deposition technique, a thin and continuous Ni coating layer could be formed on the surface of the CNTs as shown in Figure 2.11. Alternatively, MgO was chosen as the coating material for CNTs due to the availability of an established coating technique [114, 115] and the ability of MgO to form a coherent interface with α-Mg matrix [116]. Based on the coating materials used in the literature, a few guidelines can be drawn for the selection of the suitable CNTs coating material for the fabrication of Mg matrix composites which include the wettability of the coating material with the Mg matrix, the adhesion of the material coating on the CNTs for example based on the bonding strength and wetting property, and the feasibility of the coating technique and its ability to preserve the structural integrity of the CNTs.

Figure 2.9 compares the tensile properties of Mg matrix composites reinforced with as-received CNTs and coated CNTs as reported in the literature. In most cases, the addition of as-received (i.e, uncoated) CNTs led to an improvement in the tensile yield strength and ultimate tensile strength of the composites in comparison to the unreinforced Mg. Subsequently, when coated CNTs were used, the mechanical properties of the composites were found to be significantly larger than those of the Mg-As received CNTs composites. These findings demonstrate the effectiveness of CNTs coating in realising the strengthening potential of the CNTs. The largest increase in yield strength was observed for the AZ91-4.5 wt% Si-coated CNTs (by 216%) compared to the unreinforced Mg matrix, but its ductility was simultaneously decreased (by 64%) most likely due to the composite becoming harder and stiffer [117]. Furthermore, based on the literature works which assessed the composites over a range of CNTs loading [113, 118, 119], the tensile properties were found to increase gradually with the increase in CNTs loading

up to a maximum point after which the tensile properties would start to decrease. As seen in Figure 2.9, different maximum points were found in the literature works, for example as high as 3.0 wt% for the AZ91-MgO coated CNTs composite [119] and as low as 1.0 wt% for the AZ91-Ni coated CNTs composite [113]. This behaviour was attributed to the increase in CNTs agglomeration even for the coated CNTs as the CNTs loading became larger.

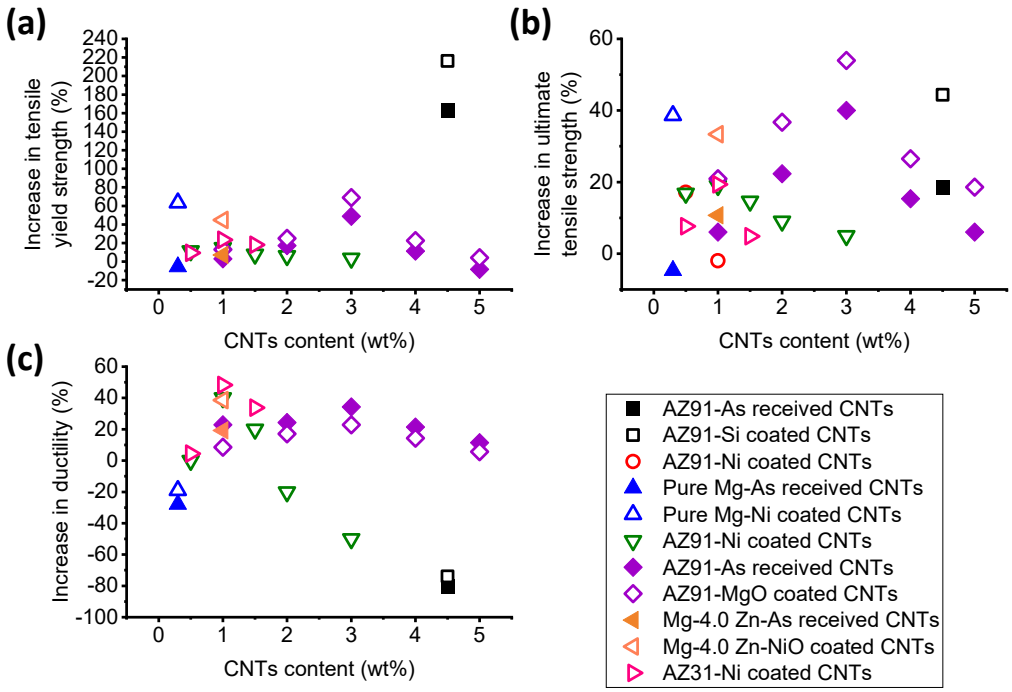


Figure 2.9. Plots showing the variation of tensile properties of Mg matrix composites reinforced with as-received and coated CNTs relative to the unreinforced Mg matrix as a function of CNTs loading based on the results reported in [113, 117-122]: (a) increase in tensile yield strength, (b) increase in ultimate tensile strength and (c) increase in ductility. Each literature work is labelled with a different symbol and colour. Mg-as received CNTs composites are labelled with filled symbols meanwhile Mg-coated CNTs composites are labelled with unfilled symbols.

Table 2.2. Properties of Mg matrix composites reinforced with as-received CNTs and coated CNTs.

CNTs coating material	Coating technique	Matrix	Composite fabrication process	As received CNTs loading (wt%)	Coated CNTs loading (wt%)	0.2 % tensile yield strength (MPa)	Ultimate tensile strength (MPa)	Ductility	Ref
Si	Ball milling	AZ91	Preparation of CNTs preform; squeeze infiltration	0		80 ± 5	205 ± 5	5 ± 2	[117]
				4.5		210 ± 2	243 ± 10	1 ± 2	
					4.5	253 ± 10	296 ± 10	1.3 ± 2	
Ni	Electroless deposition	AZ91	Melt stirring; ultrasonic processing; casting; hot extrusion; T4 treatment; T6 treatment	0		-	350	-	[120]
					0.5	-	410	-	
					1.0	-	343	-	
Ni	Commercially obtained	Pure Mg	Mechanical blending of Mg and CNTs; cold compaction; microwave assisted sintering; hot extrusion	0		126 ± 1	171 ± 2	7.9 ± 0.3	[121]
				0.3		119 ± 4	163 ± 7	5.7 ± 0.2	
					0.3	206 ± 2	237 ± 1	6.4	
Ni	Electroless deposition	AZ91	Preparation of AZ91-CNTs preform; ultrasonic processing, casting, hot extrusion; T4 treatment; T6 treatment	0		253 ± 8	321	10 ± 2	[113]
					0.5	282 ± 5	375	10 ± 1	
					1.0	291 ± 4	382	14 ± 1	
					1.5	273 ± 6	368	12 ± 1	
					2.0	269 ± 4	350	8 ± 2	
					3.0	262 ± 3	337	5 ± 1	
MgO	Surfactant	AZ91	Preparation of AZ91-CNTs preform; compaction; sintering; extrusion; T4 treatment	0		168 ± 5.0	215 ± 6.0	7.0 ± 0.2	[119]
				1.0		173 ± 4.0	228 ± 5.0	8.6 ± 0.1	
				2.0		197 ± 4.5	263 ± 5.5	8.7 ± 0.2	
				3.0		250 ± 3.8	301 ± 4.5	9.4 ± 0.1	
				4.0		187 ± 3.5	248 ± 3.9	8.5 ± 0.1	
				5.0		154 ± 4.4	228 ± 5.6	7.8 ± 0.2	
					1.0	190 ± 3.6	260 ± 4.2	7.6 ± 0.1	
					2.0	210 ± 5.0	294 ± 6.0	8.2 ± 0.2	
					3.0	284 ± 4.6	331 ± 5.0	8.6 ± 0.1	
					4.0	206 ± 3.7	272 ± 4.8	8.0 ± 0.1	
					5.0	175 ± 5.5	255 ± 5.0	7.4 ± 0.2	
Ni	Electroless deposition	Pure Mg	Preparation of Mg-CNTs powders; hot compaction; pressureless sintering; hot extrusion	0		-	-	-	[122]
				0.3		171.6	214.1	-	
				2.0		157.1	205.9	-	
					0.3	216.5	248.5	-	
					2.0	278.3	304.5	-	

NiO	Electroless deposition	Mg-4.0 Zn	Ball milling of CNTs-Zn powder; melt stirring; casting	0		98 ± 1	159 ± 4	5.7 ± 0.2	[123]
				1.0		105 ± 1.5	176 ± 5	6.8 ± 0.3	
					1.0	142 ± 2	212 ± 3.5	7.9 ± 0.4	
Ni	Electroless deposition	AZ31	Preparation of Mg-Al-Zn-CNTs mixture; hot press sintering	0		149	248	15.24	[118]
					0.5	163	267	15.91	
					1	184	296	22.59	
					1.5	176	260	20.39	

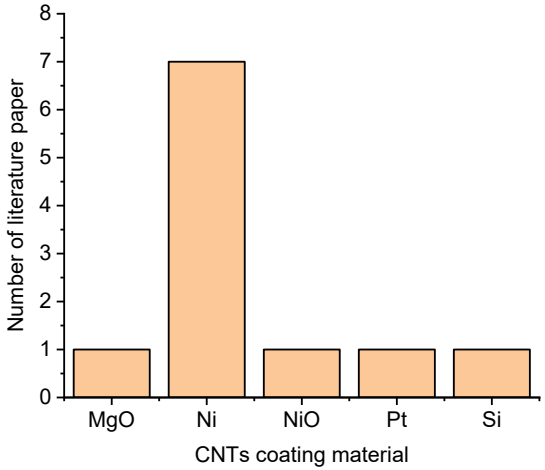


Figure 2.10. Variation in the CNTs coating material used in the fabrication of coated-CNTs reinforced Mg matrix composites as reported in the literature.

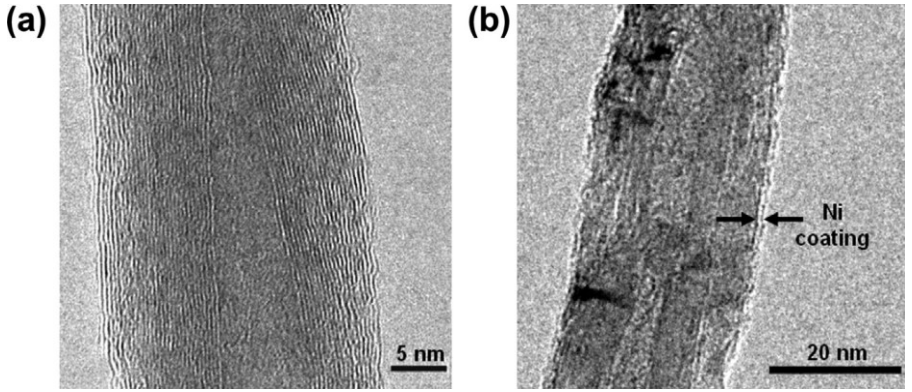


Figure 2.11. SEM images showing (a) as-received CNTs and (b) Ni-coated CNTs whereby the latter was produced using electroless deposition technique. Images reproduced from [121].

The improvement in the mechanical properties of the coated CNTs-reinforced Mg matrix composites was attributed to a few factors, namely improved wettability, grain refinement and improved CNTs dispersion. The improvement in the wettability of the CNTs and the enhancement in the interfacial bonding between the CNTs and the Mg matrix due to the presence of the coating was demonstrated through the characterisation of the CNTs-Mg interface. Individually distributed CNTs observed by Yuan et. al. in their Mg-4.0 Zn composite showed no nanopores at the CNTs-matrix indicating a good interfacial bonding [123]. On the other hand, a discontinuous nanoscale Mg_2Ni phase was observed by Han et. al. [122] at the interface of the Ni-coated CNTs and AZ91 as shown in Figure 2.12 (a) suggesting that the wettability of CNTs had been induced via the interfacial reaction between the coating layer and the matrix. They were also able to observe a coherent interface formed between the Mg_2Ni and Mg phases (Figure 2.12 (b)) which suggests a strong adhesion at the interface. The improvement in the wettability and interfacial bonding demonstrated in these reports allowed for an effective load transfer to occur from the matrix to the CNTs therefore leading to the improvement in the mechanical properties of the composites.

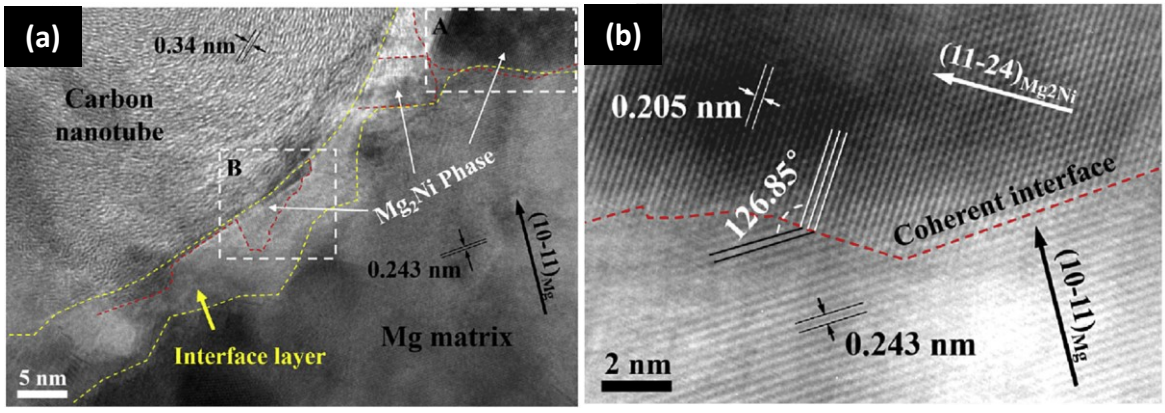


Figure 2.12. TEM images showing (a) a discontinuous Mg_2Ni layer formed at the Ni-coated CNTs-Mg matrix interface and (b) a coherent interface formed between Mg_2Ni $[11\bar{2}4]$ plane and Mg $[10\bar{1}1]$ plane with a coherent relationship angle of 126.85 °. Images reproduced from [122].

A significant reduction in the grain size of the composites from the addition of the coated CNTs had also been observed in some of the literature works which indicates that the grain refinement strengthening could also be contributing to the improvement in the mechanical properties of the composites [119, 122, 123]. For example, Nai et. al. [122] reported a grain size reduction by 83% in their pure Mg-0.3 wt% Ni coated CNTs which had shown improvement in yield strength and tensile strength by 64 and 39 %, respectively, in comparison to the pure Mg. Finally, the improvement in the mechanical properties had also been attributed to the improvement in the coated CNTs dispersion, but the evidence provided were less convincing. For example, Nai et. al. [122] argued that the lower level of porosity observed in their Mg-Ni coated CNTs composites in comparison to the Mg-As received CNTs composite could be attributed to the Ni coating role in producing less agglomeration and more uniform dispersion of the CNTs. However, no microstructural observation was provided to further support this argument.

The agglomeration of CNTs seems to be a recurring problem even for the fabrication of coated CNTs-Mg matrix composites. Other than the effect of CNTs coating on the dispersion and distribution of the CNTs in the metal matrix, several other research gaps can also be found in these literature works. For example, it is often observed that equal CNTs loading was used when comparing between the as-received CNTs and the coated CNTs. This experimental design questions if whether the concentration of the coating had also been included in the loading and if whether equivalent CNTs amounts had actually been compared. Furthermore, it is also interesting to discuss if the processing technique could have influenced the wetting/infiltration of the CNTs and also how much strengthening could be caused by the coating material itself. Therefore, in this work, a more accurate comparison will be made between the as-received CNTs and coated CNTs composite, and the effect of CNTs coating

would not only be investigated on the properties of AZ91 but also on the dispersion and distribution of the CNTs.

2.3.2 Silicon oxycarbide (SiOC) and silicon carbide (SiC) for CNTs coating

Based on the literature works, Ni coating was proven to be effective at improving the wettability of the CNTs and creating a good Mg-CNTs interface which resulted in a significant improvement in the mechanical properties of the composites. However, based on our previous work using our own composite fabrication process [80], no significant improvement could be observed in the compressive properties of the composites by adding 0.1 and 0.8 wt% of Ni-coated CNTs (which was obtained from Nanostructured & Amorphous Materials, Inc) despite of observing wetted Ni-coated CNTs in the composite microstructure. Furthermore, it is also undesirable to add Ni to Mg alloys since it can have extremely deleterious effects on the corrosion resistance of the alloy due to its low solid-solubility limit and its ability to serve as active cathodic sites for the reduction of water [42]. Therefore, a more suitable coating material had to be determined for this work.

SiC is one of the most widely used reinforcements in the fabrication of Mg matrix composites [16, 124] which could lead to a significant improvement in the mechanical properties of the composites such as the stiffness and strength. More importantly, micro- and nano-sized SiC reinforcements were always observed to be well-bonded with different Mg matrices including the AZ91 alloy [125-128] using optimised manufacturing parameters. Therefore, SiC seems to be an obvious choice of coating material for CNTs which can help to improve the wetting of CNTs by the AZ91 matrix. Figure 2.13 illustrates the reaction mechanism for SiC and Mg-Al matrix as proposed in the literature [129, 130]. Initially, the native oxide layer on the SiC

surface (i.e. SiO_2) reacts with the Mg-Al alloy which leads to the formation of MgO and Al_2O_3 as follows:

$$2Mg + SiO_2 \rightarrow 2MgO + Si \quad \text{Equation 2.7}$$

$$4Al + 3SiO_2 \rightarrow 2Al_2O_3 + 3Si \quad \text{Equation 2.8}$$

Then, the liquid Mg-Al infiltrates through the MgO and Al_2O_3 layers, comes into contact with the SiC surface and begins to dissolve the SiC to release Si and C atoms. Consequently, as the thermodynamic conditions are satisfied, the dissolved Si can react with Mg meanwhile Al may react with C as follows:

$$2Mg + Si \rightarrow Mg_2Si \quad \text{Equation 2.9}$$

$$4Al + 3C \rightarrow Al_4C_3 \quad \text{Equation 2.10}$$

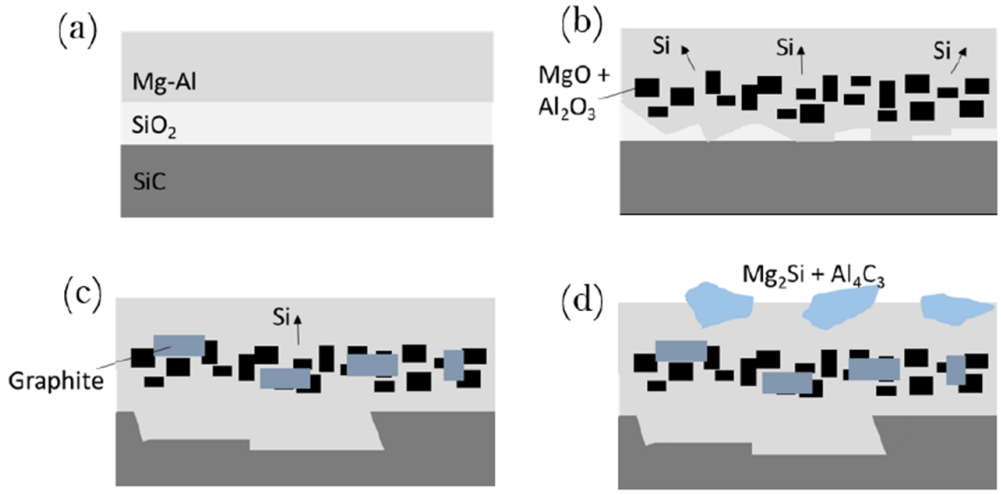


Figure 2.13. Reaction mechanism for Mg-Al/SiC system: (a) initial configuration, (b) formation of MgO and Al_2O_3, (c) dissolution of Si into Mg-Al and precipitation of C, and (d) precipitation of Mg_2Si and Al_4C_3. Figure redrawn from [129, 130].

Based on Equation 2.7 to Equation 2.10, the reaction products that may be found at the interface of Mg-Al/SiC composite are MgO, Al_2O_3, Mg_2Si and Al_4C_3. Furthermore, the occurrence of the reactions above may also depend on the Mg and Al concentrations. Based on the thermodynamic calculations provided by Shi et. al. [130] for Mg-Al/SiC system at 1173 K, the formation of Al_4C_3 happens when the concentration of Mg in the alloys is less than 94.7 mol% meanwhile Mg_2Si is formed when the concentration of Mg is in between 19.7 to 93.7 mol%.

Moreover, since SiC_p are often covered by a thin film of SiO_2, the wettability and reactivity of SiC is usually driven by the reduction of the SiO_2 film by Mg-Al, as described in Equation 2.7 and Equation 2.8, due to the instability of the SiO_2 film in Mg. SiO_2 plays an important role in the wetting of SiC by the Mg-Al matrix; therefore, it will be interesting to also consider silicon oxycarbide (SiOC) as a CNTs coating material and to investigate its wettability by the AZ91 matrix.

2.3.3 Polysiloxane conversion to SiOC and SiC

Since the pioneering work of Yajima et. al. [131, 132] for the synthesis of SiC fibres from polycarbosilanes, many other Si-based preceramic polymers such as polysiloxanes, polysilazanes and polyborosilanes have been considered to produce a wider range of ceramic materials such as SiOC, silicon nitride (Si_3N_4) and silicon carbonitride (SiCN) [133]. The advantages of using Si-based preceramic polymers include high thermal stability and chemical resistance, the feasibility to produce ceramic products upon thermal, chemical and/or radiative processes, and low processing temperature [134] in comparison to the sintering technique which requires much higher temperatures [135, 136]. For the purpose of coating, the use of Si-based polymers involves a simpler preparation technique in comparison to some other techniques such as physical vapour deposition (PVD), chemical vapour deposition (CVD),

thermal spraying and sol-gel techniques [137, 138]. Additionally, some requirements should be satisfied to enable the preparation of coatings from Si-based polymers such as an appropriate solubility in common solvents to enable coating deposition in liquid states, the presence of reactive (i.e., unsaturated) organic groups or reactive bonds to provide latent reactivity for cross-linking, and a sufficiently high molecular weight to prevent the volatilization of low molecular weight compounds during the cross-linking and ceramisation processes [133, 139, 140].

Polycarbosilane, which contains a Si-C backbone, had been previously used in a few studies as a precursor for the coating of SiC on the CNTs [141-144]. The SiC coated CNTs obtained had also been used in a polymer composite to improve the dispersion of CNTs which resulted in the improvement of the tensile strength, storage modulus and thermal decomposition temperature of the polymer composite [141]. Inspired by this technique, another type of Si-based polymer, i.e. polysiloxane was chosen as a precursor for the coating of SiOC and SiC on the CNTs in this work. Another technique for coating SiC on the CNTs reported in the literature [117, 145] involves the mechanical blending of CNTs and Si powder together using ball milling before annealing at high temperature. However, the use of ball milling may potentially be damaging to the structural integrity of CNTs and may not be very effective to ensure that the CNTs are well dispersed during the powder coating. On the other hand, polysiloxanes can be very effective for dispersing CNTs as demonstrated by the use of polysiloxanes as surfactants for the dispersion of CNTs in a few studies [146, 147]. Therefore, coupled with ultrasonication, the use of polysiloxane as a coating precursor seems to be a promising technique for producing uniformly coated CNTs.

Polysiloxanes (also called silicones) contain alternating silicon (Si) and oxygen (O) atoms in the backbone structure, and are one of the most widely used preceramic polymers other than polycarbosilanes. Several advantages of using polysiloxane precursors include easy storage and processing, high ceramic yield, excellent mechanical strength even in the amorphous phase and good thermochemical stability [148-152]. The production of SiOC and SiC from polysiloxane precursors generally involves the polymer-to-ceramic transformation via the crosslinking and pyrolysis steps. Table 2.3 shows the production of SiOC and SiC using various types of polysiloxane precursors and the production parameters. Various curing techniques had been used for crosslinking the polysiloxane precursor meanwhile the production of ceramic materials can be achieved from using a pyrolysis temperature of as low as 800 °C for SiOC and as high as 1700 °C for SiC.

Crosslinking (or curing) is an essential step to transform the liquid preceramic polymers into rigid thermoset polymers in order to reduce the volatilisation of low molecular weight polymers in the following pyrolysis step so that a high ceramic yield can be obtained. Crosslinking of polysiloxanes can be carried out using different techniques such as heat treatment, catalysis and non-conventional treatments using laser or ionizing radiation.

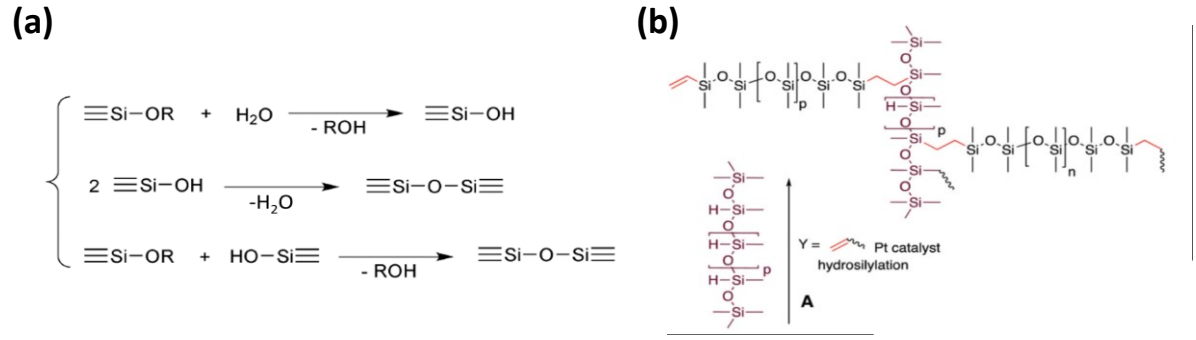


Figure 2.14. Crosslinking of polysiloxanes can be carried out via (a) hydrolysis and condensation reactions, and (b) platinum catalyst assisted hydrosilylation reaction. Images modified from [153, 154].

Table 2.3. Various types of polysiloxane precursors used in the literature for the production of SiOC and SiC ceramics, and their processing parameters.

Polysiloxane precursor(s)	Curing technique	Pyrolysis parameters		Final ceramic product	Ref.
		Environment	Heat treatment		
Polymethylhydrosiloxane	Hexa-1,5-diene cross-linker	Ar	1000 °C for 5 hr at 5 °C/min	$SiO_{1.38}C_{1.52}H_{0.55}$	[155]
			1500 °C for 5 hr at 5 °C/min	$SiO_{0.11}C_{0.96}$	
	Hexane-1,6-diol cross-linker		1000 °C for 5 hr at 5 °C/min	$SiO_{1.67}C_{0.73}H_{0.40}$	
			1500 °C for 5 hr at 5 °C/min	$SiO_{1.61}C_{0.61}$	
Vinylmethoxysiloxane, methylsiloxane and benzoin dimethylether	Photo cross-linking by UV light for 5 min, then post curing at 200 °C for 2 hr	Ar (100 mL/min)	1000 °C for 1 hr at 0.5-5 °C/min	Amorphous SiOC	[156]
			1600 °C for 1 hr at 0.5 °C/min	Crystalline β-SiC	
		Ar + H_2O (500 mL/min)	1400 °C for 2 hr at 1°C/min	SiOC, SiO_2, C and SiC with SiO_2/SiC = 4	
Polysilsesquioxane	Addition of NH_4OH, then gelation for 48 hr	Ar	800 °C	Amorphous SiOC	[157]
Alkoxy polysiloxane	Photo cross-linking by UV light	N_2 (400 mL /min)	900 °C for 1 hr at 5 °C/min	Amorphous SiOC	[158]
Vinyl terminated-polyphenylmethylsiloxane	Using platinum catalyst, then heat treatment at 50 °C for 12 hr and at 120 °C for 6 hr	Ar (900 mL/min)	1400 °C for 2 hr at 1°C/min	$SiO_{1.16}C_{0.42}$ + 2.87C	[159]
		Ar + H_2O flow (5:1 molar ratio)		$SiO_{1.71}C_{0.14}$ + 2.62C	
Polymethylhydrosiloxane	Polycondensation reaction	Ar (50 mL/min)	1100 °C for 30 min at 10°C/min	Amorphous SiOC	[160]
		Ar (50 mL/min)	1500 °C for 30 min at 10°C/min	Mainly amorphous SiOC, some crystalline SiC detected	
Polymethyphenylhydrosiloxane	Polycondensation reaction	Ar (50 mL/min)	1100 °C for 30 min at 10°C/min	Amorphous SiOC	
		Ar (50 mL/min)	1500 °C for 30 min at 10°C/min	Crystalline SiC	
Methylsilsesquioxane	Polycondensation reaction, then stirring at room temperature for 1 day	Ar	1200 °C at 10 °C/min	$SiO_{1.69}C_{0.16}$ + 0.65 C	[161]
Phenylsilsesquioxane	Hydrosilylation with chloroplatinic acid catalyst	Ar	1200 °C at 10 °C/min	$SiO_{1.84}C_{0.08}$ + 3.18 C	[162]
Polymethylphenylsiloxane	Heat treatment in air at 250 °C for 4 hr	Vacuum	1250 °C for 1 hr at 15 °C/min	Amorphous SiOC ($SiO_{1.38}C_{0.31}$ + 2.10C)	[163]

			1500 °C for 1 hr at 15 °C/min	Crystalline SiC ($SiO_{0.08}C_{0.96}$ + 0.16C)	
Polymethylhydrosiloxane	1,3,5,7-tetravinyl-1,3,5,7-tertamethylcyclotetrasiloxane (D_4Vi) crosslinker using platinum Kardtedt's catalyst	Ar (200 mL/min)	1200 °C for 1 hr	$SiO_{1.25}C_{0.38}$ + 0.61 C	[164]
	Divinylbenzene crosslinker using platinum Kardtedt's catalyst	Ar (200 mL/min)	1200 °C for 1 hr	$SiO_{1.00}C_{0.50}$ + 0.61 C	
Linear polymethylhydrosiloxane	Divinylbenzene crosslinker using platinum Kardtedt's catalyst	Ar (150 mL/min)	1400 °C for 1 hr at 5 °C/min	SiOC with mainly amorphous SiO_2 and some β-SiC	[165]
Cyclic 1,3,5,7-tetramethyl-1,3,5,7-tetracyclotetrasiloxane	Divinylbenzene crosslinker using platinum Kardtedt's catalyst	Ar (150 mL/min)	1400 °C for 1 hr at 5 °C/min	SiOC with mainly cristobalite SiO_2 and some β-SiC	
Polysilylacetylenesiloxane	In vacuum at 120 °C for 1 hr, at 160°C for 1 hr, at 210 °C for 2hr and at 250 °C for 2 hr	Ar	900 °C for 2 hr 1500 °C for 2 hr	Amorphous SiOC Mainly crystalline β-SiC	[166]
Polymethylhydrosiloxane	Divinylbenzene crosslinker using platinum Kardtedt's catalyst, then gelation for half an hour and drying overnight	Ar	900 °C for 1 hr at 0.83 °C/min 1400 °C for 1 hr at 0.83 °C/min	Amorphous SiOC Mainly crystalline β-SiC	[167]
Polymethylhydrosiloxane	Addition of 1,4-diazabicyclo [2.2.2]octane (DABCO), then left at room temperature overnight	Ar (5 L/min)	1400 °C for 2 hr at 5 °C/min 1400 °C for 10 hr at 5 c/min	Amorphous SiOC with minimal β-SiC Amorphous SiOC with increased β-SiC	[168]
Polymethylhydrosiloxane	D_4Vi crosslinker using platinum Kardtedt's catalyst, then heating at for, then heating at 50 °C for 6 hr and 80 °C for 2 hr	Ar	1000 °C for 2 hr at 5 °C/min	Amorphous SiOC ($SiO_{0.95}C_{1.12}$)	[169]
Polymethylhydrosiloxane	D_4Vi crosslinker using platinum Kardtedt's catalyst	Ar (100 mL/min)	1000 °C for 2 hr 1600 °C for 2 hr	Amorphous SiOC β-SiC + amorphous SiO_2	[170]
	1,3,5,7-tetramethylcyclotetrasiloxane (D_4H)	Ar (100 mL/min)	1000 °C for 2 hr 1600 °C for 2 hr	Amorphous SiOC Crystalline β-SiC	
Methylphenylvinylhydrogen polysiloxane	Heat treatment in air at 200 °C for 1 hr	Ar	1700 °C for 1 hr at 1 °C/min	Crystalline β-SiC	[171]

Heat treatment is widely used due to the feasibility of curing at low temperatures (i.e., 100-400 °C) without using catalysts or high-pressure applications. Generally, the process involves hydrolysis of alkoxy (-OR) groups and condensation of hydroxy (-OH) groups that lead to the Si-O-Si bonding as shown in Figure 2.14 (a). Crosslinking is also commonly assisted by using catalysts and initiators such as platinum (Pt)-derived complexes for hydrosilylation curing (as shown in Figure 2.14 (b)), tin or titanium derivatives for moisture or room temperature vulcanization curing and azo- or peroxide catalysts for radical cure [172-174]. However, incomplete removal of catalysts may compromise the thermal stability of the material while the use of heavy metals may pose safety concerns for humans and environment [154]. Finally, unconventional crosslinking methods like laser treatment and ionising radiation using electron beam or gamma rays can also be used especially for polymers with low softening, melting or decomposition temperatures since the processing can be carried out at ambient temperature [175-177].

Next, pyrolysis is carried out via heat treatment typically at the temperatures between 1000-1700 °C whereby the thermoset polymer is converted into an amorphous or crystalline material. The ceramisation process can be very complex as it involves numerous chemical reactions taking place simultaneously. Nevertheless, the pyrolysis reactions and the resulting ceramic products can be studied and understood using various characterisation techniques such as nuclear magnetic resonance (NMR), Fourier-transform infrared spectroscopy (FTIR), thermogravimetric analysis (TGA) and X-ray diffraction (XRD) [153].

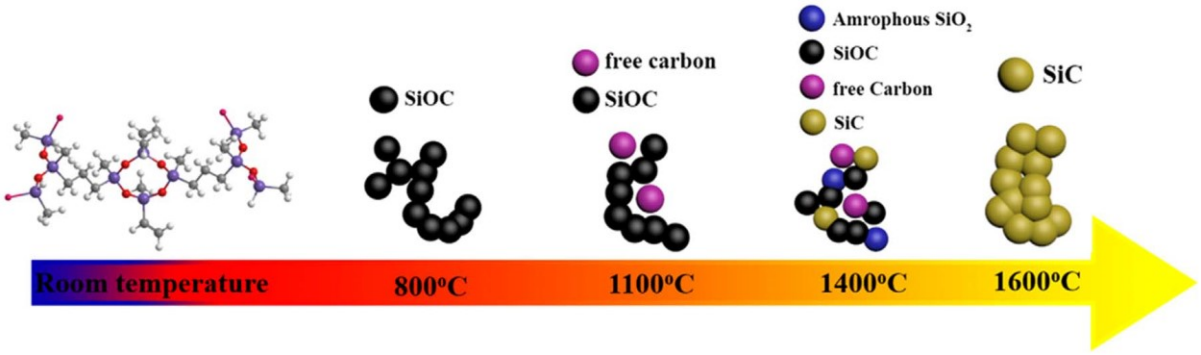


Figure 2.15. Structural evolution of crosslinked polysiloxane precursor with increasing pyrolysis temperature. Image reproduced from [178].

Figure 2.15 illustrates the structural evolution of crosslinked polysiloxane precursor as the pyrolysis temperature increases. Depolymerisation reactions occur at low pyrolysis temperatures which involve interchain and/or intrachain redistribution of Si-O-Si bonds and the decomposition of aliphatic chains which lead to the evolution of hydrocarbons and volatile oligomers [179, 180]. At the temperature below 400 °C, the presence of unreacted Si-OH and Si-OR groups may also lead to condensation between the hydroxy (-OH) and ethoxy (-OR) which results in further siloxane crosslinking [180]. Between 400-600 °C, redistribution reactions between Si-O-Si, Si-C and Si-H bonds would lead to the onset formation of amorphous SiOC network which is composed of SiC_xO_{4-x} units where $0 \leq x \leq 4$. Successive redistribution reactions may also lead to the formation of volatile silicon compounds such as SiH_4 [153, 180]. Between 600-1000 °C, cleavage of Si-C, Si-H, C-C and C-H bonds occur via homolytic bond cleave which leads to the formation of SiC units in the oxycarbide phase and the evolution of hydrogen and hydrocarbon (e.g., CH_4) [181].

At elevated temperature, i.e. >1100 °C, SiOC undergoes structural rearrangement and phase separation which leads to the formation of a multi-phase amorphous material consisting mainly of α-SiO_2, α-SiC and free carbon [156] as follows:

$$2SiOC(s) \rightarrow SiO_2(s) + C(s) + SiC(s) \qquad \text{Equation 2.11}$$

At the temperatures of 1400 °C and above, the SiOC network would become more unstable and carbothermal reduction reactions would start to occur between SiO_2 and free carbon to give SiC and CO as a byproduct:

$$SiO_2(s) + C(s) \rightarrow SiO(g) + CO(g) \qquad \text{Equation 2.12}$$

$$SiO(g) + 2C(s) \rightarrow SiC(s) + CO(g) \qquad \text{Equation 2.13}$$

2.3.4 Polymethylhydrosiloxane (PMHS) as CNTs coating precursor

Since polymethylhydrosiloxane (PMHS) had been successfully used in the literature as a polysiloxane precursor to produce SiOC and SiC products (see Table 2.3), PMHS obtained from Sigma Aldrich was selected as the preceramic precursor for the coating of SiOC and SiC on the CNTs in this work. Figure 2.16 shows the molecular structure of PMHS which consists of a Si-O backbone, hydrogen (-H) and methyl (-CH_3) side groups, and trimethylsilyl (-$Si(CH_3)_3$) end groups.

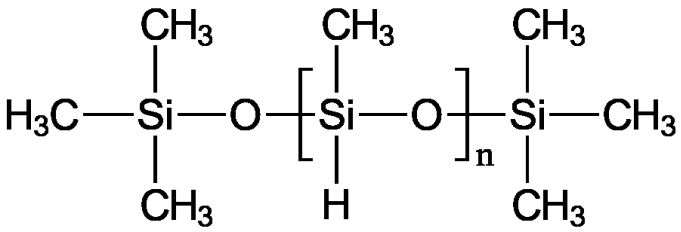


Figure 2.16. Molecular structure of polymethylhydrosiloxane (PMHS).

Several mechanisms can be proposed based on the molecular configuration of PMHS. The coating of PMHS on CNTs can be achieved via non-covalent interactions between the C-H bonds of the methyl groups and the π-electron-rich surface of the CNTs which may lead to the polymer adsorption and wrapping on the CNTs surface [182, 183]. The presence of reactive bonds such as Si-H provides a latent reactivity for cross-linking upon thermal, radiative or chemical activation which can ultimately increase the ceramic yield of the polymer [140]. Meanwhile, the methyl end groups may be able to provide a higher thermal degradation stability than reactive end groups such as vinyl to prevent the volatilisation of polymer at low temperatures [184]. Furthermore, the low viscosity of the polymer (i.e. 12-45 cps at room temperature) and its stability at room temperature would make the polymer processing easy. Finally, since the synthesis of the preceramic precursor was not considered in this work, it was also important that the PMHS can be easily obtained from commercial suppliers at a low cost.

In this work, a novel coating technique was developed using a polymethylhydrosiloxane precursor for the production of SiOC and SiC coated. The effect of coating on the CNTs morphology and dispersibility were investigated. The fabrication of AZ91 composites using the SiOC and SiC coated CNTs was carried out to assess the effect of coating on the properties of the AZ91 composites.

Chapter 3 : Experimental

This chapter describes the materials, experimental methods and characterisation techniques used in this work. The experimental methods for the production of SiOC and SiC coated CNTs, and the fabrication of AZ91 composites are described. The operating parameters for various techniques that were used for thermal, morphological and mechanical characterisations of the samples are explained.

3.1 Materials

NC7000 multi-walled carbon nanotubes (average diameter of 9.5 nm and average length of 1.5 μm) were obtained from Nanocyl. Polymethylhydrosiloxane (PMHS) with a number average molecular weight (M_N) of 1700-3200 was obtained from Sigma Aldrich. Tetrahydrofuran (THF, ≥99% stabilised, GPR RECTAPUR®), ethanol (≥99.8%, AnalaR NORMAPUR®), iso-propanol (2-propanol, ≥99.7%, AnalaR NORMAPUR®) and glacial acetic acid (≥98%, TECHNICAL) were obtained from VWR. Magnesium AZ91D in the form of chips (as shown in Figure 3.1) were obtained from non ferrum GmbH. Their elemental composition can be found in Table 3.1.



Figure 3.1. Photograph of Mg AZ91D chips.

Table 3.1. Elemental composition of the Mg AZ91D chips used in this study.

Element	Al	Zn	Mn	Si	Cu	Ni	Fe	Be	Others	Mg
Mass %	8.9100	0.5334	0.2067	0.0373	0.0052	0.0010	0.0026	0.0010	<0.010	Balance

3.2 Experimental methods

3.2.1 Production of SiOC and SiC coated CNTs

The SiOC and SiC coated CNTs production process is outlined in the flowchart below:

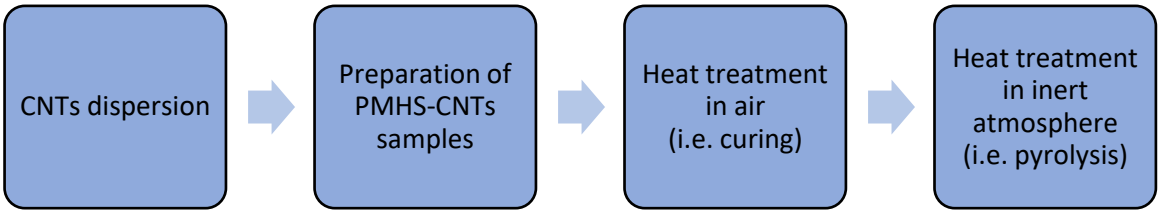


Figure 3.2. Process flowchart for the production of SiOC and SiC coated CNTs.

3.2.1.1 CNTs dispersion

CNTs dispersion was carried out to break down the large CNTs agglomerates and to allow the CNTs to be efficiently coated by the coating precusor. CNTs and THF were added to a borosilicate glass bottle at a concentration of 1 mg/mL. The bottle was clamped and kept suspended in an ice bath to prevent overheating of the solution during sonication. Sonication was performed using an ultrasonic processor with a probe fitted with a titanium tip (VCX 750, Sonics & Material, Newton, USA) in a sound enclosure (Qsonica 432A, Cole-Parmer Instrument Co. Ltd., St. Neots, UK). The following sonication parameters were used in all experiments except when stated otherwise: 30 min actual pulsing time, 5 s on and 3 s off pulser, and 25% vibrational amplitude.

3.2.1.2 Preparation of PMHS-CNTs samples

PMHS, which was used as the coating precursor, was added to the CNTs dispersion (prepared as described in Section 3.2.1.1) at the desired PMHS/CNTs w/w (i.e. weight-to-weight ratio). Then, sonication was performed for an additional 10 min with 5 s on and 3 s off pulser at 25% vibrational amplitude. Next, the mixture was transferred to a crystallising dish and stirred for 1 hr on a hotplate stirrer (US 152, Stuart, St Neots, UK) at room temperature with the crystallising dish covered with a paraffin film to prevent solvent evaporation. The paraffin film was removed, and the mixture was continually stirred at 60 °C overnight to completely remove the solvent. Finally, the PMHS-CNTs sample was collected for the subsequent steps.

3.2.1.3 Heat treatment in air and inert atmosphere

The heat treatment in air and inert atmosphere was carried out using a tube furnace (STF 15/610 + 3216 Controller, Carbolite Gero, Hope, UK) fitted with a recrystallised alumina work tube (1500 x 86 x 75 mm length, outer diameter (OD) and inner diameter (ID), respectively, Carbolite Gero, Hope, UK). The schematic diagram and photographs of the set-up are shown in Figure 3.3 and Figure 3.4, respectively. The furnace was placed on a large workbench (2500 x 750 x 900 mm length, width and height, respectively, Benchmaster Ltd., Lancashire, UK) to keep the radiated energy from heating any adjacent surfaces. A stainless steel end seal consisting of either a gas inlet and outlet was fitted to each end of the work tube. The heat treatment in air was carried out under airflow generated by an air pump (Aquarium Air Pump MA-60, Uniclife, UK). On the other hand, the heat treatment in inert atmosphere was carried out using argon (Ar) gas (Pureshield Argon, 99.998%, BOC) which was purified by a Drierite gas purifier containing indicating Drierite (calcium sulphate and cobalt chloride) and 5 Å molecular sieves (Cole-Parmer Instrument Co. Ltd., St. Neots, UK).

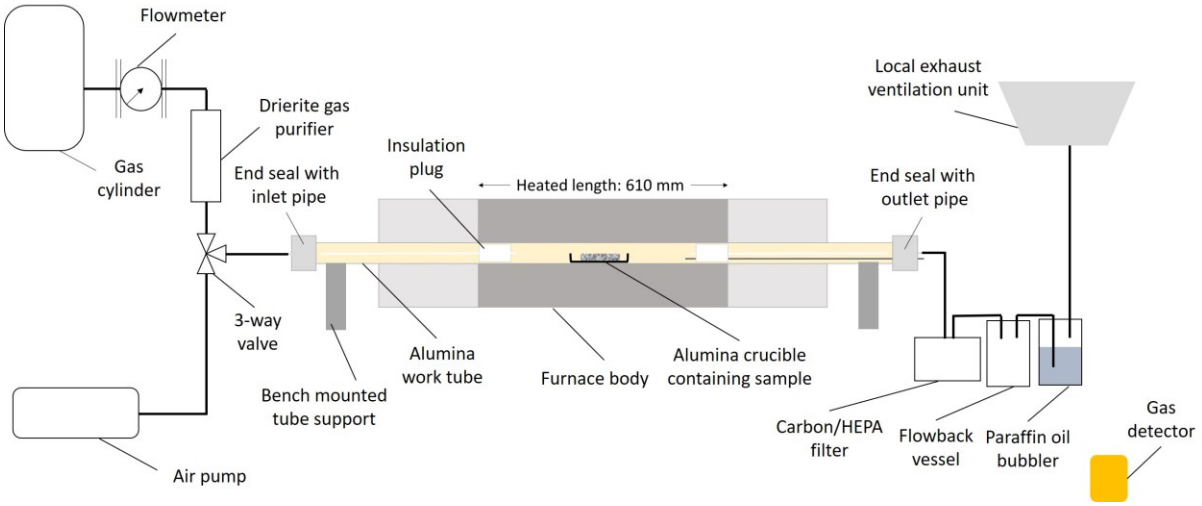


Figure 3.3. Schematic diagram of the tube furnace set up showing the air and inert gas connections at the inlet, and the exhaust gas route at the outlet.

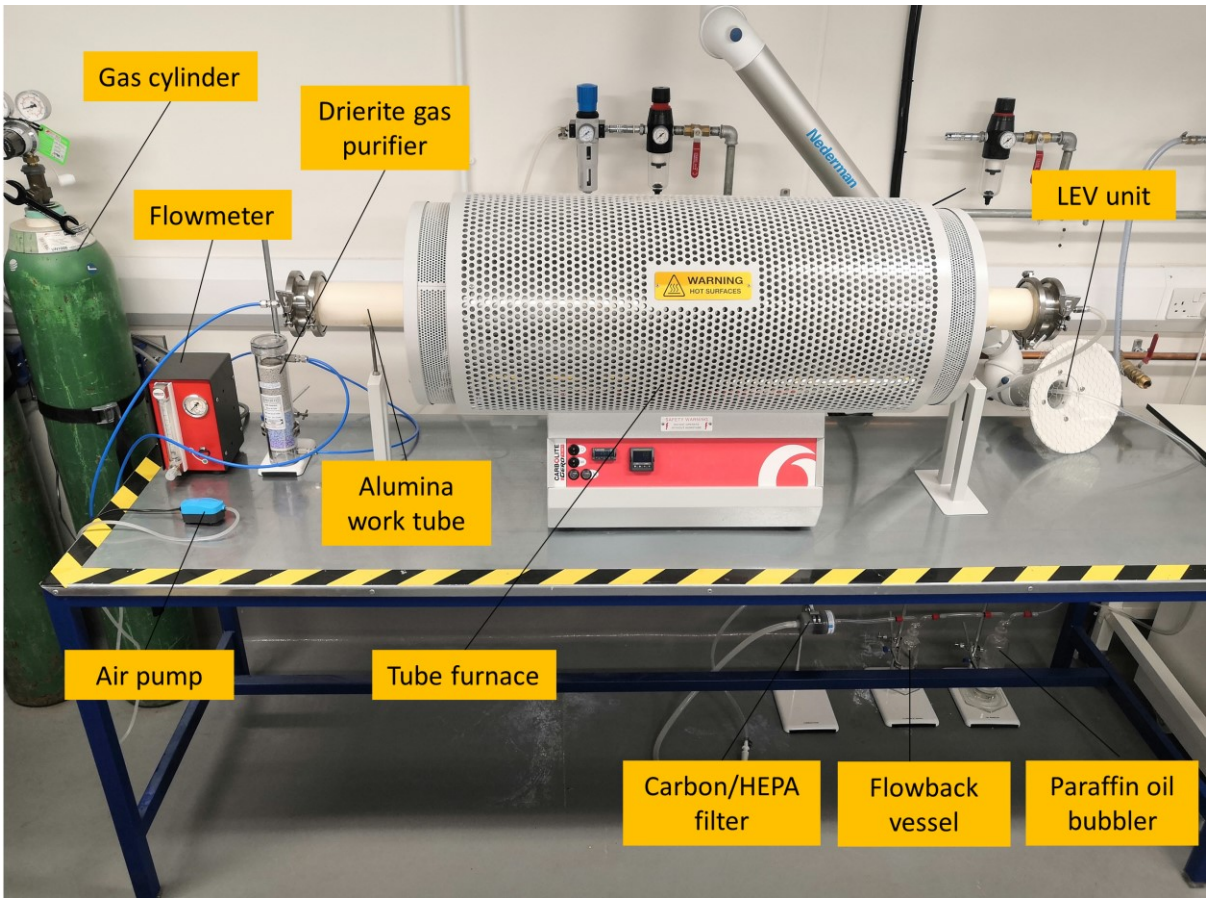


Figure 3.4. Photograph of the tube furnace set-up used for the heat treatment of samples in air or inert atmosphere.

Prior to heating in Ar, the work tube was continuously flushed with Ar at a flow rate of 1 L/min for 1 hr. The connection between the air pump and the gas cylinder was controlled using a 3-way valve. The exhaust gases were passed through a carbon/HEPA filter (Whatman Carbon Cap 150, Sigma Aldrich, Dorset, UK) to trap any hazardous hydrocarbon gases and loose CNTs in the gas flow, followed by a paraffin bubbler which was used to maintain the inert atmosphere inside the apparatus, before finally extracted by a local exhaust ventilation (LEV) unit. A gas detector (GasAlert Extreme – O2, BW Technologies) was also placed at the exhaust gas outlet for detection of exhaust gas leakage, if any. Each sample was held in a flat bottom alumina boat (80 x 30 x 16 mm length, width and height, respectively, Almath Crucibles Ltd., Suffolk, UK) and covered with a lid, if necessary. Since the furnace has a uniform hot zone of about 500 mm (see Figure A.1 in Appendix), up to three alumina boats can be placed at a time during the heat treatment.

The determination of the curing procedure will be discussed in Section 4.2.1. The curing procedure was carried out via heat treatment in air at a heating rate of 10 °C/min at 160 °C for 45 min, 170 °C for 75 min, 190 °C for 30 min and 210 °C for 30 min, and followed by cooling down to room temperature. Following the flushing of the work tube with Ar gas for 1 hr, the pyrolysis procedure was carried out in Ar at a flowrate of 83 mL/min from room temperature to a maximum pyrolysis temperature at a heating rate of 5 °C/min and a holding time of 1 hr, followed by cooling down to room temperature. The maximum pyrolysis temperature used for the production of SiOC and SiC products were 900 and 1500 °C, respectively.

The curing, pyrolysis and ceramic yield of PMHS are calculated as follows:

$$Curing\ yield\ of\ PMHS = \frac{Mass\ of\ crosslinked\ PMHS}{Initial\ mass\ of\ PMHS} \times 100\% \qquad \text{Equation 3.1}$$

$$Pyrolysis\ yield\ of\ PMHS = \frac{Mass\ of\ pyrolysis\ product}{Mass\ of\ crosslinked\ PMHS} \times 100\% \qquad \text{Equation 3.2}$$

$$Ceramic\ yield\ of\ PMHS = \frac{Mass\ of\ pyrolysis\ product}{Initial\ mass\ of\ PMHS} \times 100\% \qquad \text{Equation 3.3}$$

On the other hand, the total curing, pyrolysis and ceramic yield of PMHS-CNTs:

$$Total\ curing\ yield\ of\ PMHS - CNTs = \frac{Total\ mass\ of\ crosslinked\ product}{Initial\ mass\ of\ PMHS - CNTs} \times 100\% \qquad \text{Equation 3.4}$$

$$Total\ pyrolysis\ yield\ of\ PMHS - CNTs = \frac{Total\ mass\ of\ SiOC/SiC\ coated\ CNTs}{Total\ mass\ of\ crosslinked\ product} \times 100\% \qquad \text{Equation 3.5}$$

$$Total\ ceramic\ yield\ of\ PMHS - CNTs = \frac{Total\ mass\ of\ SiOC/SiC\ coated\ CNTs}{Initial\ mass\ of\ PMHS - CNTs} \times 100\% \qquad \text{Equation 3.6}$$

Assuming that the mass of CNTs is unchanged throughout the curing and pyrolysis processes, the SiOC/SiC coating concentration in the SiOC/SiC coated CNTs are calculated as follows:

$$SiOC/SiC\ coating\ concentration\ in\ SiOC/SiCcoated\ CNTs = \frac{Total\ mass\ of\ SiOC/SiC\ coated\ CNTs - Initial\ mass\ of\ CNTs}{Total\ mass\ of\ SiOC/SiC\ coated\ CNTs} \times 100\% \qquad \text{Equation 3.7}$$

The expected SiOC/SiC coating concentration and coating thickness in the SiOC/SiC coated CNTs are calculated as follows:

$$Expected\ SiOC/SiC\ coating\ concentration = \frac{Initial\ mass\ of\ PMHS \times Expected\ ceramic\ yield\ of\ PMHS}{Initial\ mass\ of\ PMHS \times Expected\ ceramic\ yield\ of\ PMHS + Initial\ mass\ of\ CNTs} \times 100\% \qquad \text{Equation 3.8}$$

$$Expected\ SiOC/SiC\ coating\ thickness$$

$$= \frac{Outer\ diameter\ of\ SiOC/SiC\ coating\ - Outer\ diameter\ of\ CNT}{2}$$

Equation 3.9

where

$$Outer\ diameter\ of\ SiOC/SiC\ coating$$

$$= 2\sqrt{\frac{Cross\ sectional\ area\ of\ SiOC/SiC\ coating}{\pi} + \left(\frac{Outer\ diameter\ of\ CNT}{2}\right)^2}$$

Equation 3.10

$$Cross\ sectional\ area\ of\ SiOC/SiC\ coating$$

$$= Cross\ sectional\ area\ of\ CNT \times \frac{Volume\ fraction\ of\ SiOC}{1 - Volume\ fraction\ of\ SiOC}$$

Equation 3.11

$$Cross\ sectional\ area\ of\ CNT$$

$$= \pi\left(\left(\frac{Outer\ diameter\ of\ CNT}{2}\right)^2 - \left(\frac{Inner\ diameter\ of\ CNT}{2}\right)^2\right)$$

Equation 3.12

$$Volume\ fraction\ of\ SiOC/SiC$$

$$= \frac{\frac{Expected\ SiOC/SiC\ coating\ concentration/100}{Density\ of\ SiOC/SiC}}{\frac{Expected\ SiOC/SiC\ coating\ concentration/100}{Density\ of\ SiOC/SiC} + \frac{Expected\ CNT\ concentration/100}{Density\ of\ graphene}}$$

Equation 3.13

3.2.2 Stir casting

The stir casting process was carried out using an automated vertical tube furnace (FVRT-150/300/1100-Special, Linn High Therm GmbH, Eschenfelden, Germany) fitted with a Kanthal APM work tube (600 x 100 x 110 mm length, OD and ID, respectively, Linn High Therm GmbH, Eschenfelden, Germany) and enclosed in a poly(methyl methacrylate) (PMMA) housing as shown in Figure 3.5. The operation of the tube furnace was automatically controlled using a control system (SE-702) connected to the tube furnace. Generally, 180 g of Mg AZ91 chips was used for each casting. The chips were first added to a H13 tool steel crucible (see Figure A.2 in Appendix for the crucible design) which was precoated with boron nitride (Combat® Boron Nitride Aerosols, Precision Ceramics). Then, the crucible was placed on the bottom lifting unit and elevated into the furnace. The upper lifting unit which was fitted with a boron nitride coated stirrer (see Figure A.3 in Appendix for the stirrer design) was brought down to seal the furnace. The stirrer was positioned above the crucible during the heating up stage before stirring was performed. Simultaneously, a permanent steel mould (see Figure A.4 in Appendix for mould design) was also precoated with boron nitride and preheated at 200 °C in an oven (VT 6025, Thermo Scientific, Langenselbold, Germany). Next, Ar gas was introduced at a flow rate of 500 L/min and the furnace was heated to 650 °C. The flow rate was further increased to about 875 L/min when the temperature reached 400 °C to reduce the risk of oxidation at the higher temperature. Once the temperature reached 650 °C, the stirrer was lowered into the crucible and stirring was performed at 390 rpm for 30 minutes. After stirring was completed, the temperature was increased to 680 °C, the crucible was brought down and the melt was poured into the mould as shown in Figure 3.6 (a) while the casting area was continuously flushed with a large volume of Ar gas. The cast was left to cool down in air at room temperature before the sample (as shown in Figure 3.6 (b)) was retrieved.

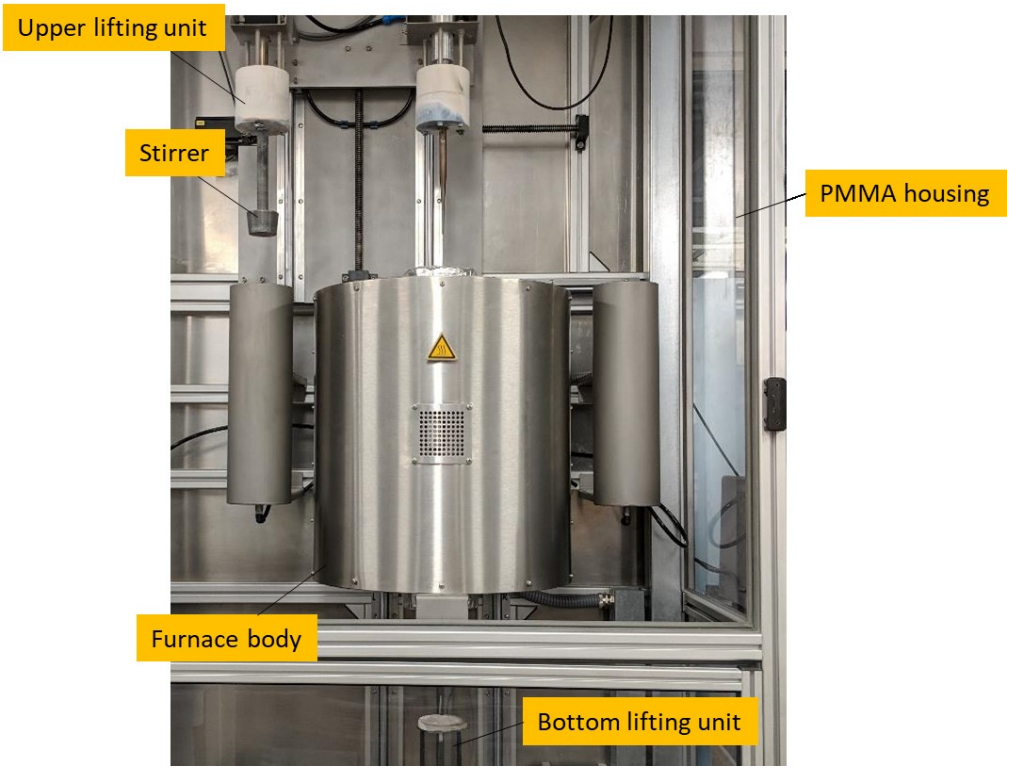


Figure 3.5. Photograph of the automated vertical tube furnace used in the stir casting process.

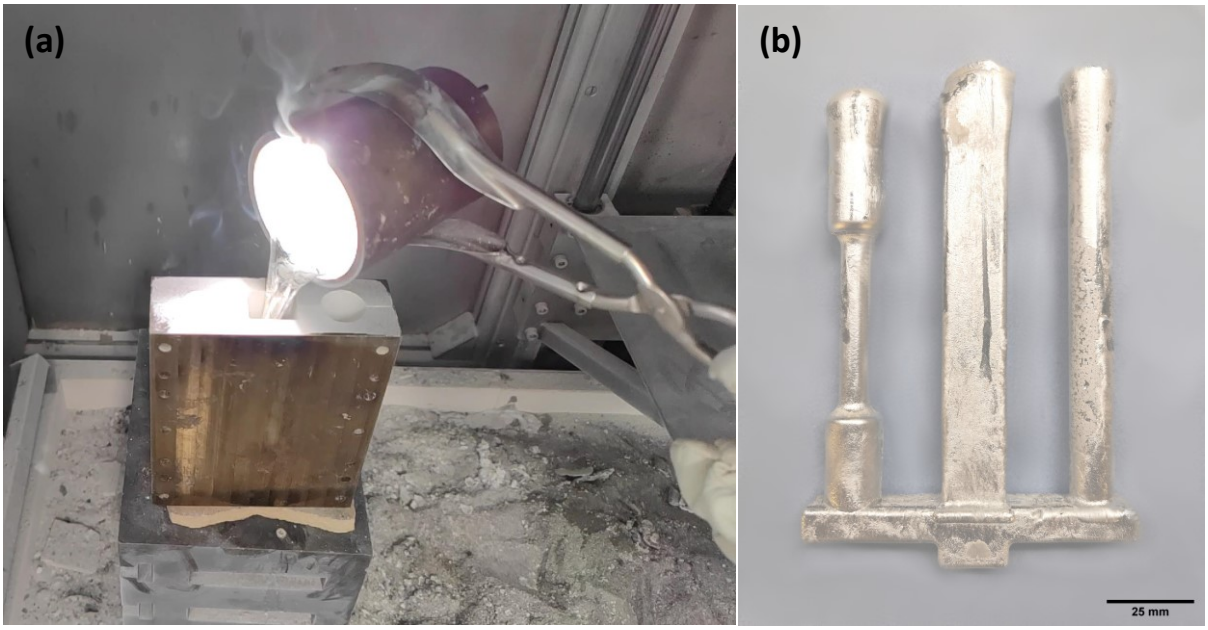


Figure 3.6. Photographs showing (a) gravity casting of AZ91 melt into the mould and (b) as-cast sample obtained after cooling down to room temperature.

3.2.3 CNTs addition to AZ91 melt

The CNTs powder sample was grinded using mortar and pestle for 10 min with a few mL of THF to break down any large clumps. The paste was transferred to a borosilicate glass bottle and the remaining THF was added to achieve a concentration of 1 mg/mL. (Note: The concentration is defined as the equivalent as-received CNTs amount per mL of THF.) Then, the mixture was ultrasonicated according to the sonication parameters in Section 3.2.1.1. Next, the dispersion was transferred to a crystallising dish and stirred at 60 °C overnight on a hotplate stirrer to completely remove the solvent. Simultaneously, three Al parcels, each with the dimension of 7.8 x 8.6 cm in width and length, respectively, and weighing about 0.2 g, were prepared. The dry products were collected and transferred evenly into the Al parcels which were then folded as shown in Figure 3.7. Before adding the parcels to the AZ91 melt, the parcels were kept in a vacuum environment using the drying vacuum oven. Once the furnace temperature reached 650 °C, the bottom lifting unit holding the crucible (see Figure 3.5) was brought down while the emergency Ar gas was activated to apply a large volume of protective gas in the area. Then, the parcels were added to the melt with a pair of tongs and the crucible was lifted again into the furnace. After waiting for a few minutes for the temperature to stabilise, stirring was carried out at the desired duration before the melt was finally casted.

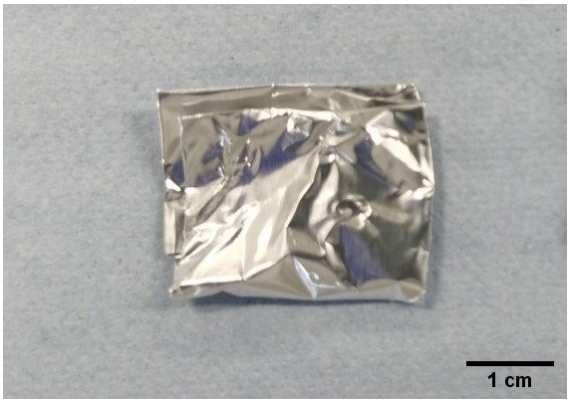


Figure 3.7. Photograph of an Al parcel containing the nanoparticle powder sample.

3.2.4 Post-processing treatment

As-cast samples which would be subjected to hot rolling were first machined into rolling slabs each with the dimension of 50 x 16 x 5 mm in length, width and height, respectively, as shown in Figure 3.8 (a). The solution (or homogenisation) heat treatment was carried out by heating the sample at 400 °C for 22 hours in air [185] with a chamber furnace (N 41/H, Naberthem GmbH, Lilienthal, Germany) followed by quenching in room temperature water. The hot rolling process was carried out using a rolling mill (DRM C130, Durston Tools, High Wycombe, UK) with a single 65 mm in diameter flat roller that was kept at room temperature at a rolling speed of 0.009 m/s. The procedure for each hot rolling pass is illustrated in Figure 3.9 where the rolling slab was preheated to 400 °C for 10 min, hot rolled at a 10% reduction per pass and quenched in a room temperature water in a quenching tank. The process was repeated to a total of eight hot rolling passes. Finally, cold rolling was performed by rolling the slab at room temperature at a 5% reduction to a final thickness of around 2.20 mm as shown in Figure 3.8 (b).

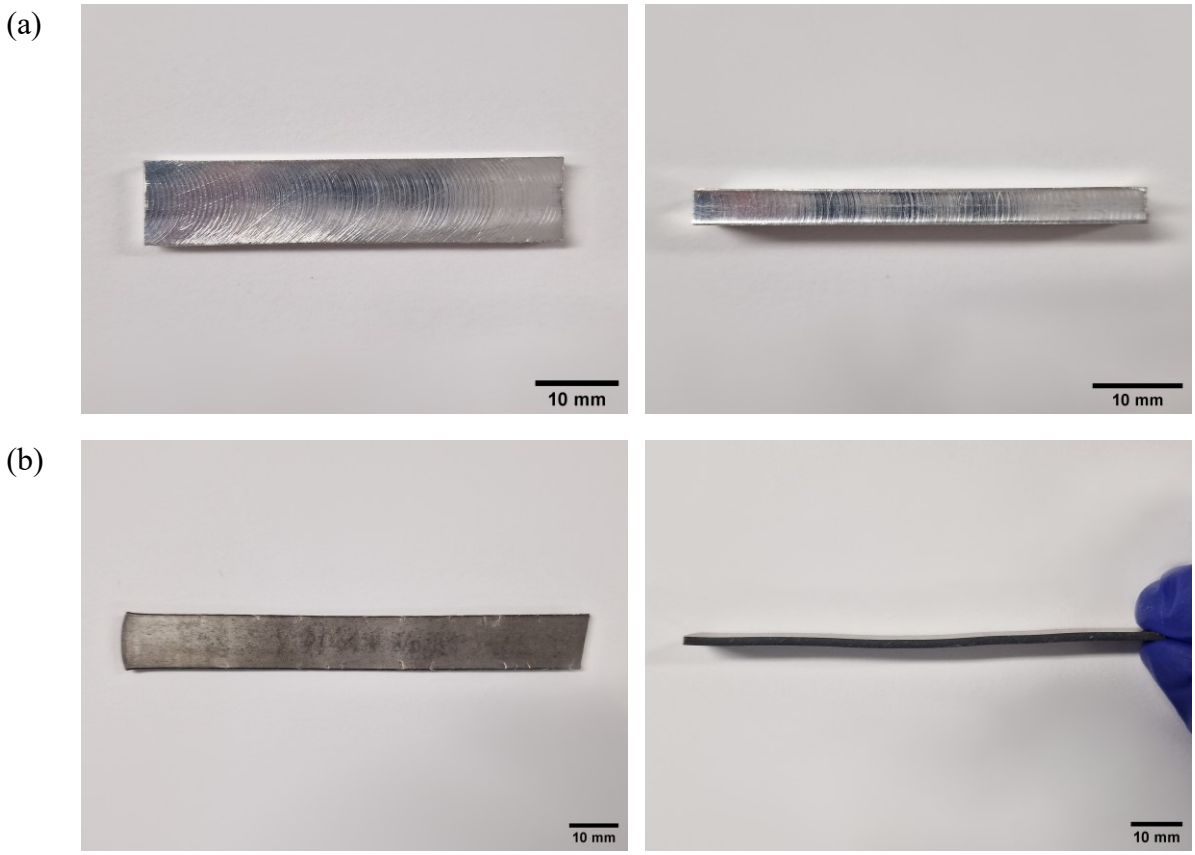


Figure 3.8. Photographs of the rolling slab produced (a) from the as-cast sample prior to rolling and (b) after the hot and cold rolling processes showing the parallel (left) and transverse (right) planes relative to the rolling direction.

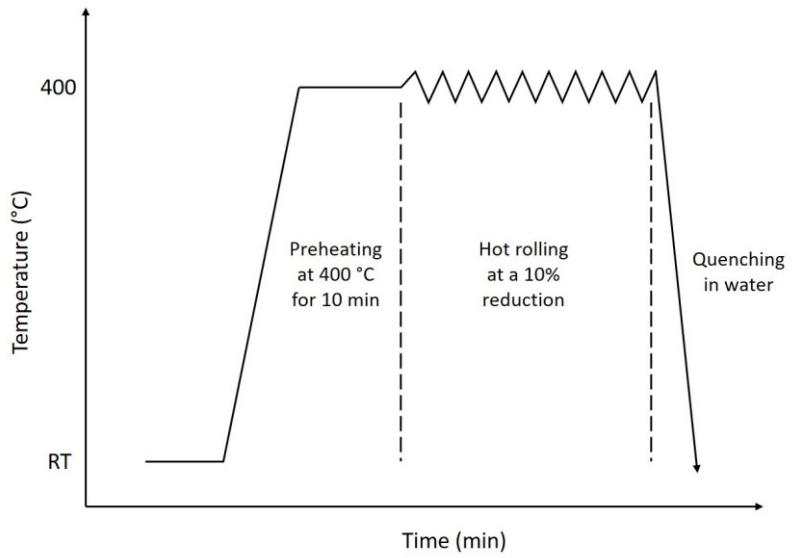


Figure 3.9. Schematic diagram of a single hot rolling pass.

3.2.5 Metallographic sample preparation

Prior to the microstructural and mechanical characterisation, a flat and polished surface of the sample may need to be produced. Firstly, the sample was sectioned with a hand saw and then mounted in 25 mL of resin (Black Phenolic Standard Mounting, Spectrographic Limited) by using a mounting press (CitoPress-20, Struers ApS, Ballerup, Denmark) using the following parameters: heating temperature of 180 °C, heating time of 3 min, heating pressure of 250 bar, high cooling rate and cooling time of 2 min. Then, manual grinding and polishing were carried out using a polishing machine (Saphir 350 E, ATM GmbH, Altenkirchen, Germany). Grinding was done successively with P180, P600, P1200, P2500 and P4000 grit size silicon carbide grinding papers (DISCS 250mm dia PSA, MetPrep Ltd.) using water and ethanol (only with P4000) as lubricants. Polishing was done with a napless porous synthetic cloth (Chemicloth M, MetPrep Ltd.) using 0.04-micron colloidal silica suspensions (OPUS non crystallising colloidal silica suspension, MetPrep Ltd.) as lubricant until a mirror-like finish was achieved. Finally, the polished sample was ultrasonicated in ethanol and isopropanol, successively, to remove any polishing lubricant contaminants.

3.3 Characterisation techniques

The techniques used to characterise the samples produced throughout this work are summarised in Table 3.2.

Table 3.2. Summary of the characterisation techniques used at different processes throughout this work.

Process	Technique	Purpose
Transformation of PMHS to SiOC and SiC	DSC	• Thermal analysis of PMHS • Determination of curing temperature and duration
	TGA-MS	• Thermal analysis of PMHS • Analysis of gaseous byproducts
	SEM	• Morphological characterisation of crosslinking and pyrolysis products
	IR spectroscopy	• Identification of polymer structures.
	XRD	• Identification of phase composition and crystallographic structure of crosslinking and pyrolysis products
Production of SiOC and SiC coated CNTs	SEM-EDX	• Morphological and elemental characterisation of CNTs samples
	TEM-EDX	• High resolution morphological and elemental characterisation of CNTs samples
	TGA	• Thermal analysis of CNTs samples
Dispersion of CNTs	OM	• Qualitative characterisation of degree of dispersion of CNTs samples
	UV-Vis spectroscopy	• Quantitative characterisation of degree of dispersion of CNTs samples
Characterisation of pure AZ91 and AZ91-CNTs composites	OM	• Microstructural imaging of polished cross sections • Grain structure imaging of etched cross sections
	SEM-EDX	• Microstructural and elemental characterisation of pure alloy and composite samples
	Archimedes density measurement	• Density and porosity measurement of pure alloy and composite samples
	Hardness measurement	• Hardness measurement of pure alloy and composite samples
	Tensile testing	• Tensile properties measurement of pure alloy and composite samples
	Compression testing	• Compressive properties measurement of pure alloy and composite samples

3.3.1 Infrared (IR) spectroscopy

Infrared (IR) spectroscopy is primarily used for the identification of molecular structure of polymers and it can also be used to monitor polymerisation reactions such as curing [186]. IR spectra are conventionally reported for the mid-infrared region which is in the range of 4000-400 cm^{-1} and a correlation table such as in Figure 3.10 is typically used to assign the absorption band to the vibrational mode associated with the specific functional group. In this work, an FT-IR spectrometer (Alpha-P, Bruker) equipped with a diamond attenuated total reflectance (ATR) accessory was used for the measurement of liquid and solid samples.

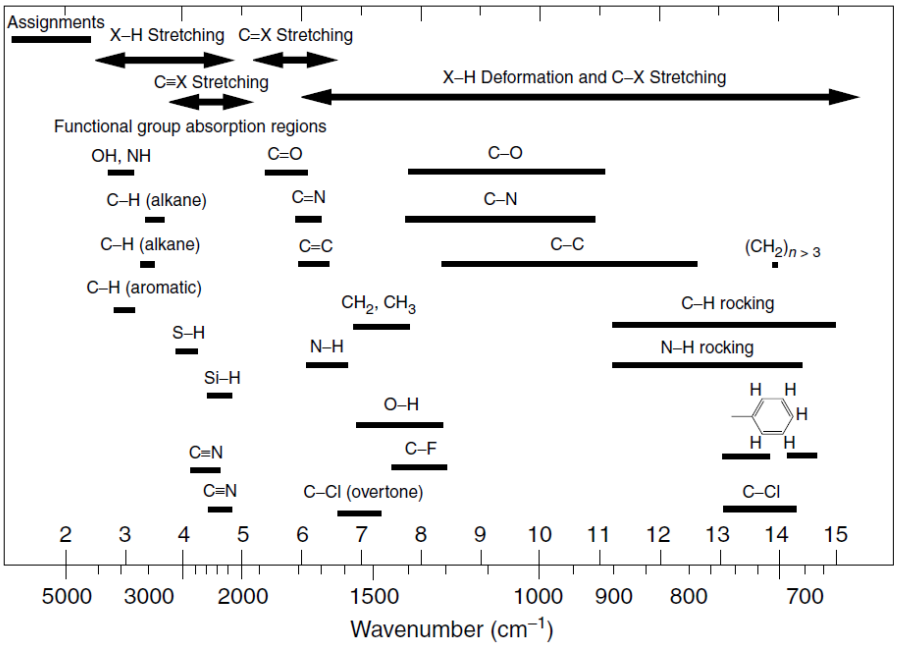


Figure 3.10. Correlation table for the assignment of absorption band to the specific functional group. Image reproduced from [187].

3.3.2 Ultraviolet-visible (UV-Vis) spectroscopy

Ultraviolet-visible (UV-Vis) spectroscopy is a simple technique used to measure the light absorbance of the sample in the wavelength range of 190-800 nm. The absorbed energy reduces the intensity of the light transmitted through the sample (I) from the intensity of the incident light (I_0). Therefore, transmittance (T) is defined as:

$$T = \frac{I}{I_0} \qquad \text{Equation 3.14}$$

while absorbance (A) is defined as:

$$A = -\log_{10} T = \log_{10} \frac{I_0}{I} \qquad \text{Equation 3.15}$$

According to the Beer-Lambert law, absorbance is related to ε (molar absorption coefficient of the analyte), b (light pathlength) and c (concentration of the solution) as follows:

$$E = \varepsilon bc \qquad \text{Equation 3.16}$$

UV-Vis spectroscopy had been used extensively in the literature to evaluate the dispersibility of single walled and multi walled CNTs in aqueous and organic solvents [188-191]. While bundled CNTs are hardly active in the UV-Vis region due to the electronic intertube coupling, clear absorption peaks can be observed from individual CNTs exfoliated from the bundle [192]. Therefore, it is possible to correlate between the absorbance in the UV-Vis spectrum with the amount of individually dispersed CNTs in a dispersion.

In this work, a double beam UV-Vis spectrophotometer (Lambda 365, Perkin Elmer, South Korea) was used to measure the absorbance of as-received and coated CNTs dispersions. The dispersion was prepared by sonicating the CNTs in THF for 30 min as described in Section 3.2.1.1 at a concentration of 1 mg of as-received CNTs equivalent per mL. Then, the suspension was centrifuged at 8000 rpm (equivalent to 10 375 g of relative centrifugal force) for 1 hr (SIGMA 4-16S, SciQuip Ltd., UK), and the supernatant was carefully decanted. The centrifugation process was repeated two more times until no large agglomerates were observed in the final supernatant solution. The supernatant was diluted by a factor of 10 prior to the UV-Vis absorbance measurement.

3.3.3 X-ray diffraction (XRD)

X-ray diffraction (XRD) is a fast and non-destructive technique which is primarily used for the identification of phase composition and crystallographic structure of a sample. In this work, XRD measurement was performed with a Panalytical X'Pert MPD Multi-Purpose Diffractometer operating under 40 kV at 40 mA. Powder samples were generally deposited on a monocrystalline silicon zero diffraction plate and flattened with a glass slide before the plate was fixed into the sample holder. CNTs powder samples, however, must be sealed with a Kapton film using an air-tight sample holder to prevent CNTs from becoming airborne. On the other hand, solid samples could just be fixed on the sample holder with a plasticine before flattened with a glass slide.

3.3.4 Thermogravimetric analysis (TGA)

Thermogravimetric analysis (TGA) works by measuring the change in the sample mass as a function of temperature in a controlled atmosphere such as air or inert gas. This technique can be used to measure the thermal stability of materials and to provide information relating to specific chemical occurrences such as decomposition, oxidation and reduction processes. Additionally, the TGA instrument can also be coupled with a mass spectrometer (MS) to obtain qualitative information on the evolved gases during the heating procedure.

TGA measurement was done with a Discovery TGA (TA Instruments, Elstree, UK) under air or nitrogen (N_2) at a flow rate of 50 mL/min. For each measurement, 2-3 mg of sample was loaded to a platinum pan. TGA-MS was carried out with a METTLER TGA/DSC 1 (Mettler-Toledo International, Beaumont Leys Leicester, UK) coupled with an HPR-20 QIC R&D mass spectrometer (Hiden Analytical Ltd., Warrington, UK).

3.3.4.1 Determination of coating concentration in coated CNTs samples

In this work, TGA was used to determine the coating concentration in the coated CNTs samples by heating the sample from room temperature to 100 °C at 10 °C/min, dwelling at 100 °C for 1 hr to remove any moisture and heating from 100 to 800 °C at 10 °C/min. The measurement will need to be performed for the as-received CNTs and the coated CNTs of interest. Then, the following equation is generally used to determine the coating concentration:

$$Coating\ concentration\ in\ coated\ CNTs\ sample = Residual\ weight\ \%\ of\ coated\ CNTs\ at\ 800\ ℃ - Residual\ weight\ \%\ of\ as - received\ CNTs\ at\ 800℃$$

Equation 3.17

3.3.5 Differential scanning calorimetry (DSC)

Differential scanning calorimetry (DSC) measures the change in the difference in the heat flow rate of a sample and a reference material as a function of temperature. This technique is used to characterise a broad range of materials especially polymers in terms of their endothermic or exothermic processes by evaluating the heat input or output from the sample, heat flow rates, total and partial heat of reaction, and characteristic temperature of a reaction or transition [193]. Some parameters such as the type of DSC pan (crimped, hermetic, pinhole or open pan), sample size and heating rate should be considered to achieve reliable and reproducible measurement [194].

DSC was performed using a Discovery DSC (TA Instruments, Elstree, UK) under air or N_2 atmosphere. 4-6 mg of sample was loaded to a Tzero aluminium pan while no sample was added to the reference pan. In both cases, no lids were used (i.e. open pans) to allow for the

maximum interaction between the sample and the controlled atmosphere, and for the escape of the volatile byproducts.

3.3.5.1 Degree of cure measurement

The degree of cure (or crosslinking) measurement was involved in the determination of curing procedure of PMHS which will be discussed in Section 4.2.1. Initially, DSC measurement of the uncured sample was carried out and the total heat of reaction (H_T) was measured from the area under the exothermic peak. Then, DSC measurement was carried out on the cured sample and the heat of reaction (H_S) was determined from the area under the exothermic peak. These values were used to calculate the degree of cure as follows [195, 196]:

$$Degree\ of\ cure = \left(1 - \frac{H_s}{H_T}\right) \times 100\% \qquad \text{Equation 3.18}$$

3.3.6 Optical microscopy (OM)

Optical microscopy (OM) (or also light microscopy) uses visible light (which is in the range of 400-700 nm) and a series of lenses to magnify the images of small samples down to the submicron level [197]. In this work, a light microscope (Olympus BX53M) was used to characterise the dispersion of CNTs samples and to characterise the microstructure of polished AZ91 samples. For the dispersion characterisation, the CNTs sample was ultrasonicated in 20 mL of THF according to the parameters in Section 3.2.1.1 at a concentration of 1 mg equivalent of as received CNTs per mL of THF in a glass vial. Then, liquid was drawn from the middle location of the solution in the glass vial using a pipette and a single drop (less than 1 mL) was deposited on a glass well slide. The dispersion was tightly sealed in the well using a cover slip and some vacuum grease before imaging was carried out under light microscope.

3.3.7 Scanning electron microscopy (SEM)

Scanning electron microscopy (SEM) is an invaluable technique for the morphological characterisation of micro- and nanostructured materials. Some micro analysis techniques such as energy-dispersive X-ray spectroscopy (EDX) and electron backscatter diffraction (EBSD) can also be carried out in SEM to perform elemental and structural analyses of the sample. EDX is a convenient technique for elemental identification and quantification of the sample meanwhile EBSD, which requires a higher energy than secondary electron imaging, can provide crystallographic information of the specimen such as the crystal orientations, texture, grain size and grain boundaries [198, 199].

In this work, SEM was performed with an Auriga Cross Beam (Carl Zeiss NTS GmbH, Oberkochen, Germany) at an acceleration voltage of 5 kV and a working distance of 5 mm using an in-lens detector for a high-resolution image acquisition. Chemical analysis with EDX was carried out on the Oxford Instruments INCA where a higher voltage may be used. The sample was mounted on a sample stub using carbon adhesive to provide a conductive pathway and to prevent charging. If necessary, other alternatives were also employed such as the application of conductive silver paint and the coating of sample with a thin chromium (Cr) coating via sputtering. SEM had also been used to characterise dispersed CNTs samples as follows: the CNTs sample was ultrasonicated in 20 mL of THF according to the parameters in Section 3.2.1.1 at a concentration of 1 mg equivalent of as received CNTs per mL of THF in a glass vial. Then, liquid was drawn from the middle location of the solution in the glass vial using a pipette and a single drop (less than 1 mL) was deposited on an Al foil surface which had been adhered to an SEM sample stub by using carbon adhesive. The THF solvent was completely dried in air before imaging under SEM.

3.3.8 Transmission electron microscopy (TEM)

Transmission electron microscopy offers a magnificent spatial and analytical resolution making it an essential tool for the characterisation of nanoscale materials. However, due to its sampling size, it is strategic to understand the material at a low magnification first, for example by using visible light microscopy and SEM, before TEM is considered. Typically, bright field imaging is done to generate images in TEM where the mass and thickness of the specimen region influences the image brightness meanwhile the contrast can be enhanced by inserting the objective aperture [200]. Similar to SEM, X-ray analysis techniques such as EDX can also be employed in TEM to obtain qualitative and quantitative elemental information of the specimen [201].

In this work, TEM was performed using a JEOL STEM/TEM 2100 Plus at an operating voltage of 200 kV and a beam current of 104-108 μA. Image acquisition, processing and analysis were done in Gatan Microscopy Suite. EDX was carried out with Oxford Instruments ultra-thin window. Powder samples were prepared by dispersing a small amount of powder (less than 1 mg) in ethanol using bath sonication. A TEM grid (lacey carbon films on copper TEM grids, Agar Scientifics) was immersed in the solution for a few seconds and then dried in air on a filter paper for a few minutes. A single tilt holder was used to load the grid into the TEM instrument.

3.3.9 Density measurement

Density measurement was performed based on the Archimedes method with an electronic balance and a density determination kit (OHAUS) using water as the auxiliary liquid. This technique offers a high accuracy and reproducibility density determination for bulk solid

samples [202]. At least three measurements were performed for each sample. The density of the sample ρ was calculated as follows:

$$\rho = \frac{A}{A-B}(\rho_0 - \rho_L) + \rho_L \qquad \text{Equation 3.19}$$

where A is the weight of sample in air, B is the weight of sample in water, ρ_0 is the temperature-dependant density and ρ_L=0.0012 g/cm^3 is the air density. Subsequently, the porosity was calculated based on the theoretical and measured densities as follows:

$$Porosity = \frac{Theoretical\ density - Measured\ density}{Theoretical\ density} \times 100\% \qquad \text{Equation 3.20}$$

where theoretical density was measured based on the theoretical density of the material and the rule of mixture in the case of the composites. The measured density was calculated using Equation 3.19.

3.3.10 Grain size measurement

Grain size measurement was carried out to determine the grain coarsening or refinement effect in the material. Colour etching was performed to reveal the grains of Mg matrix samples according to the method developed by Maltais et. al. [203, 204]. Polished specimens (prepared as described in Section 3.2.5) were immersed in an etching solution consisting of glacial acetic acid, distilled water and ethanol in the ratio of 1:44:156 by volume for 180-240 seconds. Then, they were rinsed with ethanol and dried with compressed air. The etched specimens were examined under a light microscope (Olympus BX53M) using a U-TP530 wave plate and a U-AN360-3 rotatable analyser (Olympus, Japan). The optical contrast between the grains was

achieved under the polarized light due to the birefringence produced from the etched films which were aligned to the orientation of the underlying grains [203].

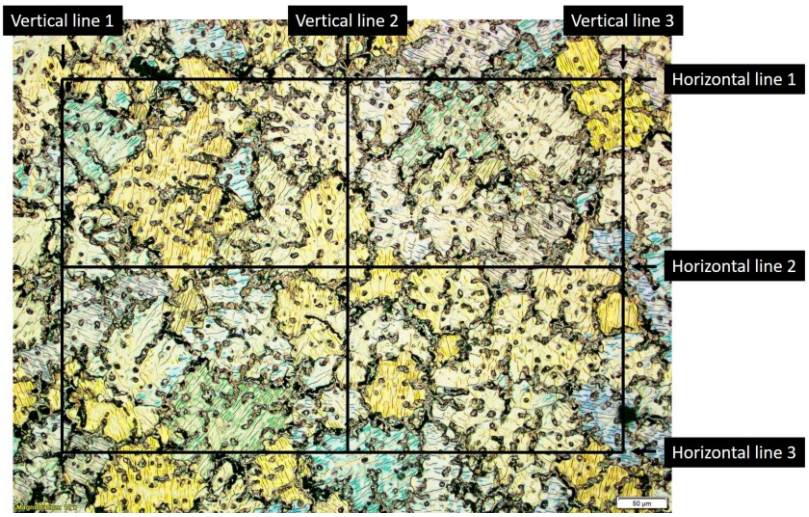


Figure 3.11. Optical micrograph of the etched surface of Mg matrix sample showing six test lines (three horizontal and three vertical lines) drawn for the measurement of average grain size using the mean linear intercept method.

The average grain size ($\bar{d}$) was measured using the linear intercept method [205] according to the following equation:

$$\bar{d} = \frac{L}{P} \qquad \text{Equation 3.21}$$

where L is length of the test line and P is the grain boundary intersection count. Six principal test lines consisting of three horizontal and three vertical lines were drawn for each image field as shown in Figure 3.11. P is determined based on the number of times the test line cuts across a grain boundary (counted as 1 intersection), is tangent to the grain boundary (counted as 1 intersection) or coincides with the junction of three grains (counted as 1 ½ intersections). A sufficient number of images were acquired until at least 500 grain boundary intersections were counted so that a reliable average grain size can be determined for each sample [206].

3.3.11 Hardness test

Hardness of a material can be defined as its resistance to localized plastic deformation [66]. Indentation hardness test is a simple and fast technique to characterise the mechanical property of a material such that other mechanical properties such as the tensile strength can also be extrapolated from the hardness data [207].

In this work, macroindentation and microindentation tests were performed on polished specimens (prepared as described in Section 3.2.5) using a Vickers square-based pyramidal diamond indenter [208]. Macroindentation test was carried out using a 6030 LKV Vickers hardness tester (Zwick Roell Indentec, Brierley Hill, UK) with a load of 3kgf and load time of 10 s. Microindentation test was carried out using a Wilson VH1202 microhardness tester (Buehler, Shanghai, China) with a load of 1 kgf and load time of 10 s. The Vickers hardness (HV) value was determined as follows:

$$HV = 1.8544 \times \frac{F}{d^2} \qquad \text{Equation 3.22}$$

where F is the indentation test force in kilograms-force (kgf) and d is the mean indentation diagonal length as shown in Figure 3.12. Indentation diagonal length and the hardness value were determined and calculated by using an image analyser software on the computer connected to the indenter equipment.

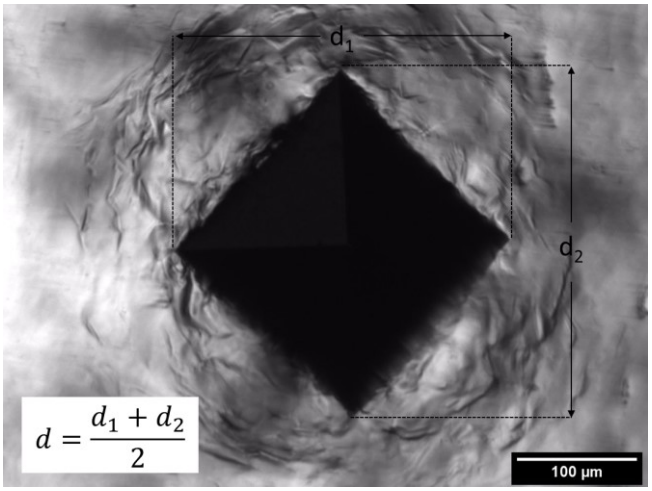


Figure 3.12. Optical micrograph showing a Vickers indentation made on a Mg matrix sample and the measurement of the mean indentation diagonal length (d) in the inset.

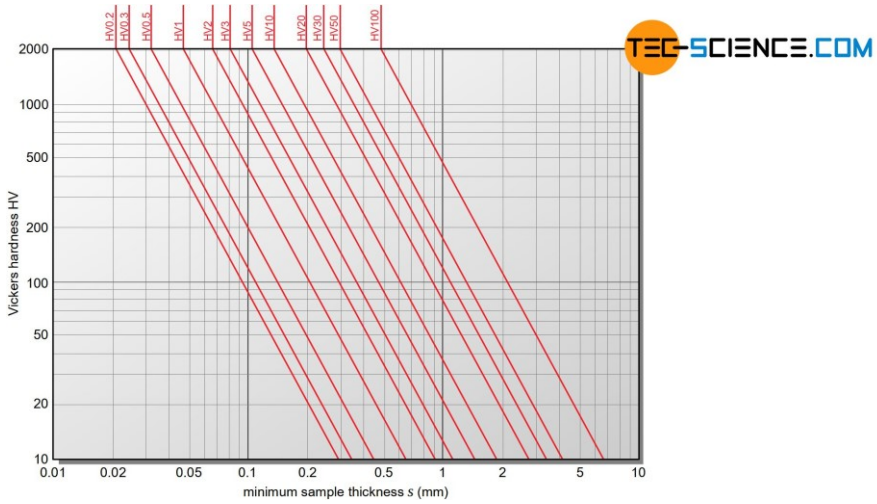


Figure 3.13. Minimum sample thickness required based on the indentation load and Vickers hardness value. Image reproduced from: https://www.tec-science.com/material-science/material-testing/vickers-hardness-test/

At least three specimens were tested for each sample. The thickness of the specimen was kept at least 1.5 times as large as the diagonal length of the indentation. A chart as shown in Figure 3.13 can be used to determine the minimum specimen thickness according to the load and the hardness value. Depending on the size of the specimen, between 5-9 indentations were made on each specimen. The spacing between indentations and from the edge was kept 2.5 times the

indentation diagonal length [208] to prevent the overlapping of the plastic-elastic zones of the adjacent indentations which could influence the hardness measurement [209].

3.3.12 Tension test

Tension test is used to assess the strength and ductility of materials under a uniaxial tensile load [210] as illustrated in Figure 3.14 (a). During the testing, the specimen is elongated at a constant rate while the instantaneous applied load and the elongation are measured simultaneously [66]. Load and elongation are normalised to stress (σ) and strain (ϵ), respectively, according to the following equations to produce a stress-strain curve as shown in Figure 3.15.

$$\sigma = \frac{F}{A_0} \qquad \text{Equation 3.23}$$

$$\epsilon = \frac{l - l_0}{l_0} \qquad \text{Equation 3.24}$$

where F is the instantaneous applied load, A_0 is initial the cross-sectional area of the specimen, l is the instantaneous length and l_0 is the initial length of the specimen [66].

In a stress-strain curve, elastic deformation is represented by a linear relationship whereby the slope corresponds to the modulus of elasticity (E) (or Young's modulus). As the load increases, plastic deformation occurs whereby the material is permanently deformed and the yield strength which is the stress at which plastic deformation of the material has begun can be determined. Since the precise point is difficult to measure, yield strength is determined, conventionally, from the intersection of the stress strain curve and a line drawn parallel to the elastic portion of the stress strain curve at a strain offset of 0.2% as drawn in Figure 3.15. Tensile strength (or also called ultimate tensile strength) is the maximum tensile stress that can

be sustained by the material at which a small constriction or neck begins to form in the material that progresses towards fracture [66, 211, 212].

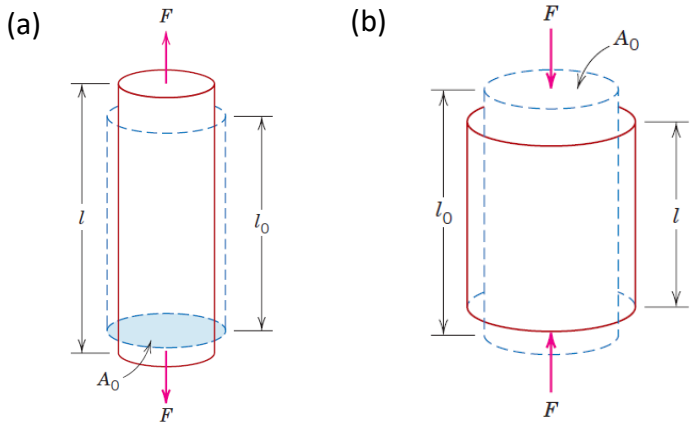


Figure 3.14. Schematic diagram of (a) a uniaxial tensile loading which produces an elongation and a positive linear strain and (b) a uniaxial compressive loading which produces a contraction and a negative linear strain. Images reproduced from [66].

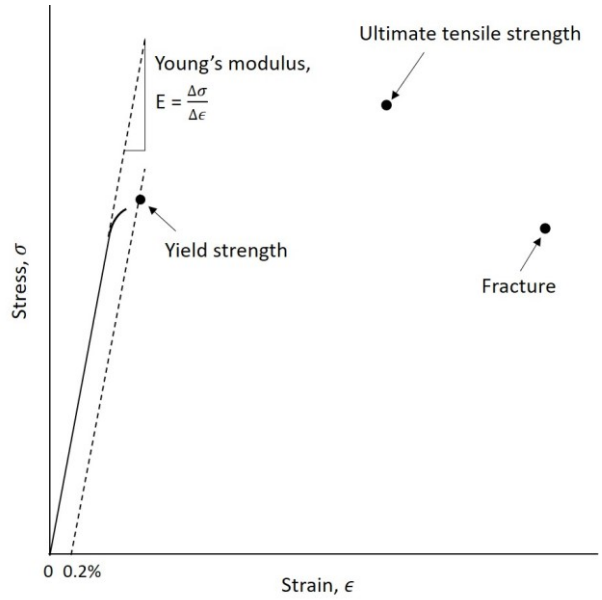


Figure 3.15. Typical engineering stress-strain curve under tensile load.

In this work, tensile testing was performed using a 50 kN Instron 5969 test machine and an Imetrum optical strain measurement system at a strain rate of 0.016 mm/s. Each test specimen was machined into a "dogbone" configuration with a gauge length of 17 mm, width of 3 mm and thickness according to the original sample's thickness (see Figure A.6 in Appendix for the tensile test specimen configuration).

3.3.13 Compression test

Compression test involves the application of a uniaxial compressive load and a subsequent contraction of the specimen along the direction of the stress [213] as shown in Figure 3.14(b). Equation 3.23 and Equation 3.24 can be used to determine the compressive stress and strain but instead with the compressive load (F) and strain taken to be negative since the instantaneous length (l) is smaller than the initial length (l_0). Compressive properties are interesting for the assessment of materials which are subjected to compressive or bending loads in material applications such as structural support and in material processing such as forging and rolling [214]. A typical compressive stress-strain curve can also be represented by Figure 3.15 but instead with ultimate compressive strength as the maximum compressive stress that the material can sustain [211]. Compression testing is a convenient method to determine the stress-strain response of materials under large plastic strains which is limited in tensile testing due to the unstable flow of stress that leads to necking. However, compression testing can be affected by errors due to specimen buckling and barrelling which create nonuniform stress and strain distributions. Buckling, which occurs due to unstable material deflection under compressive stresses, can be mitigated by using a low length-to-diameter ratio (of less than 2) specimen geometry and by ensuring that the loading train is properly aligned. On the other hand, barrelling occurs due to friction at the loading faces of the specimen and can be reduced by using lubricant at the loading surfaces of the specimen [214, 215].

In this work, compression testing was performed using a 50 kN Instron 5969 test machine and an Imetrum optical strain measurement system at a strain rate of 0.016 mm/s. At least five specimens must be tested for each sample [213] and each test specimen was produced in the form of solid circular cylinder with a length of 7 mm and diameter of 5 (i.e. length to width ratio of 1.4).

Chapter 4 : Development of CNTs coating process

4.1 Introduction

Polysiloxanes are a versatile group of preceramic polymers which can be converted to SiOC and SiC via heat treatment processes. The use of preceramic polymers offers a feasible route for the production of ceramics in comparison to solid state reaction sintering which can be more complex and requires much higher processing temperatures [136, 216]. As discussed in Section 2.3.3, various types of polysiloxanes can be used to produce monolith SiOC and SiC ceramic products. Subsequently, polysiloxane-derived SiOC and SiC composites had also been fabricated using different types of fillers [134, 153, 217-220]. However, to the author's knowledge no attempts had been made to use polysiloxane as a preceramic precursor for the coating of SiOC or SiC on the CNTs. Inspired by the use of polycarbosilane as a precursor for SiC coating on CNTs in a few works [141-144], polymethylhydrosiloxane (PMHS) was used as a preceramic precursor for the coating of CNTs with either SiOC or SiC in this work. This coating technique will not only allow the coating of either SiOC or SiC using the same polysiloxane precursor, but it is also a non-damaging coating process that can potentially offer a more uniform coating on the CNTs in comparison to some other known techniques for producing SiC coated CNTs [117, 145, 221].

Since various curing and pyrolysis techniques can be used for the conversion of polysiloxane precursors to SiOC and SiC, this chapter will initially demonstrate the conversion process of PMHS to SiOC and SiC. The determination of a simple, catalyst-free curing procedure is

demonstrated, and the importance of crosslinking is discussed. Then, the behaviour of the polymer during pyrolysis is studied and the crystallographic structure and thermal properties of the pyrolysis products are investigated. Subsequently, the application of PMHS as the coating precursor is explored. The coating behaviour of the polymer on the CNTs is investigated through a preliminary production of SiOC coated CNTs.

4.2 Transformation of polymethylhydrosiloxane (PMHS) to silicon oxycarbide (SiOC) and silicon carbide (SiC)

Polysiloxane precursor can be converted to SiOC/SiC ceramics via the crosslinking and pyrolysis processes as explained in Section 2.3.3 and summarised in Figure 4.1. The next two sections explain the procedures established in this work and the processes occurring during crosslinking and pyrolysis.

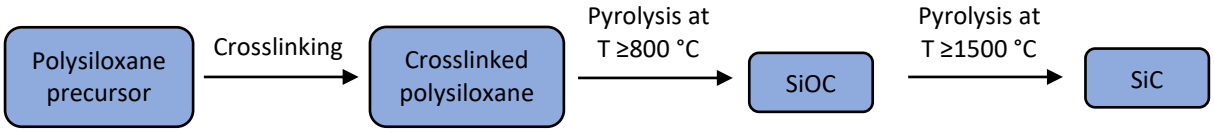


Figure 4.1. Process flowchart for the conversion of polysiloxane precursor to SiOC and SiC ceramics.

4.2.1 Crosslinking via thermal oxidation

Crosslinking (or curing) is an essential step to prevent the depolymerisation of polymer at low temperatures and to produce a good ceramic yield upon pyrolysis. Various methods can be employed for the crosslinking of PMHS (see Table 2.3) which mainly involve the use of crosslinkers and catalysts to induce crosslinking via hydrosilylation reactions [155, 164, 167-170]. While this is a popular technique for curing PMHS, the presence of heavy metal catalysts may compromise the structural integrity and thermal stability of the CNTs coating and diminish the lightweight quality of the final composite materials. Therefore, this work aims to establish a simple curing process without using catalysts or additives. The high concentration of Si-H

bonds in PMHS can be exploited to promote the crosslinking of the polymer by a simple heat treatment in the presence of oxygen. A few parameters were investigated to establish an optimum curing procedure for PMHS via heat treatment, namely the curing environment, temperature(s) and duration.

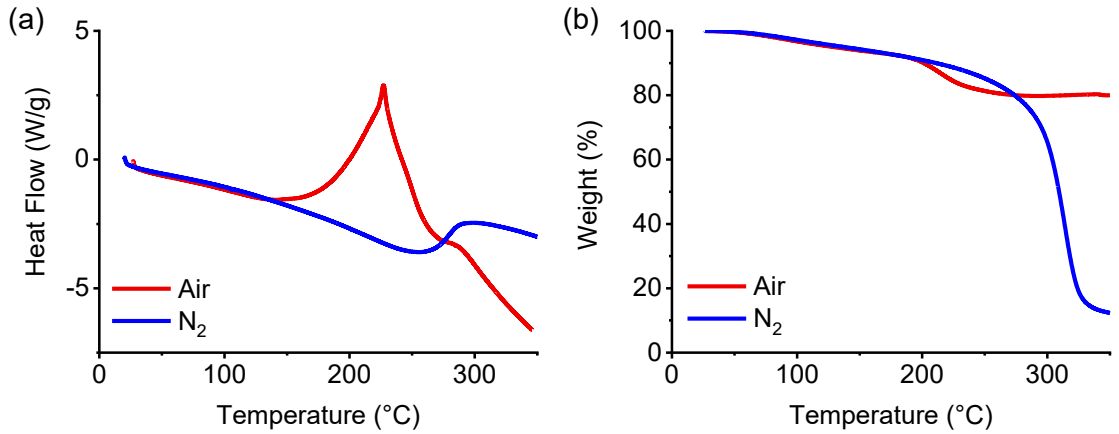


Figure 4.2. (a) DSC and (b) TGA curves of as-received PMHS under heating in air and N_2.

For the purpose of crosslinking at low temperatures, the thermal reactivity of PMHS in air and N_2 (i.e. inert atmosphere) was investigated using DSC by heating the polymer from room temperature to 350 °C at a heating rate of 10 °C/min as shown in Figure 4.2 (a). Heat treatment of PMHS in air exhibited a large exothermic peak at 227 °C and a broad peak at 289 °C which can be attributed to bond forming reactions (i.e. crosslinking). On the other hand, heating the polymer in N_2 led to an endothermic reaction with a peak temperature of 300 °C which indicates bond-breaking reactions (i.e. depolymerisation). Furthermore, TGA measurement under the same conditions (Figure 4.2 (b)) showed that the thermal stability of PMHS was higher in air than in N_2 such that a large yield (i.e. 80%) was retained after the heat treatment of PMHS in air up to 350 °C. On the other hand, the polymer was almost completely decomposed (i.e. 12% yield) when heated in N_2. Therefore, these findings indicate that air is a

suitable curing environment for the crosslinking of PMHS meanwhile heating in inert atmosphere at low temperatures would only lead to the decomposition of the polymer.

The appropriate curing temperature(s) and duration were determined by identifying the onset temperature(s) of the exothermic peaks and heating the polymer isothermally at that temperature for an appropriate amount of time until a maximum degree of cure was achieved. The degree of cure was calculated according to Equation 3.18 whereby the total heat of reaction (H_T) was measured from the area under the exothermic peaks of the as-received (i.e. uncrosslinked) PMHS. On the other hand, the heat of reaction (H_s) was obtained from the area under the exothermic peaks of the PMHS sample that had been subjected to a heat treatment in air. Step by step DSC experiments and degree of cure measurement for the determination of curing temperature(s) and duration are provided in Appendix A.7. Figure 4.3 shows the DSC heat ramp measurement of PMHS samples which had been subjected to various curing treatments as described in Table 4.1. Isothermal heating at the onset temperatures of the exothermic peaks led to an increase in the degree of cure of the polymer until a completely crosslinked sample, crosslinked PMHS D, was obtained where no remaining exothermic peaks could be observed in the DSC curve. Based on the DSC experiments, the optimum curing procedure of PMHS was established through the heat treatment in air at a heating rate of 10 °C/min at 160 °C for 45 min, 170 °C for 75 min, 190 °C for 30 min and 210 °C for 30 min, and followed by cooling down to room temperature.

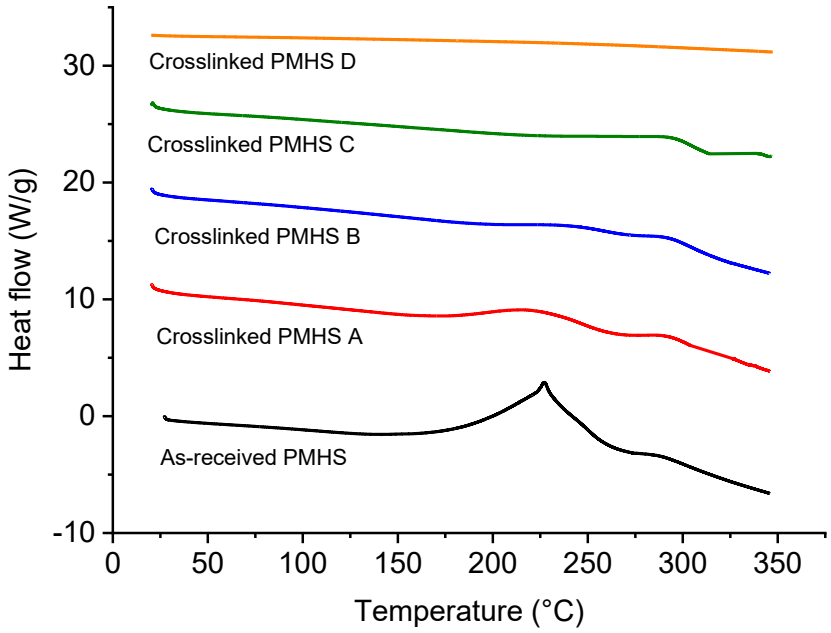


Figure 4.3. DSC curves of as-received and crosslinked PMHS samples. The crosslinked PMHS samples had been subjected to various curing treatments as described in Table 4.1.

Table 4.1. Degree of cure measurement of as-received and crosslinked PMHS samples based on the DSC measurement in Figure 4.3.

Sample	**Applied curing treatment (in air)**	**Total heat of reaction, H_T (J/g)**	**Heat of reaction, H_S (J/g)**	**Degree of cure (%)**
As-received PMHS	None	1482.4	-	0
Crosslinked PMHS A	160 °C for 45 min	-	503.4	66.0
Crosslinked PMHS B	160 °C for 45 min + 170 °C for 75 min	-	192.0	87.0
Crosslinked PMHS C	160 °C for 45 min + 170 °C for 75 min + 190 °C for 30 min	-	70.4	95.3
Crosslinked PMHS D	160 °C for 45 min + 170 °C for 75 min + 190 °C for 30 min + 210 °C for 30 min	-	0	100.0

The curing procedure was simulated using TGA as shown in Figure 4.4 and the curing yield was determined to be 87.1% (see Equation 3.1 for the calculation of curing yield). The mass

loss experienced during crosslinking was due to the evolution of water as shown by the mass spectrometry measurement in Figure 4.4. Water (H_2O, m/z = 18) was evolved in the range of 157 to 170 °C which is consistent with the temperature range of the large exothermic peak observed in the DSC measurement in Figure 4.2. This observation suggests that the crosslinking of PMHS in air had occurred via the condensation reactions between the polymeric chains.

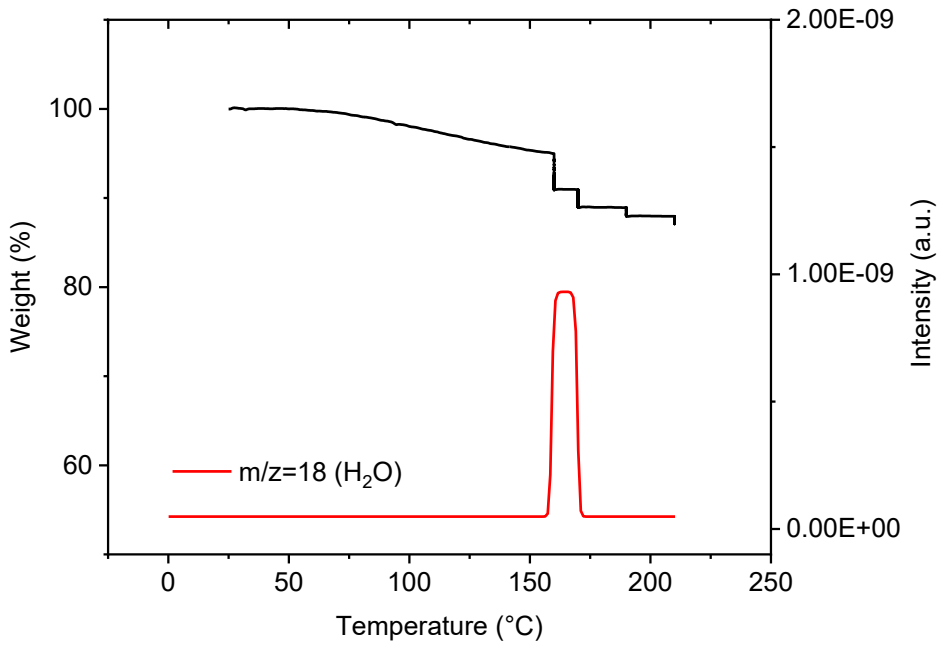


Figure 4.4. TGA-MS of as-received PMHS in air under the established curing procedure.

The molecular structure of the cured PMHS was investigated with FT-IR spectroscopy as shown in Figure 4.5. In comparison to the as-received PMHS and the partially cured PMHS (heat treated in air only at 210 °C for 30 min), the completely cured PMHS showed reduced intensity for the Si-H peak at 2100 cm^{-1} and the Si-CH_3 peaks at 1260, 840 and 755 cm^{-1} suggesting that these bonds had been highly involved in the crosslinking reactions. The reduced intensity observed for Si-O-Si peak in the cured PMHS products in the range of 1130-1100

cm^{-1} may be interpreted as an effect of crosslinking as the bond vibrations were likely reduced due to the rigidity of the crosslinked network. Additionally, a small Si-C peak could also be detected in the cured PMHS samples at 800 cm^{-1} indicating the presence of SiO_xC_{4-x} (where $0 \leq x \leq 4$) phases at this stage. XRD measurement of the completely cured PMHS will be discussed together with the pyrolysis products in the next section.

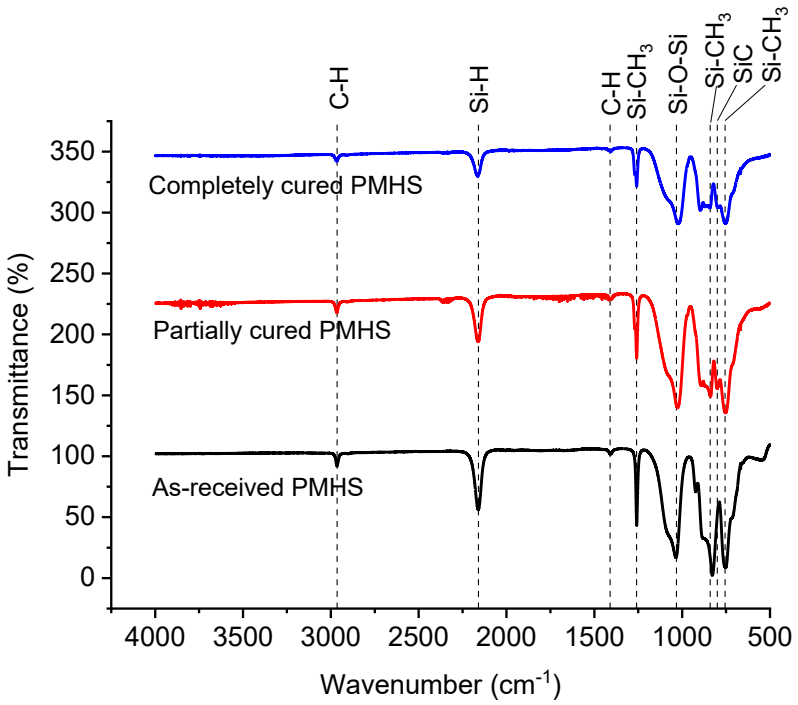


Figure 4.5. FT-IR spectra of as-received, partially cured and completely cured PMHS.

Based on the thermal analysis of the curing process and the characterisation of the cured product, the crosslinking reactions had most likely occurred via the oxidation of Si-H and Si-CH_3 groups to produce silanols (Si-OH). Then, the condensation of silanols would lead to the crosslinking of the polymeric chains via Si-O-Si bonding and the evolution of water as byproducts [153, 154]. The involvement of Si-H and Si-CH_3 bonds during crosslinking can be confirmed from the IR spectroscopy results in Figure 4.5 meanwhile the evolution of water as crosslinking byproduct is consistent with the TGA-MS measurement in Figure 4.4. The crosslinking mechanism of PMHS via heat treatment in air may occur as follows:

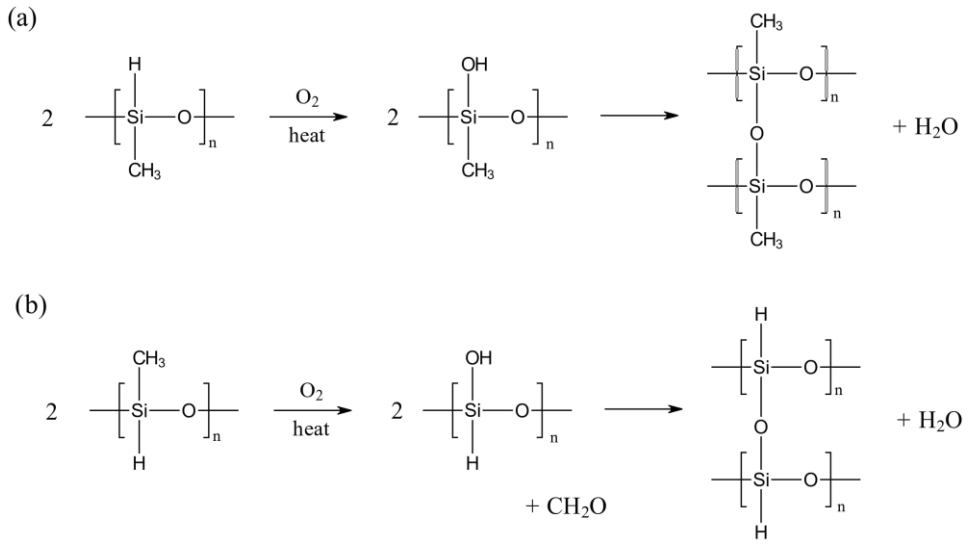


Figure 4.6. Possible mechanism for the crosslinking of PMHS via heat treatment in air by the oxidation of (a) Si-H and (b) Si-CH_3 groups which leads to the formation of Si-O-Si bonds and the evolution of water.

The effect of crosslinking on the pyrolytic behaviour of the polymer was investigated using TGA by simulating the pyrolysis process via heat treatment in N_2 from room temperature to 800 °C at a heating rate of 10°C/min as shown in Figure 4.7. The pyrolysis and ceramic yield were notably improved for the completely cured PMHS in comparison to the as-received and partially cured PMHS as also reported in Table 4.2 (see Equation 3.2 and Equation 3.3 for the calculation of pyrolysis and ceramic yield, respectively). The completely cured PMHS also exhibited an obvious improvement in thermal stability in the low to moderate temperature range such that the decomposition of the polymer only started to occur at 342 °C in comparison to the uncrosslinked PMHS which began to decompose immediately upon heating and was completely decomposed at 360 °C. On the other hand, the partially cured PMHS showed a lower onset degradation temperature at about 200 °C and a lower ceramic yield than those of the completely cured PMHS which highlights that an incomplete crosslinking would inevitably lead to the volatilisation of the remaining uncrosslinked chains and the reduction in ceramic yield. This investigation shows that the crosslinking of PMHS is an essential step to prevent

the decomposition of the polymer at low to moderate temperatures which subsequently leads to an enhancement in the ceramic yield.

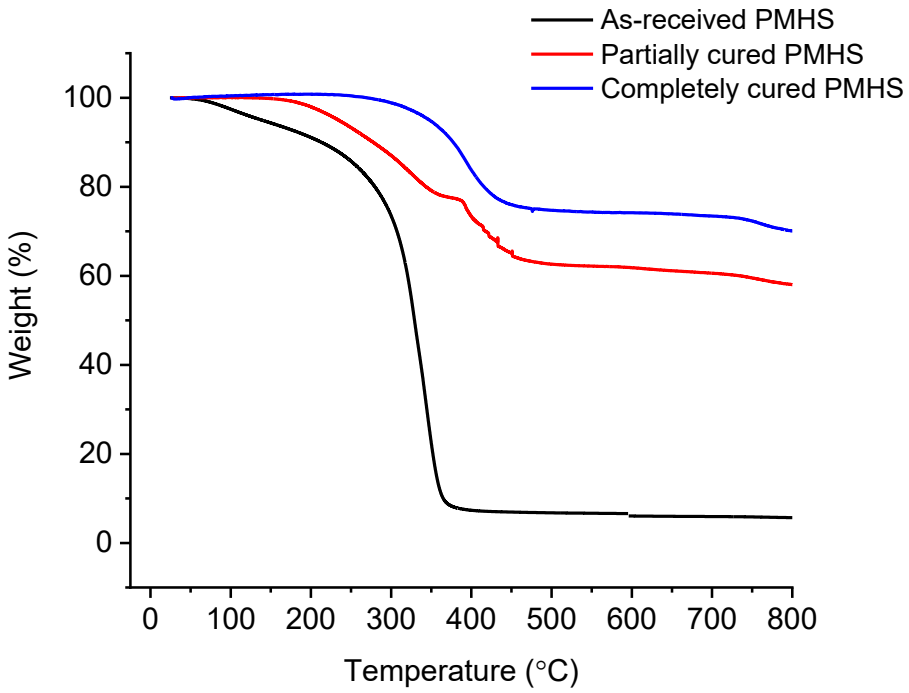


Figure 4.7. TGA of as-received, partially cured and completely cured PMHS in N_2.

Table 4.2. Curing, pyrolysis and ceramic yield of as-received, partially cured and completely cured PMHS based on the TGA investigation in Figure 4.7.

Sample	**Curing yield (%)**	**Pyrolysis yield at 800 °C (%)**	**Ceramic yield at 800 °C (%)**
As-received PMHS	-	5.7	5.7
Partially cured PMHS	88.9	56.2	50.0
Completely cured PMHS	85.5	68.1	58.2

4.2.2 Ceramisation via pyrolysis

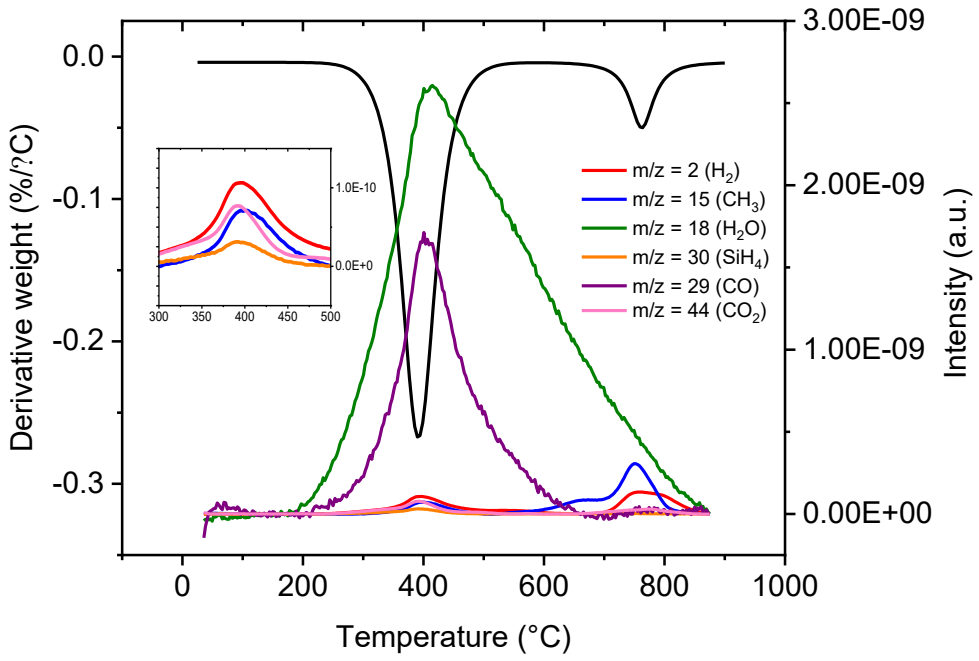


Figure 4.8. DTG-MS of crosslinked PMHS in N_2. Inset showing a close-up for m/z = 2, 15, 30 and 44 between 300 to 500 °C.

The pyrolytic behaviour of the crosslinked PMHS was further analysed from the derivative thermogravimetry-mass spectrometry (DTG-MS) curves as shown in Figure 4.8 which were obtained via the heat treatment of the crosslinked PMHS in N_2 from room temperature to 900 °C at a heating rate of 10 °C/min. No mass loss was recorded below 200 °C which indicates the absence of any depolymerisation reactions as a result of the crosslinking of polymeric chains. The first stage of mass loss occurred in the 300-500 °C temperature range due to the evolution of hydrogen (H_2, m/z = 2), methane (CH_3 m/z = 15), water (H_2O, m/z = 18), silane (SiH_4, m/z = 30), carbon monoxide (CO, m/z = 29) and carbon dioxide (CO_2, m/z = 44) as detected by the mass spectrometry measurement. The evolution of hydrogen, methane and silane gases at this stage can be explained by the increase in the thermal stability of the crosslinked PMHS which allowed the redistribution reactions between Si-H and Si-O bonds to

occur that leads to the formation of an amorphous SiO_xC_{4-x} network [180]. On the other hand, water was largely evolved at this temperature range and continued to be released up to 900 °C most likely due to the condensation reactions between the unreacted Si-OH groups which led to a further formation of siloxane linkages [222]. The second stage of mass loss occurred between 600-900 °C which was accompanied by the release of hydrogen and methane. This observation was consistent with the literature reports whereby cleavage of Si-H, Si-C, C-C and C-H bonds was expected to occur via the formation of free radicals, hydrogen abstraction and combination and/or rearrangement reactions which would lead to the evolution of hydrogen and hydrocarbon gases [181, 222]. The evolution of carbon monoxide and carbon dioxide were also observed between 200-700 °C and 300-500 °C, respectively, suggesting that the carbothermal reduction reactions had probably already initiated below 1000 °C. These reactions had most likely taken place due the formation of SiO_xC_{4-x} mixed units and free carbon from the redistribution and bond cleavage reactions. Based on the mass loss experienced by the cured PMHS and the evolution of the gaseous byproducts, this investigation signifies the transformation of the polymer to an inorganic material during pyrolysis.

This work aims to produce SiOC and SiC ceramics for the coating of CNTs. As explained in Section 2.3.3, SiOC can be produced by carrying out pyrolysis at the temperature of 800 °C and above meanwhile SiC can be produced from pyrolysis at the temperature of 1500 °C and above. Therefore, two different temperatures, i.e. 900 and 1500 °C, were used during the pyrolysis of crosslinked PMHS using the procedure described in Section 3.2.1.3. For simplicity, the pyrolysis products were labelled as PMHS-900 and PMHS-1500 in this section based on the maximum temperature used during pyrolysis. Figure 4.9 shows the crosslinked PMHS changing from clear to opaque brown upon pyrolysis at 900 °C and to iridescent black at 1500 °C signifying the change in the composition of the materials at the different temperature

stages. The cracks observed in the crosslinked and pyrolysis products were due to the shrinkage and densification effects during the crosslinking and ceramisation processes which are negligible in this work since the PMHS will be used as a coating precursor instead of producing monoliths.

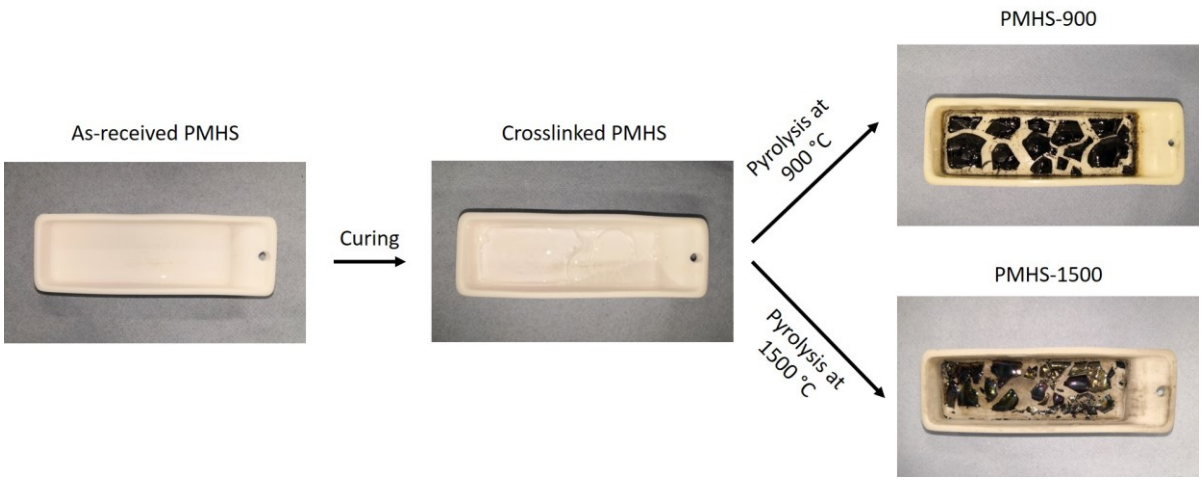


Figure 4.9. Photographs of the as-received PMHS, the crosslinked PMHS and the pyrolysis products, PMHS-900 and PMHS-1500, contained in flat boat alumina boats.

The curing, pyrolysis and ceramic yield of PMHS-900 and PMHS-1500 were calculated and are presented in Table 4.3. The curing yield for both samples were found to be similar which highlights the consistency in the degree of crosslinking of PMHS in the laboratory experiments; however, the yield was found to be slightly higher (by 7%) than it was measured from TGA (see Table 4.2). The higher curing yield can probably be attributed to the incomplete crosslinking of polymer due to the increase in the sample size in the actual experiments (i.e. 32 mg for TGA measurement vs. 2000 mg for the actual experiment) and/or the incomplete removal of crosslinking byproducts (i.e. water) during the curing process. Nevertheless, the evolution of water in Figure 4.8 suggests the remaining crosslinking reactions and removal of water byproducts could still be accomplished during pyrolysis. Finally, the pyrolysis and ceramic yield of PMHS-1500 were found to be lower than those of PMHS-900 which can be

explained by the additional mass loss resulting from the onset of carbothermal reduction reactions at a higher pyrolysis temperature to produce the SiC products.

Table 4.3. Curing, pyrolysis and ceramic yield of PMHS-900 and PMHS-1500.

Sample	Curing yield (%)	Pyrolysis yield (%)	Ceramic yield (%)
PMHS-900	93.8 ± 2.9	69.5 ± 2.7	64.9 ± 2.2
PMHS-1500	92.7 ± 1.8	61.4 ± 1.3	57.0 ± 1.9

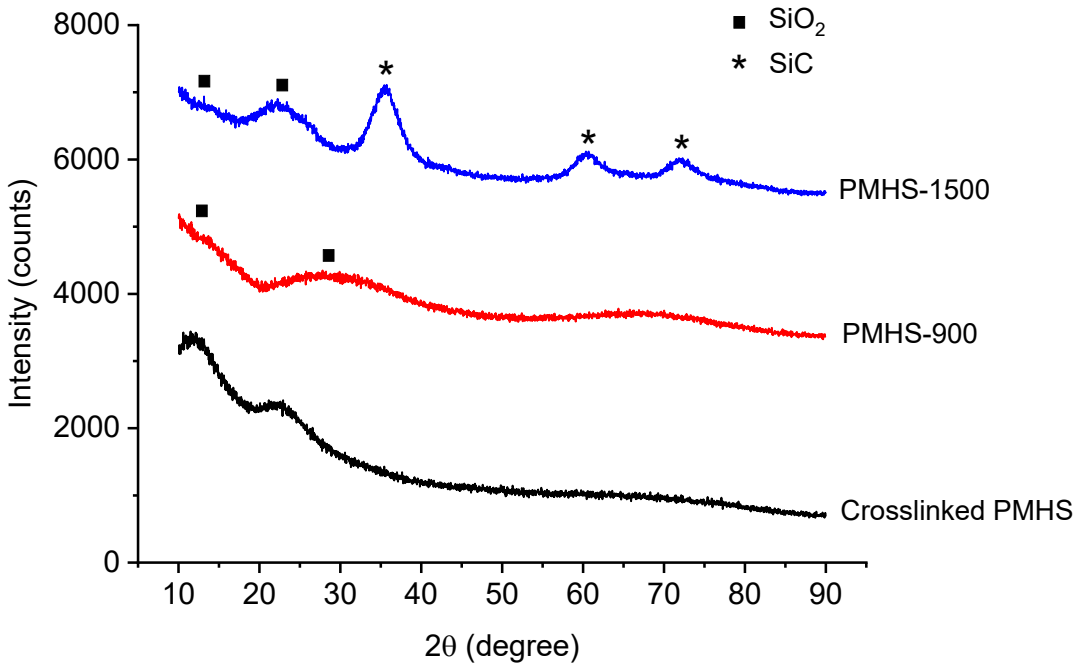


Figure 4.10. XRD patterns of crosslinked PMHS and the pyrolysed products, PMHS-900 and PMHS-1500.

The phase composition and the crystallographic structure of the crosslinked PMHS and the pyrolysis products were investigated using XRD as shown in Figure 4.10. The XRD pattern of the crosslinked product shows two diffraction halos centred at 2θ = 11.9° and 22.9° which indicates the amorphous nature of the crosslinked PMHS due to the immobilisation of the polymer chains and the formation of disordered crosslinked network during the curing process. After the pyrolysis at 900 °C, the resulting PMHS-900 still appeared to be highly amorphous

as expected for SiOC glasses whereby diffraction halos are observed at 2θ = 13.1 and 27.9° indicating the presence of amorphous SiO_2 phase. Additionally, the broad peak centred at around 2θ = 67.3° seems to indicate an onset of SiC crystallisation which is also consistent with the evolution of carbon monoxide and carbon dioxide as previously observed in Figure 4.8. The presence of SiO_2 and the onset of SiC crystallisation indicates that a phase separation must have occurred from the SiOC network (see Equation 2.11) in the PMHS-900 sample. Subsequently, when the pyrolysis was carried out at 1500 °C, SiC phase could be detected in the resulting PMHS-1500 sample based on the peaks at 2θ = 35.6, 60.0 and 71.8°, in addition to the broad peaks at 2θ = 13.1° and 22° which can be assigned to SiO_2. The presence of SiO_2 in this sample indicates that the SiC phase was mainly yielded by the phase separation of SiOC instead of the carbothermal reduction reactions. Based on the TGA-MS and XRD results, the PMHS-900 and PMHS-1500 samples can be characterised as predominantly SiOC and SiC, respectively. Therefore, as a general rule, any samples which undergoes pyrolysis at 900 and 1500 °C will be denoted as SiOC and SiC, respectively, in later works.

4.3 PMHS as a coating precursor for CNTs

4.3.1 Wettability of carbon by PMHS

PMHS was initially screened for its application as the coating precursor for CNTs by estimating its wetting behaviour on the CNTs using the sessile drop technique where a drop of liquid PMHS was deposited on a carbon surface and the contact angle of the droplet was measured. Figure 4.11(a) shows as-received PMHS forming a thin film on the surface of a carbon substrate where the contact angle of the droplet was measured to be 11.1° indicating a very well wetting of carbon by PMHS. For comparison, carbon can also be wetted by water as shown in Figure 4.11(b) albeit at a higher contact angle of 50.1°.

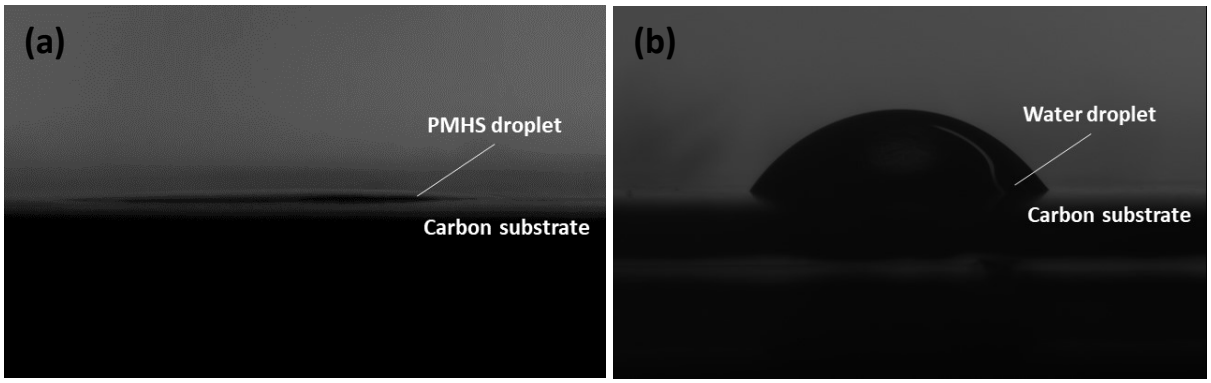


Figure 4.11. Photographs of (a) As-received PMHS and (b) water droplets on a carbon substrate.

However, these results may not necessarily reflect on the actual wettability of CNTs by these liquids as in the case of water, it is generally known that CNTs exhibit hydrophobicity [223, 224] due to their graphitic surface and some experimental works had reported non-wetting behaviour of CNTs by water with contact angles ranging between 90-156° [225, 226]. Nevertheless, PMHS is still expected to achieve a good wetting on the CNTs as the presence of methyl side groups may induce non-covalent interactions with the sp^2 surface of CNTs leading to the polymer adhesion on the CNTs [182, 183]. Furthermore, as found by Dujardin et. al., the wetting of CNTs can be achieved by liquids with surface tensions below ~130 mN/m

[105, 227]; therefore, the low surface tension of PMHS (i.e. 17-19 mN/m [228]) strongly suggests the ability of the polymer to wet the CNTs.

4.3.2 CNTs dispersion in organic solvents

The state of agglomeration of as-received NC7000 multiwalled CNTs is depicted in Figure 4.12 and Figure 4.13 where bundle-like structures of CNTs can be observed. Therefore, the dispersion of CNTs needs to be carried out to ensure that the large CNTs agglomerates are broken down and the individual tubes are separated so that PMHS can be efficiently coated on the individual tubes during the preparation of PMHS-CNTs samples.

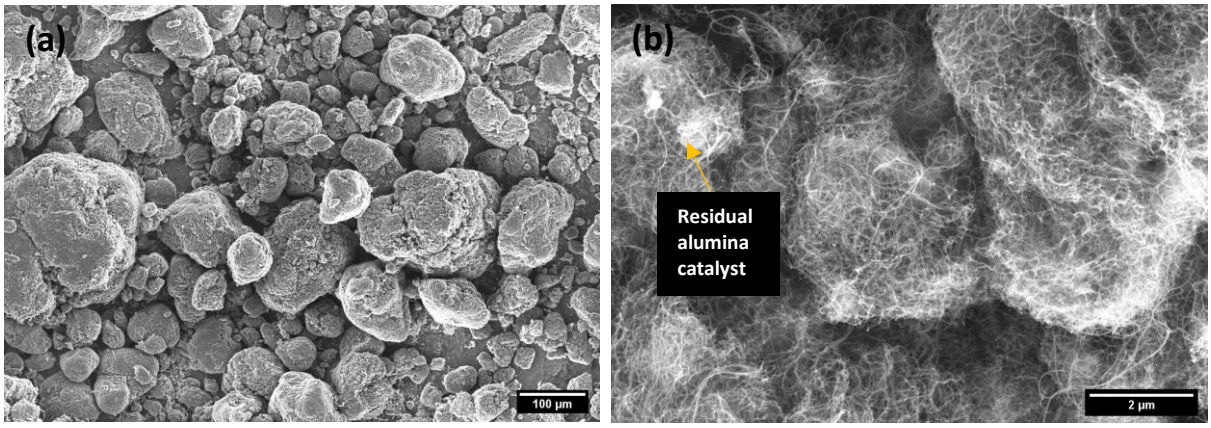


Figure 4.12. SEM images of as-received NC7000 multiwalled CNTs at (a) low and (b) high magnifications.

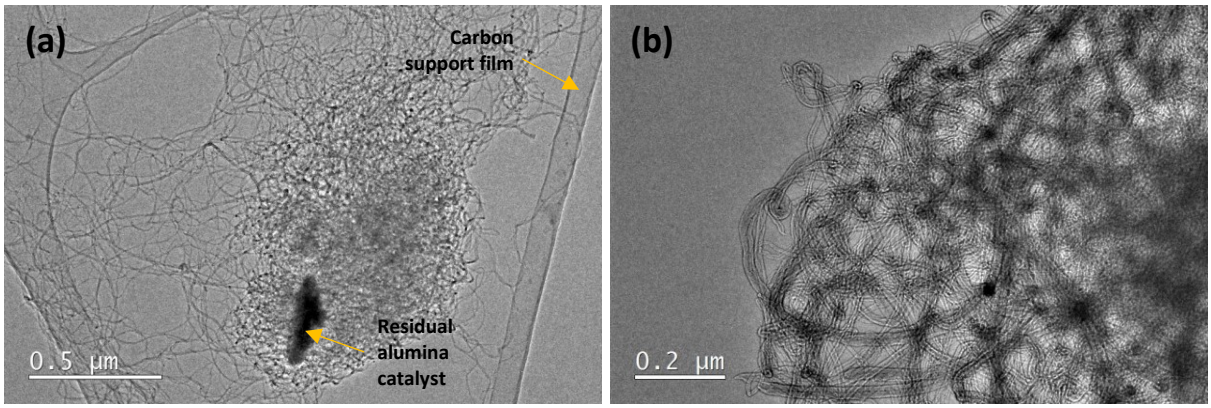


Figure 4.13. TEM images of as-received NC7000 multiwalled CNTs at (a) low and (b) high magnifications.

Ultrasonication is a very effective dispersion techniques which requires a good solvent to effectively debundle and disperse the CNTs. Additionally, the solvent must also be able to dissolve the PMHS well, can be easily removed during sample preparation and can be safely handled at large volumes. Most of the solvents which were identified to be good at dispersing CNTs such as NMP, DMF, DMA, N12P and DMF [190] have high boiling points ranging around 150-200 °C; therefore, they are unsuitable for the preparation of coated CNTs. Consequently, the dispersibility of CNTs in a few common solvents with low boiling points, namely acetone, ethanol and THF, were investigated by preparing the dispersions of CNTs (according to the procedure described in Section 3.2.1.1) at a concentration of 1 mg/mL each.

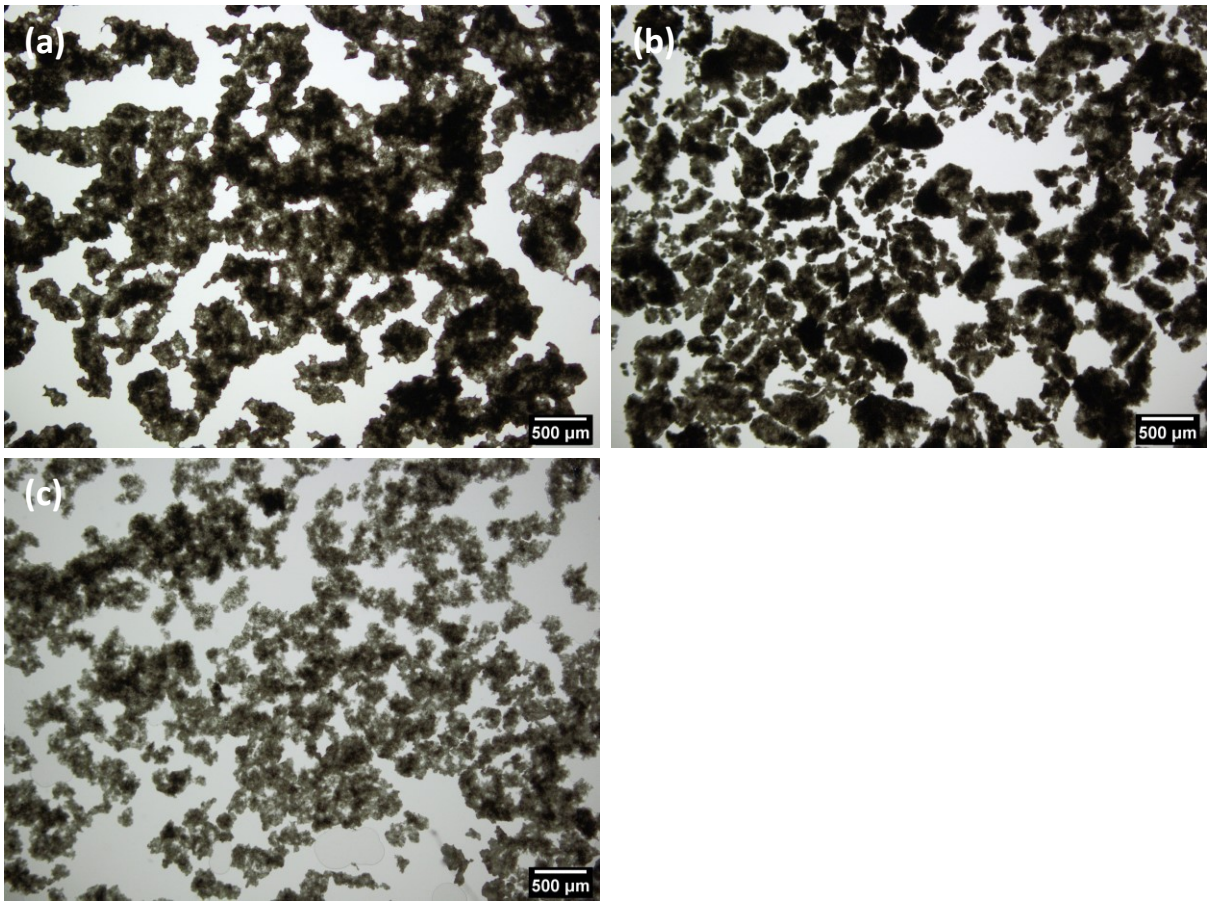


Figure 4.14. Optical micrographs of CNTs dispersions in (a) acetone, (b) ethanol and (c) THF each at a concentration of 1 mg/mL after ultrasonication for 30 min.

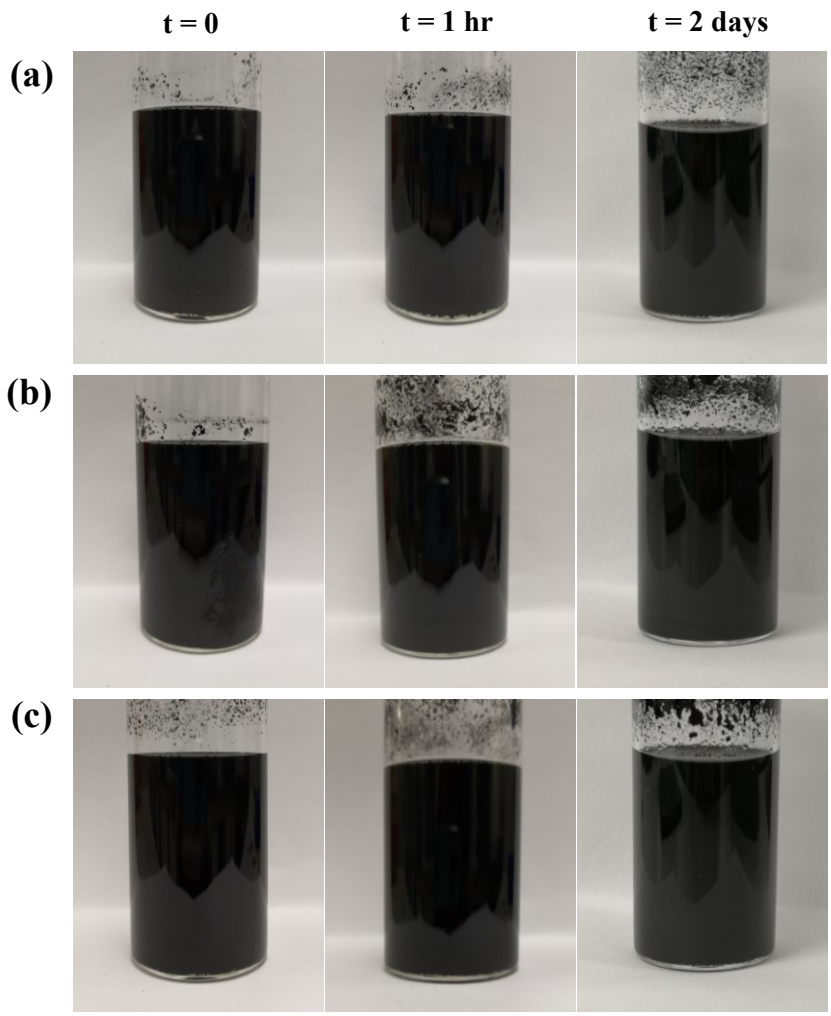


Figure 4.15. Photographs of CNTs dispersions in (a) acetone, (b) ethanol and (c) THF at t=0, 1 hr and 2 days after 30 min ultrasonication.

The optical micrographs in Figure 4.14 show that the best dispersion of CNTs was produced in THF where smaller and thinner agglomerates could be observed in comparison to the larger and thicker CNTs agglomerates found in acetone and ethanol dispersions. The increased dispersibility of CNTs in THF than acetone and ethanol had also been reported elsewhere [191, 229]. Furthermore, the stability of the CNTs dispersions was also investigated by observing the dispersions at t = 0, 1 hr and 2 days after the ultrasonication. However, as shown in Figure 4.15, all dispersions showed similar results where they appeared to be stable after 2 days without any phase separation nor sedimentation. Nevertheless, since the preparation of PMHS-CNTs requires the mixing of PMHS and the CNTs dispersion for an hour at room temperature

(see Section 3.2.1.2), this finding ensures that CNTs reaggregation and sedimentation would not occur at this stage. Based on the qualitative assessment of the degree of CNTs dispersion and the dispersion stability, THF was selected as the most suitable organic solvent to be used for the preparation of coated CNTs. Even though CNTs dispersions in acetone and ethanol had also shown stable suspensions after a few days, the agglomerates observed in these solvents were larger and denser. Furthermore, the high solubility of PMHS in THF [230] and the low boiling point of THF at 65 °C are suitable for the preparation of the PMHS-CNTs samples and the subsequent removal of the solvent prior to the curing process.

4.3.3 Coating morphology of SiOC coated CNTs

The effect of PMHS concentration in the PMHS-CNTs samples on the coating characteristics of the final coated CNTs products was investigated through a preliminary study involving the production of SiOC coated CNTs from PMHS/CNTs w/w of 0.5/1 to 6/1 using the procedure described in 3.2.1. Assuming that the CNTs would be well wetted by PMHS and that the polymer would form a continuous coating on the individual CNTs, the coating concentration and coating thickness of the final SiOC coated CNTs products (see Equation 3.8 and Equation 3.9 for calculations) were expected to increase with the increase in the starting PMHS concentration as presented in Table 4.4.

Table 4.4. Expected SiOC coating concentration and coating thickness of the SiOC coated CNTs produced from a range of PMHS concentrations.

PMHS-CNTs samples	**SiOC coated CNTs products**	
PMHS concentration (PMHS/CNTs w/w)	**Expected SiOC coating concentration (wt%)**	**Expected SiOC coating thickness (nm)**
0.5/1	24.5	0.8
1/1	39.5	1.4
2/1	56.6	2.6
3/1	66.1	3.6
4/1	72.3	4.5
5/1	76.4	5.3
6/1	79.0	6.0

The coating morphology of as-received (i.e. uncoated) CNTs and a few selected SiOC coated CNTs products were characterised with TEM-EDX as shown in Figure 4.16. The presence of SiOC coating layer on the individual CNTs was confirmed by determining the outermost layer of the multiwalled CNTs and by the detection of Si, O and C via EDX. Based on the representative images of the SiOC coated CNTs, the thickness of the coating layer appears to be similar across all samples and had not increased with the increase in the starting PMHS concentration as predicted in Table 4.4. The variation in the coating morphology of the SiOC coated CNTs which were observed in TEM is further summarised in Figure 4.17. Regardless of the starting PMHS concentration, the coating morphology of the individual tubes in the SiOC coated CNTs products were found to consist of a combination of minimal to no apparent coating, thin and continuous layer and discontinuous layer.

Furthermore, the characterisation of the coated CNTs at a lower magnification in TEM as shown in Figure 4.18 seemed to indicate that the coating products had also been deposited on the agglomerated CNTs network. The darker region on the agglomerates was identified with EDX to consist of Si, O and C which suggests for the presence of the coating material, in addition to Al which is attributed to the residual alumina impurities in the as-received CNTs (see Figure 4.12 (b) and Figure 4.13 (a)).

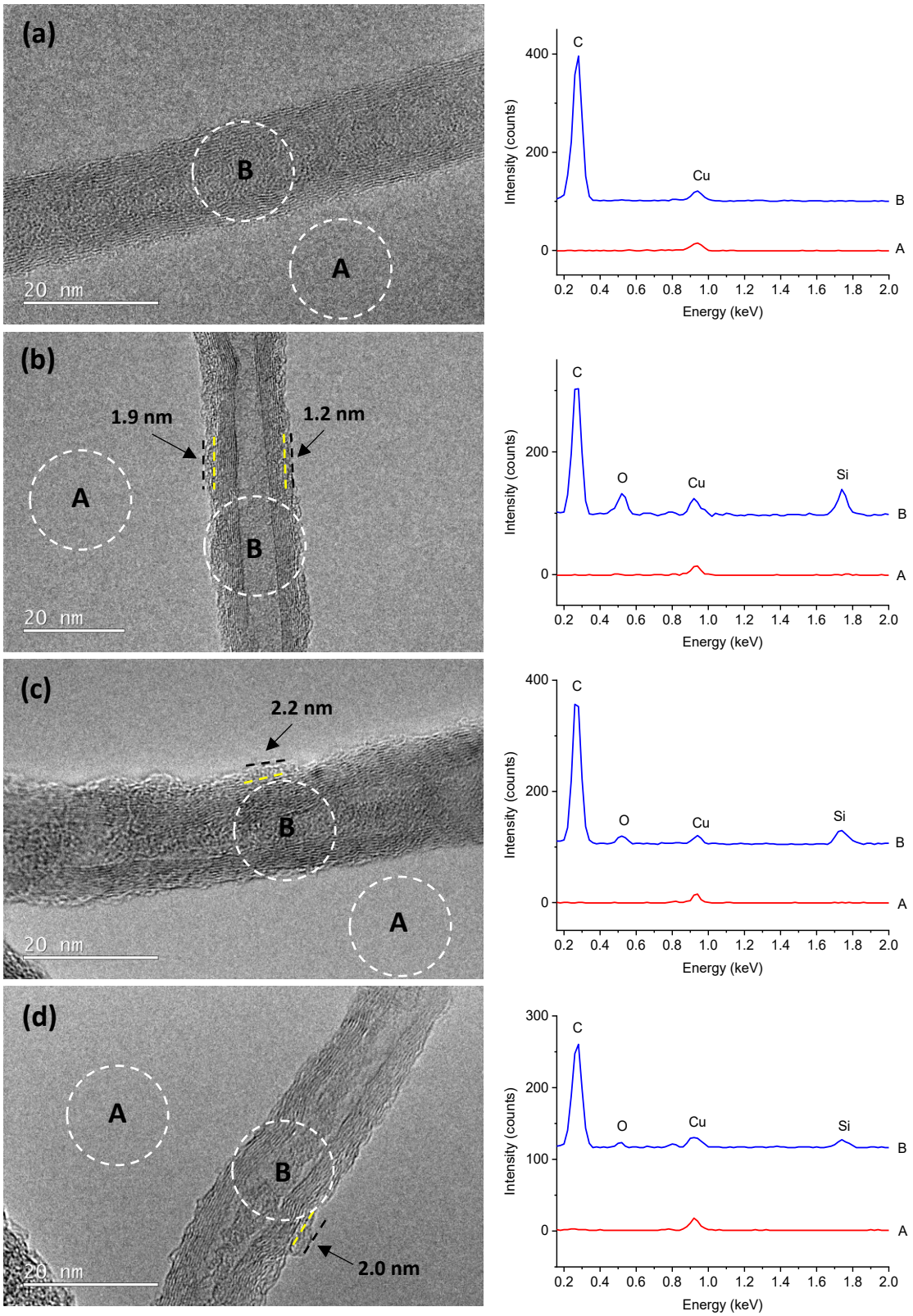


Figure 4.16. TEM images and EDX spectra of (a) as received (i.e. uncoated) CNTs and SiOC coated CNTs produced from PMHS/CNT w/w of (b) 2/1, (c) 3/1 and (d) 6/1. The outer surface of CNTs and the outer layer of SiOC coating are highlighted with yellow and black dotted lines, respectively, to outline the coating layer. The area of EDX measurement is outlined with white dotted circle. Cu detected in the EDX spectra is attributed to the TEM copper grid.

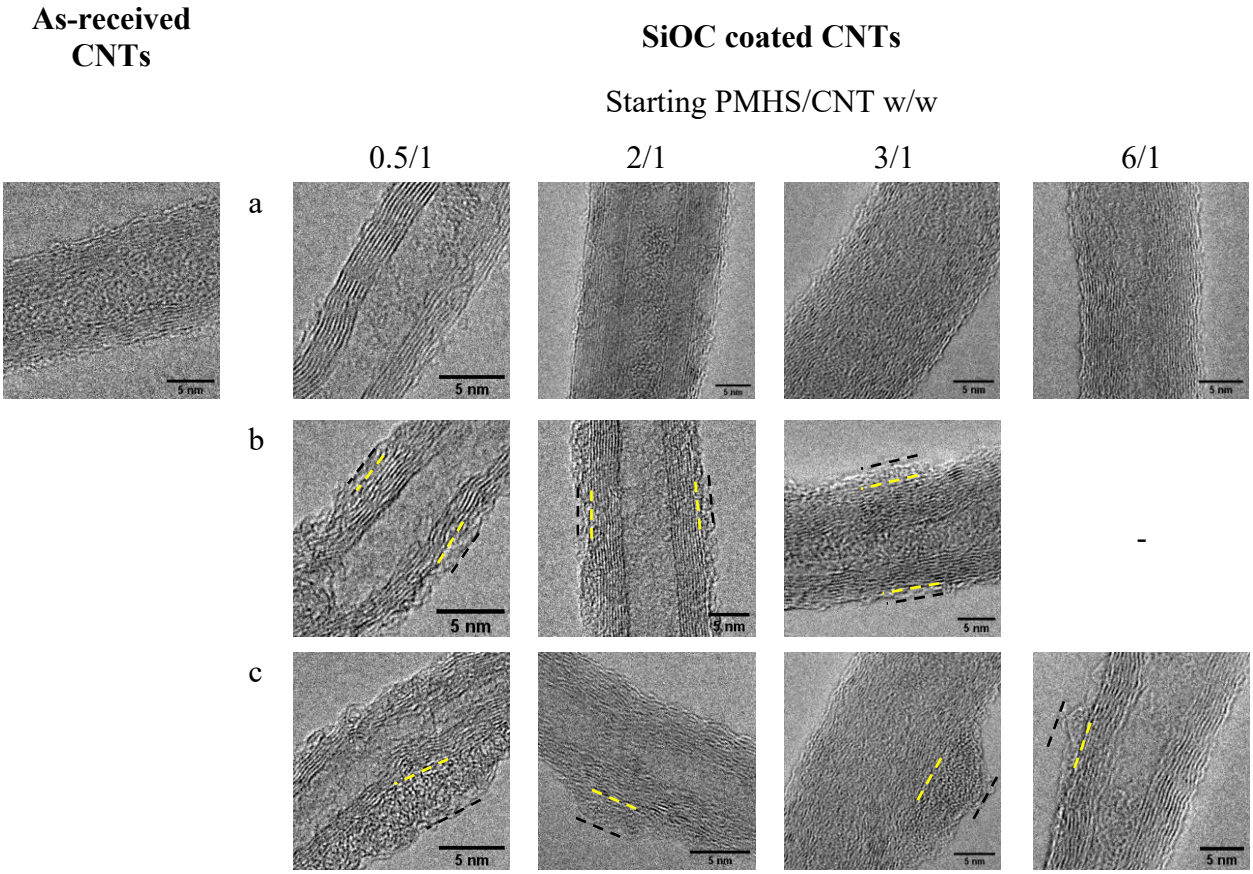
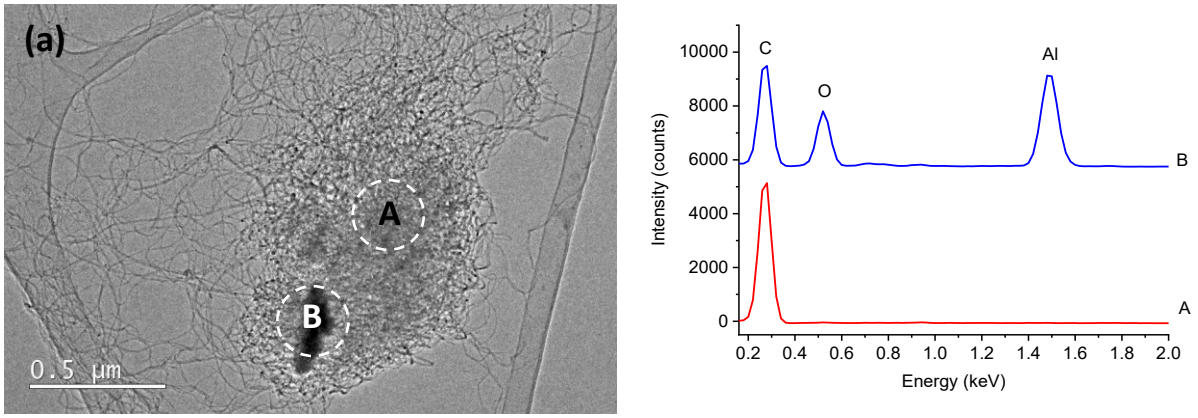


Figure 4.17. Variation in coating morphology found in the SiOC coated CNTs grouped according to (a) minimal to no apparent coating (b) thin and continuous layer and (d) discontinuous layer. The outer surface of CNTs and the outer layer of SiOC coating are highlighted with yellow and white dotted lines, respectively, to outline the coating layer.



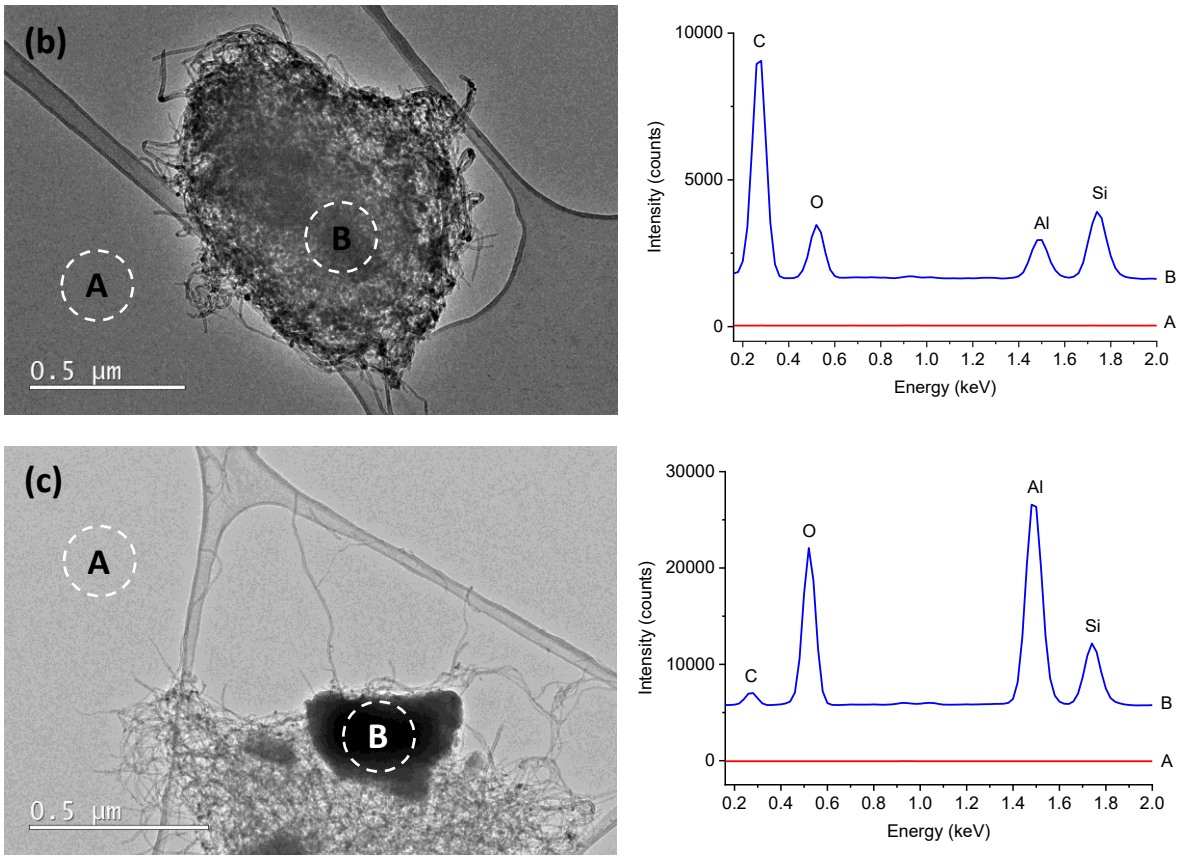


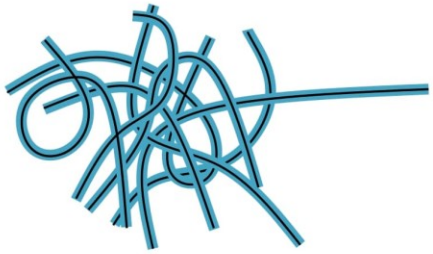
Figure 4.18. TEM images and EDX spectra of CNTs agglomerates for (a) as-received CNTs and SiOC coated CNTs produced from PMHS/CNT w/w of (b) 2/1 and (c) 3/1. The area of EDX measurement is outlined with white dotted circle and labelled with letters A and B. Al detected in EDX is attributed to the residual alumina impurity in the as-received NC7000 CNTs.

The variation in the coating morphology and the lack of increase in the coating thickness of the individual tubes may be explained by the actual wetting behaviour of PMHS on the CNTs during the sample preparation. Liquid polymer preferentially forms clam-shell and barrel-type droplets upon precipitation on the outer shell of CNTs [231] therefore resulting in the formation of a thick and discontinuous coating as observed in Figure 4.17 (c). Such conformation of liquid polymer droplets on the outer surface of fibres had been discussed and reported in the literature [232-234]. The instability of liquid films on convex surfaces occurs due the positive Laplace pressure acting on the surface of the liquid film which squeezes the liquid out of the film creating a periodic array of droplets while adhesion forces caused by liquid-solid interactions

simultaneously compete to stabilise the film [235]. Consequently, the formation of continuous coating layer on the CNTs observed in Figure 4.17 (b) could have resulted from the merging of the polymer droplets. On the other hand, the thick precipitation of coating product on the agglomerated CNTs as observed in Figure 4.18 (b) and (c) can be explained by the tendency of the liquid polymer to adhere on the interconnected network due to the wicking effect [236]. Crossover sites between CNTs attract the polymer especially during heating causing liquid droplets on the single fibres to flow into them. Therefore, this behaviour diminishes the polymer coating on the individual CNTs and leads to polymer pooling between the entangled CNTs. Additionally, the adhesion of the polymer on the CNTs agglomerates may also be encouraged by the non-covalent interactions between the CNTs surfaces and the C-H bonds of the polymeric side groups. Consequently, the PMHS concentrated on the CNTs agglomerates would be converted to a thick SiOC deposit upon curing and pyrolysis.

The expected and actual SiOC coating behaviour on the CNTs are illustrated in Figure 4.19. Theoretically, the polymer was expected to form a continuous coating on the CNTs based on the wetting CNTs by PMHS. Hence, the thickness of the resulting SiOC coating was expected to increase with the increase in the starting PMHS concentration as presented in Table 4.4. However, the TEM-EDX investigations (Figure 4.16 to Figure 4.18) revealed that the SiOC coated CNTs products were made up of individually coated CNTs with various types of coating morphology and agglomerated regions covered with SiOC precipitates. Due to the actual behaviour of the polymer on the individual CNTs and the CNTs crossover sites, the SiOC coating had a tendency to form a discontinuous layer on the individual CNTs and to pool on the agglomerated networks as shown in Figure 4.19 (b). Since SiC coating would also be formed using the same polysiloxane precursor, the coating behaviour of SiC is also expected to be similar as the SiOC coating. Further investigations are shown in Chapter 5 and Chapter 6.

(a) Expected coating behaviour



(b) Actual coating behaviour

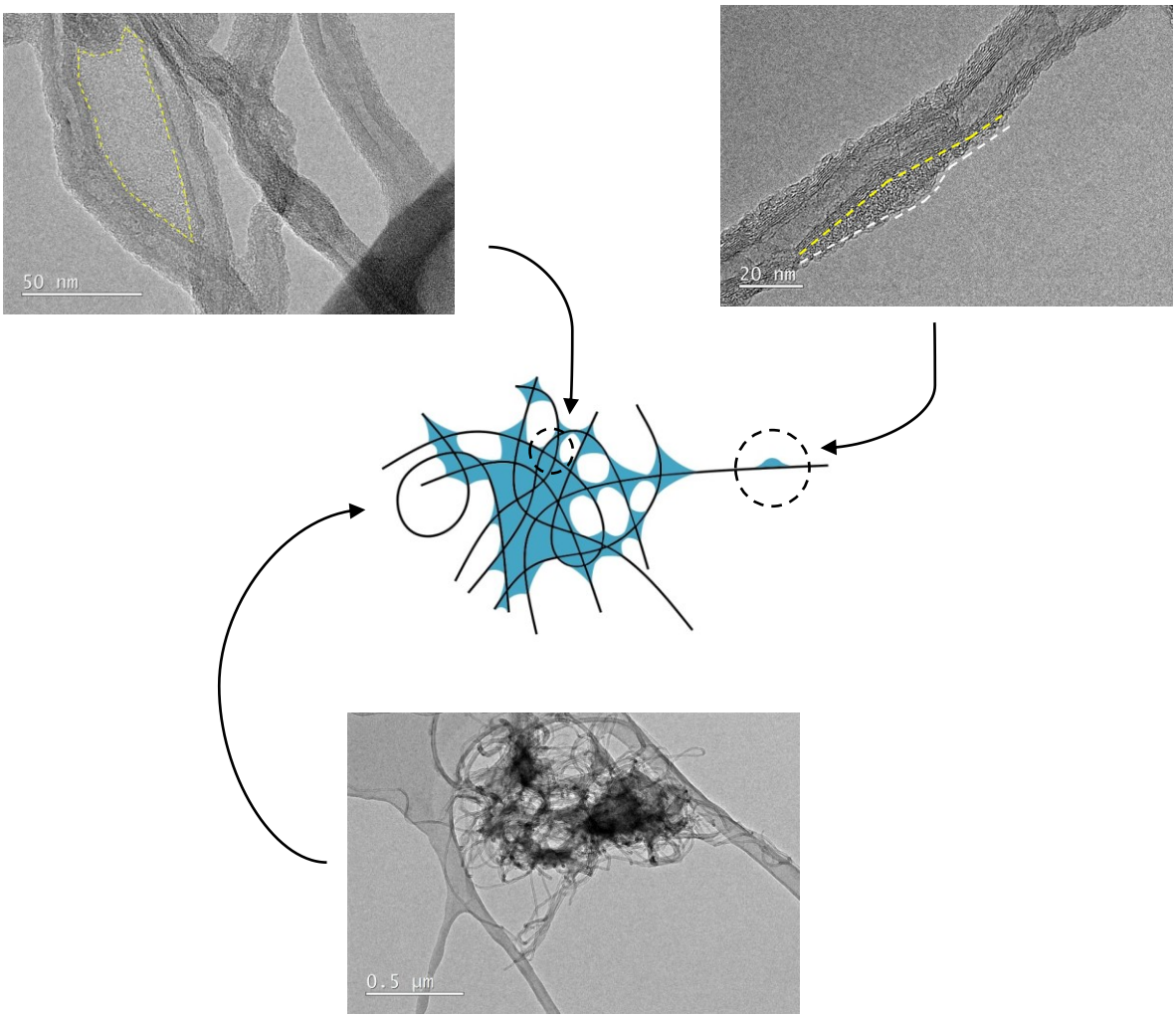


Figure 4.19. (a) Expected and (b) actual SiOC coating behaviour of on the CNTs. SiOC is denoted in blue while the CNTs are represented as black lines. The outer surface of CNTs and the outer layer of SiOC coating are highlighted with yellow and white dotted lines, respectively

Generally, a continuous coating of CNTs is desirable to ensure that the CNTs can be sufficiently wetted by the Mg matrix so that load transfer could happen effectively from the matrix to the CNTs. However, as shown in our previous work [237], discontinuous coating layers on the CNTs may also be desirable as they can act as geometrical spacers to prevent CNTs agglomeration, and as 'nano-rivets' to enhance the interfacial shear stress as embedded CNTs are pulled out of the matrix. Hence, discontinuous coating on the CNTs is still acceptable for the purpose of this work.

4.3.4 Effect of CNTs on PMHS decomposition

The total curing, pyrolysis and ceramic yield of PMHS-CNTs samples and the SiOC concentration in the final CNTs products were determined from the production of SiOC coated CNTs from PMHS/CNTs w/w of 2/1 and 6/1 and compared with the expected values as shown in Figure 4.20 (see Equation 3.4 to Equation 3.6 for calculations). The expected values were obtained by assuming that the total curing, pyrolysis and ceramic yield of the polymer were equivalent to those of the pure PMHS as reported in Table 4.3 and that the mass of the CNTs was unchanged throughout the whole process.

The results show that while the total curing yield calculated from the experiments were slightly lower than the expected values, the actual total pyrolysis and ceramic yields were drastically lower than expected indicating that the PMHS-CNTs samples had experienced a notably large mass loss during the organic to inorganic conversion. Since the multiwalled CNTs are expected to be stable up to at least 1000 °C in Ar flow [238, 239], the mass loss is predominantly attributed to the polymer. Consequently, the SiOC coating concentration in the final SiOC coated CNTs products were also much smaller than expected.

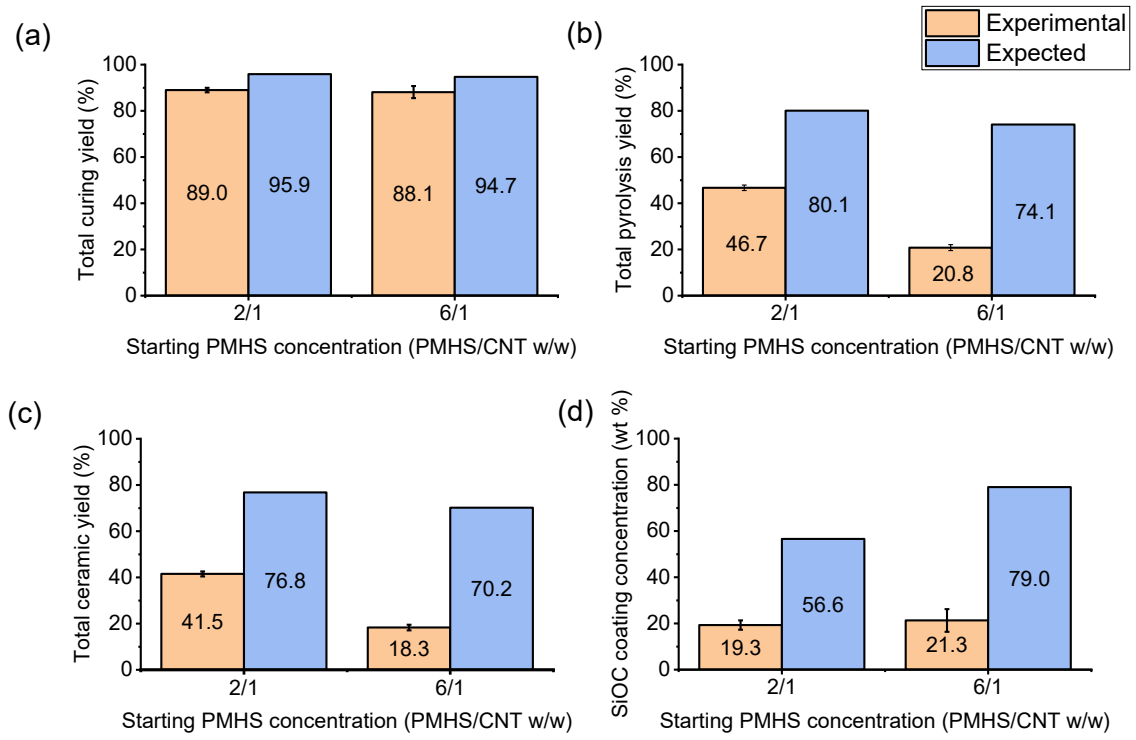


Figure 4.20. Comparison between the experimental and expected values for total curing, pyrolysis and ceramic yield and SiOC coating concentration of the SiOC coated CNTs produced from starting PMHS concentration of 2/1 and 6/1 PMHS/CNTs w/w. The expected values were calculated by assuming that the total curing, pyrolysis and ceramic yield of the polymer were equivalent to those of the pure PMHS as reported in Table 4.3 and that no mass loss occurred for the CNTs.

To understand the behaviour of the crosslinked PMHS-CNTs during pyrolysis, the pyrolysis process was simulated with TGA via heating from room temperature to 900 °C in N_2 at a heating rate of 10°C/min on the crosslinked PMHS-CNTs produced from the starting PMHS concentration of 2/1 and 6/1 PMHS/CNTs w/w as shown in Figure 4.21. The expected TGA curves of the crosslinked PMHS-CNTs were determined by assuming that the pyrolytic behaviour of the polymer is equivalent to that of a completely cured pure PMHS as shown in Figure 4.7 and that no mass loss occurs for the CNTs during pyrolysis. As summarised in Table 4.5, the actual pyrolysis behaviour of the crosslinked PMHS-CNTs were notably different than the predicted behaviour. The onset temperature for both crosslinked PMHS-CNTs samples

were slightly lower at around 280-300 °C than the expected onset temperature for crosslinked pure PMHs which is around 340 °C therefore showing that the degradation of the polymer in the PMHS-CNTs samples had initiated at a lower temperature. The actual rate of decomposition of the samples at the two major mass loss stages (i.e. 200-400 and 600-800 °C) was found to be much larger than expected which explains for the large reduction of the total pyrolysis yield. It should be noted that the total pyrolysis yield obtained in the TGA measurement Figure 4.21 (i.e. 24.1 and 51.7% for crosslinked PMHS2CNT1 and PMHS6CNT1, respectively) were different than the experimental values calculated in Figure 4.20 (46.7 and 20.8 % for crosslinked PMHS2CNT1 and PMHS6CNT1, respectively). This difference is attributed to the small sampling size used in TGA (i.e. ~ 5 mg) as compared to the bulk sample measurement obtained from the actual experiments (i.e. 750 and 1750 mg). However, even though TGA might not be accurate to measure the actual total pyrolysis yield, it was still reliable for assessing the behaviour of the crosslinked PMHS-CNTs during pyrolysis.

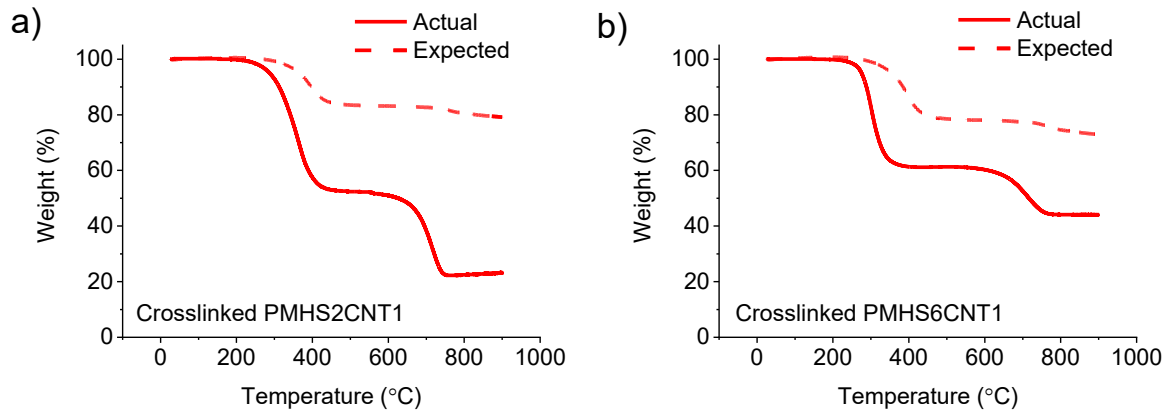


Figure 4.21. Comparison between the actual and expected TGA curves of crosslinked PMHS-CNTs produced from PMHS/CNTs w/w of 2/1 and 6/1 as performed in N_2. The expected TGA curves of the crosslinked PMHS-CNTs were determined by assuming that the pyrolytic behaviour of the polymer was equivalent to that of a completely cured pure PMHS as shown in Figure 4.7 and that no mass loss occurred for the CNTs during pyrolysis.

Table 4.5. Summary of the onset temperature and the total pyrolysis yield determined from the actual and expected TGA curves in Figure 4.21.

	Crosslinked PMHS2CNT1		Crosslinked PMHS6CNT1	
	Actual	**Expected**	**Actual**	**Expected**
Onset temperature (°C)	282.5	339.3	275.2	339.3
Total pyrolysis yield (%)				
at 400 °C	57.5	89.4	61.3	86.2
at 750 °C	22.4	81.9	45.4	76.5

The experimental and TGA results in Figure 4.20, Figure 4.21 and Table 4.5 reveal that the PMHS-CNTs samples experienced a notably large mass loss during pyrolysis due to an increased rate of decomposition of PMHS therefore resulting in much lower total ceramic yield of PMHS-CNTs and SiOC coating concentration in the final SiOC coated CNTs products. Consequently, several modifications to the established procedure were carried out such as by using a longer curing time and lower pyrolysis heating rate to improve the total ceramic yield of PMHS-CNTs. The description of the modified procedures can be found in Appendix A.8. However, as the results show in Figure 4.22, no modifications applied to the established procedure was successful at improving the total ceramic yield of the PMHS-CNTs samples.

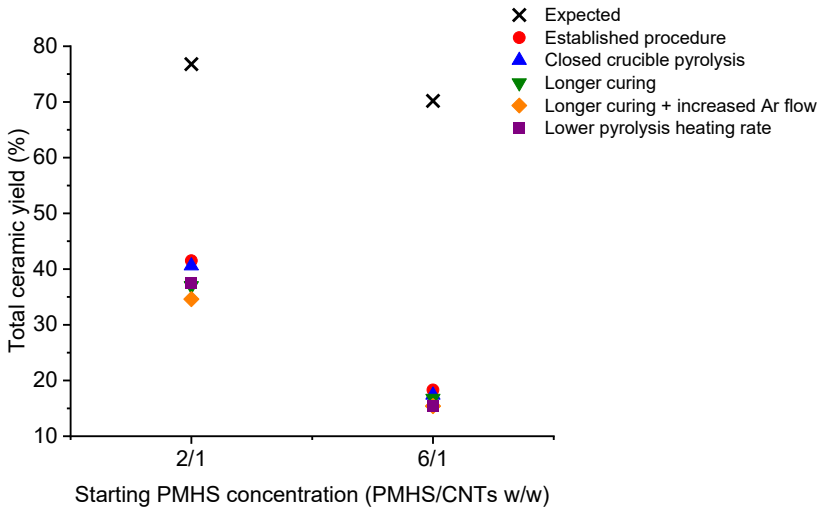


Figure 4.22. Effect of modified procedures on the total ceramic yield of PMHS-CNTs samples.

Since the modification of the sample preparation parameters had no effects on the total ceramic yield of PMHS-CNTs, further investigation was carried out to determine if whether there were any chemical and/or physical effects influencing the pyrolytic behaviour of PMHS-CNTs. The chemical effect is referring to the effect of CNTs meanwhile the physical effect is referring to the effect of the sample size on the decomposition behaviour of PMHS during pyrolysis.

The chemical effect investigation was based on the hypothesis that the pyrolysis of PMHS is catalysed by the CNTs; therefore, the higher the amount of CNTs, the lower the total ceramic yield of PMHS-CNTs. Furthermore, since the residual alumina catalysts are notably present in the as-received CNTs (see Figure 4.12 and Figure 4.13), their catalytic effects should also be considered. The chemical effect of CNTs on the total ceramic yield of PMHS-CNTs was studied by preparing PMHS-CNTs samples from PMHS/CNTs w/w of 10/1, 20/1, 40/1 and 60/1 using a fixed amount of PMHS as described in Table 4.6. The total ceramic yield was calculated after the production of SiOC coated CNTs from the PMHS-CNTs samples and the values were plotted against their CNTs loading as shown in Figure 4.23 (a).

Table 4.6. Description of PMHS-CNTs samples prepared to investigate the chemical effect of CNTs on the total ceramic yield of PMHS-CNTs.

Starting PMHS concentration (PMHS/CNTs w/w)	Starting amount of PMHS (mg)	Starting amount of as-received CNTs (mg)
10/1	500	50.0
20/1	500	25.0
40/1	500	12.5
60/1	500	8.3

The results in Figure 4.23 (a) clearly demonstrate that the increase in CNTs loading in the PMHS-CNTs samples led to a decrease in the total ceramic yield and a larger deviation from the expected values. Therefore, the presence of CNTs can be strongly associated to the large mass loss experienced by the PMHS-CNTs samples during pyrolysis. To the author's

knowledge, no works had been reported on the effect of CNTs on the pyrolytic behaviour of polysiloxanes. However, inorganic particles had been previously incorporated in polysiloxanes to act as a catalyst to reduce the activation energy of degradation of the polymer. For example, the activation energy of degradation of polydimethylsiloxane (PDMS) was reported to reduce from 175 kJ/mol to 54 and 98 kJ/mol with aluminium oxide and cesium octoates addition, respectively [240, 241]. The addition of catalyst in polysiloxane was also reported to cause a significantly large mass loss during pyrolysis such as in the case of anatase titanium oxide filled PDMS due to an unzipping depolymerisation mechanism which leads to bond dissociation and generation of cyclic volatiles [242]. Furthermore, the addition of filler particles may also suppress the crosslinking of polysiloxanes. One study found that the CNTs could inhibit the free-radical crosslinking of PDMS such that the effective crosslinking density of carbon nanotubes filled PDMS composites decreased with the increase in the CNTs loading. This behaviour was attributed to the CNTs acting as radical-trapping agents due to their large area of sp^2 hybridized structured and their strong electron affinity which subsequently hindered the free-radical crosslinking of the PDMS matrix [243]. In another study, the addition of α-iron oxide in PDMS was also suggested to cause a local suppression of crosslinking at the filler/matrix interface since the fillers may act as secondary antioxidants and scavenge free radicals locally. Otherwise, it may be possible that the mere physical presence of the filler particles slows down crosslinking at the interfaces since the polymeric chains which are located next to the thermally inert particles have a lower probability of crosslinking than the polymeric chains in the bulk phase [244].

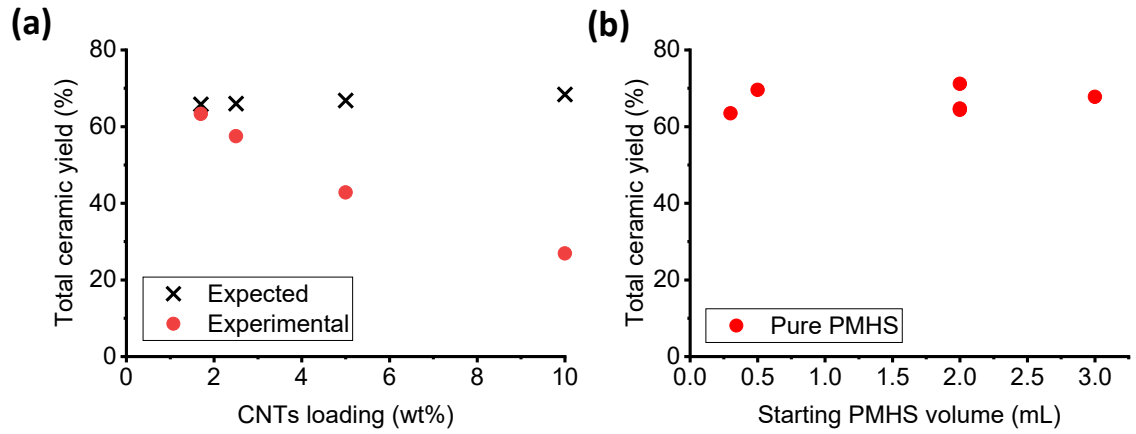


Figure 4.23. Total ceramic yield of PMHS-CNTs as a function of (a) CNTs loading and (b) starting PMHS volume.

Finally, the influence of sample size on the rate of decomposition of PMHS was also investigated to determine if the total ceramic yield was governed by any physical effects. This investigation was carried out by assessing the total ceramic yield of pure PMHS of various starting volumes as shown in Figure 4.23 (b). The results did not show any correlation between the two variables which indicates that the sample size is least likely to influence the pyrolytic behaviour of PMHS.

Based on the experimental results in Figure 4.23 and the discussion of previous literature works, the increased rate of degradation of PMHS in the PMHS-CNTs samples during pyrolysis may be explained by a combination of CNTs acting as radical traps which hinders the crosslinking of PMHS during curing and/or as a catalyst which accelerates the decomposition of the polymer during pyrolysis. Wong et. al. [154] proposed that the formation of radicals is essential in the oxidative crosslinking of Si-H containing polysiloxanes; therefore, the ability of CNTs to trap the radical species may disrupt the crosslinking progression of PMHS. As a consequence, polymeric chains that are unsuccessfully crosslinked will be easily decomposed during pyrolysis which may explain for the lower onset temperature observed for PMHS-CNTs as reported in Table 4.5. On the other hand, the presence of the residual alumina

catalyst in the CNTs may also reduce the activation energy of degradation of PMHS via some depolymerisation mechanism which leads to a higher rate of degradation of the polymer during pyrolysis. Based on the TGA profiles of the PMHS-CNTs samples in Figure 4.21, this effect seems to be predominantly affecting the total pyrolysis yield of PMHS-CNTs samples. Finally, no evidence was found to attribute the effect of sample size on the pyrolytic behaviour of PMHS.

Further investigations can be carried out in the future to confirm for the chemical effect of CNTs on the pyrolytic behaviour of PMHS. For example, the coating procedure can be repeated with other commercial CNTs with lower level of residual metal impurities such as the Baytubes C150P. Alternatively, alumina powder (or other suspected metal catalysts) can simply be added to PMHS for pyrolysis. If the metal impurities were found to have a predominant effect on the decomposition of PMHS, higher purity CNTs should be used instead for producing the coated CNTs or the purification of NC7000 can be considered. In this work, the chemical effect of CNTs is acknowledged for now since further investigations are required to improve to overcome this issue. Therefore, to mitigate this issue, further studies on SiOC and SiC coated CNTs in Chapters 5 and 6 will be using higher starting PMHS concentrations to produce a wider range of coating concentrations.

4.4 Conclusions

SiOC and SiC were successfully produced from PMHS via the curing and pyrolysis processes. A commercially obtained PMHS was selected as the preceramic precursor for the coating of CNTs with SiOC and SiC due to its molecular configuration, good processability and low cost. A simple, catalyst-free curing procedure via the heat treatment in air was established from the DSC experiments. The established curing procedure was able to achieve a 100% degree of cure for PMHS and a curing yield of 87.1%. TGA-MS and IR spectroscopy investigations revealed that the crosslinking reactions were likely to occur via the oxidation of the Si-H and Si-CH_3 groups which was followed by the condensation of the silanols to produce the Si-O-Si crosslinks. The importance of crosslinking was demonstrated by a notable improvement in the ceramic yield of the cured PMHS upon pyrolysis in comparison to the uncured PMHS. SiOC and SiC were successfully produced by using pyrolysis temperatures of 900 and 1500 °C, respectively, to give a ceramic yield of 64.9 ± 2.2 and 57.0 ± 1.9 %, respectively. The behaviour of the crosslinked PMHS during pyrolysis was also analysed with TGA-MS measurement to understand the organic to inorganic transformation process. Finally, the XRD measurement indicated that the SiOC product was made up of an amorphous structure with predominantly SiOC network and SiO_2 phases while the SiC product consisted of crystalline SiC phase and some amorphous SiO_2 phases. The production of SiOC and SiC products from PMHS is a feasible technique in which curing can be carried out via heat treatment in air without any catalysts and the SiOC or SiC products can be obtained by simply controlling the pyrolysis temperature.

Subsequently, the application of PMHS as the coating precursor for the production of SiOC/SiC coated CNTs was investigated through a preliminary production of SiOC coated CNTs. Initially, THF was found to be the most suitable solvent for the dispersion of CNTs

prior to the addition of the polymer to ensure that the large agglomerates will be broken down and that the polymer can be efficiently coated on the individual tubes. A variety of coating morphologies was found on the individual tubes of the SiOC coated CNTs which included minimal to no apparent coating, thin and continuous layer and discontinuous layer. Furthermore, the thickness of the coating layer in the final SiOC coated CNTs products had not increased with the increase in the starting PMHS concentration in the PMHS-CNTs as predicted. Based on the TEM images taken at low and high magnifications, this finding could be explained by the actual wetting behaviour of the polymer on the CNTs during the sample preparation. The tendency of the liquid polymer to form clam-shell and barrel-type droplets on tubular structures explains for the formation of the discontinuous coating of SiOC layer on the individual CNTs meanwhile the wicking effect which causes the polymer to adhere on the interconnected network of CNTs led to the formation of SiOC deposit on the agglomerated CNTs network. Finally, the decomposition behaviour of PMHS-CNTs was also studied during the production of SiOC coated CNTs. The total ceramic yield and SiOC coating concentration of the SiOC coated CNTs were found to be much lower than expected due to the increased rate of decomposition of the polymer in the PMHS-CNTs samples which led to a very large mass loss during pyrolysis in comparison to the PMHS only samples. The total ceramic yield of PMHS-CNTs was found to decrease with the increase in the CNTs loading which seems to suggest that the CNTs (including their residual alumina impurities) may act as a radical trapping agent which hinders crosslinking and/or as a catalyst which accelerates the decomposition of the polymer during pyrolysis.

Chapter 5 : AZ91-SiOC coated CNTs composites

5.1 Introduction

The fabrication of CNTs-reinforced Mg matrix composites needs to overcome the challenges of producing a homogeneous dispersion of CNTs in the matrix and to create a good interfacial bonding between the CNTs and the Mg matrix so that the strengthening potential of CNTs can be further realised. Several dispersion techniques such as ball milling [81, 88] and the use of dispersing agent [64, 89] had been used in the literature to effectively improve the dispersion and distribution of CNTs in different Mg matrices which resulted in the improvement of the mechanical properties of the composites. However, based on our previous works [58, 80], the enhancement of CNTs dispersion were still inadequate to significantly improve the mechanical properties of our CNTs-reinforced AZ91 composites due to the poor wettability of CNTs by Mg. Consequently, the coating of CNTs is considered to be a promising strategy to improve the wettability and interfacial bonding between the CNTs and Mg matrix.

Based on the literature works [117, 119, 122, 123], the addition of coated CNTs was able to show larger improvement in the tensile yield strength and ultimate tensile strength of the composites in comparison to the Mg-As received CNTs composites. These findings were mainly attributed to the interfacial reaction between the coating layer and the Mg matrix which helped to improve the interfacial bonding between the CNTs and the Mg matrix therefore allowing for an effective load transfer. However, the agglomeration of CNTs was still an issue even for the coated CNTs which had led to the deterioration of the composite at higher CNTs loading. Moreover, Ni coated CNTs which were used in most of the literature works are

deemed to be unsuitable since Ni impurity in Mg can lead to harmful effects for the corrosion resistance of Mg. Therefore, a different material had to be considered for the coating of CNTs in this work.

Based on the known wettability of SiC with the AZ91 matrix [126, 127, 129, 130], SiC is an apparent choice of coating material for CNTs. Since the native SiO_2 layer on the surface of SiC also plays a role on the wetting of SiC by Mg-Al alloy, SiOC was also considered as another promising coating material. Therefore, in this work, SiOC and SiC coated CNTs were produced using polymethylhydrosiloxane (PMHS) precursor at the pyrolysis temperatures of 900 and 1500 °C, respectively, to enhance the properties of AZ91 composites.

This chapter will mainly focus on the production of SiOC coated CNTs and the fabrication of AZ91-SiOC coated CNTs composites. Following the preliminary investigation in Section 4.3, the effect of the starting PMHS concentration on the resulting SiOC coated CNTs composition is further investigated. Then, the effect of SiOC coating concentration on the morphology and dispersibility of the coated CNTs are studied. In the second part of the chapter, the appropriate SiOC coating concentration is determined and the effect of SiOC coating on the properties of the AZ91 composites are examined over a range of CNTs loading.

5.2 SiOC coated CNTs

5.2.1 Effect of starting PMHS concentration on SiOC concentration

The investigation in Section 4.3.4 revealed that the SiOC concentration obtained in the final CNTs products was lower than expected (Figure 4.20 (d)) due to the possible catalytic effect of CNTs on the decomposition of PMHS. As a result, the production of SiOC coated CNTs using the starting PMHS/CNTs w/w of 2/1 and 6/1 were only able to produce a very similar SiOC concentrations of 19.3 and 21.3 wt%, respectively. Therefore, in order to produce SiOC coated CNTs with a wider range of SiOC concentrations, the range of the starting PMHS concentrations must be considerably extended.

SiOC coated CNTs were prepared according to the procedure described in Section 3.2.1 using PMHS-CNTs samples with the PMHS concentrations of 10/1 to 60/1 PMHS/CNTs w/w as listed in Table 5.1. For simplicity, the starting PMHS-CNTs samples prior to the production of SiOC coated CNTs were labelled as PMHSxCNTy where x/y is the PMHS/CNTs w/w. Then, TGA was performed on the resulting CNTs products as shown in Figure 5.1 (a) using the procedure described in Section 3.3.4.1 to determine the SiOC concentration The following equation was used to calculate the SiOC concentration in the CNTs products and the results are presented in Table 5.1:

$$SiOC\ concentration\ in\ CNTs\ sample = (Residual\ weight\ \%\ of\ SiOC\ coated\ CNTs\ at\ 800\ ℃ - Residual\ weight\ \%\ of\ As-received\ CNTs\ at\ 800℃) \times \frac{Molecular\ weight\ of\ SiOC}{Molecular\ weight\ of\ SiO_2}$$

Equation 5.1

The equation above was modified from Equation 3.17 based on the following considerations: (1) The residual weight % of the as-received CNTs after the TGA measurement is attributed to

the metal impurities (i.e. alumina) in the CNTs (as shown previously in Figure 4.12 (b) and Figure 4.13 (a)) and should therefore be excluded from the SiOC concentration calculation, and (2) the conversion of the SiOC coated CNTs into a white product after the TGA operation, as shown Figure 5.2, indicates that the SiOC coating had been fully oxidised to SiO_2 therefore a conversion factor (i.e. $\frac{Molecular\ weight\ of\ SiOC}{Molecular\ weight\ of\ SiO_2}$) had to be applied in the calculation.

Table 5.1. Onset temperature, residual weight % at 800 °C and calculated SiOC concentration of the of the treated CNTs according to the TGA results in Figure 5.1. The starting PMHS-CNTs sample before the production of SiOC coated CNTs is denoted as PMHSxCNTy where x/y is the PMHS/CNTs w/w (i.e. weight to weight ratio). The final sample after the production of SiOC coated CNTs is labelled as SiOCmCNTn where m and y are the SiOC and CNTs wt% in the SiOC coated CNTs product, respectively.

		TGA of the final product		
Starting sample	**Final product**	**Onset temperature (°C)**	**Residual weight % at 800 °C**	**Calculated SiOC concentration (wt%)**
As-received CNTs	As-received CNTs	572.6 ± 0.1	11.6 ± 0.5	0
PMHS10CNT1	SiOC22CNT78	679.5 ± 1.4	35.5 ± 1.4	22.3 ± 1.3
PMHS20CNT1	SiOC55CNT45	680.7 ± 1.2	70.7 ± 1.9	55.1 ± 1.7
PMHS30CNT1	SiOC68CNT32	687.6 ± 1.3	84.8 ± 0.5	68.4 ± 0.4
PMHS40CNT1	SiOC67CNT33	674.5 ± 5.0	83.8 ± 0.2	67.3 ± 0.2
PMHS50CNT1	SiOC71CNT29	684.9 ± 4.1	87.7 ± 0.5	71.0 ± 0.5
PMHS60CNT1	SiOC77CNT23	686.5 ± 2.1	94.3 ± 0.4	77.2 ± 0.3

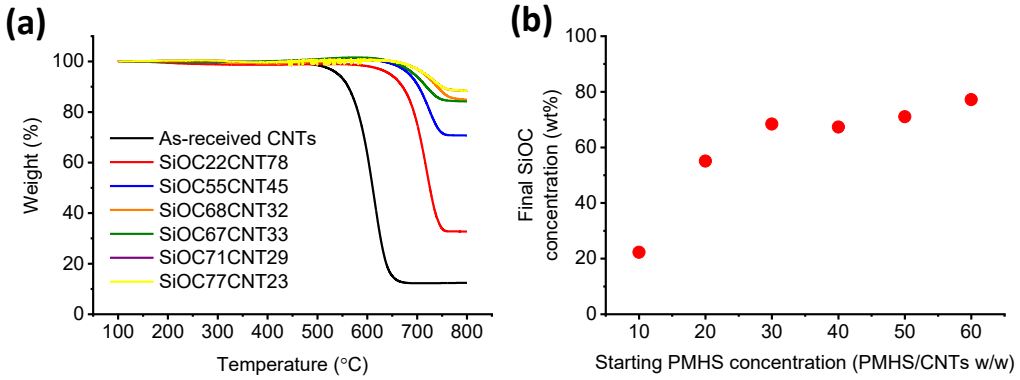


Figure 5.1. (a) TGA curves of as-received CNTs and SiOC coated CNTs as performed in air. (b) Scatter plot showing the relationship between the starting PMHS concentration in the PMHS-CNTs samples and the final SiOC concentration in the SiOC coated CNTs products.

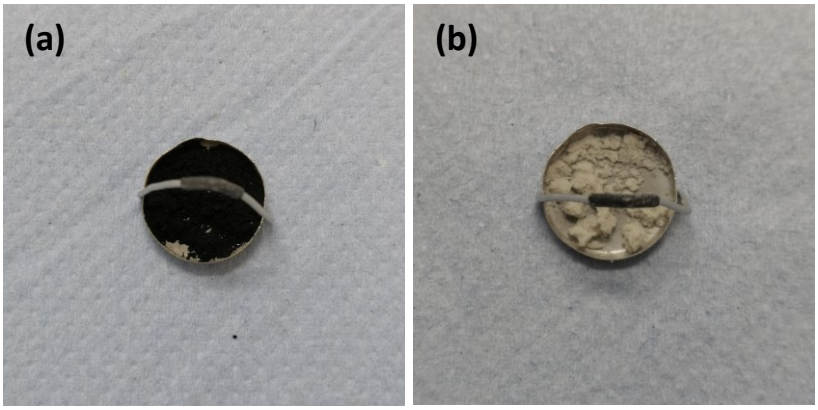
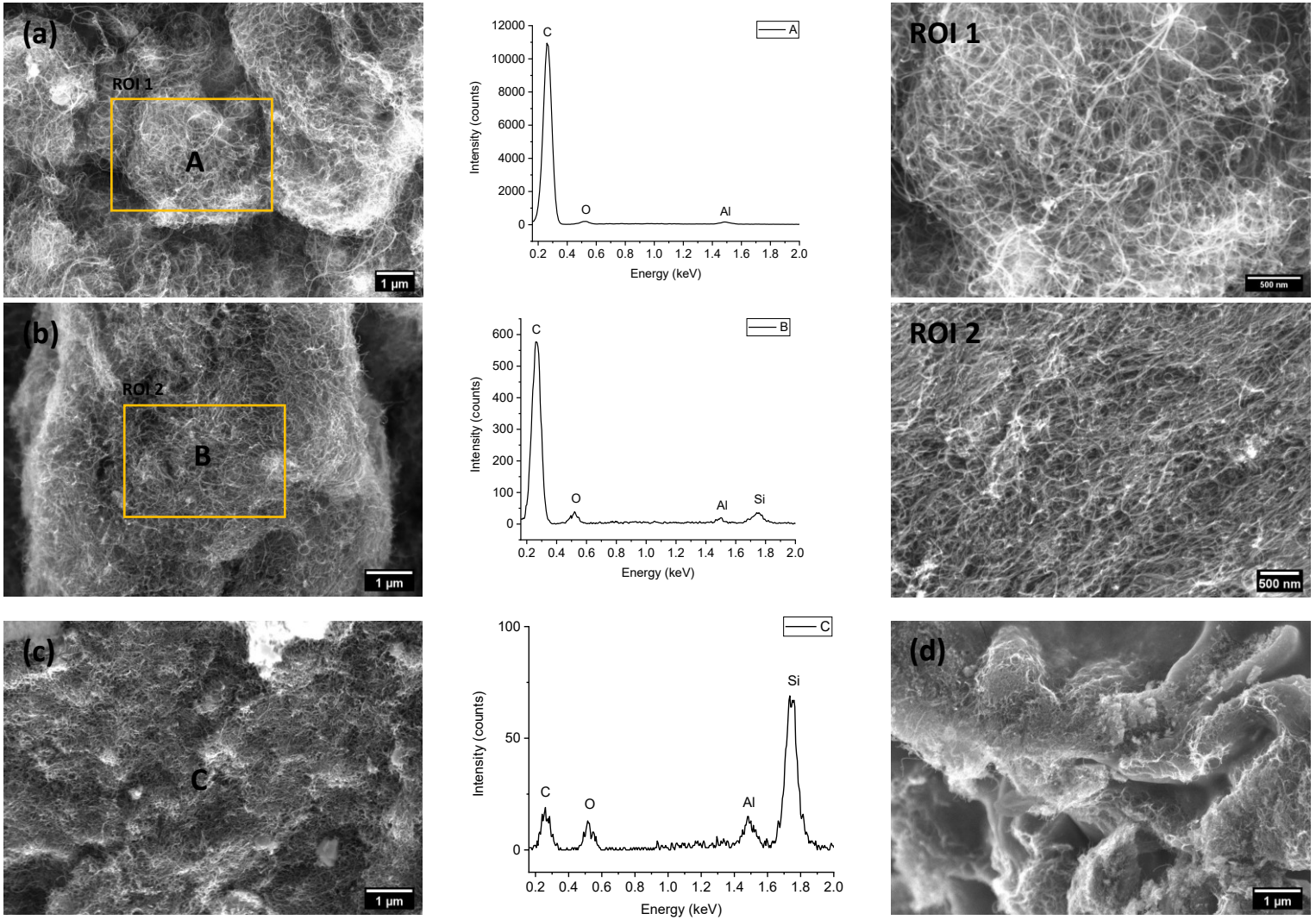


Figure 5.2. SiOC coated CNTs (shown here for SiOC22CNT78) (a) before and (b) after TGA operation in Figure 5.1 (a).

Following the determination of SiOC concentration, the final products were labelled as SiOCmCNTn where m and n are the SiOC and CNTs wt%, respectively. The effect of the starting PMHS concentration on the final SiOC concentration is plotted in Figure 5.1 (b). The plot shows that the SiOC concentration in the final product was gradually increased from 22.3 to 77.2 wt% as the starting PMHS concentration was increased from 10/1 to 60/1 PMHS/CNTs w/w. Therefore, CNTs samples with a wide range of SiOC concentrations were successfully produced which will allow the effect of SiOC concentration to be extensively investigated in the subsequent studies. In addition, the results in Table 5.1 and Figure 5.1 also reveal that the onset temperature for the decomposition of the CNTs was drastically increased with the presence of SiOC. This observation may indicate that the oxidation resistance of CNTs had been improved due to the coating of SiOC on the CNTs.

5.2.2 Effect of SiOC concentration on coating morphology

The coating morphology of some of the CNTs samples produced in the previous section was further investigated with SEM and TEM. The SEM and TEM images of the as-received CNTs and the as-produced SiOC coated CNTs are presented in Figure 5.3 and Figure 5.4, respectively. As shown in Figure 5.3 (a) and (b), the CNTs with the lowest SiOC concentration, i.e. SiOC22CNT78, appeared to be similar to the as-received CNTs. However, a small amount of Si and O could be detected on the CNTs by EDX which indicates a very low presence of SiOC coating in the sample. Subsequently, the TEM images of SiOC22CNT78 in Figure 5.4 (a) and (b) show a very low SiOC precipitation on the CNTs agglomerates and no obvious coating layer on the individual tubes (for comparison with as-received CNTs, see the TEM images in Figure 4.16 (a)). At a higher SiOC concentration, SiOC55CNT45 showed a larger amount of Si and O content on the CNTs as evident from the EDX measurement in Figure 5.3 (c). The increased precipitation of SiOC on the CNTs agglomerates can be more clearly observed in the TEM image in Figure 5.4 (c) meanwhile some of the individual CNTs also showed the presence of a discontinuous coating layer (Figure 5.4 (d)). Furthermore, the SiOC55CNT45 sample was also found to consist of dense SiOC products where CNTs could be found embedded in the SiOC solid (Figure 5.3 (d)). Subsequently, with further increase in SiOC concentration, the dense SiOC products became more commonly observed in the SiOC67CNT33 and SiOC77CNT23 samples. As shown in Figure 5.3 (e) and (f), CNTs had been found embedded in the dense SiOC products. The TEM images in Figure 5.4 (e) and (g) also show a thick coating of SiOC precipitates over the CNTs agglomerates which can be matched to the dense SiOC-CNTs products observed in SEM. Additionally, a discontinuous SiOC coating layer had also be observed on some of the individual tubes (Figure 5.4 (f) and(h)) in these samples as also confirmed with EDX.


(a)
ROI 1
A
1 µm
(b)
ROI 2
B
1 µm
(c)
C
1 µm
A
B
C
Intensity (counts)
Energy (keV)
C
O
Al
Si
ROI 1
500 nm
ROI 2
500 nm
(d)
1 µm

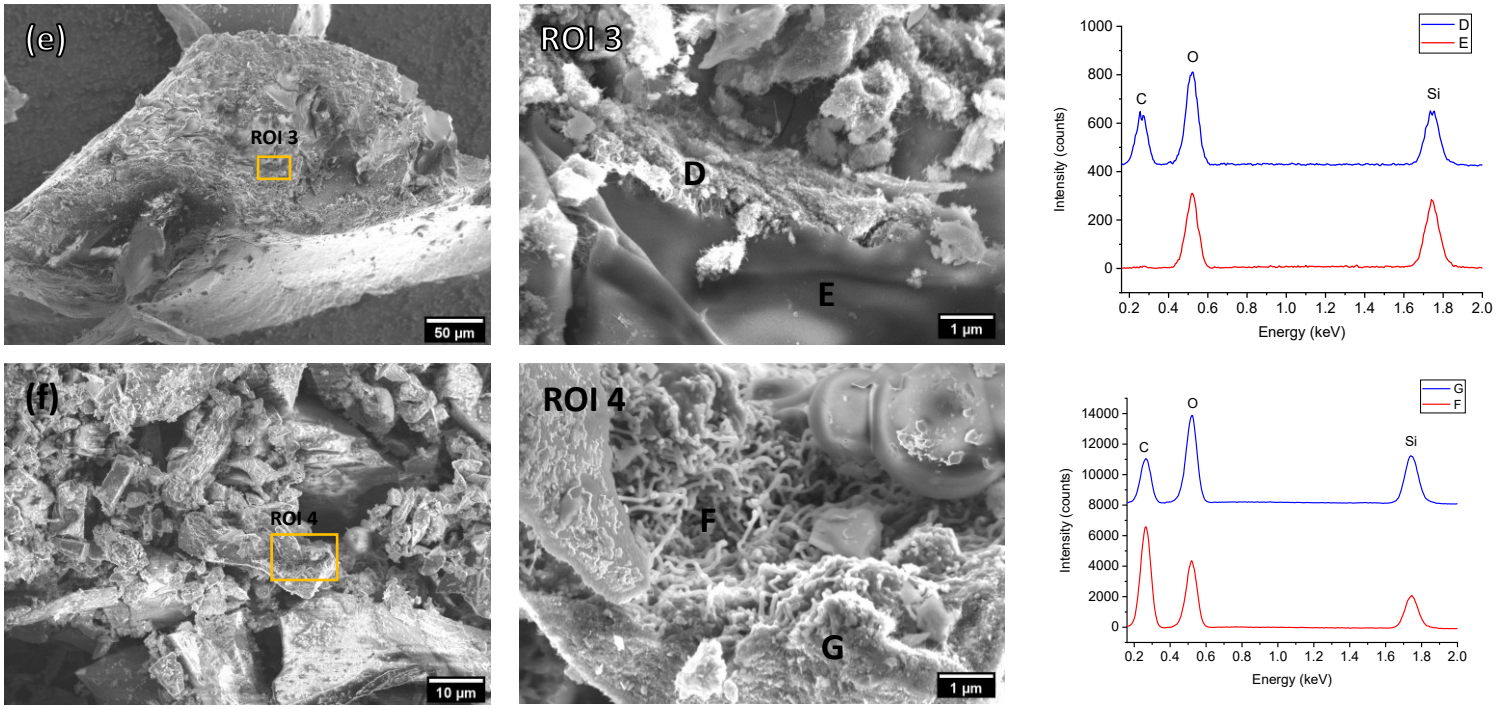
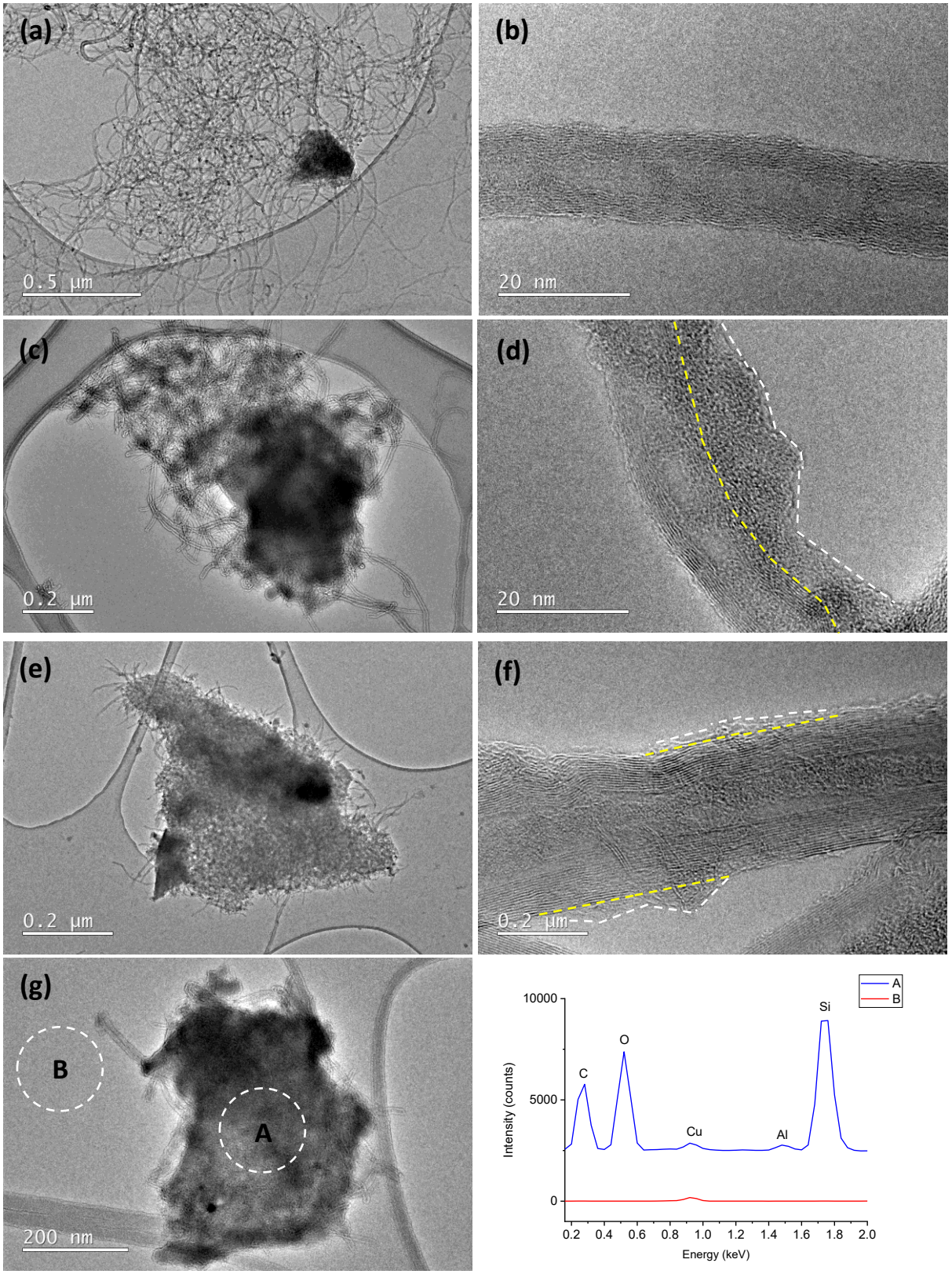


Figure 5.3. SEM images and EDX spectra of (a) as-received CNTs and as produced SiOC coated CNTs: (b) SiOC22CNT78, (c and d) SiOC55CNT45, (e) SiOC67CNT33 and (f) SiOC77CNT23. Point EDX measurement was performed at the locations marked by the capital letters A-G in the SEM images. Note that the Al shown in the EDX spectra corresponds to the alumina impurities which were originally present in the as-received NC7000 CNTs.


(a)
0.5 μm
(b)
20 nm
(c)
0.2 μm
(d)
20 nm
(e)
0.2 μm
(f)
0.2 μm
(g)
B
A
200 nm
A
B
10000
5000
0
Intensity (counts)
C
O
Cu
Al
Si
0.2
0.4
0.6
0.8
1.0
1.2
1.4
1.6
1.8
2.0
Energy (keV)

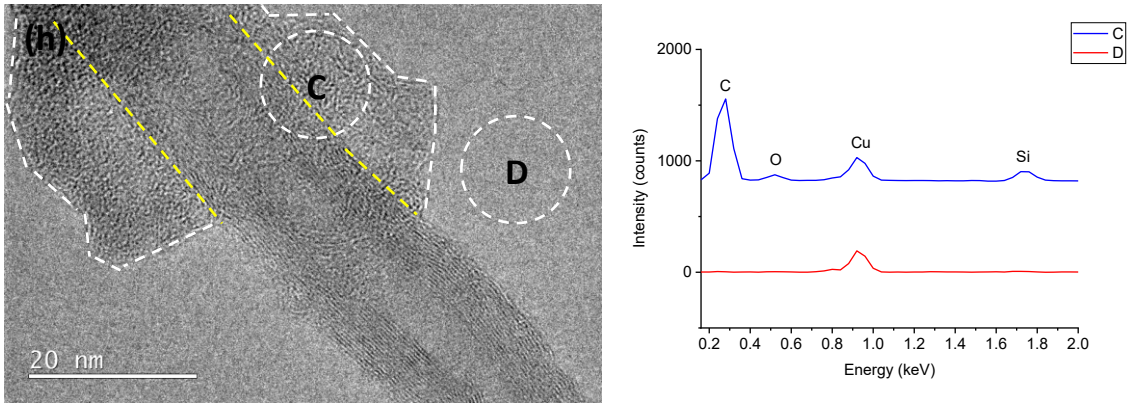


Figure 5.4. TEM images and EDX spectra of the CNTs agglomerate and individual tubes in the as-produced SiOC coated CNTs: (a and b) SiOC22CNT78, (c and d) SiOC55CNT45, (e and f) SiOC67CNT33 and (g and h) SiOC77CNT23. The outer surface of the CNTs and the outer layer of the SiOC coating are highlighted with yellow and white dotted lines, respectively, to outline the coating layer. Point EDX measurement was performed at the areas marked with white dotted circles and labelled with capital letters A-D. Cu detected in the EDX spectra is attributed to the TEM copper grid.

Based on the SEM and TEM characterisations of the SiOC coated CNTs, a model is proposed in Figure 5.5 to explain the progression of the SiOC coating morphology as the SiOC concentration increases. As proposed in Figure 4.19, the tendency of the polymer to pool between the tangled CNTs junctions and to form clam-like or barrel-like droplets on the individual CNTs surfaces lead to the precipitation of SiOC on the agglomerates and the formation of a discontinuous coating layer on the individual tubes, respectively. Therefore, at a low coating concentration, a small amount of SiOC precipitation occurs on the CNTs agglomerates meanwhile the presence of coating on the individual CNTs is expected to be very minimal as shown in Figure 5.5 (a). As the coating concentration increases (Figure 5.5 (b)), more SiOC precipitation will occur on the CNTs agglomerates meanwhile the individual tubes are more likely to be coated with a discontinuous coating layer. Finally, at a very high coating concentration (Figure 5.5 (c)), the formation of dense SiOC-CNTs products would become more predominant due to thicker precipitation of SiOC on the agglomerates CNTs. Since the model predicts that the coating tends to be formed on the agglomerated CNTs network instead

of the individual tubes, the presence of huge agglomerates during the preparation of the PMHS-CNTs samples is not desirable as the polymer will tend to adhere on the tangled CNTs therefore preventing the individual CNTs from being efficiently coated. Therefore, further optimisation should be carried out in the future to ensure that a better dispersion of CNTs is produced when preparing the PMHS-CNTs mixtures.

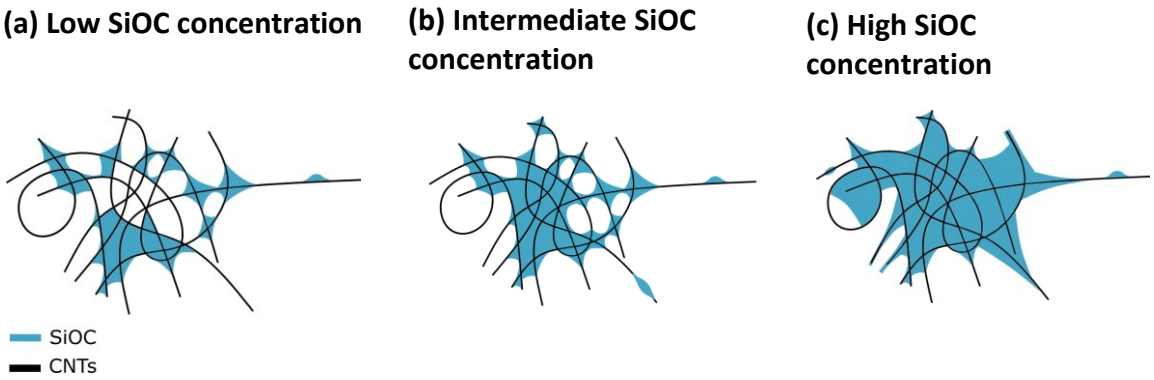


Figure 5.5. Proposed model for the evolution of the SiOC coated CNTs morphology at a different SiOC concentration: (a) low, (b) intermediate and (c) high.

5.2.3 Effect of SiOC coating on CNTs dispersibility

To investigate the state of dispersion of the as-received CNTs and SiOC coated CNTs, each CNTs sample was dispersed in THF at a concentration of 1 mg equivalent of as received CNTs per mL of THF and ultrasonicated for 30 min using the sonication parameters described in Section 3.2.1.1.

Figure 5.6 shows the appearance of the as-received CNTs and SiOC coated CNTs in THF before and after ultrasonication. The photographs of the solutions prior to sonication were taken 10 minutes after adding the CNTs to the THF. Interestingly, while the as-received CNTs and SiOC22CNT78 were found to settle immediately at the bottom of the glass vials, the SiOC coated CNTs with SiOC concentrations of 55 wt% and above appeared to be more readily dispersed in the solvent even without ultrasonication. After ultrasonication, a homogeneous black solution was obtained for each dispersion. Additionally, large particles could still be observed in the as-received CNTs and SiOC22CNT78 dispersions (could be seen more clearly on the glass walls); meanwhile, the appearance of these particles were diminished in the other dispersions.

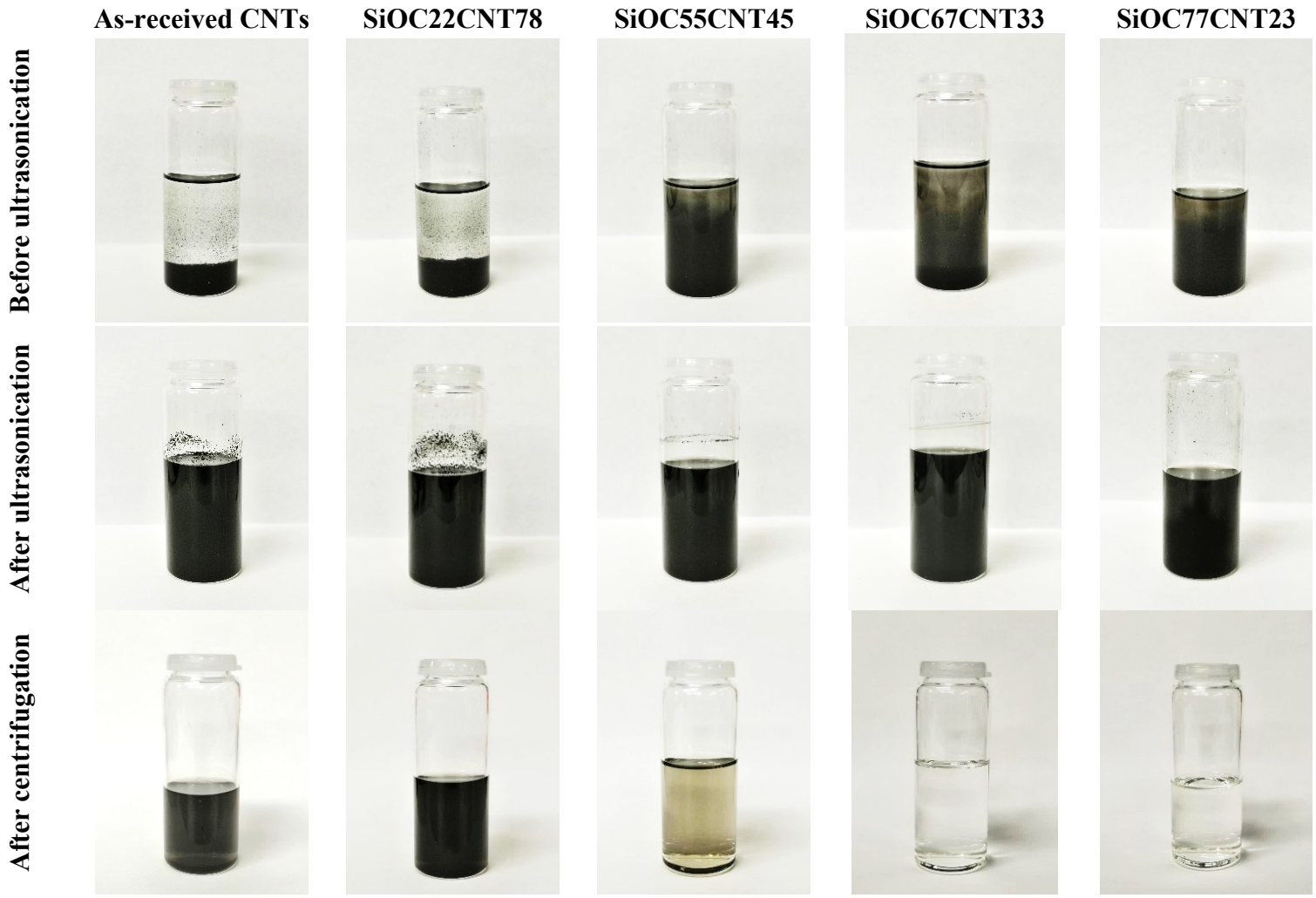


Figure 5.6. Photographs of as-received CNTs and SiOC coated CNTs in THF before and after ultrasonication, and after centrifugation. Each dispersion was prepared at a concentration of 1 mg equivalent of as-received CNTs per mL of THF.

The dispersions were then studied with optical microscopy and SEM as shown in Figure 5.7 and Figure 5.8, respectively. The characterisation techniques are described in Sections 3.3.6 and 3.3.7. For the dispersions of the as-received CNTs and SiOC22CNT78, large and dense clusters were primarily observed in the optical micrographs as shown in Figure 5.7 (a) and (b). The large particles which were previously observed in the dispersions via visual inspection in Figure 5.6 could likely correspond to these large clusters. The clusters were mainly made up of agglomerated CNTs as shown in the SEM images in Figure 5.8 (a) and (b). Subsequently, the large CNTs clusters were no longer observed in the SiOC55CNT45 to SiOC77CNT23 dispersions. The dispersion of SiOC55CNT45 in Figure 5.7 (c) shows a homogeneous dispersion of finer particles with the appearance of some yellowish-brown solids (higher magnification in Figure 5.7 (c), ROI 1). The yellowish-brown solids can most likely be identified as dense SiOC products which is consistent with the brown SiOC product obtained previously in Figure 4.9. SEM characterisation of the SiOC55CNT45 dispersion had also revealed the presence of debundled CNTs (Figure 5.8 (c)) and dense SiOC-CNTs products (Figure 5.8 (d)) which would correspond to the fine particles and yellowish-brown solids observed in the optical micrograph, respectively. Similarly, dense SiOC-CNTs solids and debundled CNTs were also found in the SiOC67CNT33 dispersion as shown in Figure 5.8 (e) and (f), respectively, however the optical micrograph in Figure 5.7 (d) seems to indicate a lower concentration of the fine particles. Finally, the presence of yellowish-brown solids seems to be increased in the SiOC77CNT33 dispersion as shown in Figure 5.7 (e) and these were also identified as dense SiOC-CNTs products as shown in Figure 5.8 (g). Debundled CNTs could also be found in this dispersion as shown in Figure 5.8 (h) albeit in a much lesser amount.

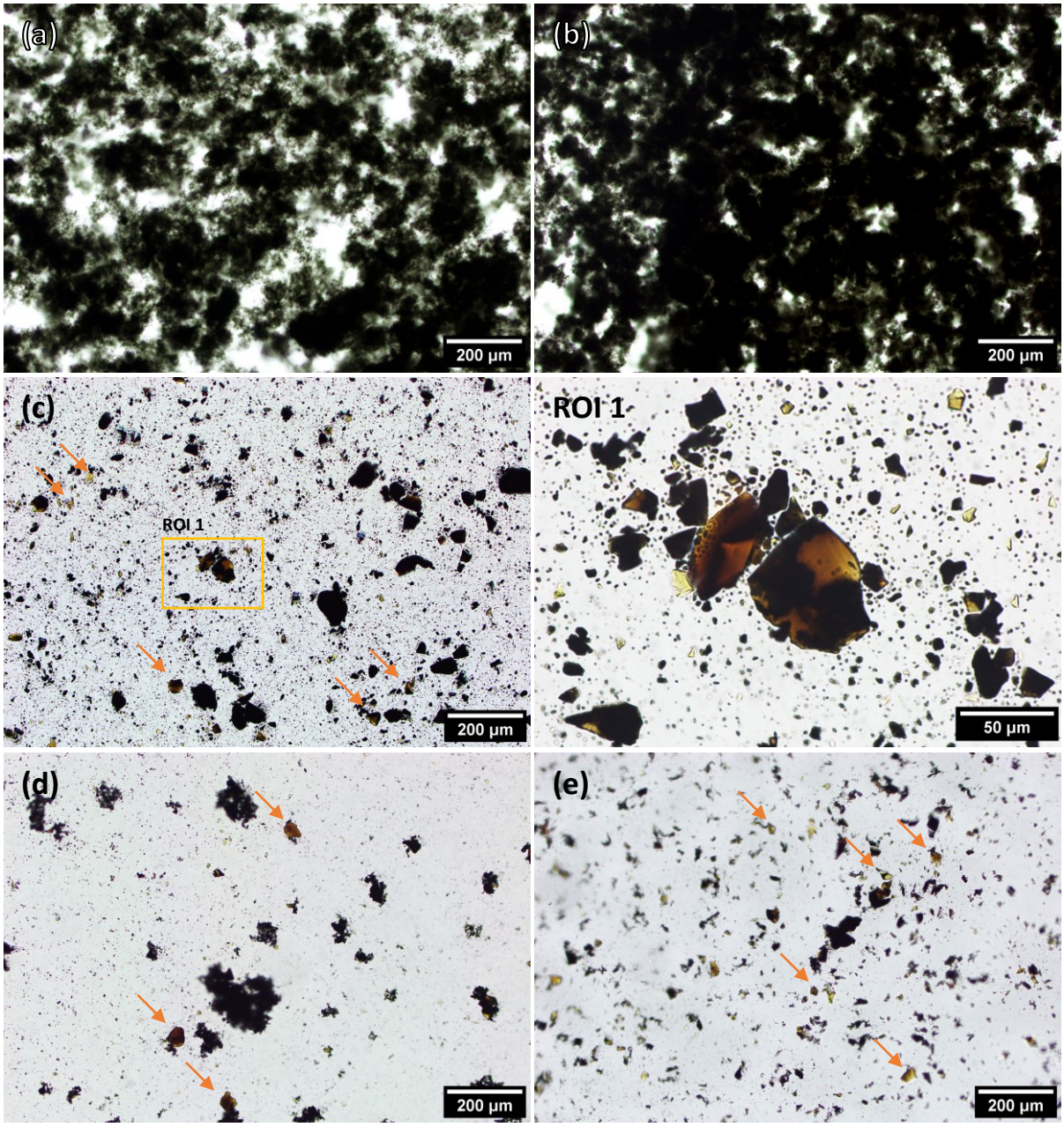
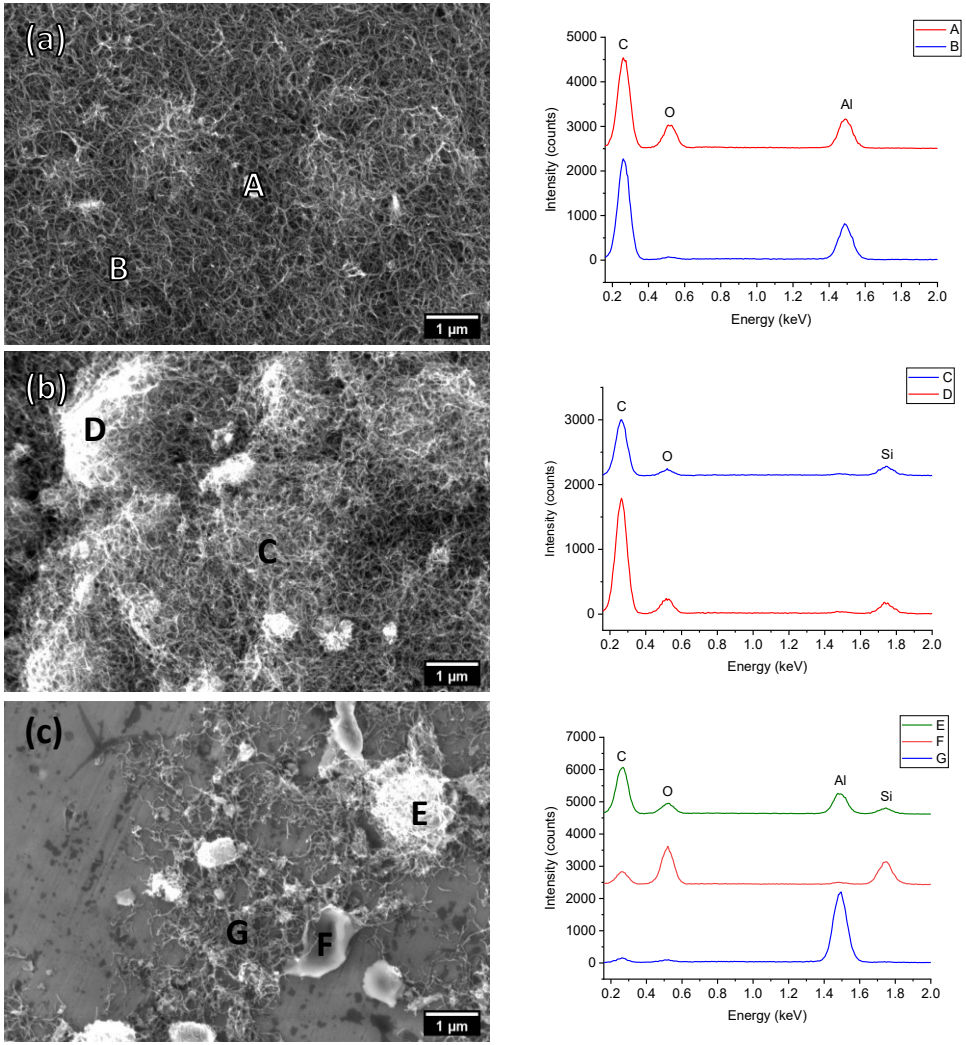
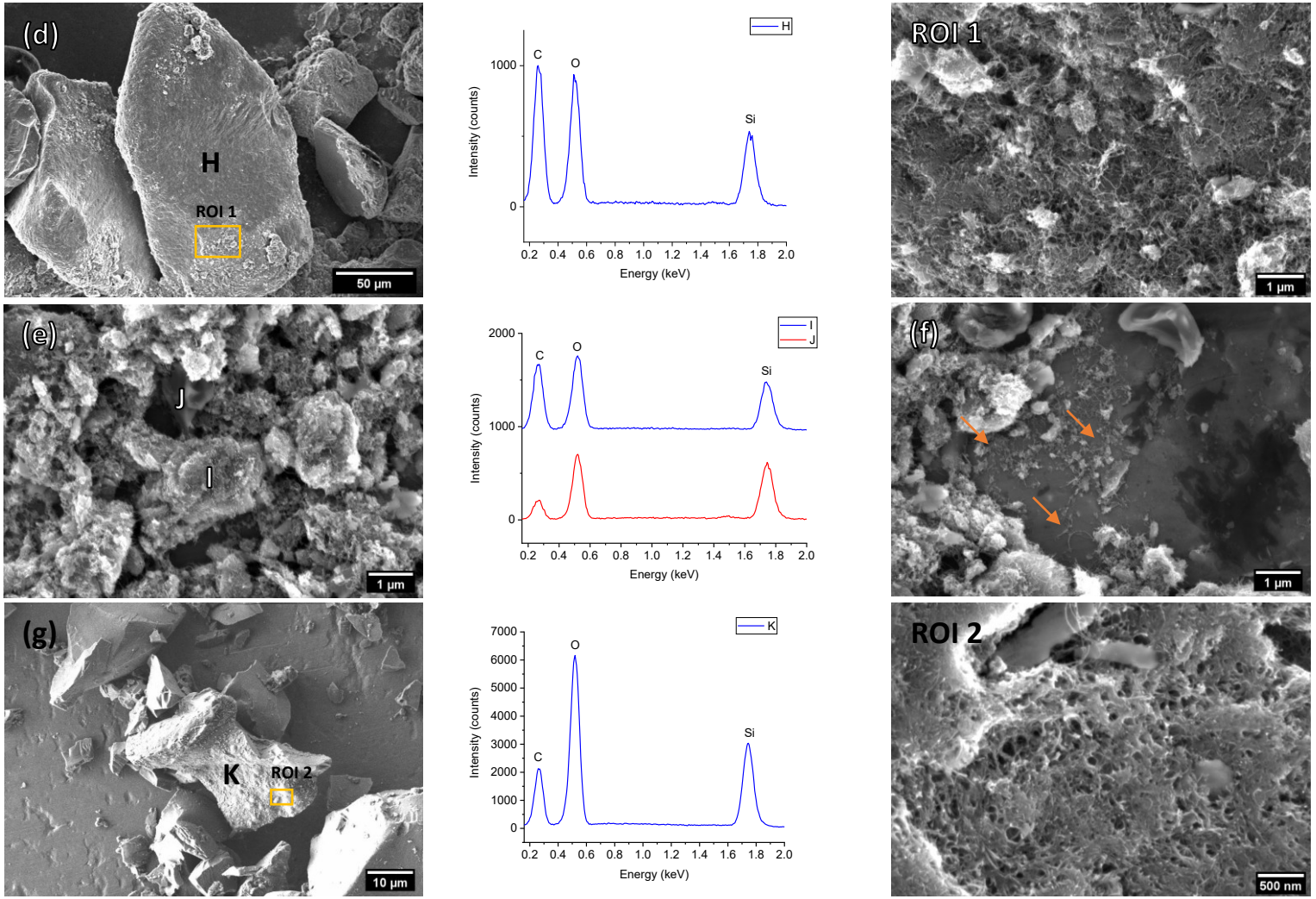


Figure 5.7. Optical micrographs of (a) as-received CNTs, (b) SiOC22CNT78, (c) SiOC55CNT45 (d) SiOC67CNT33 and (e) SiOC77CNT23 dispersions in THF after 30 min ultrasonication. Each dispersion was prepared at a concentration of 1 mg equivalent of as-received CNTs per mL of THF. Some of the yellowish-brown particles are highlighted by the arrows.


(a)
A
B
1 μm
(b)
D
C
1 μm
(c)
E
G
F
1 μm
A
B
C
O
Al
Intensity (counts)
Energy (keV)
C
D
C
O
Si
Intensity (counts)
Energy (keV)
E
F
G
C
O
Al
Si
Intensity (counts)
Energy (keV)


(d)
H
ROI 1
50 µm
H
C
O
Si
1000
0
Intensity (counts)
0.2 0.4 0.6 0.8 1.0 1.2 1.4 1.6 1.8 2.0
Energy (keV)
ROI 1
1 µm
(e)
J
I
1 µm
I
J
2000
1000
0
C
O
Si
Intensity (counts)
0.2 0.4 0.6 0.8 1.0 1.2 1.4 1.6 1.8 2.0
Energy (keV)
(f)
1 µm
(g)
K
ROI 2
10 µm
K
7000
6000
5000
4000
3000
2000
1000
0
C
O
Si
Intensity (counts)
0.2 0.4 0.6 0.8 1.0 1.2 1.4 1.6 1.8 2.0
Energy (keV)
ROI 2
500 nm

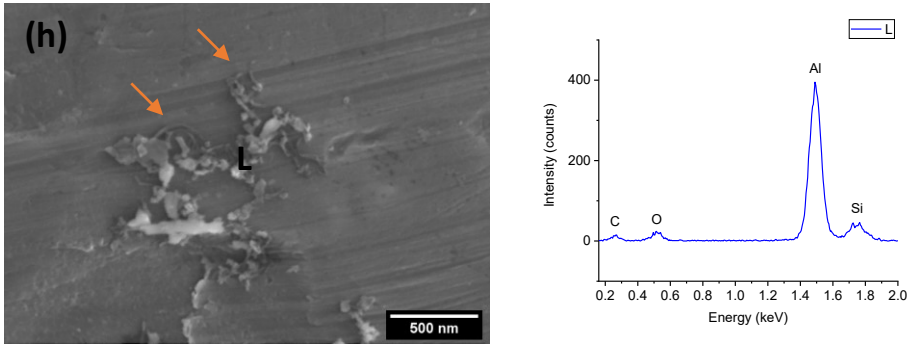


Figure 5.8. SEM images of ultrasonically dispersed CNTs deposited on Al foil: (a) As-received CNTs, (b) SiOC22CNT78, (c and d) SiOC55CNT45, (e and f) SiOC67CNT33 and (g and h) SiOC77CNT23. Point EDX measurement was performed on the locations marked by the capital letters A-L. Some of the debundled individual CNTs are highlighted by the orange arrows. Al detected in the EDX is attributed to the Al foil.

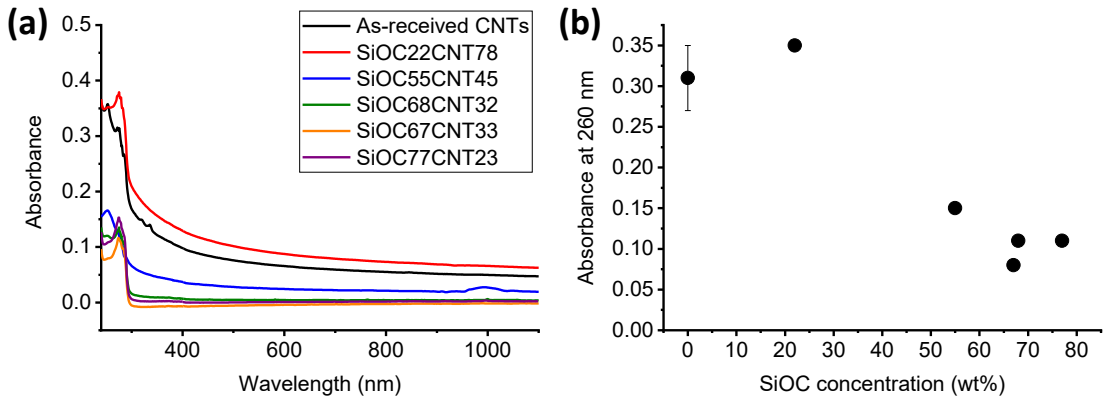


Figure 5.9. (a) UV-Vis spectra of as-received CNTs and SiOC coated CNTs supernatant solutions. (b) Plot showing the absorbance value of the supernatant solutions at 260 nm as a function of SiC concentration in the CNTs sample.

Following the dispersion of the as-received CNTs and SiOC coated CNTs by ultrasonication, the large bundles were removed by centrifugation as described in Section 3.3.2. Then, the supernatants were extracted, as shown in Figure 5.6, and further diluted by a factor of 10 before taken to the UV-Vis-near IR absorbance measurement as shown Figure 5.9.

From Figure 5.6, homogeneous black dispersions can be observed for the as-received CNTs and SiOC22CNT78 supernatants after centrifugation. Subsequently, the dispersions turned drastically lighter for the SiOC55CNT45 to SiOC77CNT33 dispersions. Based on the assumptions that the large CNTs agglomerates would settle as sediment and the individually dispersed CNTs are suspended in the supernatant after centrifugation, the UV-Vis absorbance value of each dispersion at 260 nm was determined as shown in Figure 5.9 to evaluate the degree of individually dispersed CNTs produced in each dispersion. In comparison to the as-received CNTs, the absorbance value was found to increase in the SiOC22CNT78 dispersion which may indicate that the amount of individually dispersed CNTs was increased in the dispersion. Then, the absorbance value was found to decrease in the subsequent dispersions which therefore indicates the decrease in the amount of individually dispersed CNTs. However,

individually dispersed CNTs which have been coated with a dense layer of SiOC could have also been sedimented during the centrifugation instead of suspending in the supernatant. Therefore, in this case, further investigation such as the characterisation of the sediment products still needs to be carried out to confirm the reliability of the UV-Vis results. Nevertheless, since dense SiOC-CNTs products were commonly observed in the SiOC55CNT45 to SiOC77CNT33 dispersions (Figure 5.8 (d), (e) and (g)), it can be postulated that the increased formation of these dense products had also led to the decrease in the amount of individually dispersed CNTs.

Additionally, the absorbance measurement in Figure 5.9 also seems to correlate well with the visual observation of the supernatants in Figure 5.6 whereby the lighter coloured solution corresponds to the lower the absorbance value. Although clear solutions were essentially observed for the SiOC67CNT33 and SiOC77CNT23 supernatants, a small absorbance could be still recorded in their UV-Vis-near IR spectra which may indicate a small presence of debundled CNTs as it was previously observed in SEM (Figure 5.8 (f) and (h)).

Based on the characterisation of the as-received and SiOC coated CNTs dispersions, the effect of SiOC coating concentration on the dispersibility of CNTs can be summarised as follows: at a low SiOC coating concentration, large CNTs agglomerates would mainly be found in the SiOC22CNT78 dispersion after ultrasonication as similarly observed for the as-received CNTs dispersion. However, the removal of these agglomerates via centrifugation revealed that a higher degree of individually dispersed CNTs could be found in in the SiOC22CNT78 dispersion than in the as-received CNTs dispersion. At the higher SiOC coating concentrations, large CNTs agglomerates would no longer be observed in the dispersions of SiOC55CNT45 to SiOC77CNT23. Instead, smaller sized particles consisting of debundled CNTs and dense

SiOC-CNTs solids were found. The absorbance measurement of the supernatants after centrifugation also showed that the higher the SiOC coating concentration in the CNTs sample, the lower the absorbance value. The lower absorbance values recorded for these dispersions could be explained by the sedimentation of the dense SiOC products during centrifugation which were either adhered to the debundled CNTs such as in Figure 5.8 (c) and (f), or those which were formed as dense SiOC-CNTs solids such as in Figure 5.8 (d), (e) and (g). The increased formation of dense SiOC-CNTs products could have also led to the decrease in the amount of individually dispersed CNTs; however, further investigations are required to confirm this hypothesis.

5.3 AZ91 composites

The characterisation of the composite samples in Section 5.3.2 and Section 5.3.3 were carried out on the as-cast and post-processing treated samples, respectively. Therefore, the general microstructure of as-cast and post-processing treated AZ91 samples is firstly discussed in Section 5.3.1.

5.3.1 General microstructure of pure AZ91

Pure AZ91 casting was produced using the procedure described in Section 3.2.2 by stirring at 650 °C for 30 minutes. To assess the microstructure within the casting, three specimens (each with the length of 1 cm) were cross sectioned from the cylindrical section of each casting and labelled according to the top, middle and bottom locations as shown in Figure 5.10. The microstructure of the polished cross sections was observed under optical microscopy as shown in Figure 5.11 where some defects can be found in each specimen.

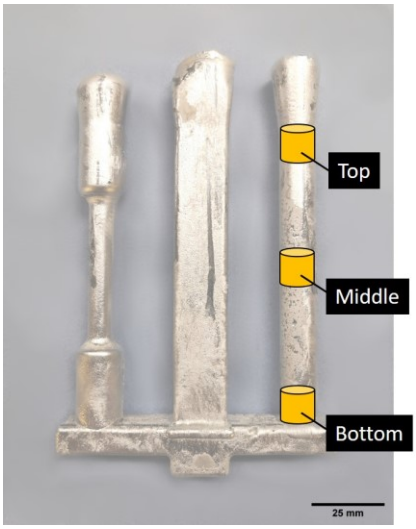


Figure 5.10. Photograph showing the as-cast pure Mg AZ91 and the locations at which specimens were taken for microstructural characterisation.

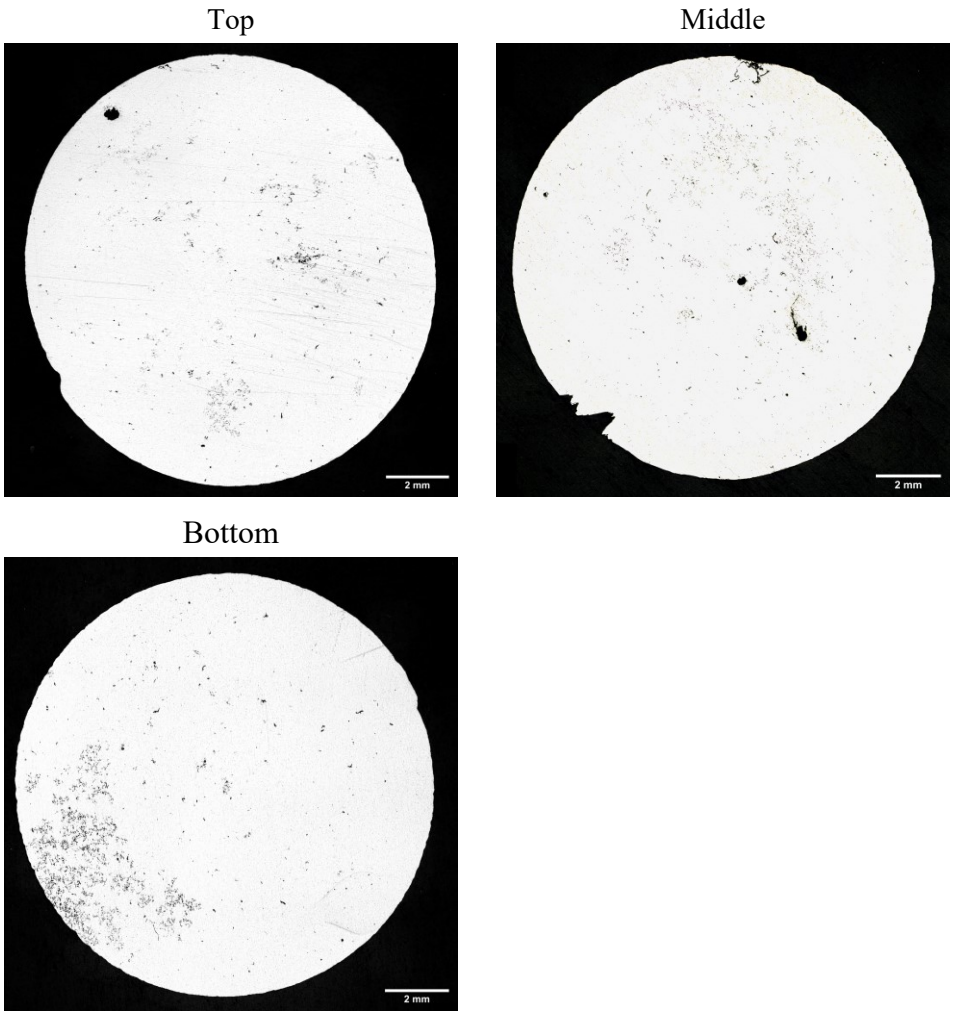


Figure 5.11. Optical micrographs showing the polished cross sections of pure Mg AZ91 specimens taken from the top, middle and bottom locations of the cylindrical section of the casting.

Further investigations with optical microscopy and SEM revealed that the defects mainly consisted of shrinkage porosity and gas porosity. Shrinkage pores, as shown in Figure 5.12 (c) and (d), are irregularly shaped and formed due to the lack of molten metal supply (or feeding) during the solidification contraction which leads to a porosity between the dendritic arms [245]. In alloys of short freezing range such as Mg AZ91, shrinkage porosity is usually expected to concentrate near the centre of the casting, however, such trend had not been observed in this work. On the other hand, gas pores are usually spherical as shown in Figure 5.12 (e and f) and may originate either from hydrogen gas evolved from the reaction between moisture in the atmosphere and Mg, and/or pre-existing gas bubbles entrapped during casting [246].

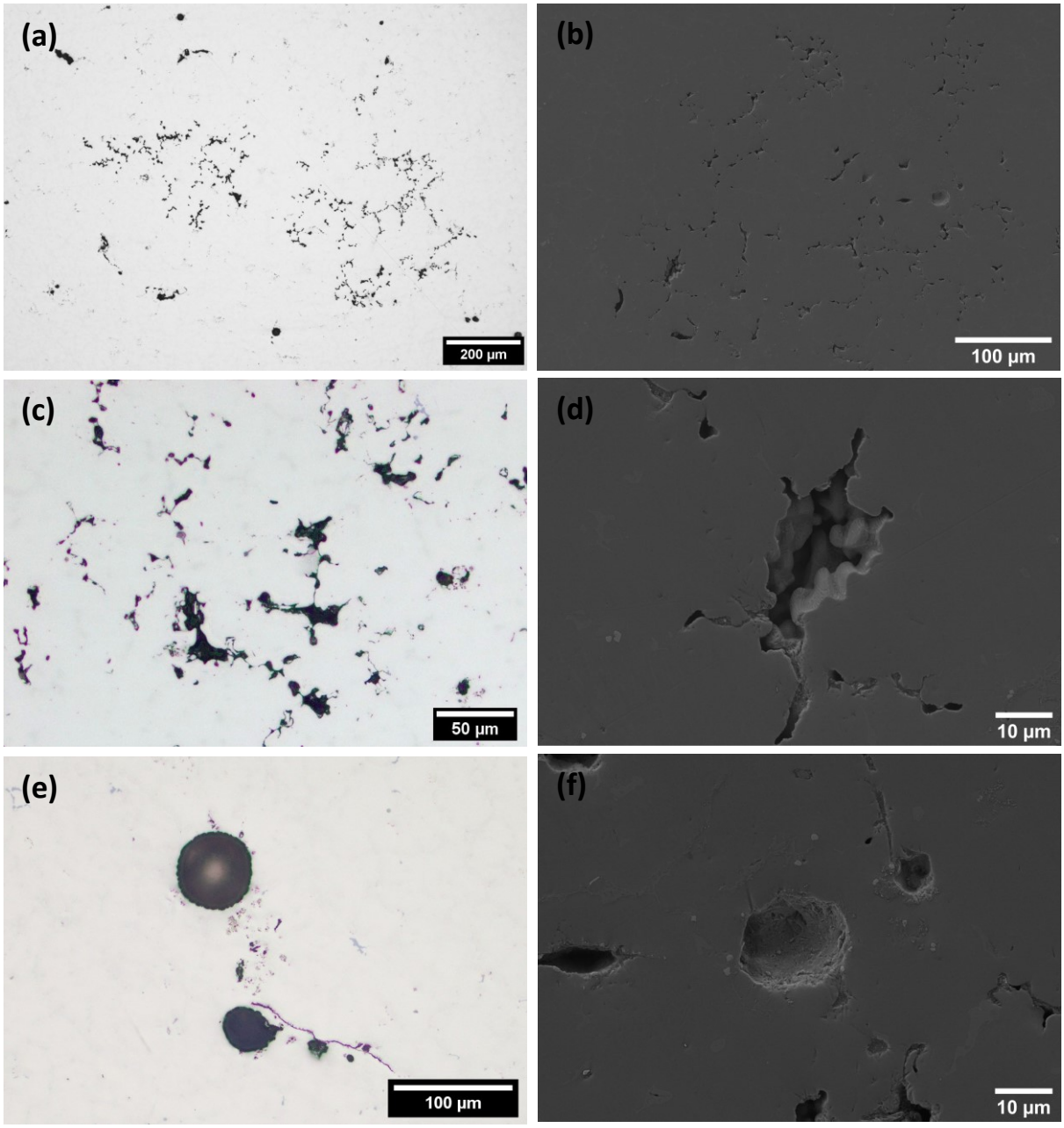


Figure 5.12. Optical micrographs (left) and SEM images (right) showing the casting defects typically found in the as-cast pure Mg AZ91 sample: (a and b) at low magnification, (c and d) shrinkage porosity at a higher magnification and (e and f) gas porosity at a higher magnification.

Since the fabrication of Mg alloys by gravity casting introduces internal porosities and defects which may significantly alter the microstructure and mechanical properties of the samples, the solution heat treatment and hot rolling were performed on the as-cast samples to optimise the microstructure and therefore improve the mechanical properties of the alloy. Figure 5.13 (a) and (b) show the polished cross section and grain structure, respectively, of the as-cast pure

Mg AZ91. Then, the solution heat treatment was carried out whereby the alloy was heated to a temperature within the α-phase field (refer to the Mg-Al binary phase diagram in Figure A.5 in Appendix) for a sufficient amount of time to completely dissolve the β-phase. The supersaturation of the solid solution would increase the densification of the alloy matrix and simultaneously reduce the appearance of the pores [247] as shown in Figure 5.13 (c). Grain coarsening would also be observed as shown in Figure 5.13 (d) due to the coalescence of subgrains during annealing which leads to the grain growth [248, 249]. Next, hot rolling was performed to impart the formability of the alloy due to the limited ductility and poor formability of Mg alloys at room temperature. Large plastic deformations that occurred during hot rolling would cause the change in the morphology of the pores and the welding of the internal surfaces of the pores [250] eventually leading to the pores closure as shown in Figure 5.13 (e) and (g). A drastic decrease in grain size, as shown in Figure 5.13 (f) and (h), could also be observed as a result of the dynamic recrystallisation processes that occurred due to the activation of the non-basal slip systems [251, 252].

The as-cast pure AZ91 alloy typically exhibits a dendritic microstructure which can be more clearly seen after etching (see Figure 5.13 (b)). The characterisation of the polished cross section with SEM in Figure 5.14 (a) and (c) shows that the as-cast AZ91 predominantly consists of the α-Mg and β-$Mg_{17}Al_{12}$ phases. Island-like β-phase is generally distributed along the grain boundaries in the interdendritic spaces and may be surrounded by lamellar structures of the divorced eutectic α+β phase which is formed due to the non-equilibrium solidification [253]. Following the solution heat treatment, the β-phase would be completely dissolved which would lead to a notable loss of the β-phase as observed in Figure 5.14 (b).

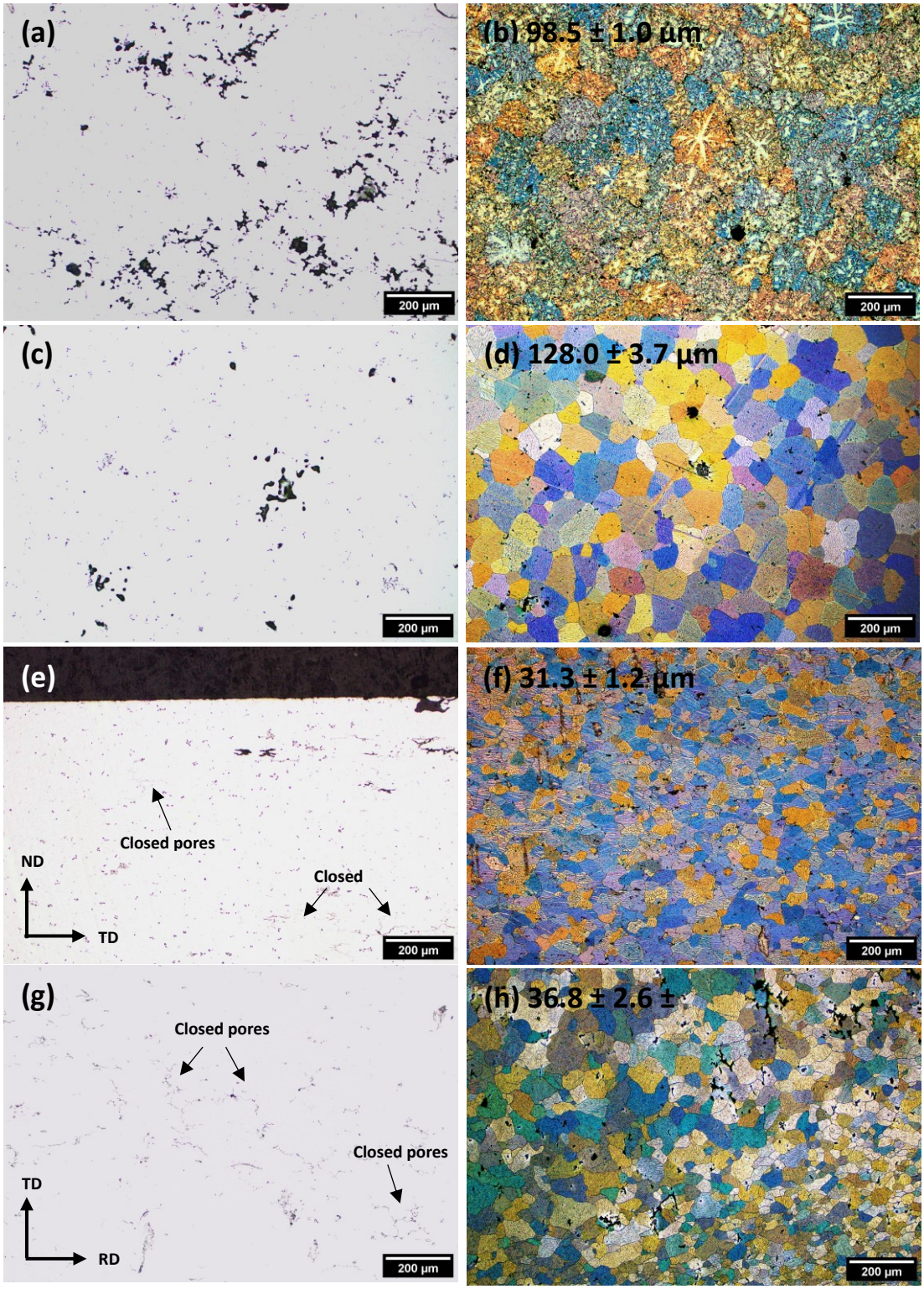


Figure 5.13. Optical micrographs of polished (left) and etched (right) cross sections of pure Mg AZ91 alloys at different conditions: (a) as-cast, (b) after solution heat treatment and natural ageing (i.e. T4 treatment), and (c and d) after solution heat treatment and hot rolling. ND, TD and RD refer to the normal, transverse and rolling directions, respectively. The grain sizes are denoted in the grain structure images.

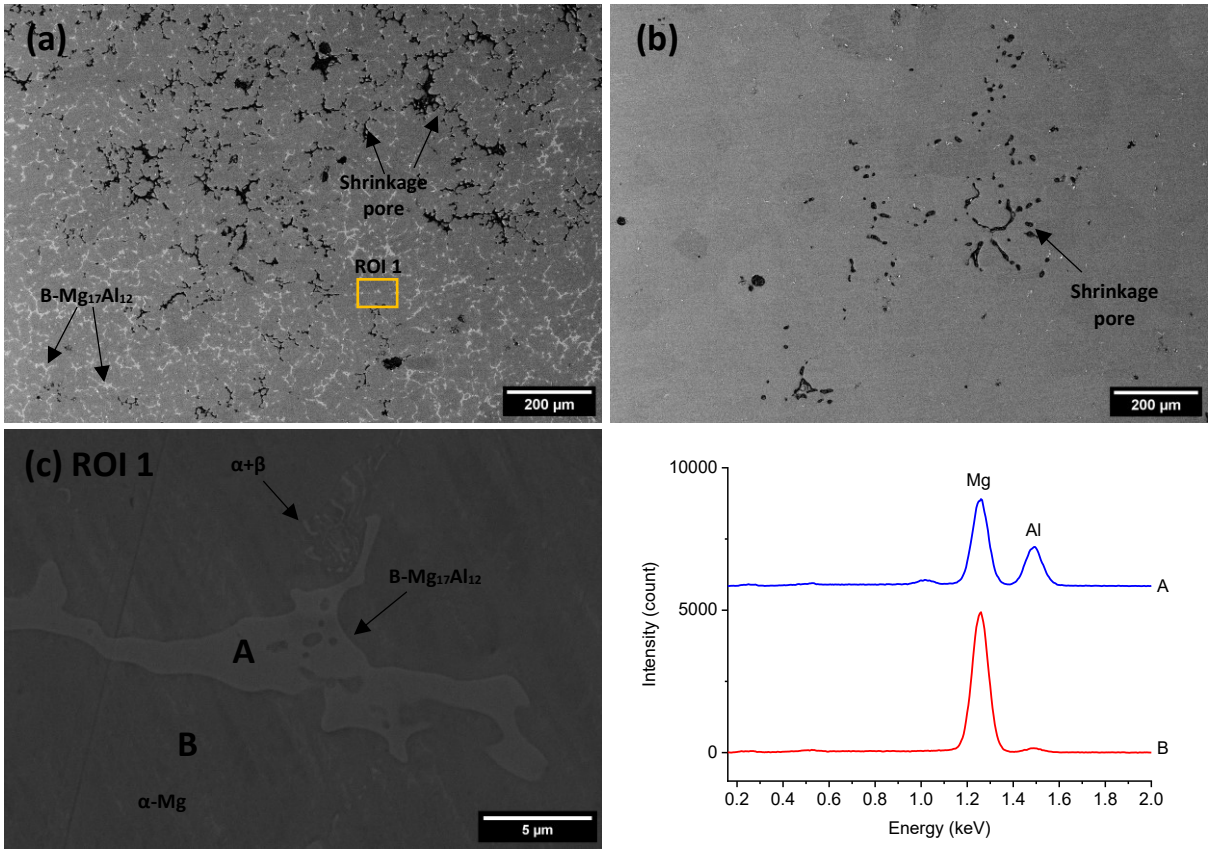


Figure 5.14. SEM images of pure Mg AZ91 alloys at different conditions: (a) as-cast and (b) after solution heat treatment and natural ageing (i.e. T4 treatment). (c) is a magnification of an area in (a). Point EDX measurement was carried out at the locations marked with the capital letters.

In summary, the solution heat treatment and hot rolling treatments are effective for improving the microstructure of the as-cast AZ91 castings by reducing the casting pores and refining the grain structures. Nevertheless, the post-processing treatments will only be applied in the final studies in Chapter 5 and Chapter 6 where the effect of CNTs on the strengthening of the AZ91 composites were investigated.

5.3.2 Effect of SiOC coating on AZ91 composite properties

Pure AZ91 and AZ91 composites reinforced with as-received and SiOC coated CNTs were fabricated as listed in Table 5.2 to investigate how the SiOC concentration in the CNTs (and therefore the resulting morphologies) would affect the properties of the AZ91 composites. The AZ91 samples were fabricated via stir casting as described in Section 3.2.2 by stirring at 650 °C for 30 minutes. The CNTs samples were added to the melt using Al parcels as described in Section 3.2.3 at an equivalent as-received CNTs loading of 0.3 wt%. For consistency, blank Al parcels had also been added to the pure AZ91 sample. Note that a different total nanoparticles loading was added to each sample to account for the SiOC concentration in each CNTs sample. One casting was fabricated for each sample for the microstructural and mechanical properties characterisations.

Table 5.2. List of Mg AZ91 samples fabricated to investigate the effect of SiOC coating concentration in the CNTs on the properties of AZ91 composites.

Sample	Total nanoparticles loading (wt%)	Equivalent as-received CNTs loading (wt%)
Pure AZ91	0	0
AZ91-As received CNTs	0.30	0.3
AZ91-SiOC22CNT78	0.38	0.3
AZ91-SiOC55CNT45	0.67	0.3
AZ91-SiOC67CNT33	0.91	0.3
AZ91-SiOC77CNT23	1.30	0.3

Initially, a few interesting observations were made during the casting of AZ91-As received CNTs and AZ91-SiOC22CNT78 composites. Some as-received CNTs were found to be completely left out of the casting or pushed to the outer surface of the casting upon solidification as shown in Figure 5.15 (a). On the other hand, a very large pore was formed in the AZ91-SiOC22CNT78 casting, as shown in Figure 5.15 (b), where CNTs could be found embedded. On the contrary, no such behaviour was observed on the remaining AZ91 composites for example the AZ91-SiOC55CNT45 composite shown in Figure 5.15 (c).

Therefore, these observations were preliminary indications for the poor wettability of CNTs with none to low SiOC coating.

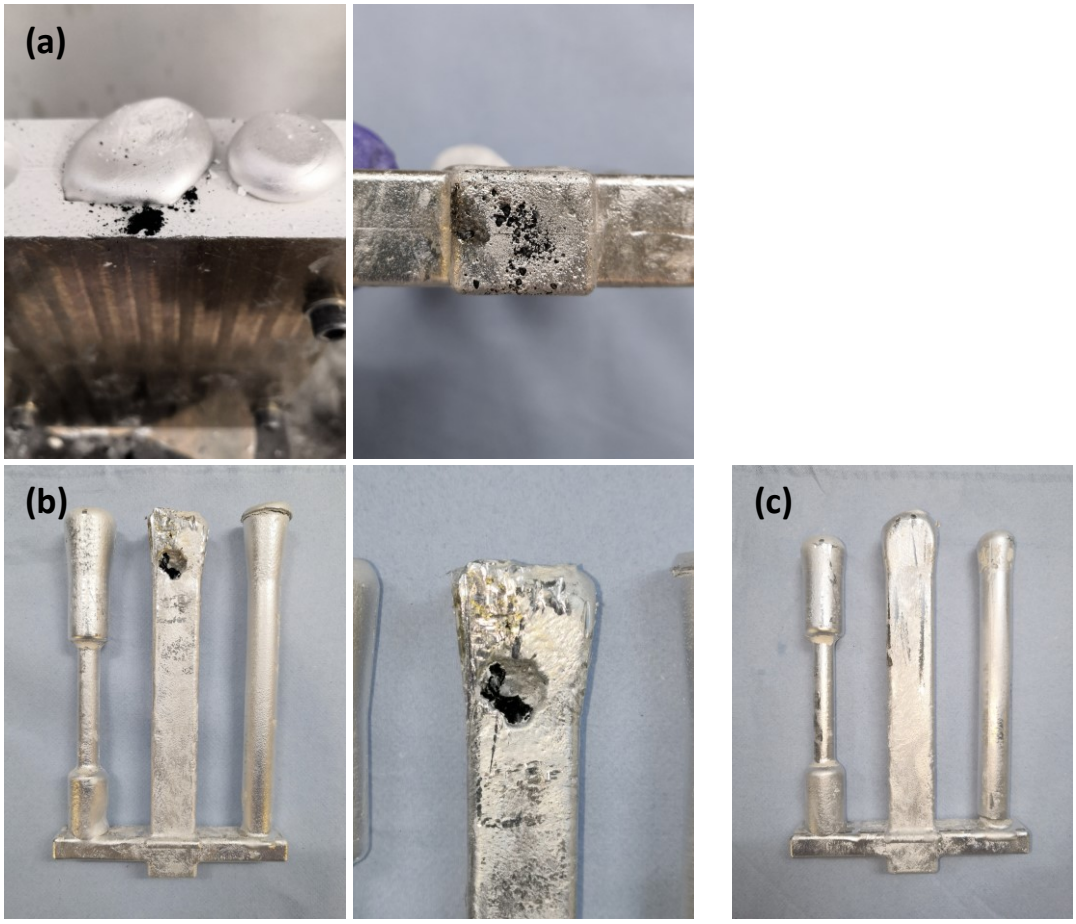


Figure 5.15. Photographs of (a) AZ91-As received CNTs, (b) AZ91-SiOC22CNT78 and (c) AZ91-SiOC45CNT55 castings.

Figure 5.16 compares the polished cross sections of the AZ91 samples. By visual inspection, the appearance of defects appears to be the highest in the AZ91-SiOC22CNT78 composite (Figure 5.16 (c)). The porosity results, as shown in Table 6.3 and Figure 5.17, seem to also agree with the microstructural observation where the porosity level was measured to be the highest for AZ91-SiOC22CNT78 and the lowest for AZ91-SiOC55CNT45 among the composites samples.

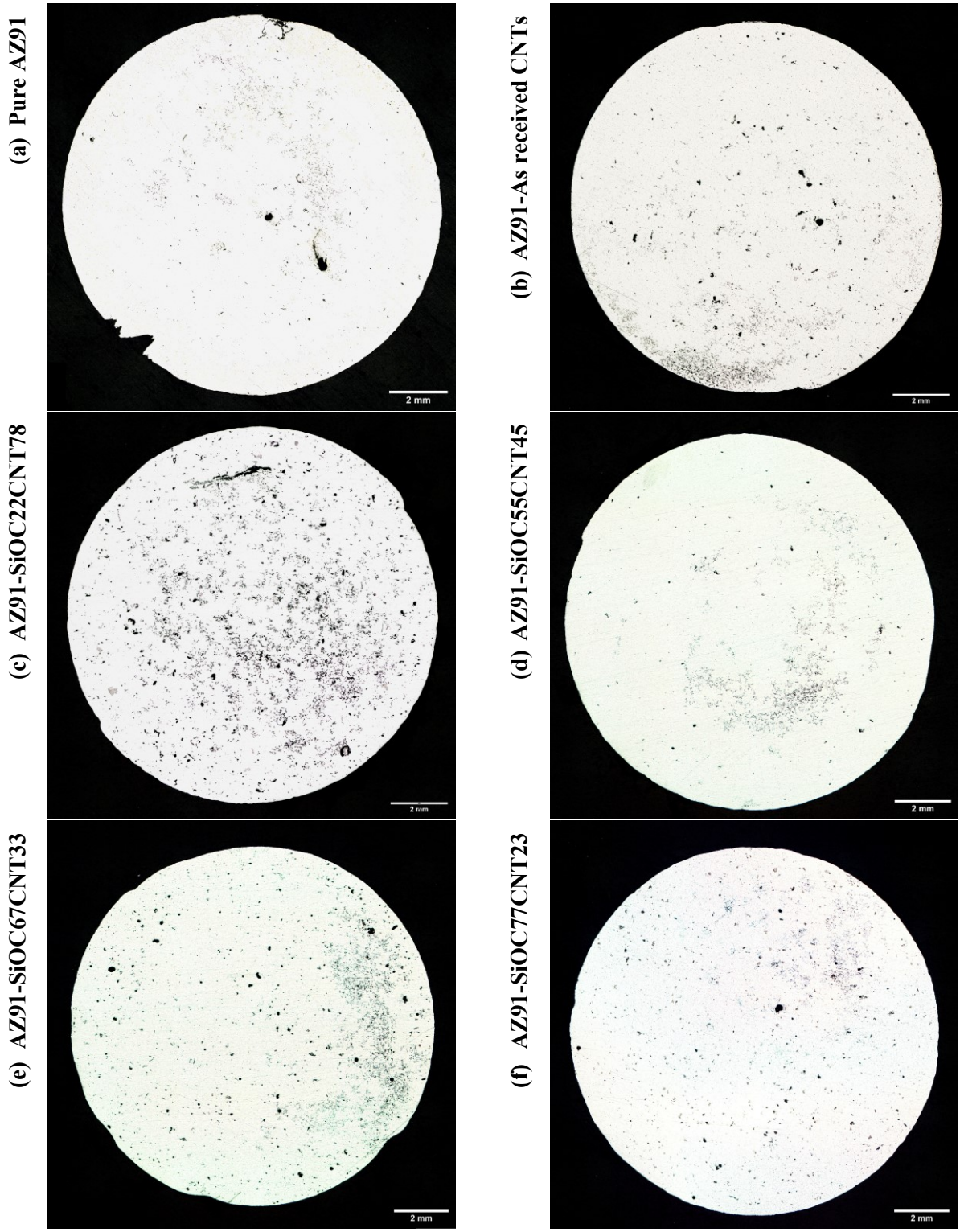


Figure 5.16. Optical micrographs showing the cross sections of as-cast (a) pure AZ91 and AZ91 composites reinforced with (b) As-received CNTs, (c) SiOC22CNT78, (d) SiOC55CNT45, (e) SiOC67CNT33 and (f) SiOC77CNT23. Each cross section was taken from the middle location of the cylindrical part of the casting (see Figure 5.10).

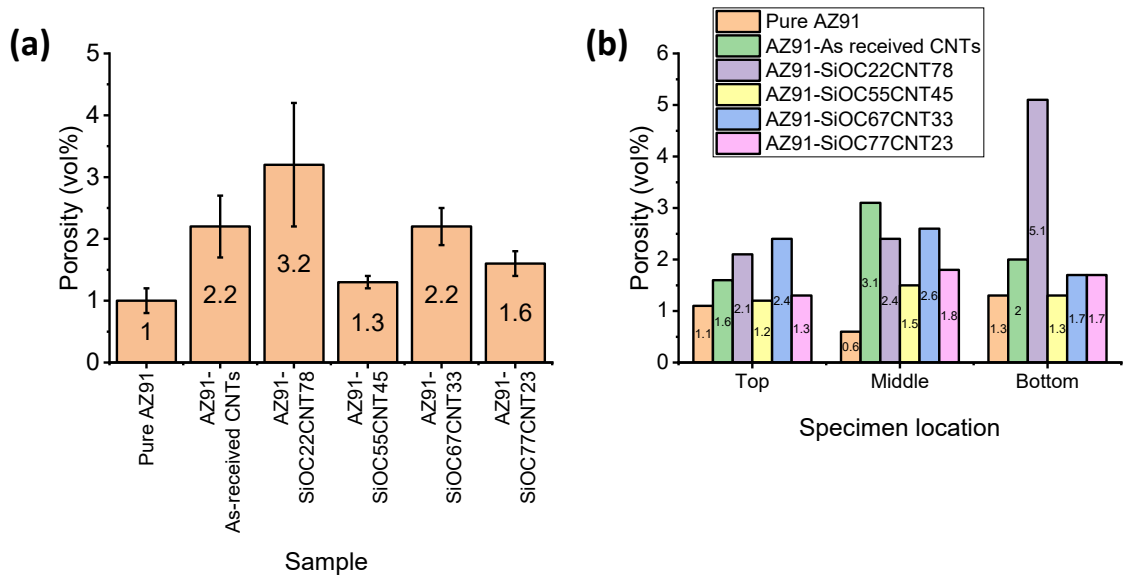


Figure 5.17. Porosity comparison between the as-cast pure AZ91 and AZ91 composites (a) by average and (b) by specimen location (see Figure 5.10). A single measurement was performed for each specimen location.

Subsequently, further characterisations were carried out with optical microscopy and SEM to investigate the source of porosity in each composite. Generally, the optical micrographs in Figure 5.18 show that the large pores observed in the AZ91 composites were irregularly shaped and non-rounded which are different than the gas and shrinkage pores that are typically observed in a pure AZ91 casting (see Figure 5.12). For the AZ91-As received CNTs composite, oxide films were mainly found on the internal surface of the pores as shown Figure 5.19 (a). On the other hand, an increased presence of oxide inclusions were observed for the AZ91-SiOC22CNT78 composite and large SiOC coated CNTs agglomerates were also found embedded inside the pore as shown in Figure 5.19 (b) based on the identification of tubular structures and the EDX measurement. Similarly, large SiOC coated CNTs agglomerate could also be found inside the pore of AZ91-SiOC55CNT45 casting as shown in Figure 5.19 (c). However, smaller particles had also been found embedded in the matrix as shown in Figure 5.19 (d) and (e). Together with the EDX measured they were assumed to be smaller SiOC

coated CNTs agglomerates that had been completely wetted by the matrix. Finally, large particles could be found aggregated within the pores of the AZ91-SiOC67CNT33 casting as shown in Figure 5.18 (d) and these were identified with SEM in Figure 5.19 (f) as dense solid particles. The solid particles would most likely correspond to the dense SiOC-CNTs products that were previously observed in the as-produced SiOC67CNT33 (Figure 5.3 (e)). From this investigation, it can be concluded that SiOC22CNT78 with the lowest amount of coating could not be sufficiently wetted by the matrix which led to the increased level of porosity in the composite. On the other hand, with the increase in the SiOC concentration such as in the case of SiOC67CNT33, a higher amount of dense SiOC-CNTs solids would be found in the SiOC coated CNTs sample and the aggregation of these particles would lead to the formation of porosity in the composites. Therefore, coupled with the microstructural evidence from optical microscopy and SEM, the lowest level of porosity observed for the AZ91-SiOC55CNT45 composite may indicate that SiOC55CNT45 could be most effectively wetted by the matrix among the coated CNTs samples.

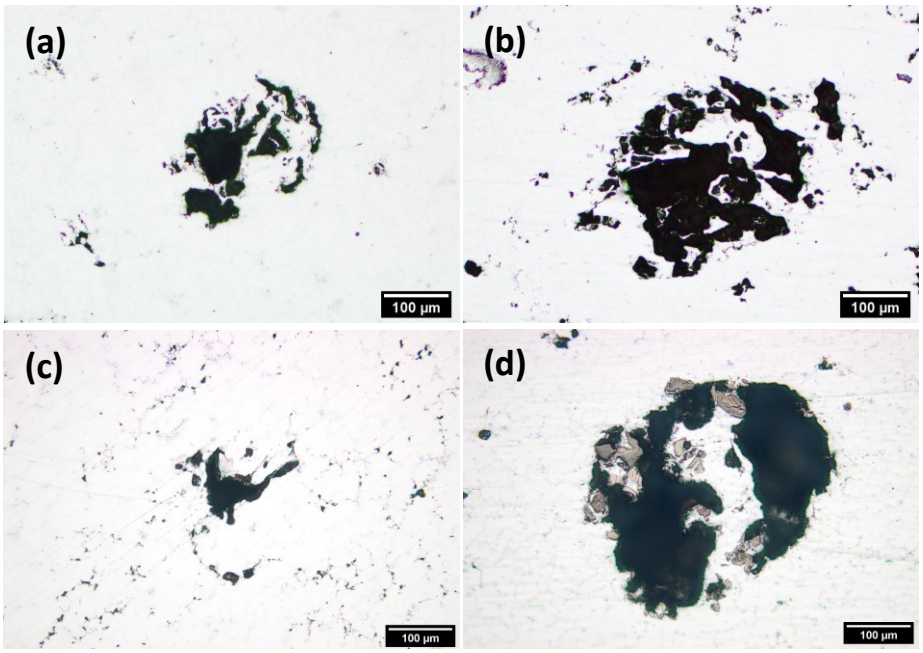
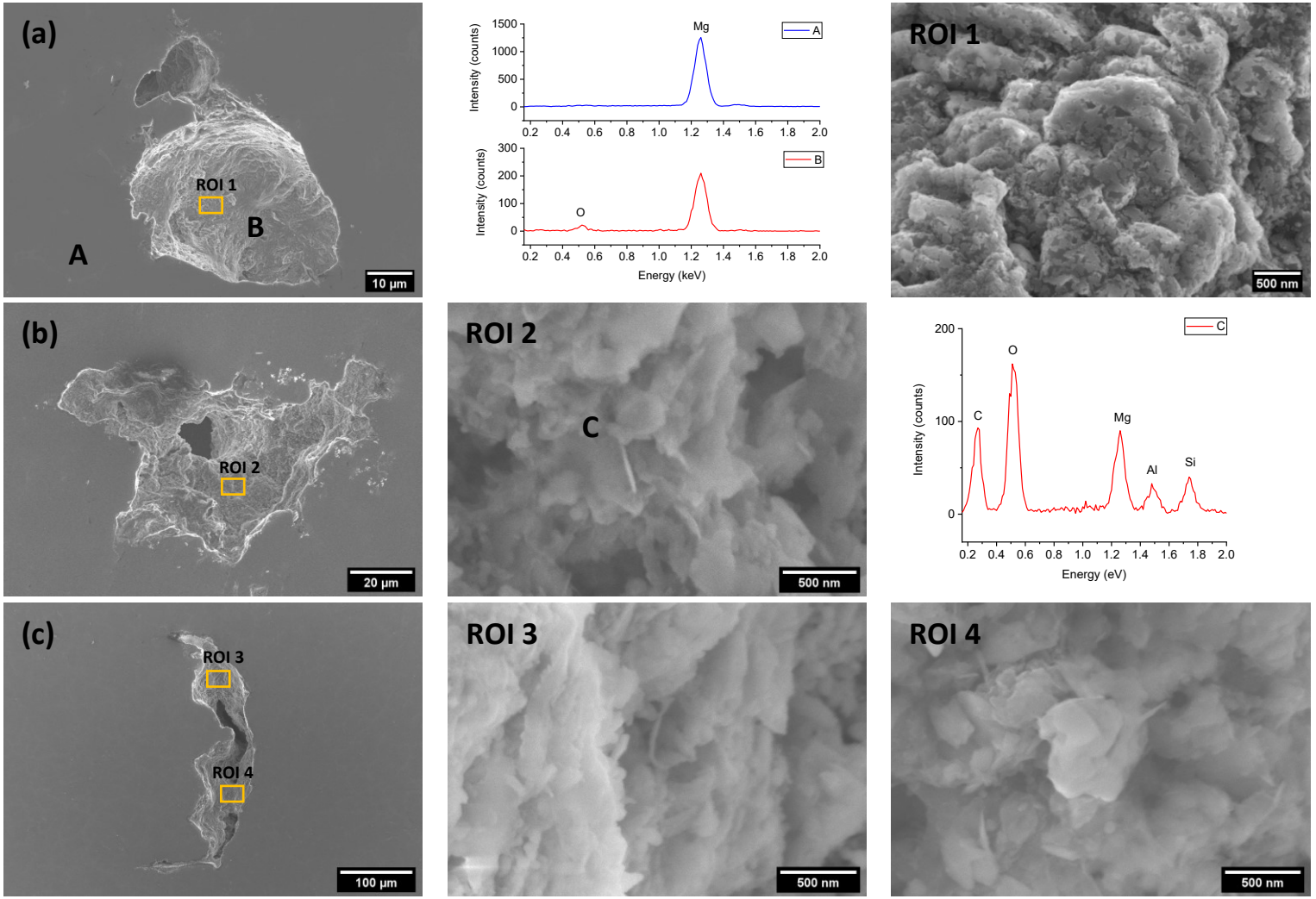


Figure 5.18. Optical micrographs showing the porosity formation in the AZ91 composites reinforced with (a) as-received CNTs, (b) SiOC22CNT78, (c) SiOC55CNT45 and (d) SiOC67CNT33.


(a)
ROI 1
A
B
10 µm
Intensity (counts)
Mg
A
O
B
Energy (keV)
ROI 1
500 nm
(b)
ROI 2
20 µm
ROI 2
C
500 nm
Intensity (counts)
C
O
Mg
Al
Si
Energy (eV)
(c)
ROI 3
ROI 4
100 µm
ROI 3
500 nm
ROI 4
500 nm

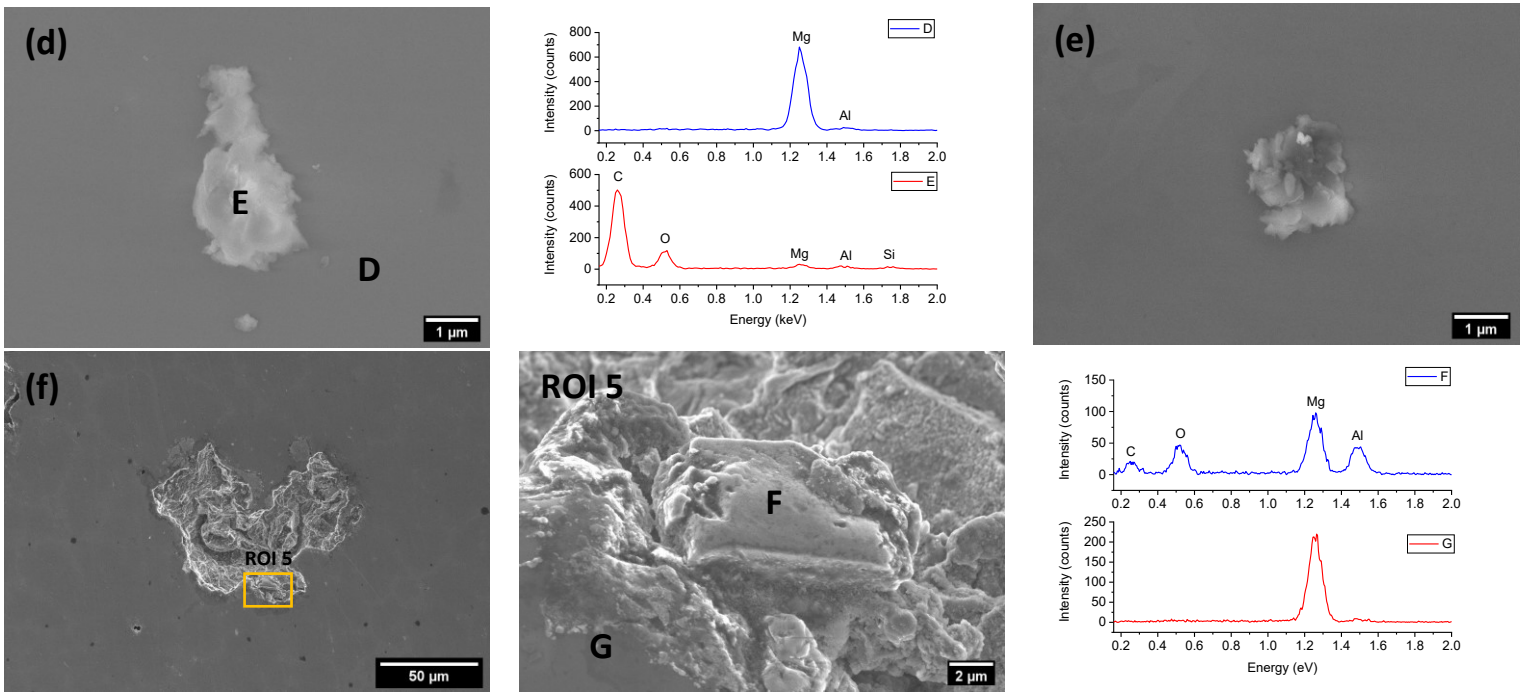


Figure 5.19. SEM images showing the cross-section of as-cast AZ91 composites reinforced with (a) as-received CNTs, (b) SiOC22CNT78, (c and d) SiOC55CNT45 and (f) SiOC67CNT33 along with their corresponding EDX spectra. Point EDX measurement was performed at the locations marked by the capital letters A-G in the SEM images.

Table 5.3. Density, porosity, grain size and hardness results of pure AZ91 and AZ91 composites reinforced with as-received and SiOC coated CNTs. A single measurement was performed for each specimen location.

Sample	Specimen location	Density (g/cm^3)	Porosity (vol %)	Grain size (µm)	Hardness (HV3)
Pure AZ91	Top	1.79	1.1	96.2 ± 1.5	62.0 ± 2.1
	Middle	1.80	0.6	95.2 ± 1.3	64.7 ± 1.7
	Bottom	1.79	1.3	104.3 ± 1.6	61.8 ± 2.3
	Average	**1.80 ± 0.00**	**1.0 ± 0.2**	**98.6 ± 0.9**	**62.9 ± 1.2**
AZ91-As received CNTs	Top	1.79	1.6	76.2 ± 2.1	64.2 ± 0.5
	Middle	1.76	3.1	70.9 ± 1.9	63.0 ± 1.1
	Bottom	1.78	2.0	75.1 ± 1.8	64.1 ± 1.0
	Average	**1.78 ± 0.00**	**2.2 ± 0.5**	**74.0 ± 1.1**	**63.8 ± 0.5**
AZ91-SiOC22CNT78	Top	1.78	2.1	75.1 ± 1.9	63.4 ± 1.9
	Middle	1.77	2.4	73.6 ± 1.9	60.4 ± 1.6
	Bottom	1.72	5.1	65.2 ± 1.6	62.3 ± 2.1
	Average	**1.76 ± 0.02**	**3.2 ± 1.0**	**71.2 ± 1.1**	**62.0 ± 1.1**
AZ91-SiOC55CNT45	Top	1.79	1.2	94.2 ± 2.6	62.5 ± 1.5
	Middle	1.79	1.5	91.0 ± 2.5	64.5 ± 0.8
	Bottom	1.79	1.3	85.7 ± 2.2	64.8 ± 0.7
	Average	**1.79 ± 0.00**	**1.3 ±0.1**	**90.3 ± 1.4**	**63.9 ± 0.7**
AZ91-SiOC67CNT33	Top	1.77	2.4	75.0 ± 2.4	65.1 ± 1.1
	Middle	1.77	2.6	62.9 ± 1.4	67.3 ± 0.7
	Bottom	1.78	1.7	62.3 ± 1.7	65.5 ± 1.2
	Average	**1.77 ± 0.00**	**2.2 ± 0.3**	**66.8 ± 1.1**	**66.0 ± 0.6**
AZ91-SiOC77CNT23	Top	1.79	1.3	68.5 ± 1.6	64.1 ± 2.5
	Middle	1.78	1.8	62.0 ± 1.6	66.4 ± 1.1
	Bottom	1.78	1.7	61.1 ± 1.6	65.2 ± 1.2
	Average	**1.78 ± 0.0**	**1.6 ± 0.2**	**63.9 ± 1.0**	**65.2 ± 1.0**

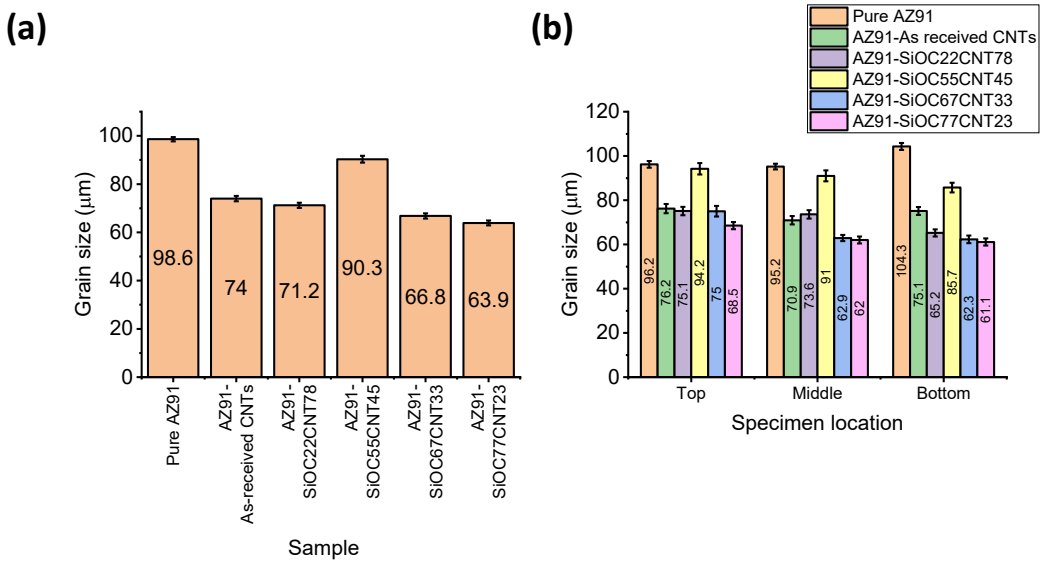


Figure 5.20. Grain size comparison between the as-cast pure AZ91 and AZ91 composites (a) by average and (b) by specimen location. A single measurement was performed for each specimen location.

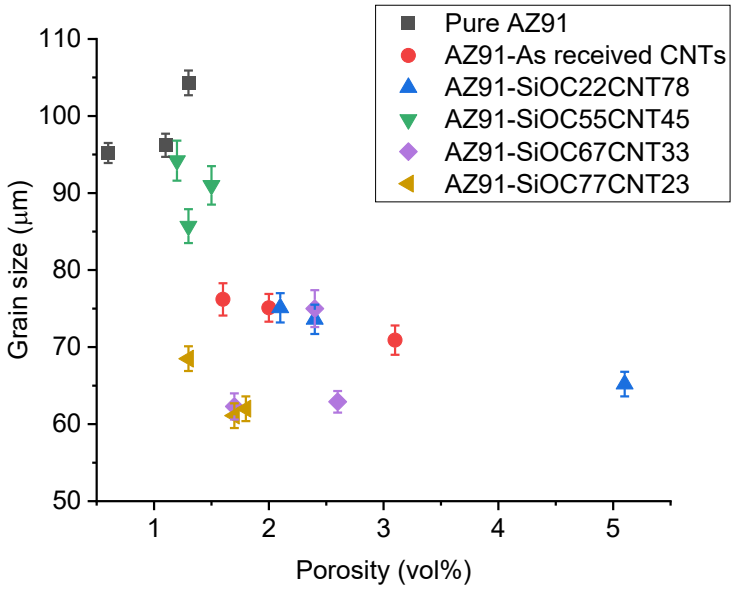


Figure 5.21. Relationship between the porosity and grain size of pure AZ91 and AZ91 composites reinforced with as-received and SiOC coated CNTs.

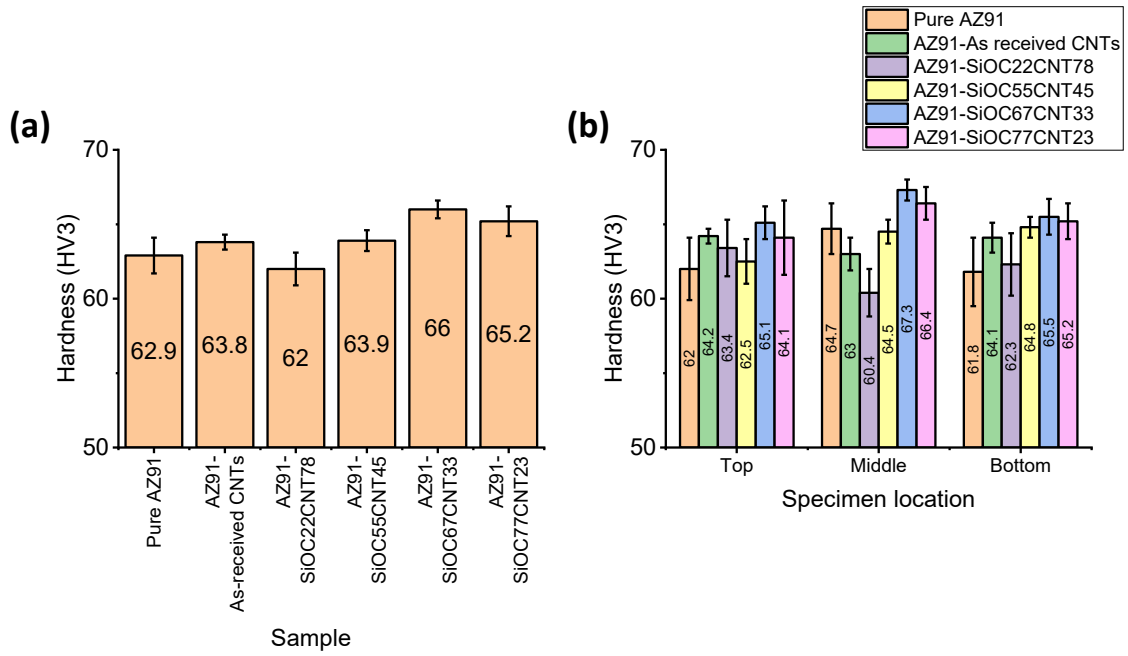


Figure 5.22. Hardness comparison between the as-cast pure AZ91 and AZ91 composites (a) by average and (b) by specimen location.

The effect of SiOC concentration in the CNTs on the AZ91 properties was further investigated by measuring the grain size and hardness of the AZ91 samples. The grain size results in Figure

5.20 shows that 25-35% of grain size reduction were observed from the addition of as-received CNTs, SiOC22CNT78, SiOC67CNT33 and SiOC77CNT23 meanwhile only 8% of grain size reduction was found in the AZ91-SiOC55CNT45 composite. Figure 5.21 was plotted to find any correlation between the porosity and grain size of the AZ91 composites since pores may also cause a Zenner pinning effect by imposing a restraining stress on the growing grain boundary during solidification therefore inhibiting the growth of grains and resulting in a smaller grain size [254, 255]. The results show a moderately negative correlation between the two quantities which suggests that the grain refinement observed in most of the composites could be attributed to their higher level of porosity; therefore, the low grain refinement effect in the AZ91-SiOC55CNT45 composite may be explained by its lower level of porosity. Finally, the results in Figure 5.22 did not show much improvement in the hardness of the composites in comparison to that of pure AZ91. However, slightly higher hardness was measured in the AZ91-SiOC67CNT33 and AZ91-SiOC77CNT23 which may be attributed to the presence of dense SiOC-CNTs products which were predominant in the CNTs samples. Additionally, it is also interesting to note that the specimen locations had no obvious effects on the grain size (Figure 5.20 (b)) and hardness (Figure 5.22 (b)) results.

The results from this section were then analysed together with those from the previous sections to determine the most suitable SiOC coated CNTs sample for the final study. Even though a high amount of individually dispersed CNTs were found in the SiOC22CNT78 dispersion, the low amount of coating would still result in the formation of large agglomerates and a poor wettability by the AZ91 matrix which eventually led to the increased level of porosity in the composites. On the other hand, higher SiOC concentration in the CNTs samples, such as in the case of SiOC67CNT33 and SiOC77CNT23, would result in the increased formation of dense SiOC-CNTs products and therefore the difficulty to debundle the individual CNTs.

Furthermore, the dense solids products were also found to cause the formation of porosity in the composite as they can sometimes be found as aggregates and could not be wetted properly by the matrix using the current processing parameters. Therefore, the coating concentration in SiOC55CNT45 was determined to be the most suitable to be used in the following study since the intermediate coating concentration provides a good balance between producing smaller sized agglomerates and debundled CNTs upon dispersion, and achieving a sufficient wetting with the matrix.

5.3.3 Effect of CNTs loading on AZ91 composite properties

Pure AZ91 and AZ91 composites reinforced with as-received CNTs and SiOC55CNT45 were fabricated as described in Table 5.4 to investigate the effectiveness of SiOC coating on improving the wettability and distribution of CNTs in AZ91 while increasing the CNTs loading. The AZ91 samples were fabricated via stir casting as described in Section 3.2.2 by stirring at 650 °C for 30 minutes. The CNTs samples were added to the melt via the Al parcel technique as described in Section 3.2.3 in a range of equivalent as-received CNTs loading from 0.1 to 1.0 wt%. For consistency, blank Al parcels had also been added to the pure AZ91 sample. Note that a different total nanoparticles loading was added to each AZ91-SiOC55CNT45 composite in comparison to the AZ91-As received CNTs composite to account for the SiOC coating concentration. One casting was produced for each sample for the microstructural and mechanical properties characterisations.

Table 5.4. Mg AZ91 samples fabricated to investigate the effectiveness of SiOC coating on improving the wettability and distribution of CNTs in the Mg matrix while increasing the CNTs loading.

Sample	Total nanoparticles loading (wt%)	Equivalent as-received CNTs loading (wt%)
Pure AZ91	0	0
AZ91-As received CNTs	0.10	0.1
	0.30	0.3
	0.50	0.5
	1.00	1.0
AZ91-SiOC55CNT45	0.22	0.1
	0.67	0.3
	1.11	0.5
	2.22	1.0

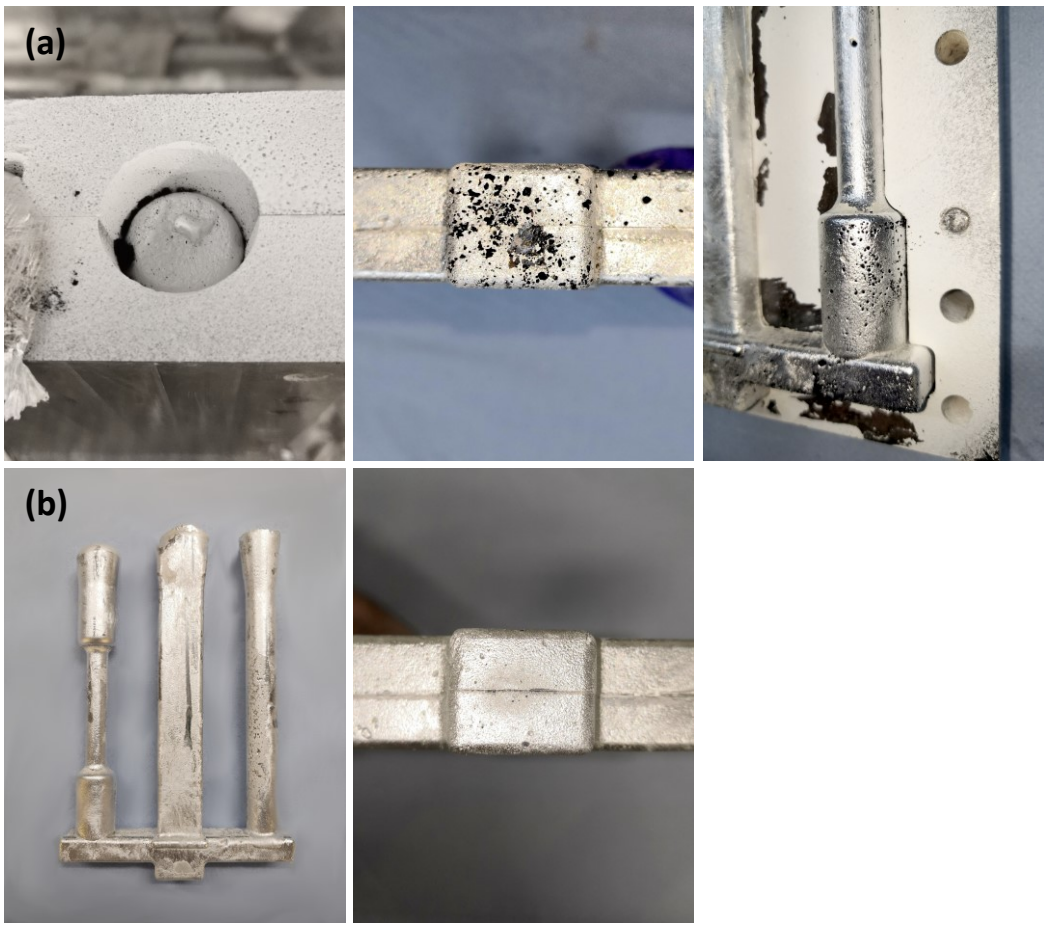


Figure 5.23. Photographs of as-cast (a) AZ91-1.0 wt% As received CNTs and (b) AZ91-2.22 wt% SiOC55CNT45 composites.

Previously, unwetted CNTs had been found directly after the casting of the AZ91 composite reinforced with 0.3 wt% as-received CNTs (Figure 5.15 (a)). As the loading was increased to

1.0 wt%, similar behaviour could still be observed after casting in which a large amount of as-received CNTs could not be sucessfully incorporated into the matrix leading to the CNTs powder being left out or pushed to the outer surface of the casting upon solidification as shown in Figure 5.23 (a). On the contrary, at the same equivalent CNTs loading, such behaviour was not observed for the AZ91-2.22 wt% SiOC55CNT45 composite, as shown in Figure 5.23 (b), which further indicates that SiOC coated CNTs could be better wetted by the matrix than the uncoated CNTs.

In this study, solution heat treatment and hot rolling were performed on the as-cast samples as described in Section 3.2.4 prior to the microstructural and mechanical properties characterisations to minimise the effect of porosity on the sample properties. However, only the solution heat treatment was performed on the specimens used for compression testing since hot rolling could not be carried out to produce the compression test coupons due to the size limitation (see Section 3.3.13 for compression testing requirement). As a side note, the ageing heat treatment was also not carried out in this study to avoid the re-precipitation of the β-$Mg_{17}Al_{12}$ phases so that only the strengthening effect of CNTs could be studied.

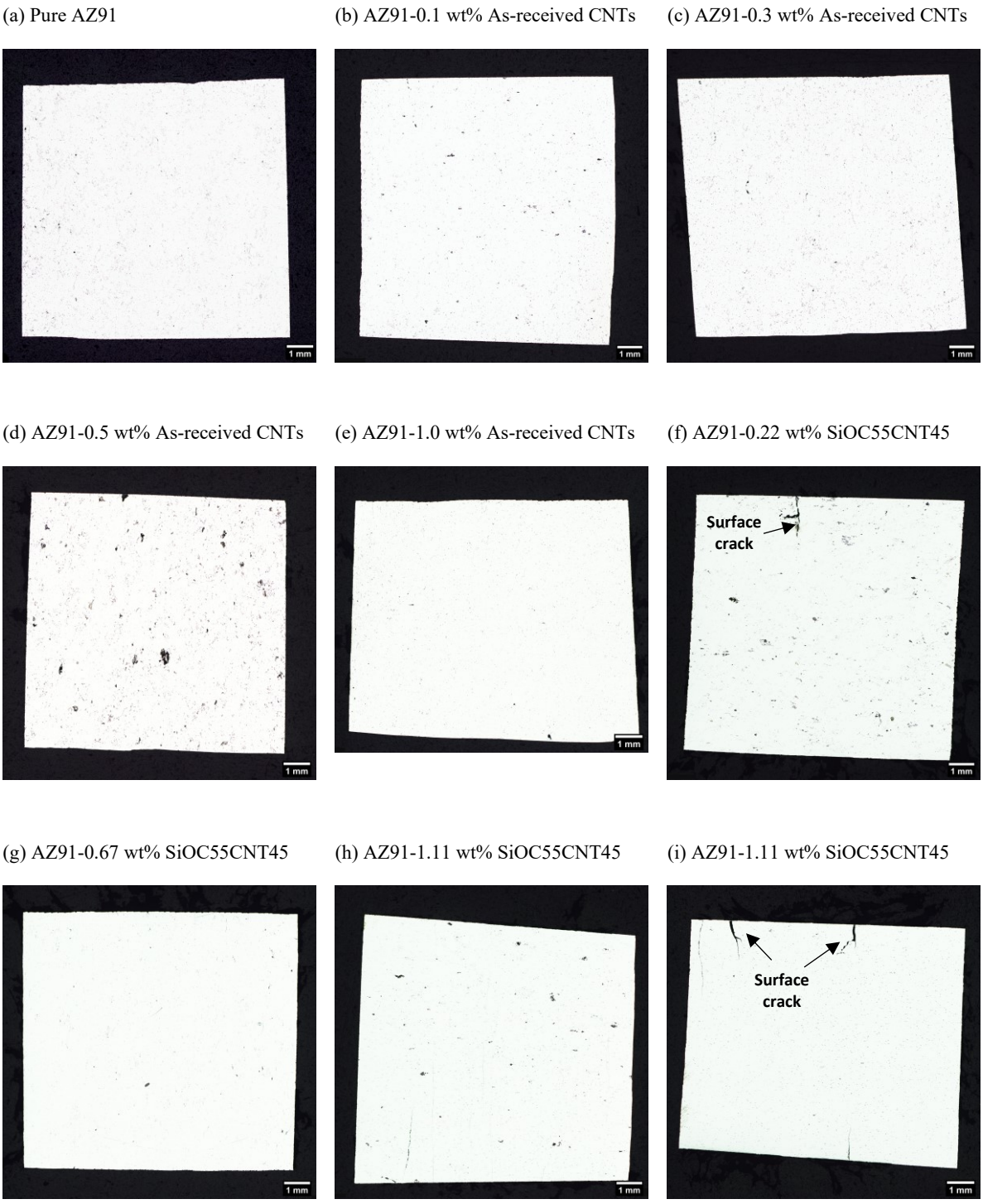


Figure 5.24. Optical micrographs showing the cross sections of solution treated-hot rolled (a) pure AZ91 and AZ91 composites reinforced with (b-e) As-received CNTs and (f-i) SiOC55CNT45 in a range of equivalent as received CNTs loading.

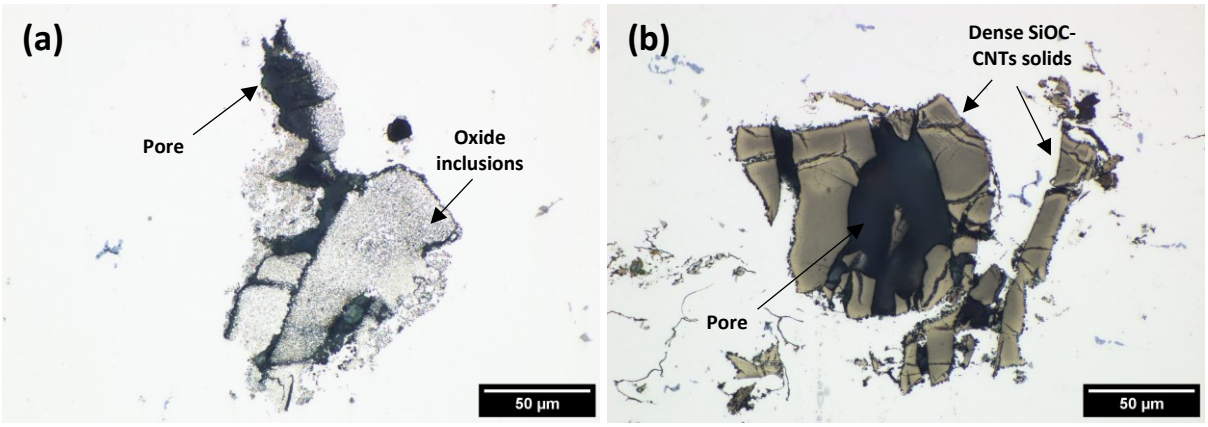


Figure 5.25. Optical micrographs showing the porosity formed in the solution treated-hot rolled AZ91 composites reinforced with (a) as-received CNTs and (b) SiOC55CNT45.

The cross sections of the solution treated-hot rolled AZ91 samples are compared in Figure 5.24. In general, a low amount of porosity was observed in all samples as a result of the hot rolling treatment as it was previously discussed in Section 5.3.1 Among the AZ91-As received CNTs composites, the highest amount of porosity was observed in the AZ91 composite containing 0.5 wt% as-received CNTs loading (Figure 5.24 (d)). The pores also appeared to be accompanied by oxide inclusions as shown in Figure 5.25 (a). Interestingly, as the loading was increased to 1.0 wt%, only a small amount of porosity was observed in the cross section in Figure 5.24 (e). Based on the observations made during the casting of AZ91-As received CNTs composites in Figure 5.15 (a) and Figure 5.23 (a), it can be inferred that the addition of as-received CNTs in the matrix would lead to the formation of porosity due to the poor wettability of the as-received CNTs. As the loading was increased to a larger amount such as in the case of 1.0 wt% as-received CNTs, the poor wetting had led to a bulk rejection of the CNTs and a much lower CNTs loading in the matrix thereby giving the appearance of a lower porosity in some areas in the composite. On the other hand, no obvious trend could be observed from the cross-sections of AZ91-SiOC55CNT45 composites which showed a low amount of porosity across all samples. Since the SiOC coated CNTs were found to be fully incorporated in the matrix during the casting, this finding may indicate a generally better wetting of the CNTs due

to the SiOC coating. Nevertheless, the small amount of porosity formed in these composites seemed to be caused by the aggregated dense SiOC-CNTs products as shown in Figure 5.25 (b) which could not be effectively wetted by the matrix nor closed via hot rolling.

Table 5.5. Density and porosity results of pure AZ91 and AZ91 composites reinforced with as-received CNTs and SiOC55CNT45 for the solution treated-naturally aged and solution treated-hot rolled samples. The solution treated-hot rolled samples were used for all sample characterisations except for compression testing where the solution treated-naturally aged samples were used.

		Solution treated-naturally aged (used for compression testing)		**Solution treated-hot rolled** (used for grain size measurement, hardness and tensile testing)	
Sample	**Theoret. density (g/cm^3)**	**Measured density (g/cm^3)**	**Porosity (vol%)**	**Measured density (g/cm^3)**	**Porosity (vol%)**
Pure AZ91	1.81	1.79 ± 0.00	0.9 ± 0.1	1.81 ± 0.01	0.3 ± 0.3
AZ91-0.10 wt% As received CNTs	1.81	1.79 ± 0.00	1.4 ± 0.2	1.80 ± 0.00	0.5 ± 0.2
AZ91-0.30 wt% As received CNTs	1.81	1.78 ± 0.00	2.0 ± 0.2	1.78 ± 0.02	1.9 ± 1.3
AZ91-0.50 wt% As received CNTs	1.81	1.76 ± 0.00	2.8 ± 0.2	1.81 ± 0.00	0.2 ± 0.1
AZ91-1.00 wt% As received CNTs	1.83	1.77 ± 0.01	3.2 ± 0.4	1.80 ± 0.00	1.2 ± 0.1
AZ91-0.22 wt% SiOC55CNT45	1.81	1.78 ± 0.01	1.8 ± 0.3	1.81 ± 0.00	-0.1 ± 0.1
AZ91-0.67 wt% SiOC55CNT45	1.81	1.78 ± 0.01	2.1 ± 0.3	1.81 ± 0.00	0.3 ± 0.2
AZ91-1.11 wt% SiOC55CNT45	1.81	1.74 ± 0.00	4.2 ± 0.2	1.81 ± 0.00	0.1 ± 0.1
AZ91-2.22 wt% SiOC55CNT45	1.82	1.77 ± 0.00	2.3 ± 0.2	1.80 ± 0.00	0.8 ± 0.3

Next, the density and porosity results are reported in Table 5.5 and illustrated in Figure 5.26. Theoretically, only a slight increase in the density of the AZ91 composite was expected from the addition of the nanoparticles. The porosity results are shown for both the solution treated-naturally aged and solution treated-hot rolled samples since both types of samples were considered in the subsequent sample characterisations. In general, the porosity of the solution treated-hot rolled samples were notably lower than the porosity of the solution treated-naturally aged samples as was expected. For the AZ91-As received CNTs composites, the solution treated-naturally aged samples seemed to be much more affected by the change in the CNTs loading such that the porosity was increased with the increase in CNTs loading which is

consistent with the expected behaviour of the uncoated CNTs with the AZ91 matrix. This trend was not as obvious in the solution treated-naturally aged AZ91-SiOC55CNT45 composites where the highest porosity was recorded for the AZ91-1.11 wt% SiOC55CNT45 (equivalent as-received CNTs loading of 0.3 wt%). Nevertheless, for both as-received CNTs and SiOC55CNT45, the porosity that during the casting were effectively reduced via the hot rolling treatment.

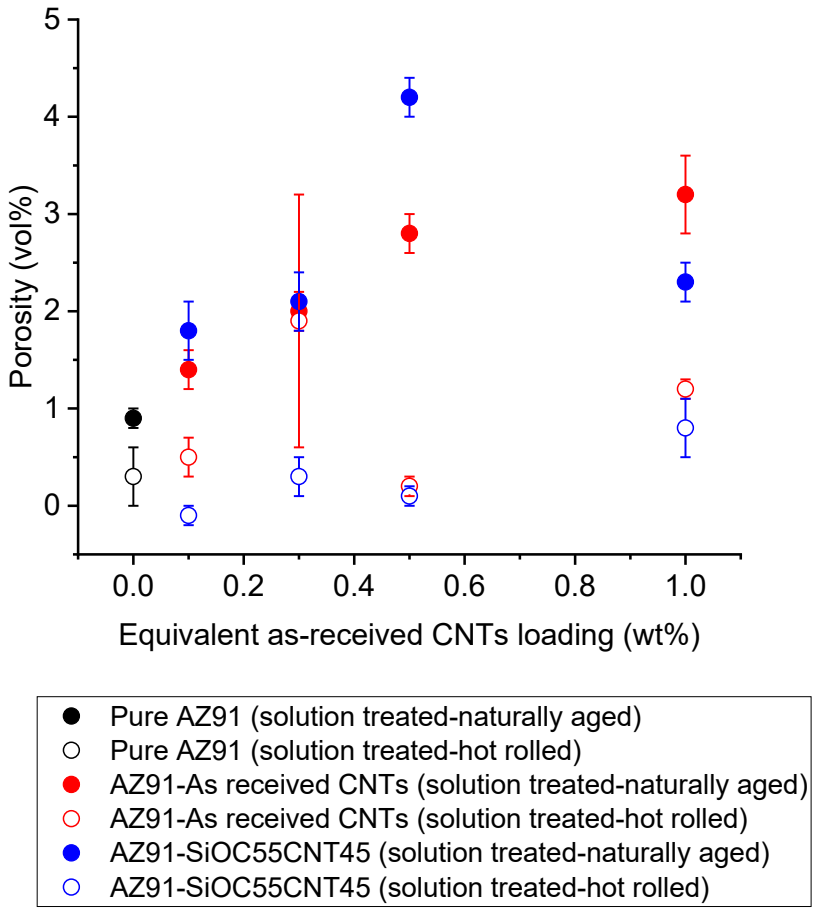


Figure 5.26. Scatter plot showing the porosity of pure AZ91 and AZ91 composites reinforced with as-received CNTs and SiOC55CNT45 for the solution treated-naturally aged and solution treated-hot rolled samples.

Table 5.6. Grain size, hardness and tensile properties of solution treated-hot rolled pure AZ91 and AZ91 composites reinforced with as-received CNTs and SiOC55CNT45. Individual data are presented for the tensile results since only a limited number of specimens were tested.

Sample	Grain size (µm)	Hardness (HV3)	Young's modulus (GPa)	0.2% tensile yield strength (MPa)	Ultimate tensile strength (MPa)	Ductility (%)
Pure AZ91	37.5 ± 1.2	62.1 ± 2.3	14.8	98.7	248.2	5.8
AZ91-0.10 wt% As received CNTs	39.7 ± 0.7	63.2 ± 1.0	11.8	99.3	252.9	9.5
AZ91-0.30 wt% As received CNTs	36.7 ± 0.6	60.9 ± 0.4	15.2; 14.7	98.4; 95.5	235.5; 245.5	6.2; 6.3
AZ91-0.50 wt% As received CNTs	38.3 ± 0.7	61.6 ± 0.5	Not measured due to sample defect			
AZ91-1.00 wt% As received CNTs	34.9 ± 0.6	64.6 ± 0.4	Not measured due to sample defect			
AZ91-0.22 wt% SiOC55CNT45	24.2 ± 0.3	68.5 ± 1.0	19.9; 20.9; 18.7	109.2; 117.2; 107.6	251.3; 257.2; 261.5	6.5; 5.5; 8.3
AZ91-0.67 wt% SiOC55CNT45	18.6 ± 0.3	70.7 ± 0.9	19.9; 20.2; 19.4	117.4; 98.9; 119.6	237.9; 240.9; 230.6	4.5; 4.9; 4.0
AZ91-1.11 wt% SiOC55CNT45	19.8 ± 0.8	72.6 ± 1.9	Not measured due to sample defect			
AZ91-2.22 wt% SiOC55CNT45	14.3 ± 0.1	71.1 ± 0.7	Not measured due to sample defect			

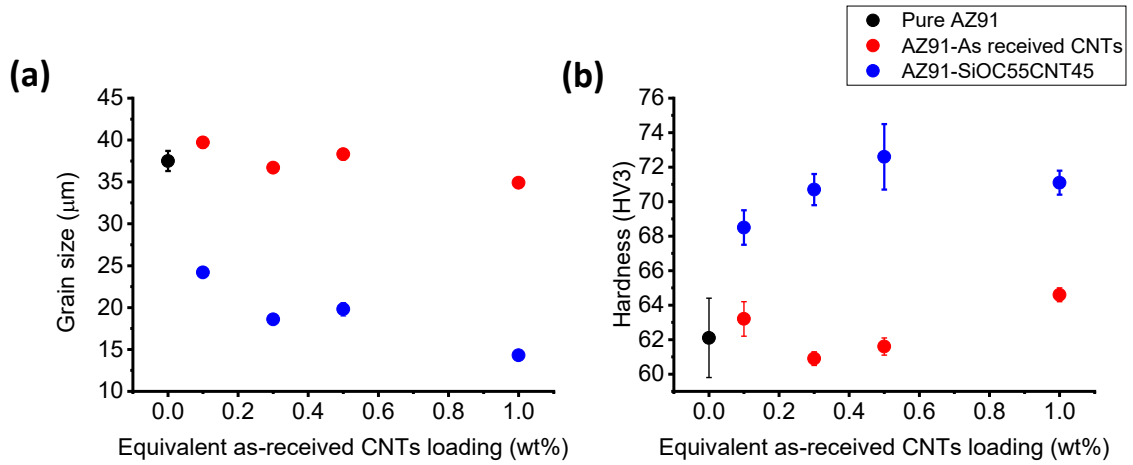


Figure 5.27. (a) Grain size and (b) hardness comparison the pure AZ91 and AZ91 composites reinforced with as-received CNTs and SiOC55CNT45.

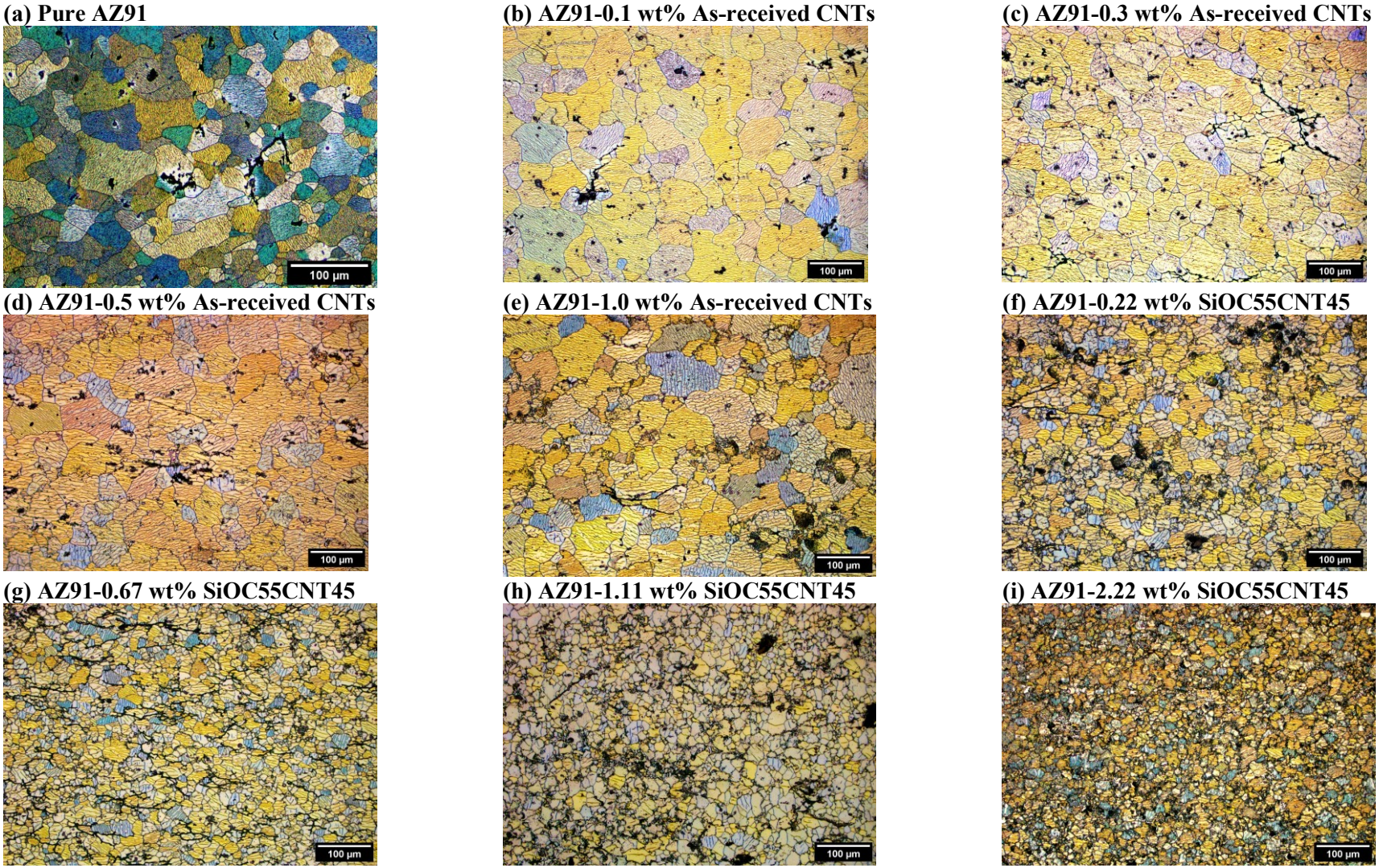


Figure 5.28. Optical micrographs showing the grain structures of solution treated-hot rolled (a) pure AZ91 and AZ91 composites reinforced with (b-e) as received CNTs and (f-i) SiOC55CNT45 at various CNTs loadings.

Table 5.6 presents the results for the grain size, hardness and tensile properties of the solution treated-hot rolled AZ91 samples. As shown in Figure 5.27 (a) and Figure 5.28, the grain size of the AZ91-SiOC55CNT45 composite was found to be remarkably lower than that of the AZ91-As received CNTs composite at each equivalent as-received CNTs loading such that up to 62% of grain size reduction could be achieved with the addition of 2.22 wt% SiOC55CNT45. Furthermore, for both composites, a strong negative correlation was found between the grain size and the CNTs loading which may imply that grain size was reduced when the CNTs loading was increased. Next, the hardness results in Figure 5.27 (b) show that the hardness of the AZ91-SiOC55CNT45 composite is notably higher by 8-18 % than that of the AZ91-As received CNTs composite at each equivalent as-received CNTs loading. For both composites, the hardness seems to be moderately correlated to the CNTs loading such that the increase in the CNTs loading would lead to an increase in the hardness of the composite.

The tensile properties are compared in Figure 5.29. Some specimens were found to be defective from the hot rolling process, therefore the tensile results are not shown for some samples. Consequently, tensile results are only shown for the composites with 0.1 and 0.3 wt% equivalent as-received CNTs loading were investigated. It is important to note that since only a limited number of specimens were available for the tensile testing, these tensile results should be treated as preliminary. The yield strength of the AZ91-SiOC coated CNTs composites were generally found to be higher than those of the pure AZ91 and AZ91-As received CNTs composites as shown Figure 5.29 (b). On the other hand, the ultimate tensile strength was initially increased by the addition of as-received CNTs and SiOC55CNT45 but decreased when the loading was increased to 0.3 wt% (Figure 5.29 (c)). Similarly, the ductility was also initially increased at the lowest nanoparticle loading but was decreased at the higher loading (Figure 5.29 (d)). Finally, the Young's modulus of the AZ91-SiOC55CNT45 composites were found

to be higher than that of the pure AZ91 and AZ91-As-received CNTs composites. For future works, more specimens should be tested for each sample to improve the reliability of the tensile results and the characterisation of the tensile fracture surface should also carried out to understand the mechanism of fracture. The latter was not carried out in this work due to time constraint.

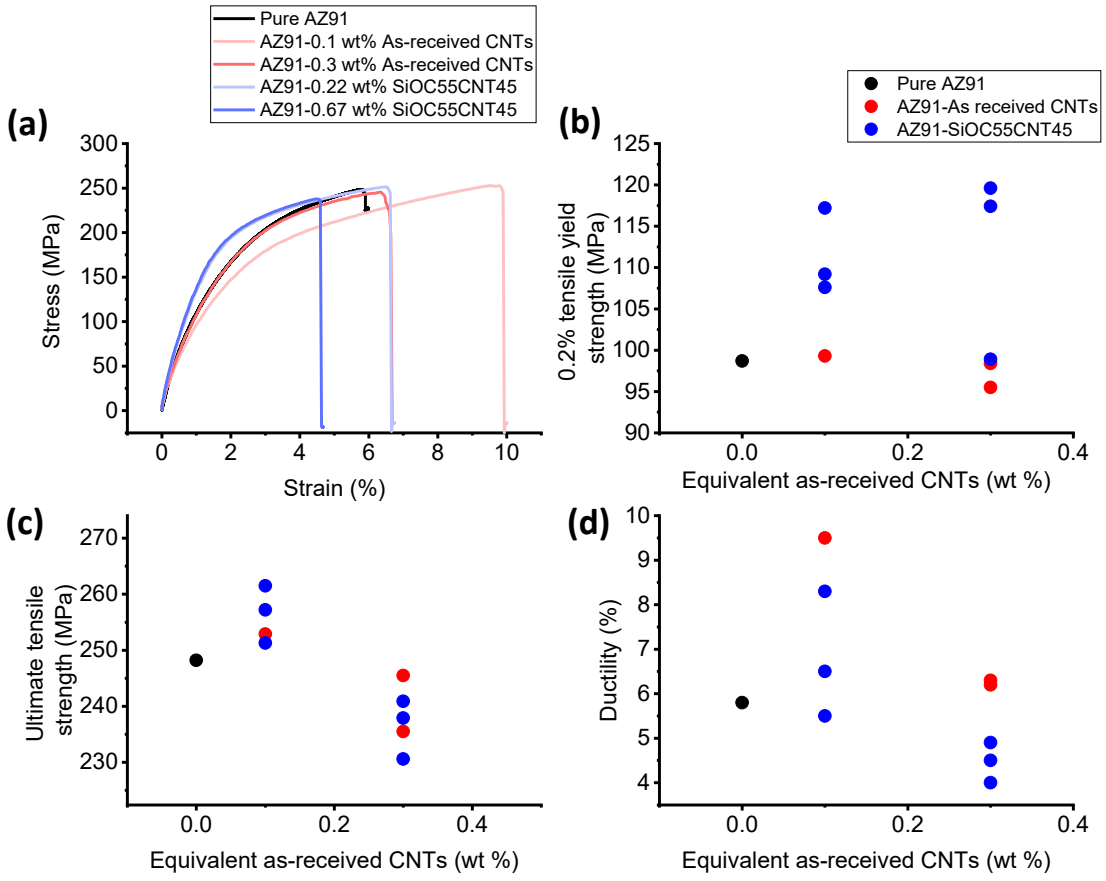


Figure 5.29. (a) Stress-strain curves, (b) 0.2% tensile yield strength, (c) ultimate tensile strength and (d) ductility of solution treated-hot rolled pure AZ91 and AZ91 composites reinforced with as-received CNTs and SiOC55CNT45.

Next, compression testing was performed on the solution treated-naturally aged samples and the results are presented in Table 5.7 and illustrated in Figure 5.30. As previously mentioned, hot rolling could not be practically performed on the compression test specimens therefore only

solution heat treatment was carried out. Nevertheless, testing the solution treated-naturally aged samples would allow us to examine the effect of the actual behaviour between the CNTs and the matrix on the mechanical properties of the composite. The analysis of the yield strength in Figure 5.30 (b) reveals that the yield strength was decreased with the increase in the CNTs loading for the AZ91-As received CNTs composites meanwhile the trend was reversed in the AZ91-SiOC55CNT45 composites where the yield strength was increased with the increase in the CNTs loading. On the other hand, the ultimate compressive strength results in Figure 5.30 (c) show a similar trend for both composites where the ultimate strength was lowered with the increase in the CNTs loading. Interestingly, for the AZ91-SiOC55CNT45 composites, the ultimate strength was initially decreased from the addition of the lowest CNTs loading at 0.22 wt% yet the strength was increased again at the highest loading at 2.22 wt%. Finally, the compression at failure results in Figure 5.30 (c) show a slight decrease with the addition of either as-received CNTs or SiOC55CNT45; however, no obvious trend could be clearly observed. Similarly, no obvious trend can also be deduced from the Young's modulus of the composites.

Table 5.7. Compressive properties of solution treated-naturally aged pure AZ91 and AZ91 composites reinforced with as-received CNTs and SiOC55CNT45.

Sample	**Young's modulus (GPa)**	**0.2% compressive yield strength (MPa)**	**Ultimate compressive strength (MPa)**	**Compression at failure (%)**
Pure AZ91	27.6 ± 1.8	97.6 ± 0.8	440.2 ± 1.3	20.1 ± 0.8
AZ91-0.10 wt% As received CNTs	32.0 ± 2.5	102.1 ± 4.1	446.3 ± 4.3	20.1 ± 0.7
AZ91-0.30 wt% As received CNTs	43.0 ± 5.3	85.7 ± 2.9	442.2 ± 7.7	20.2 ± 1.2
AZ91-0.50 wt% As received CNTs	29.7 ± 3.4	95.8 ± 3.9	429.1 ± 8.4	19.0 ± 1.0
AZ91-1.00 wt% As received CNTs	33.6 ± 4.2	92.2 ± 4.3	421.7 ± 13.3	19.4 ± 0.7
AZ91-0.22 wt% SiOC55CNT45	36.6 ± 6.6	98.1 ± 4.9	426.5 ± 8.2	18.7 ± 1.4
AZ91-0.67 wt% SiOC55CNT45	38.9 ± 10.5	101.2 ± 5.1	418.7 ± 11.3	19.0 ± 0.7
AZ91-1.11 wt% SiOC55CNT45	32.2 ± 3.6	102.2 ± 3.9	419.2 ± 3.8	18.5 ± 0.6
AZ91-2.22 wt% SiOC55CNT45	26.4 ± 2.1	112.1 ± 3.3	440.7 ± 3.4	19.6 ± 0.5

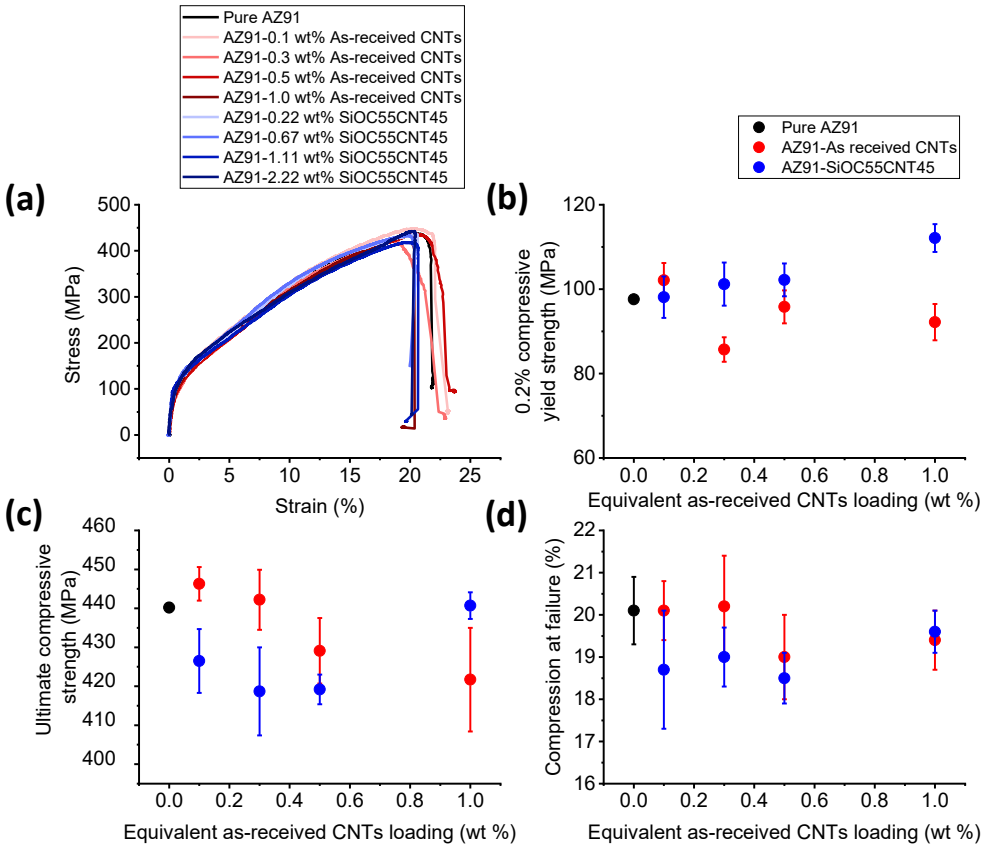


Figure 5.30. (a) Stress-strain curves, (b) 0.2% compressive yield strength, (c) ultimate compressive strength and (d) compression at failure of solution treated-naturally aged pure AZ91 and AZ91 composites reinforced with as-received CNTs and SiOC55CNT45.

Subsequently, the effect of porosity on the ultimate compression strength of the composite was examined in Figure 5.31 where it is clear that the level porosity in the composites could be associated with the strength of the composites. Figure 5.31 (b) shows that the diminishing effect of porosity on the strength of the AZ91-As received CNTs composite was more strongly observed at the higher loading such that an ultimate compressive strength of 306 MPa was measured for an AZ91-1.0 wt% As-received CNTs specimen with 6.3 vol% porosity. A similar trend could also be observed in the AZ91-SiOC55CNT45 composites in Figure 5.31 (c) where the increase in porosity level would lead to the decrease in the ultimate strength of the composite.

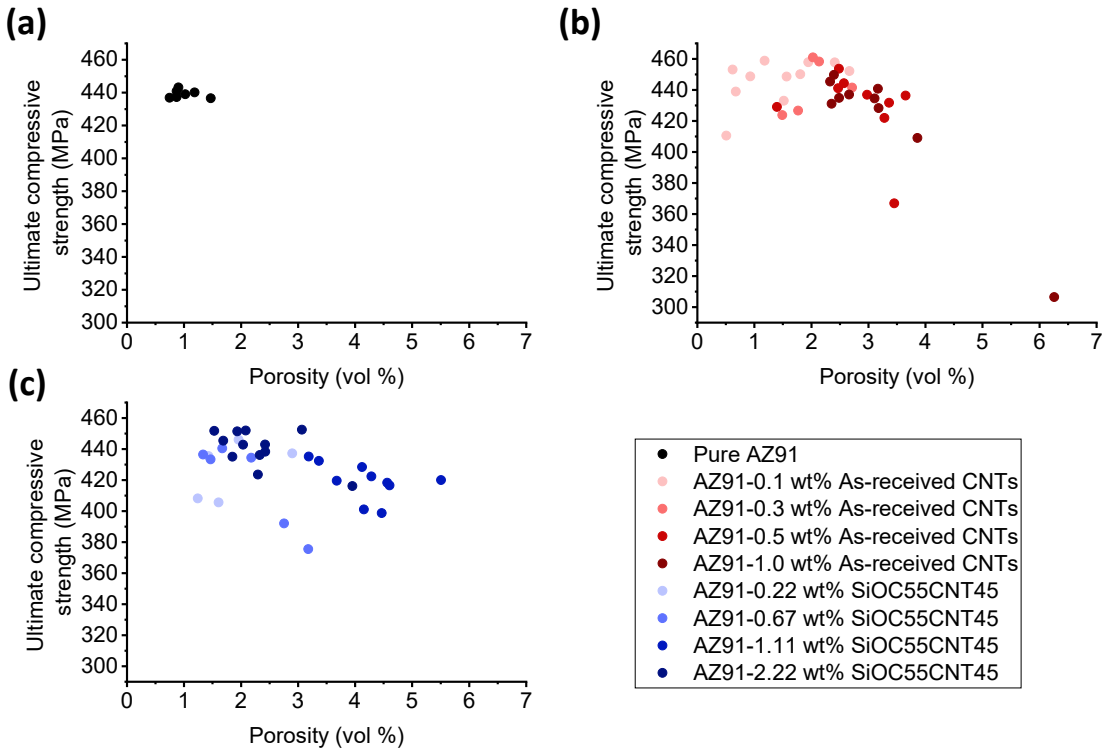
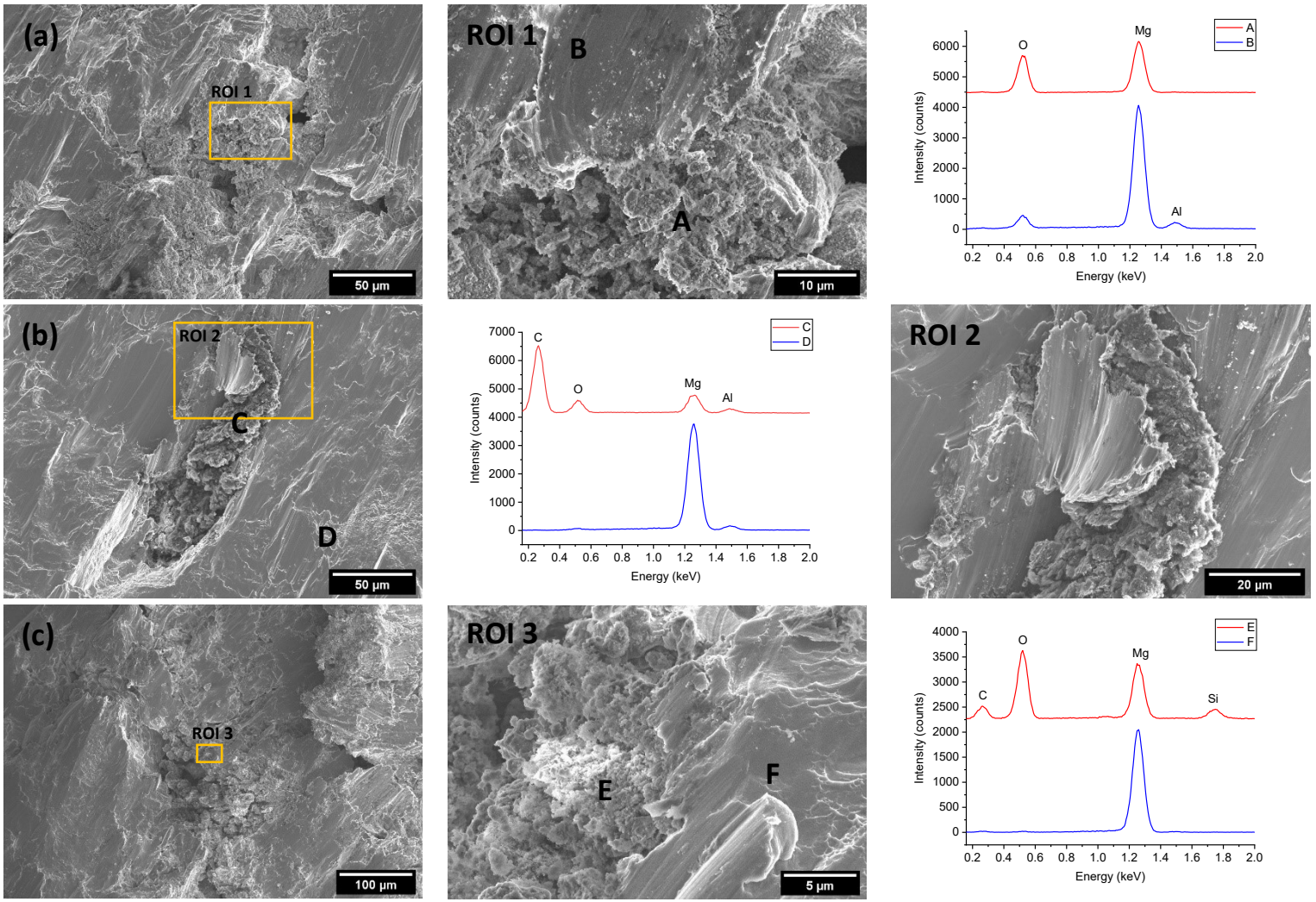


Figure 5.31. Scatter plots showing the relationship between porosity and ultimate compressive strength of the solution treated-naturally aged (a) pure AZ91, (b) AZ91-As received CNTs and (c) AZ91-SiOC55CNT45.

Following the compression test, the fracture surface of the composites was studied with SEM especially focusing on the pores. For the AZ91-As received CNTs composites, MgO was mostly observed on the internal surface of the pores while no CNTs had been found as shown in Figure 5.32 (a). However, in the rare events where CNTs were found such as in Figure 5.32 (b), the CNTs appeared to be unwetted by the matrix. For the AZ91-SiOC55CNT45 composites, the CNTs were more likely to be found within the pores as shown in Figure 5.32 (c) where they appear to exist as agglomerates and are partially wetted by the matrix. Furthermore, individual SiOC coated CNTs had also been found on the fracture surface as shown in Figure 5.32 (d) and (e) which seem to indicate that they had been wetted by the matrix and pulled out during fracture.

In summary, the presence of SiOC coating had led to a grain refinement of the AZ91 matrix and an increase in the hardness of the composite in comparison to the pure AZ91 and AZ91-As received CNTs composites. The tensile and compression results showed that the yield strength was increased due to the presence of the coating. Consequently, the increase in the CNTs loading would increase the yield strength of the AZ91-SiOC55CNT45 composites meanwhile the yield strength was decreased in the AZ91-As received CNTs composites. On the other hand, no improvement was observed in the ultimate compressive strength of both the AZ91-SiOC55CNT45 and AZ91-As-received CNTs composites but the preliminary tensile measurement showed an improvement in the ultimate tensile strength of the composites at the lowest equivalent CNTs loading (i.e. 0.1 wt%) before the value was dropped again at a higher loading. Subsequently, fracture surface analysis were carried out to explain the findings from the mechanical testing. The poor wettability of the as-received CNTs would increase the probability of air entrainment as the CNTs that were rejected to the surface of the melt would continuously to be mixed into the melt during the melt stirring process. Consequently, the lack of interfacial bonding between the CNTs and the matrix would lead to the decrease in the yield strength meanwhile the increase in porosity level and oxide formation would decrease the maximum strength of the composite. On the contrary, the presence of SiOC coating was proven to be effective at improving the interfacial bonding between the CNTs and the matrix as evident from the CNTs found embedded on the fracture surface. As a result, the yield strength was improved as the CNTs loading was increased. However, the presence of coated CNTs agglomerates had also resulted in the formation of porosity and eventually the lowering of the ultimate strength. Therefore, in future work, it is imperative to improve on the dispersability of the coated CNTs, for example by optimising the coating procedure and the stir casting parameters, so that the distribution of CNTs in the matrix could be optimised.


(a)
ROI 1
50 µm
ROI 1
B
A
10 µm
A
B
O
Mg
Al
Intensity (counts)
Energy (keV)
(b)
ROI 2
C
D
50 µm
C
D
C
O
Mg
Al
Intensity (counts)
Energy (keV)
ROI 2
20 µm
(c)
ROI 3
100 µm
ROI 3
E
F
5 µm
E
F
C
O
Mg
Si
Intensity (counts)
Energy (keV)

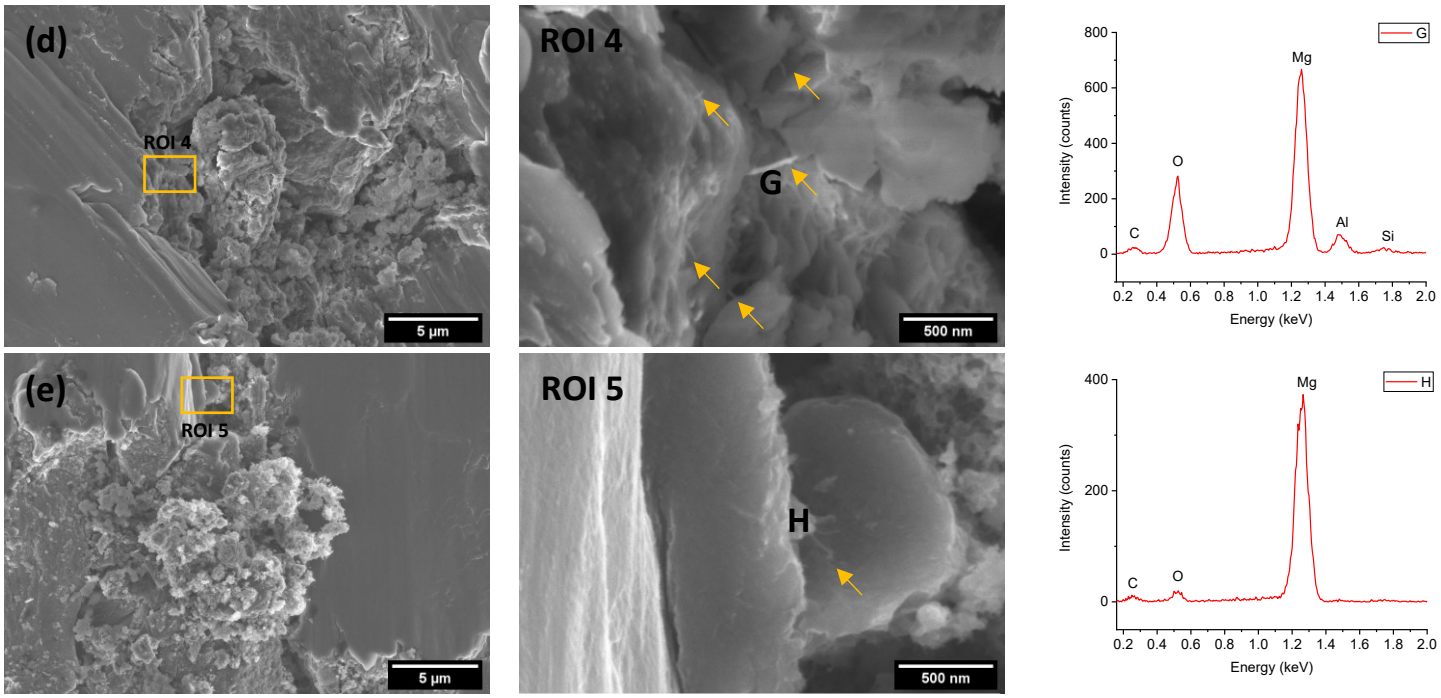


Figure 5.32. SEM images showing the fracture surface of AZ91 composites reinforced with (a-b) as-received CNTs and (c-e) SiOC55CNT45 after compression test. Point EDX measurement was performed at the locations marked by the letters A-H in the SEM images. Individual CNTs found on the fracture surface are denoted by the yellow arrows.

5.4 Conclusions

A wide range of SiOC coated CNTs samples consisting between 22.3 to 77.2 wt% of SiOC concentration was produced from the starting PMHS concentrations of 10/1 to 60/1 PMHS/CNTs weight-to-weight ratio. The morphology of SiOC22CNT78 appeared to be similar to the as received CNTs however a small amount of SiOC coating could still be detected by EDX. As the SiOC concentration was increased in the sample, SiOC precipitation was more likely to occur on the agglomerated CNTs which led the formation of dense SiOC-CNTs products. Furthermore, a discontinuous coating layer could also be found on the individual tubes. The characterisation of the CNTs dispersions showed that large CNTs agglomerates were predominantly observed in the as-received CNTs and SiOC22CNT78 dispersions after ultrasonication, but the dispersions were still able to yield a high degree of individually dispersed CNTs after centrifugation. As the SiOC concentration in the CNTs became larger, the size of the particles found in the dispersions was notably reduced. Although debundled CNTs were found in the dispersion, the presence of dense SiOC-CNTs products was also increased which seemed to have led to the decrease in the amount of the individually dispersed CNTs in the dispersions.

Subsequently, the effect of the SiOC coated CNTs composition on the properties of the AZ91 matrix was investigated. CNTs with 22 wt% SiOC concentration could not be sufficiently wetted by the matrix which led to an increased level of porosity in the composite. On the other hand, SiOC coated CNTs samples with very high SiOC concentrations, as in the case of SiOC77CNT23 and SiOC77CNT23, were also found to cause an increase in the level of porosity in the composite due to ineffective wetting of the dense SiOC-CNTs solids. Therefore, SiOC55CNT45 was found to be the most suitable composition for SiOC coated CNTs which was able to reduce the agglomeration of the CNTs and provide a sufficient wetting by the AZ91

matrix. To investigate the effect of CNTs loading on the mechanical properties of the AZ91-As received CNTs and AZ91-SiOC55CNT45 composites, the as-cast samples were treated via solution heat treatment and hot rolling to minimise the effect of porosity on the microstructure and mechanical properties of the samples. The presence of SiOC coating had led to a notable reduction in grain size and increase in hardness in the AZ91 composites in comparison to the pure AZ91 and AZ91-As received CNTs composite. Based on the tensile and compression test results, the yield strength was found to increase with the increase in CNTs loading for the AZ91-SiOC55CNT45 composites meanwhile the trend was reversed for the AZ91-As received CNTs composites. This finding could be correlated to the improvement in the wetting of the CNTs due to the presence of SiOC coating as evident by the wetted CNTs found on the fracture surface of the composites. However, the ultimate strength was found to decrease as the CNTs loading was increased in both composites which can be explained by the increase in the porosity level due to the MgO formation in the AZ91-As received CNTs composites and the agglomerated SiOC coated CNTs in the AZ91-SiOC55CNT45 composites.

Chapter 6 : AZ91-SiC coated CNTs composites

6.1 Introduction

Based on the successful conversion of polymethylhydrosiloxane (PMHS) precursor to SiC in Section 4.2, SiC coated CNTs were produced in this work by carrying out pyrolysis on the crosslinked PMHS-CNTs at 1500 °C. The generation of SiC is expected to occur above the temperature of 800 °C via the phase separation of SiOC (Equation 2.11) and the carbothermal reduction reaction between the SiO_2 phase and free carbon at the temperatures of 1400 °C and above (Equation 2.12 and Equation 2.13). Following the investigation of SiOC coated CNTs in Chapter 5, this chapter will then focus on the production of SiC coated CNTs and the fabrication of AZ91-SiC coated CNTs composites. Initially, the effect of the starting PMHS concentration on the SiC concentration in the CNTs samples is shown. Then, the effect of SiC concentration on the morphology and dispersibility of the CNTs are investigated. The appropriate SiC coated CNTs composition is then determined and the effect of SiC coating on the properties of the AZ91 composites is investigated.

6.2 SiC coated CNTs

6.2.1 Effect of starting PMHS concentration on SiC concentration

SiC coated CNTs were prepared using the procedure described in Section 3.2.1 from PMHS-CNTs samples using the starting PMHS concentrations of 10/1 to 50/1 as listed in Table 6.1. Subsequently, TGA was performed on the SiC coated CNTs products as shown in Figure 6.1 (a) using the procedure described in Section 3.3.4.1 to determine the SiC concentration in each

sample. The following equation was used to calculate the SiC concentration in the CNTs samples and the results are presented in Table 6.1:

$$SiC\ concentration\ in\ CNTs\ sample = (Residual\ weight\ \%\ of\ SiC\ coated\ CNTs\ at\ 800\ ℃ - Residual\ weight\ \%\ of\ as-received\ CNTs\ at\ 800℃) \times \frac{Molecular\ weight\ of\ SiC}{Molecular\ weight\ of\ SiO_2}$$

Equation 6.1

Similar to Equation 5.1, the equation above was modified from Equation 3.17 based on the following considerations: (1) The residual weight % of the as-received CNTs after the TGA measurement is attributed to the alumina impurities in the CNTs (as shown previously in Figure 4.12 (b) and Figure 4.13 (a)) and should therefore be excluded from the SiC calculation and (2) the conversion of the SiC coated CNTs into a white product after the TGA operation, as shown in Figure 6.2, indicates that the SiC coating had been fully oxidised to SiO_2 therefore a conversion factor (i.e. $\frac{Molecular\ weight\ of\ SiC}{Molecular\ weight\ of\ SiO_2}$) was included in the calculation.

Table 6.1. Onset temperature, residual weight % at 800 °C and calculated SiC coating concentration of the as-received and SiC coated CNTs according to the TGA results in Figure 6.1 (a). The starting PMHS-CNTs sample before the production of SiC coated CNTs is denoted as PMHSxCNTy where x/y is the PMHS/CNTs w/w (i.e. weight to weight ratio). On the other hand, the final product after the production of SiC coated CNTs is labelled as SiCmCNTn where m and y are the SiC and CNTs wt% in the SiC coated CNTs product, respectively.

		TGA of the final product		
Starting sample	**Final product**	**Onset temperature (°C)**	**Residual weight % at 800 °C**	**Calculated SiC coating concentration (wt%)**
As-received CNTs	As-received CNTs	572.6 ± 0.1	11.6 ± 0.5	0
PMHS10CNT1	SiC25CNT75	684.0 ± 4.6	47.4 ± 0.6	24.8 ± 0.4
PMHS18CNT1	SiC45CNT55	667.8 ± 3.5	77.4 ± 3.7	44.9 ± 2.5
PMHS20CNT1	SiC53CNT47	664.0 ± 1.6	90.2 ± 0.9	53.4 ± 0.6
PMHS30CNT1	SiC56CNT44	649.3 ± 2.5	93.6 ± 0.8	55.7 ± 0.6
PMHS40CNT1	SiC57CNT43	630.3 ± 7.2	96.0 ± 0.8	57.3 ± 0.5
PMHS50CNT1	SiC58CNT42	623.6 ± 3.4	97.6 ± 0.3	58.3 ± 0.2

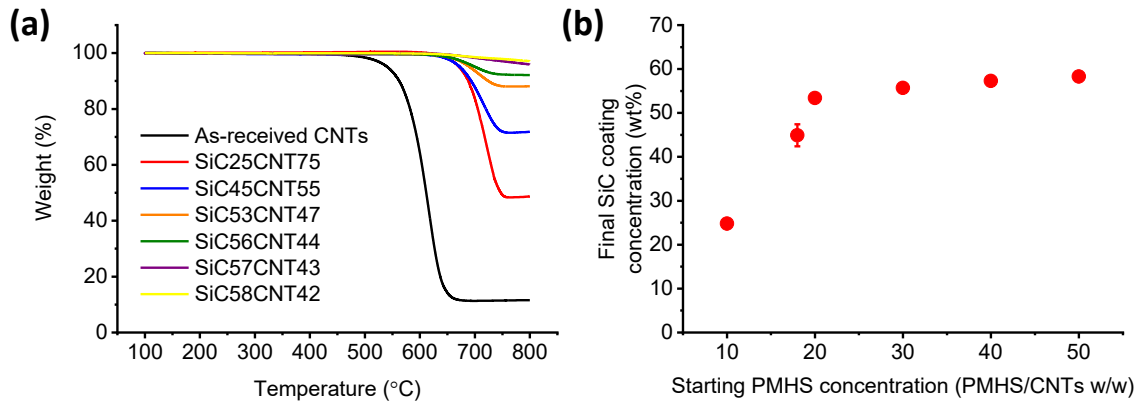


Figure 6.1. (a) TGA curves of as-received CNTs and SiC coated CNTs as performed in air. (b) Scatter plot showing the relationship between the starting PMHS concentration in the PMHS-CNTs samples and the final SiC coating concentration in the SiC coated CNTs products.

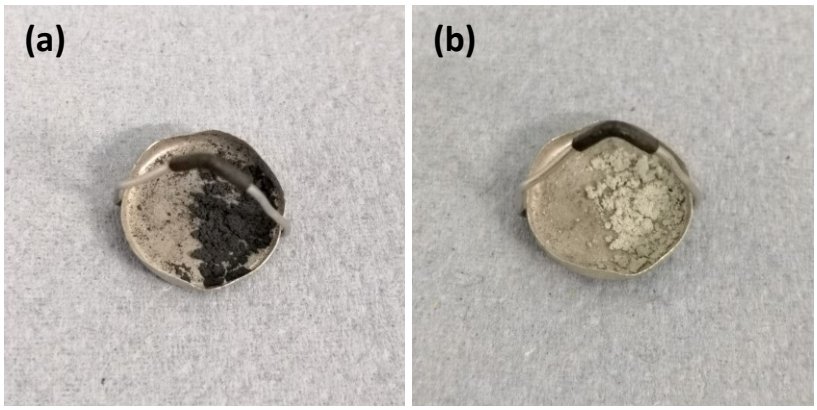


Figure 6.2. SiC coated CNTs (shown here for SiC45CNT55) (a) before and (b) after TGA operation in Figure 6.1 (a).

Figure 6.1 (b) shows that the SiC concentration in the final CNTs product was increased from 24.8 to 58.3 wt% as the starting PMHS concentration was increased from 10/1 to 50/1 PMHS/CNTs w/w. It is interesting to note that only about 1 wt% increment in SiC concentration was achieved from using 20/1 to 50/1 PMHS/CNTs w/w. In comparison, as reported in Section 5.2.1, a wider range of SiOC concentrations was produced in the CNTs (i.e. between 22.3 to 71.0 wt%) for the same range of starting PMHS concentration. This observation can be explained by the lower ceramic yield obtained for SiC (i.e. 57%) than SiOC

(64.9%) as reported in previously Table 4.3 which can be attributed to the loss of material during the carbothermal reduction reaction for producing SiC (Equation 2.12 and Equation 2.13).

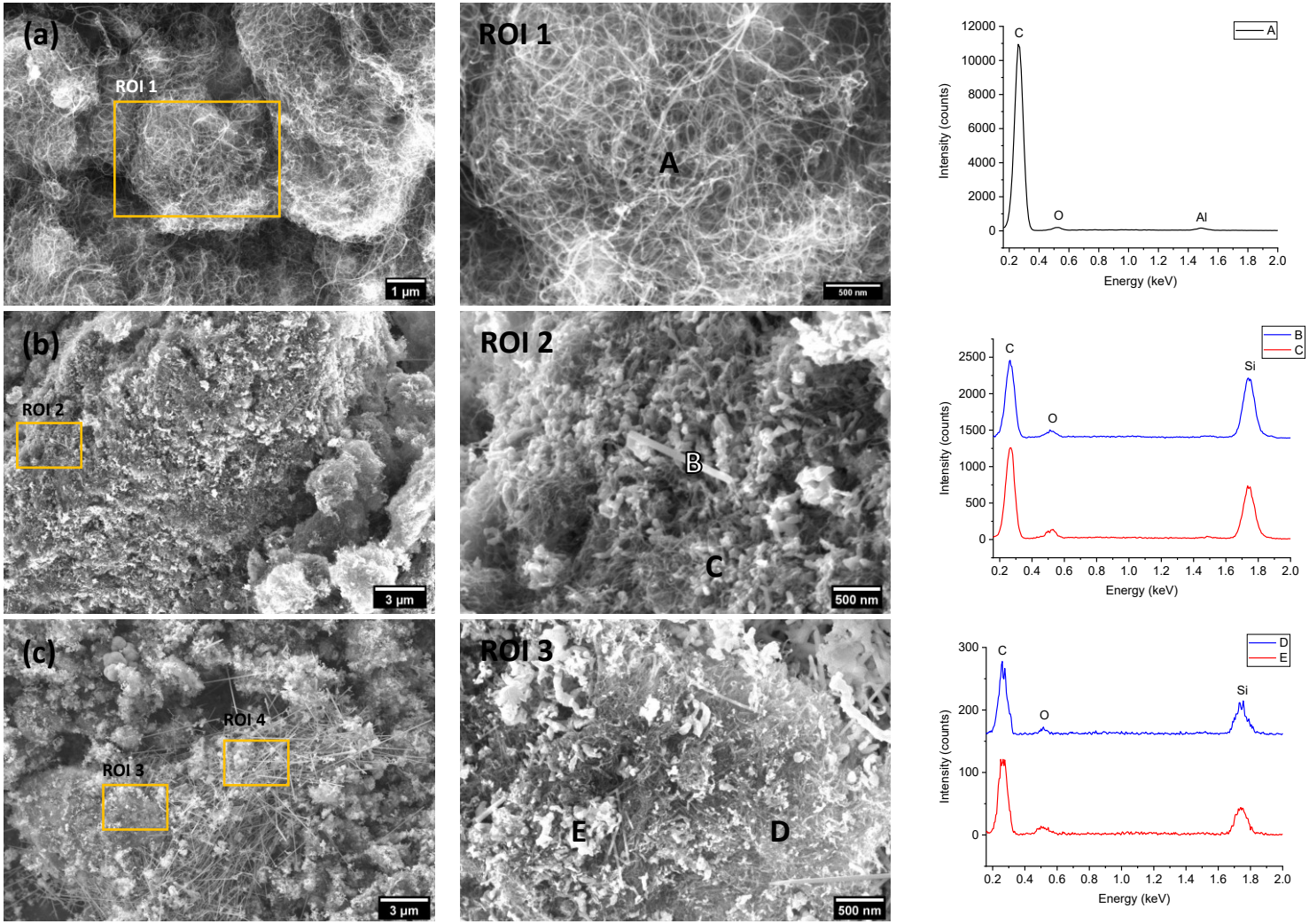
Additionally, as shown in Table 6.1 and Figure 6.1, the onset temperature of the SiC coated CNTs was found to be notably higher than the as-received CNTs which highlights the improvement in the oxidation resistance of CNTs due to the presence of SiC coating. Similar to the SiOC coated CNTs, the effect of SiC concentration will be further investigated in the subsequent studies.

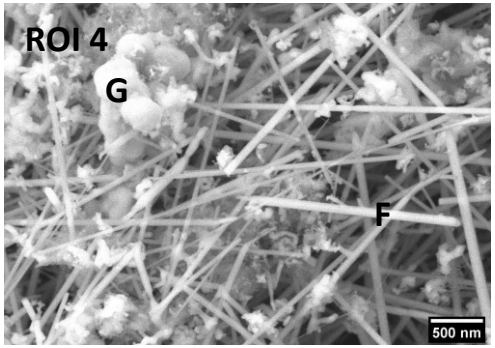
6.2.2 Effect of SiC concentration on coating morphology

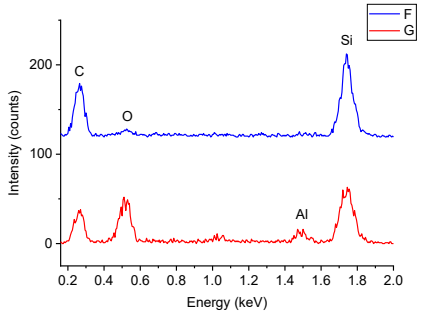
SEM and TEM characterisations were carried out on some of the CNTs samples produced in the previous section as shown in Figure 6.3 and Figure 6.4, respectively, to investigate the effect of SiC concentration on the morphology of the CNTs products. In comparison to the as-received CNTs in Figure 6.3 (a), the SEM image of SiC25CNT75 in Figure 6.3 (b) shows an increase in the thickness of some of the individual CNTs while the EDX measurement shows the presence of Si and C on the CNTs indicating the presence of SiC coating on the CNTs. It is worth noting that a small amount of O was also detected in the EDX measurement which can be attributed to the native SiO_2 layer formed on the SiC surface [16, 124]. On the other hand, the TEM imaging of the SiC25CNT75 in Figure 6.4 (a) showed a small amount of SiC precipitation on the CNTs agglomerate where the SiC precipitate appeared to have grown in a cylindrical manner on the CNTs (outlined by the dotted orange lines in the image). Besides, no apparent coating layer had been observed on the individual CNTs. Additionally, a small amount of SiC whiskers had also been found in the sample as shown under SEM in Figure 6.3 ((b), ROI 2). The SiC whisker was further identified with TEM in Figure 6.4 (e).

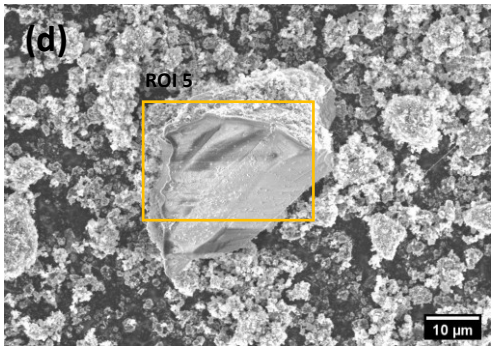
Subsequently, as the coating concentration was increased to 45 wt%, a few different types of morphologies could be observed in the SiC45CNT55 sample: firstly, the presence of SiC coating on the CNTs was observed as shown in the SEM image and EDX measurement in Figure 6.3 (c, ROI 3). From the TEM characterisation, an increased amount of SiC precipitation was found on the CNTs agglomerate as shown in Figure 6.4 (b) where the SiC had also seemed to grow cylindrically along the tangled CNTs. Secondly, differently from the SiOC coated CNTs, no apparent coating layer had been observed on the individual CNTs as shown in Figure 6.4 (c). Next, SiC whiskers were also found in this sample at a seemingly a higher amount as shown in Figure 6.3 (c, ROI 4). Finally, dense SiOC-CNTs products (which were also observed in the SiOC coated CNTs samples) could also be found in the SiC45CNT55 sample as shown in Figure 6.3 (d).

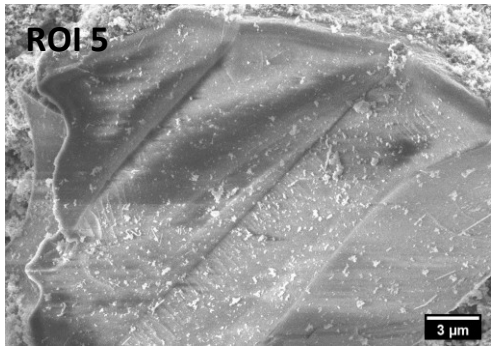
At a higher coating concentration, the dense SiOC-CNTs products were predominantly observed in the SiC56CNT44 sample as shown in the SEM image and EDX measurement in Figure 6.3 (e). TEM characterisation of the sample, as shown in Figure 6.4 (d), shows that a thick SiOC precipitate was coated largely over the CNTs agglomerates.

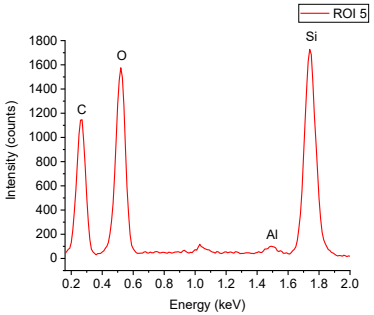

(a)
ROI 1
1 µm
ROI 1
A
500 nm
(b)
ROI 2
3 µm
ROI 2
B
C
500 nm
(c)
ROI 4
ROI 3
3 µm
ROI 3
E
D
500 nm
A
C
O
Al
Intensity (counts)
Energy (keV)
B
C
C
O
Si
Intensity (counts)
Energy (keV)
D
E
C
O
Si
Intensity (counts)
Energy (keV)

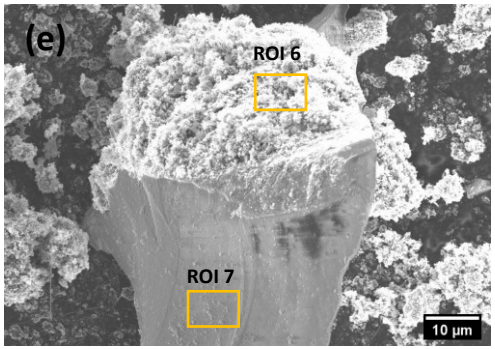

ROI 4
G
F
500 nm

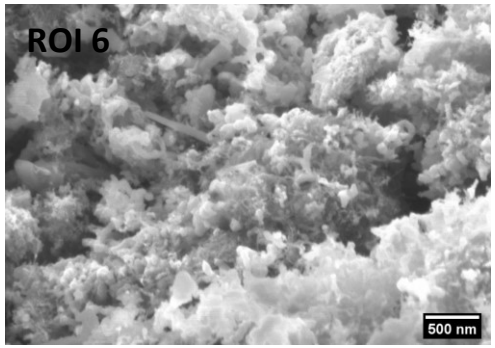

F
G
Si
C
O
Al
Intensity (counts)
Energy (keV)

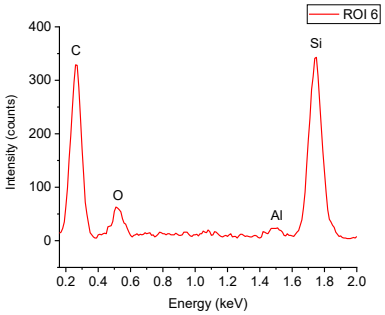

(d)
ROI 5
10 µm


ROI 5
3 µm


ROI 5
Si
O
C
Al
Intensity (counts)
Energy (keV)


(e)
ROI 6
ROI 7
10 µm


ROI 6
500 nm


ROI 6
Si
C
O
Al
Intensity (counts)
Energy (keV)

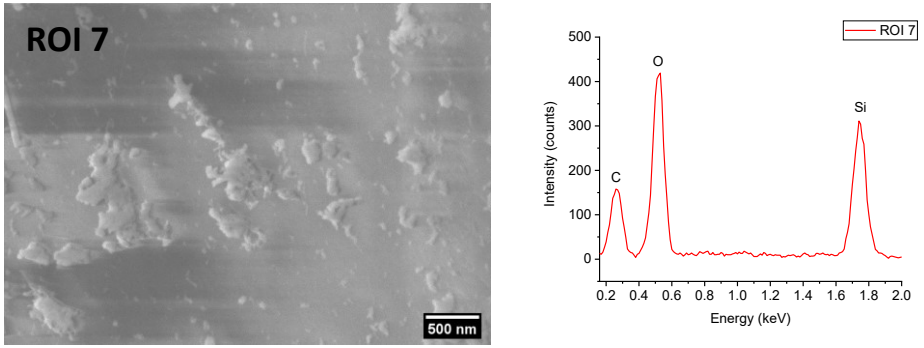
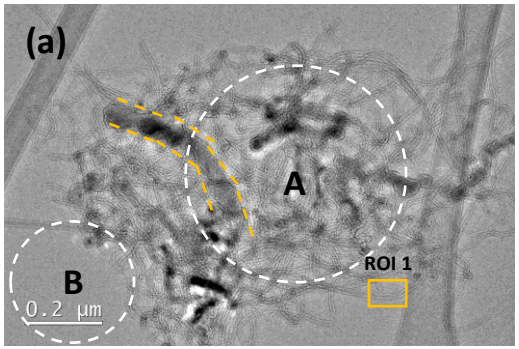
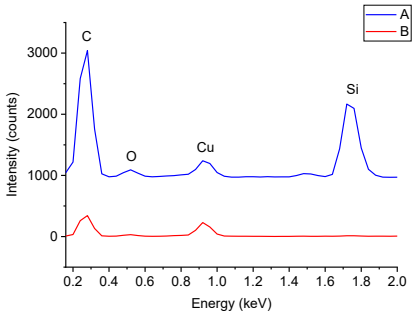
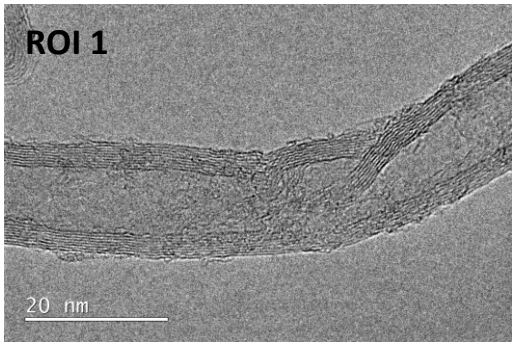
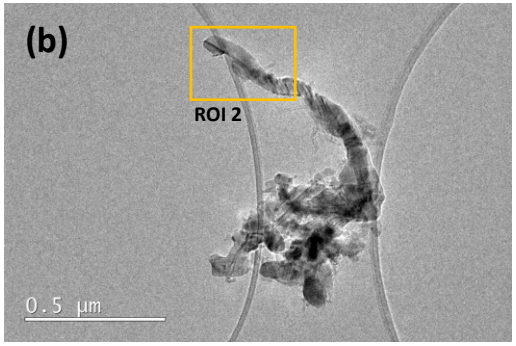


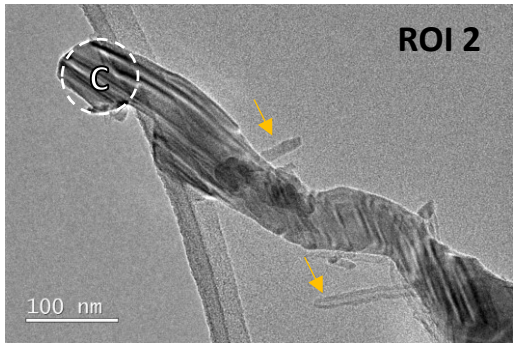
Figure 6.3. SEM images and EDX spectra of as produced SiC coated CNTs: (a) as-received CNTs, (b) SiC25CNT75, (c and d) SiC45CNT55 and (e) SiC56CNT44. Point EDX measurement was performed at the locations marked by the capital letters A-G in the SEM images meanwhile EDX mapping was performed on the areas marked with 'ROI #'. Note that the Al shown in the EDX spectra is attributed to the alumina residue which was originally present in the starting NC7000 CNTs.

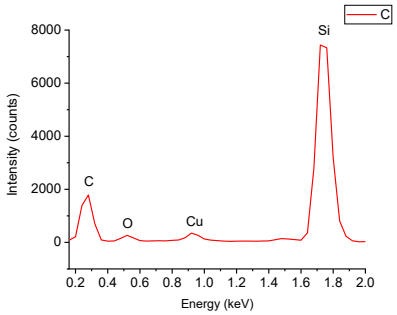

(a)
A
B
ROI 1
0.2 μm

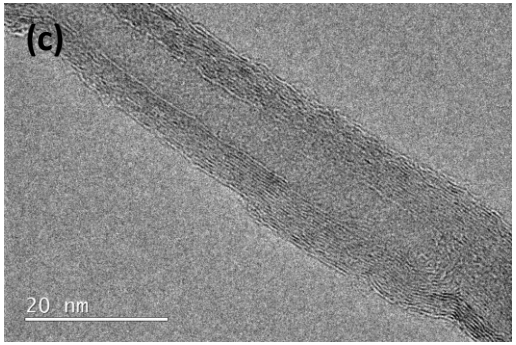

A
B
C
O
Cu
Si
Intensity (counts)
Energy (keV)


ROI 1
20 nm


(b)
ROI 2
0.5 μm


C
ROI 2
100 nm


C
Si
C
O
Cu
Intensity (counts)
Energy (keV)


(c)
20 nm

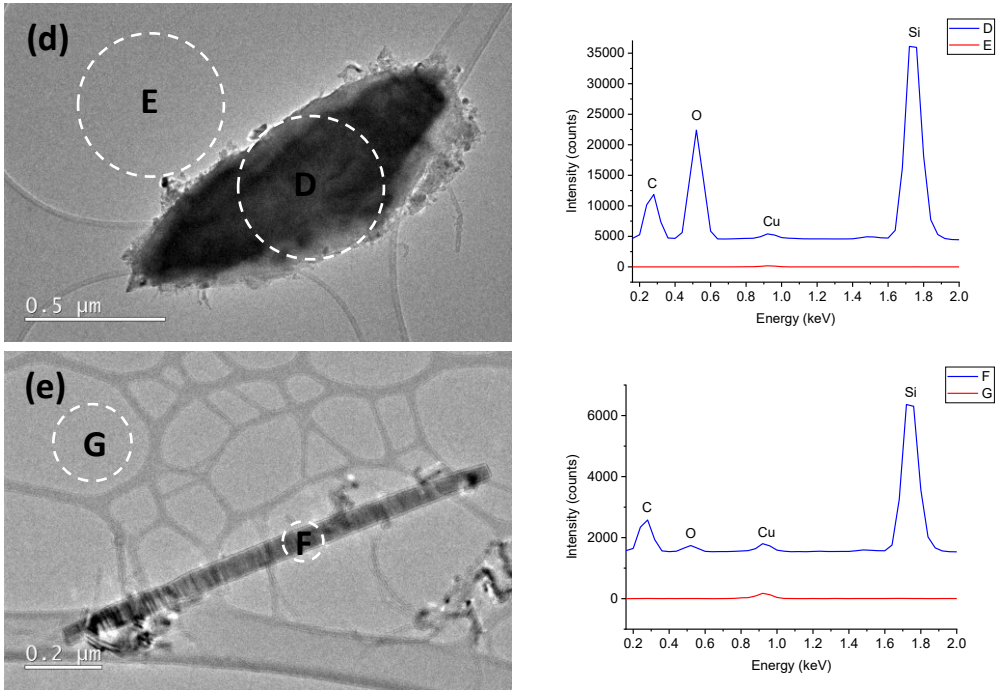


Figure 6.4. TEM images and EDX spectra of as-produced (a) SiC25CNT75, (b and c) SiC45CNT55, (d) SiC56CNT44 and (e) the SiC whisker found in some of the samples. The area of EDX measurement is outlined with white dotted circle and marked by capital letters A-G. Cu detected in the EDX spectra is attributed to the TEM copper grid. Dotted orange lines are used to outline the cylindrical SiC precipitate on SiC25CNT75 image.

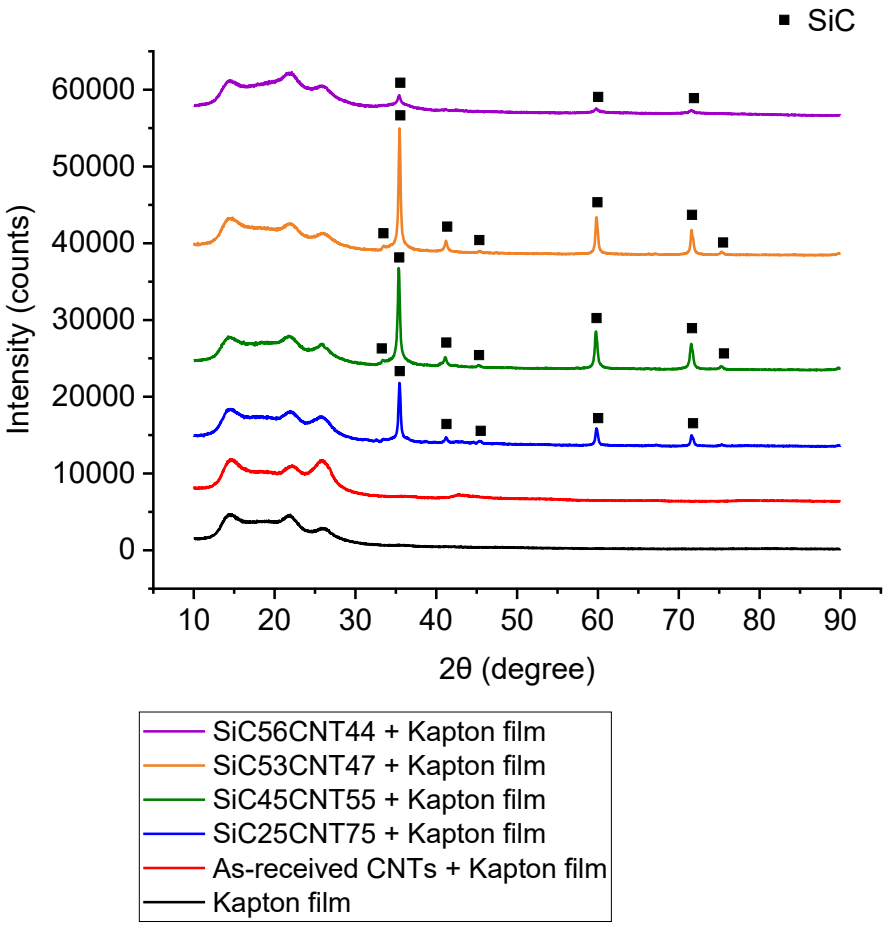


Figure 6.5. XRD patterns of as-received CNTs and SiC coated CNTs: SiC25CNT75, SiC45CNT55, SiC53CNT47 and SiC56CNT44.

Following the SEM and TEM findings, the composition of the CNTs samples was further analysed using XRD as shown in Figure 6.5. The SiC peaks could clearly be identified in all the SiC coated CNTs samples. On the other hand, the 002 plane reflection from the CNTs (at $2\theta = 26.5°$) could not be found in the XRD patterns due to the intense reflections from the Kapton film. (Note: As mentioned in Section 3.3.3, the CNTs samples had to be sealed with Kapton film during the XRD measurement to prevent the CNTs from becoming airborne). Furthermore, the intensity of the SiC peak, especially at $2\theta = 35.6°$, was found to increase as the SiC concentration increases from 25 to 53 wt%. This observation can most likely be attributed to both the increased formation of the SiC whiskers and SiC coating on the CNTs.

Subsequently, the intensity of the SiC peaks was drastically reduced for the SiC56CNT44 sample. Coupled with the SEM and TEM findings in Figure 6.3 (e) and Figure 6.4 (d), the results suggest that the SiC56CNT44 sample consisted predominantly of SiOC coated CNTs and only a small amount of SiC coated CNTs. These results also point out the inaccuracy in the calculated composition for SiC56CNT44 in Table 6.1; nevertheless, the composition is kept as it is throughout this work since it is not significant to determine the actual coating composition of this sample.

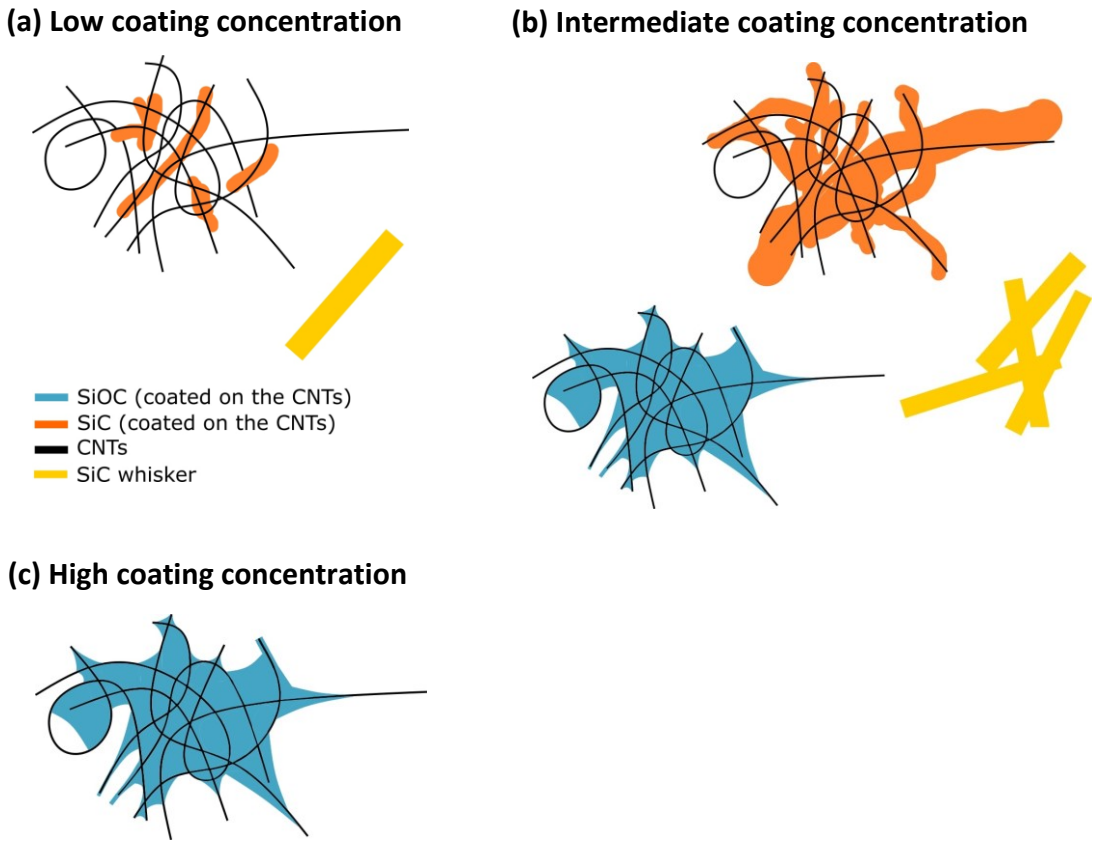


Figure 6.6. Proposed model for the evolution of the 'SiC coated CNTs' morphology at different coating concentrations: (a) low, (b) intermediate and (c) high.

Figure 6.6 proposes a model to explain the change in the morphology of the coated CNTs as the coating concentration increases. Similar to the coating behaviour of SiOC on the CNTs (see Figure 5.5), the SiC coating was also expected to form predominantly on the CNTs

agglomerates instead of the individual tubes. At a low coating concentration (Figure 6.6 (a)), a small amount of SiC coating would be formed on the agglomerates in a cylindrical manner. A small amount of SiC whiskers could also be found at this stage. At the intermediate coating concentration (Figure 6.6 (b)), the formation of the cylindrical SiC coating on the CNTs agglomerates and the presence of SiC whiskers would be increased. Additionally, a small amount of SiOC-CNTs products would also be found in the sample which indicates that some of the SiOC products (which was formed at the lower pyrolysis temperature) had not been successfully converted to SiC at the higher pyrolysis temperature. Finally, at the high coating concentration (Figure 6.6 (c)), SiOC-CNTs products would predominantly be found in the sample. This behaviour is assumed to be caused by a slowdown in the rate of phase separation and carbothermal reduction reactions to convert SiOC to SiC due to the increase in coating concentration. Further investigation needs to be carried out to confirm this hypothesis. Nevertheless, based on this investigation, it seems unreasonable to use a very high concentration of PMHS for the production of SiC coated CNTs as it did not ensure an efficient conversion of SiOC to SiC during the pyrolysis process.

The formation of SiC whiskers in the coated CNTs sample can most likely be explained by the carbothermal reduction reactions involving the CNTs. This assumption was based on a few similar reports in the literature in which nanosized SiC whiskers were formed in the presence of carbon substrates. For example, Gumula, T. et. al. reported that carbon fibres/SiC composites prepared from carbon fibres/polysiloxane composites consisted of nanosized SiC filaments which were mainly deposited on the carbon fibres [217]. Furthermore, the synthesis of SiC whiskers using activated carbon fibres substrate had also been reported by Ryu, Z. et. al. who proposed that the growth of SiC whiskers occurred via a vapour-solid mechanism in which the SiO gas released from the carbothermal reduction reaction between SiO_2 and free carbon (see

Equation 2.12) is condensed to super fine SiO_2 which reacts with the activated carbon fibres to synthesize the SiC whiskers [256]. Therefore, in the current investigation, it can be postulated that the SiC whiskers were formed from the reaction between the condensed super fine SiO_2 and the CNTs acting as the substrate:

$$SiO_{2,super\ fine}(s) + C_{CNTs}(s) \rightarrow SiC_{whisker}(s) + CO(g)$$

Equation 6.2

6.2.3 Effect of SiC coating on CNTs dispersibility

The state of dispersion of the as-received CNTs and SiC coated CNTs was compared by dispersing each CNTs sample in THF at a concentration of 1 mg equivalent of as-received CNTs via ultrasonication for 30 min according to the parameters described in Section 3.2.1.1. Figure 6.7 shows the appearance of the dispersions before and after ultrasonication. It is interesting to note that prior to ultrasonication, the SiC coated CNTs appeared to be readily dispersed in THF especially for the CNTs samples with the SiC concentrations of 45 wt% and above. After sonication, a black homogeneous solution was produced for each dispersion. By visual inspection, it is also interesting to note that large particles could still be observed in the as-received CNTs, SiC25CNT75 and SiC45CNT55 dispersions (can be more clearly seen from the deposition on the glass bottle wall), but for higher SiC concentrations no obvious deposition was observed.

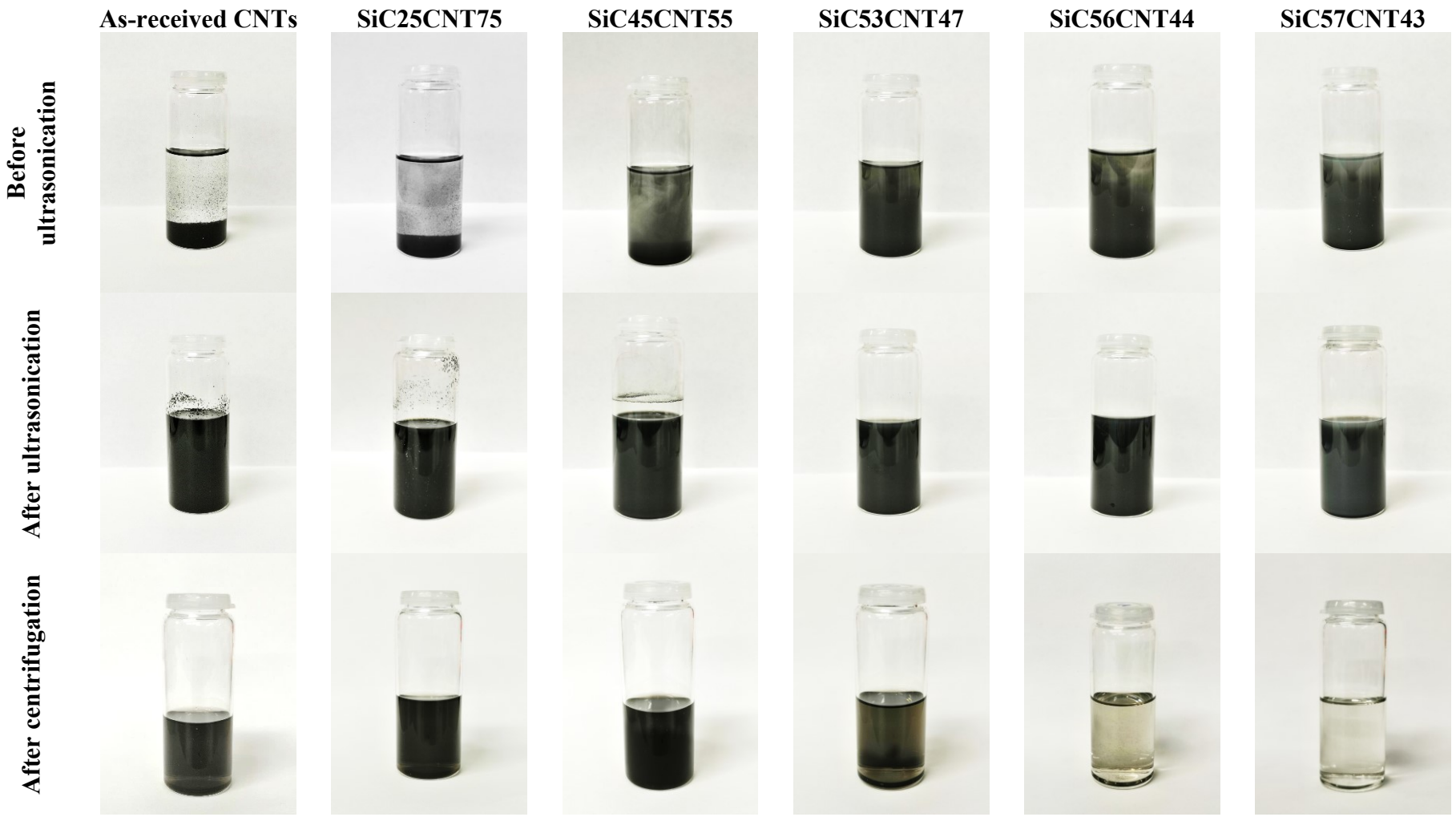


Figure 6.7. Photographs of as-received CNTs and SiC coated CNTs in THF before and after ultrasonication, and after centrifugation. Each dispersion was prepared at a concentration of 1 mg equivalent of as-received CNTs per mL of THF.

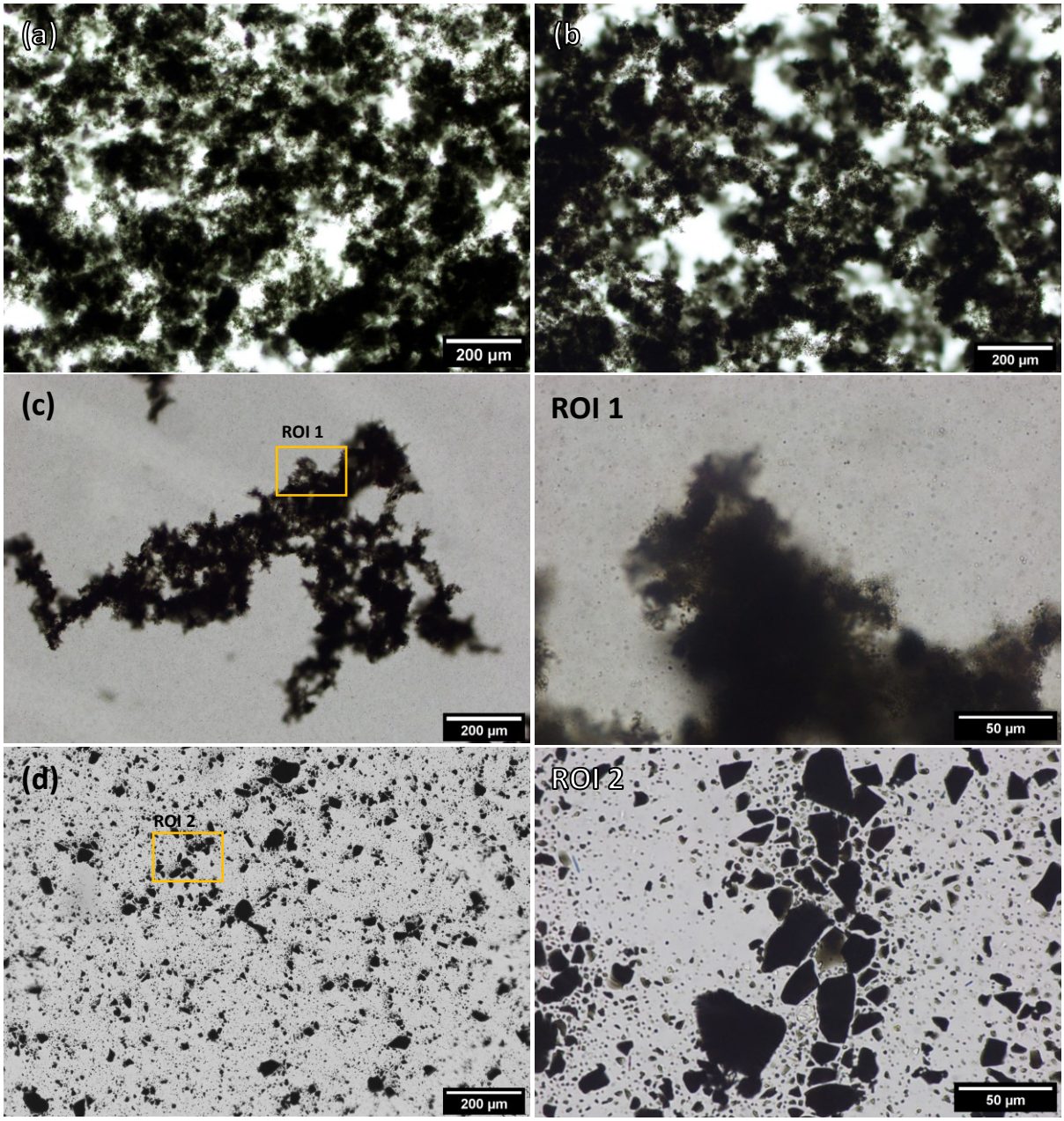
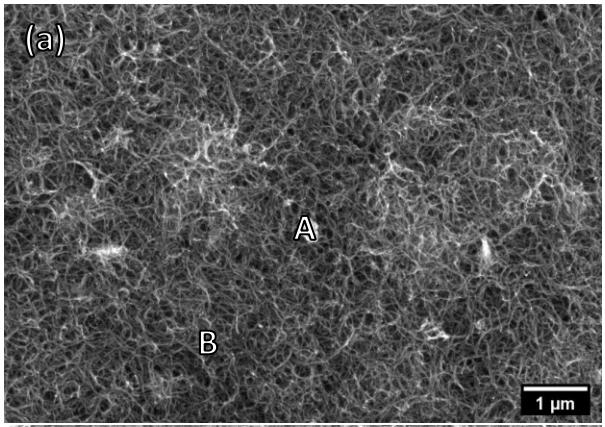
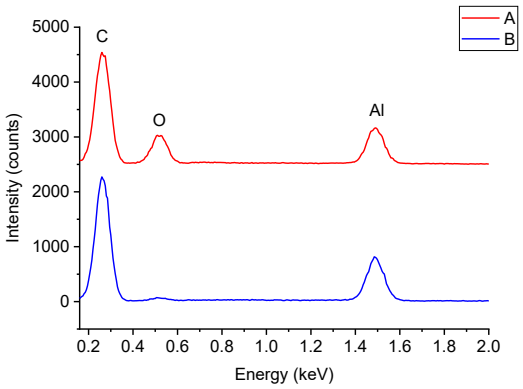
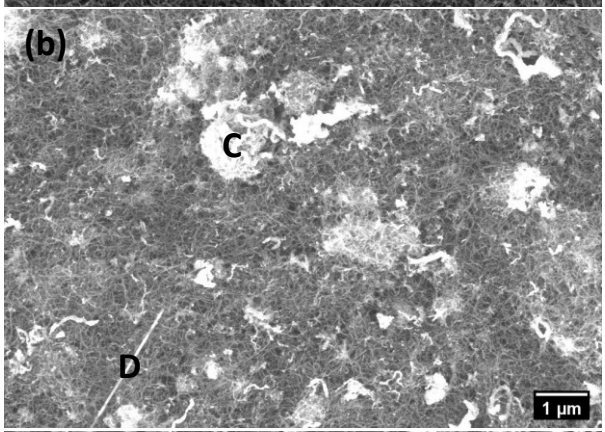
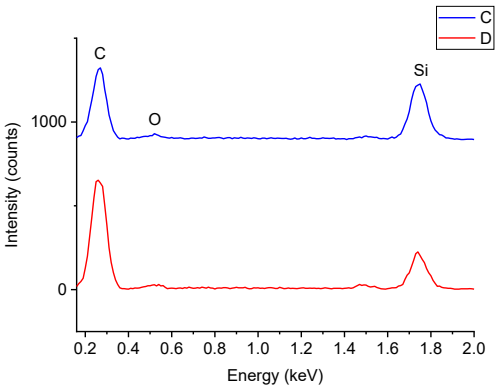


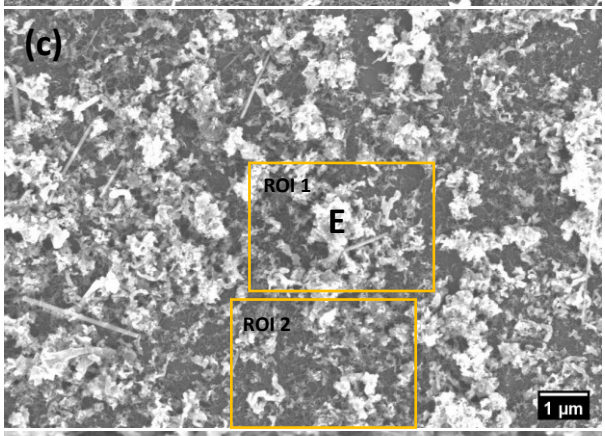
Figure 6.8. Optical micrographs of (a) as-received CNTs, (b) SiC25CNT75, (c) SiC45CNT55 and (d) SiC56CNT47 dispersions in THF after 30 min ultrasonication. Each dispersion was at a concentration of 1 mg equivalent of as-received CNTs per mL of THF.

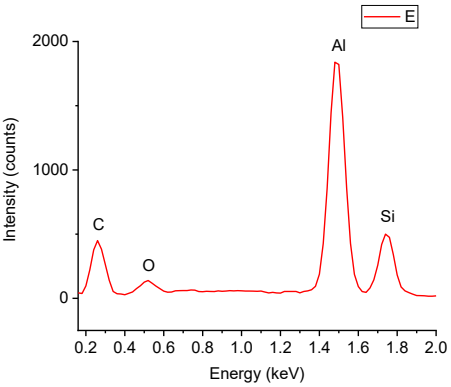

(a)
A
B
1 µm

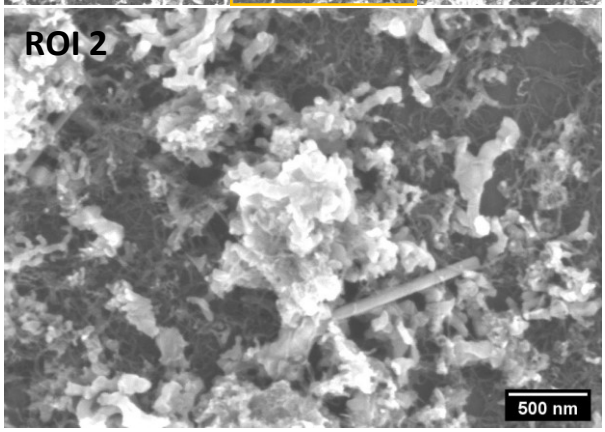

A
B
C
O
Al
Intensity (counts)
Energy (keV)

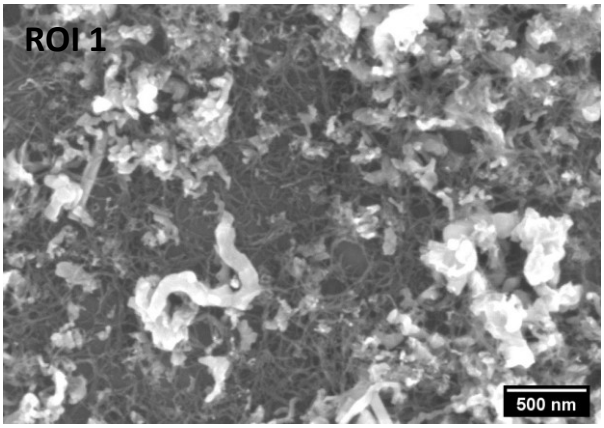

(b)
C
D
1 µm


C
D
C
O
Si
Intensity (counts)
Energy (keV)


(c)
ROI 1
E
ROI 2
1 µm


E
Al
C
O
Si
Intensity (counts)
Energy (keV)


ROI 2
500 nm


ROI 1
500 nm

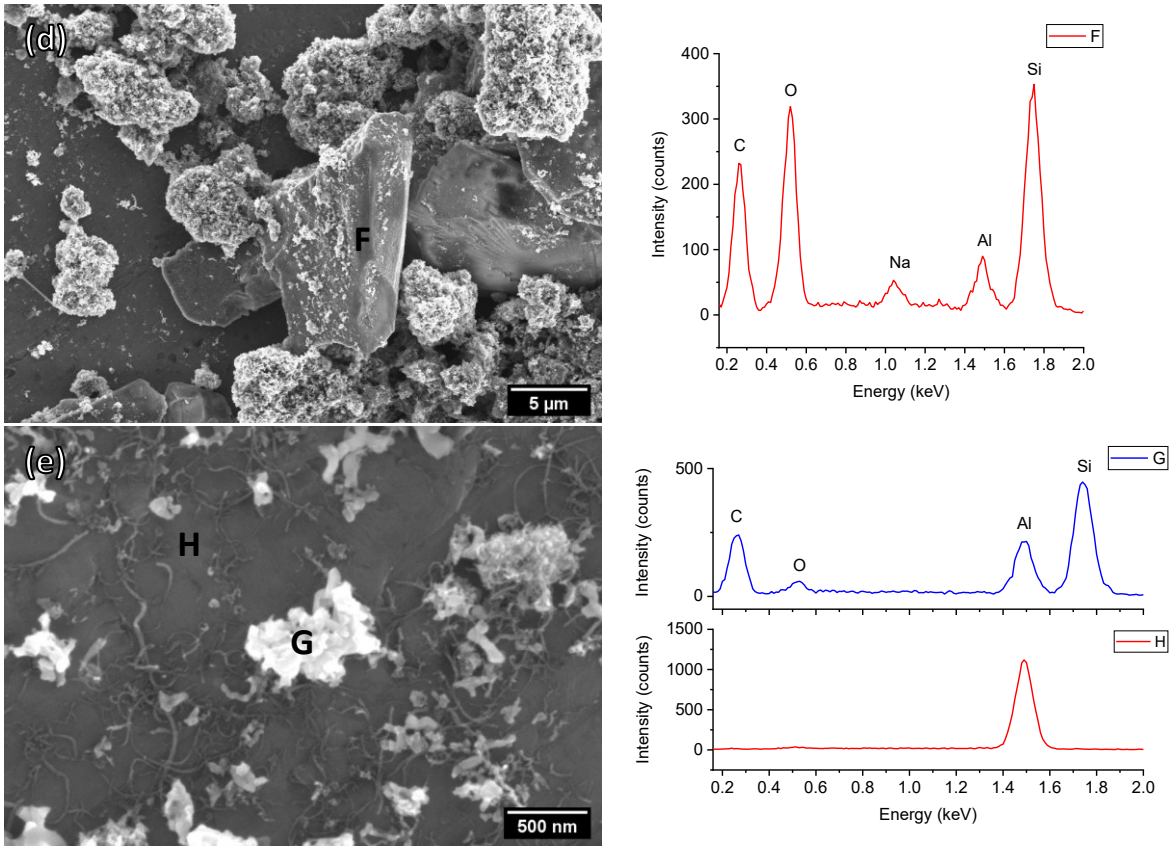


Figure 6.9. SEM images of ultrasonically dispersed CNTs deposited on Al foil: (a) as-received CNTs, (b) SiC25CNT75, (c) SiC45CNT55 and (d and e) SiC56CNT44. Point EDX measurement as performed at the locations marked by the capital letters. Al detected in the EDX is attributed to the Al foil.

The CNTs dispersions were further studied with optical microscopy and SEM as shown in Figure 6.8 and Figure 6.9, respectively. The SiC25CNT47 dispersion consists predominantly of large clusters as shown in Figure 6.8 (b) as similarly observed for the as-received CNTs dispersion in Figure 6.8 (a). Using SEM-EDX, these clusters were further identified as CNTs agglomerates with some presence of SiC coating as shown in Figure 6.9 (b). Next, the size of the clusters were found to be remarkably reduced in the SiC45CNT55 dispersion as shown in Figure 6.8 (c). Furthermore, very fine particles were also observed in the THF solution as shown Figure 6.8 (c, ROI 1) which can probably be attributed to the debundled CNTs as seen in the SEM images in Figure 6.9 (c). Finally, the dispersion of SiC56CNT44 was found to consist of much smaller particles which also appeared to be angular in shape as shown in Figure

6.8 (d). These particles are most likely attributed to the dense SiOC-CNTs products as shown in the SEM image in Figure 6.9 (d). Finally, debundled CNTs could also be found in this dispersion as shown in Figure 6.9 (e) albeit in a small amount.

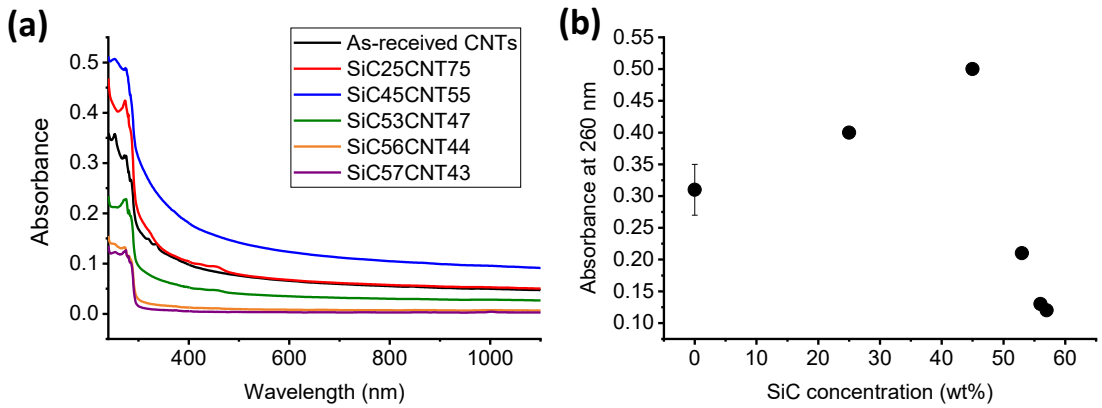


Figure 6.10. (a) UV-Vis spectra of as-received CNTs and SiC coated CNTs supernatant solutions. (b) Plot showing the absorbance value of the supernatant solutions at 260 nm as a function of SiC concentration in the CNTs sample.

Using the procedure in Section 3.3.2, the agglomerates and dense particles in each dispersion were segregated via centrifugation and the supernatant was extracted as shown in Figure 6.7. Then, UV-Vis measurement was performed on the supernatant solutions and taken to the UV-Vis measurement as shown in Figure 6.10 (a) to assess the degree of individually dispersed CNTs in each dispersion based on the assumptions that the large CNTs agglomerates would be segregated as sediment and the individually dispersed CNTs are suspended in the supernatant after centrifugation. Figure 6.10 (b) shows that the absorbance of the CNTs dispersion increases as the SiC concentration in the CNTs increases up to 45 wt% after which the absorbance drastically reduced to lower than that of the as-received CNTs dispersion. Therefore, this finding seems to suggest that the highest degree of individually dispersed CNTs was found in the SiC45CNT55 dispersion. The lower absorbance values measured for the SiC53CNT47 to SiC57CNT43 dispersions could have probably been explained by the increased formation of

dense SiOC-CNTs products in the sample. However, their small absorbance values seem to indicate that a small amount of individually dispersed CNTs can still be found in the dispersions as previously observed in Figure 6.9 (e). Finally, the UV-Vis results also seem to correlate well with the visual observation of the supernatant solutions in Figure 6.7 in which the lighter the colour of the solution, the lower the UV-Vis absorbance value.

The results of this study showed that the dispersibility of the CNTs could be affected by the SiC concentration (and therefore the CNTs morphologies) in the sample. Even though large agglomerates were mainly observed in the SiC25CNT75 dispersion, the degree of the individually dispersed CNTs was notably higher than in the as-received CNTs dispersion which suggests that the coating might have helped to promote the debundling of the CNTs agglomerates. As the SiC concentration in the CNTs was increased to 45 wt%, the size of the agglomerates became smaller while the amount of individually dispersed CNTs was further increased. However, for the CNTs samples with the SiC concentrations of 53 wt% and above, the dispersibility of the CNTs appeared to be worse than the as-received CNTs. This behaviour was likely attributed to the increased formation of the dense SiOC-CNTs products in the samples which had restricted the debundling of the CNTs that were embedded in the solids as similarly found in the study in Section 5.2.3.

6.3 AZ91 composites

6.3.1 Effect of SiC coating on AZ91 composite properties

Pure AZ91 and AZ91 composites reinforced with as-received CNTs and SiC coated CNTs were fabricated as listed in Table 6.2 to investigate the effect of SiC concentration (and therefore the CNTs morphologies) in the CNTs on the properties of the AZ91 composites. The pure AZ91 and AZ91-As received CNTs composites samples had been previously used for comparison with the AZ91-SiOC coated CNTs composites in Section 5.3.1. The AZ91 samples were fabricated via stir casting according to the procedure in Section 3.2.2 by stirring at 650 °C for 30 minutes. The CNTs samples were added to the melt via the Al parcel technique as described in Section 3.2.1.1 at an equivalent as-received CNTs loading of 0.3 wt%. For consistency, blank Al parcels had also been added to the pure AZ91 sample. Note that a different total nanoparticle loading was added for each sample due to the difference in the SiC coating concentration. One casting was produced for each sample for the microstructural and mechanical properties characterisations.

Table 6.2. List of Mg AZ91 samples fabricated to investigate the effect of SiC coating concentration in the CNTs on the properties of AZ91 composites.

Sample	Total nanoparticles loading (wt%)	Equivalent as-received CNTs loading (wt%)
Pure AZ91	0	0
AZ91-As received CNTs	0.30	0.3
AZ91-SiC25CNT75	0.40	0.3
AZ91-SiC45CNT55	0.55	0.3
AZ91-SiC53CNT47	0.64	0.3
AZ91-SiC56CNT44	0.68	0.3

As shown previously in Figure 5.15 (a), as-received CNTs were found to exhibit a poor wettability by the AZ91 matrix during the casting of the composite. In the current study, a similar behaviour was observed during the casting of AZ91-SiC25CNT75 composite as shown in Figure 6.11 where a large amount of CNTs were not successfully incorporated into the matrix

which led to the CNTs being left out of the casting or pushed to the outer surface of the casting which indicates the poor wettability of the SiC25CNT75 sample. It is also worth noting that at a similar coating concentration, the SiOC22CNT78 sample also exhibited a poor wettability by the matrix (see Figure 5.15 (b)). This behaviour had not been observed during the casting of other AZ91-SiC coated CNTs composites samples for example as shown for the AZ91-SiC4CNT55 sample in Figure 6.11 (b).

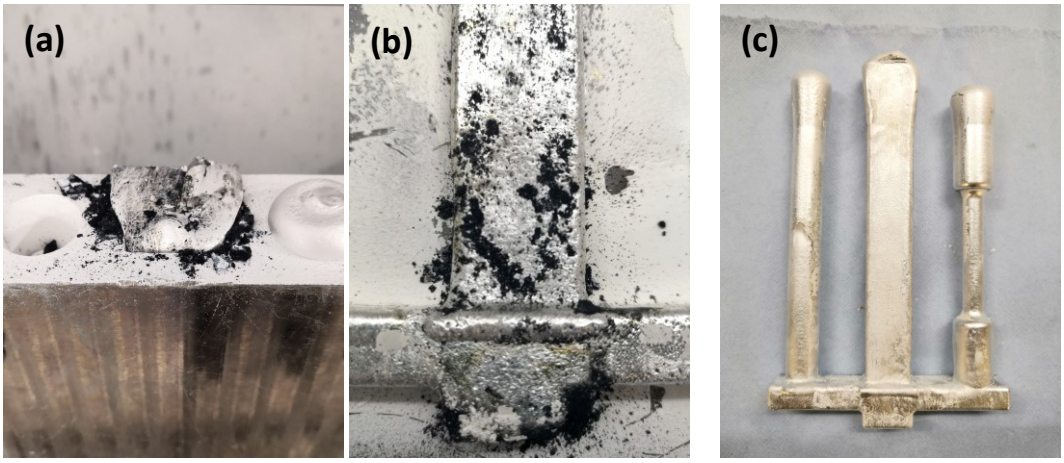


Figure 6.11. Photographs of (a and b) AZ91-SiC25CNT45 and (c) AZ91-SiC45CNT55 castings.

Figure 6.12 compares the cross sections of the as-cast AZ91 composites reinforced with the SiC coated CNTs samples. For comparison, the cross sections of pure AZ91 and AZ91-As received CNTs castings can be found in Figure 5.16 (a) and (b), respectively. By visual comparison, AZ91-SiC56CNT44 composite appeared to have the highest density of defects meanwhile the same level of defects were observed for other composite samples.

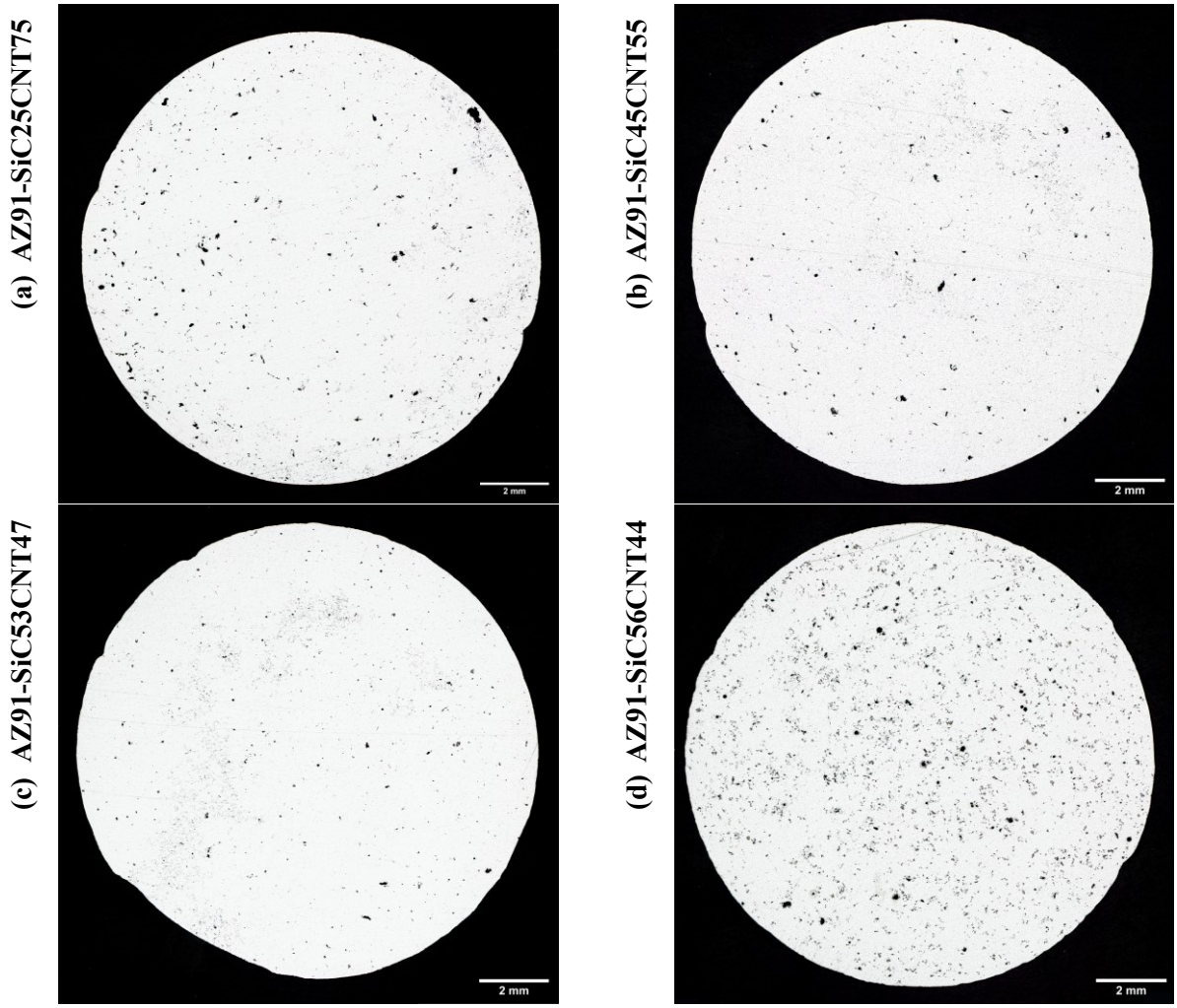


Figure 6.12. Optical micrographs showing the cross sections of as-cast AZ91 composites reinforced with (a) SiC25CNT75, (b) SiC45CNT55, (c) SiC53CNT47 and (d) SiC56CNT44. Each cross section was taken from the middle location of the cylindrical part of the casting (see Figure 5.10).

Table 6.3. Density and porosity of pure AZ91 and AZ91 composites reinforced with as-received and SiC coated CNTs. A single measurement was performed for each specimen location.

Sample	Specimen location	Density (g/cm^3)	Porosity (vol %)
Pure AZ91	Top	1.79	1.1
	Middle	1.80	0.6
	Bottom	1.79	1.3
	Average	**1.80 ± 0.00**	**1.0 ± 0.2**
AZ91-As received CNTs	Top	1.79	1.6
	Middle	1.76	3.1
	Bottom	1.78	2.0
	Average	**1.78 ± 0.00**	**2.2 ± 0.5**
AZ91-SiC25CNT75	Top	1.77	2.6
	Middle	1.78	2.2
	Bottom	1.79	1.7
	Average	**1.78 ± 0.01**	**2.2 ± 0.3**
AZ91-SiC45CNT55	Top	1.78	2.0
	Middle	1.79	1.6
	Bottom	1.79	1.6
	Average	**1.79 ± 0.00**	**1.7 ± 0.1**
AZ91-SiC53CNT47	Top	1.79	1.7
	Middle	1.79	1.9
	Bottom	1.79	2.6
	Average	**1.79 ± 0.00**	**2.1 ± 0.3**
AZ91-SiC56CNT44	Top	1.80	2.0
	Middle	1.79	2.4
	Bottom	1.77	3.6
	Average	**1.78 ± 0.01**	**2.7 ± 0.5**

Table 6.3 reports the density and porosity measurement of the AZ91 samples. As plotted in Figure 6.13, the porosity results seem to agree with the microstructural observation whereby the porosity level was measured to be the highest for AZ91-SiC56CNT44 among the composite samples. Additionally, the lowest porosity was measured for the AZ91-SiC45CNT55 composite. Further investigation as shown in Figure 6.14 revealed that the increase level of porosity in the AZ91-SiC56CNT44 composite could most likely be attributed to the dense SiOC-CNTs products whereby the aggregation of these particles seems to lead to an ineffective wetting by the AZ91 matrix. This behaviour had also been previously observed in the AZ91-SiOC67CNT33 composite (see Figure 5.18 (d)). The previous study for the AZ91-SiOC coated CNTs composites in Section 5.3.2 showed that the nanoparticle addition did not seem to show any notable improvement on the grain size and hardness of the as-cast composites which can

be due to the low loading of nanoparticles. Therefore, the grain size and hardness assessments are not deemed to be necessary for the current study.

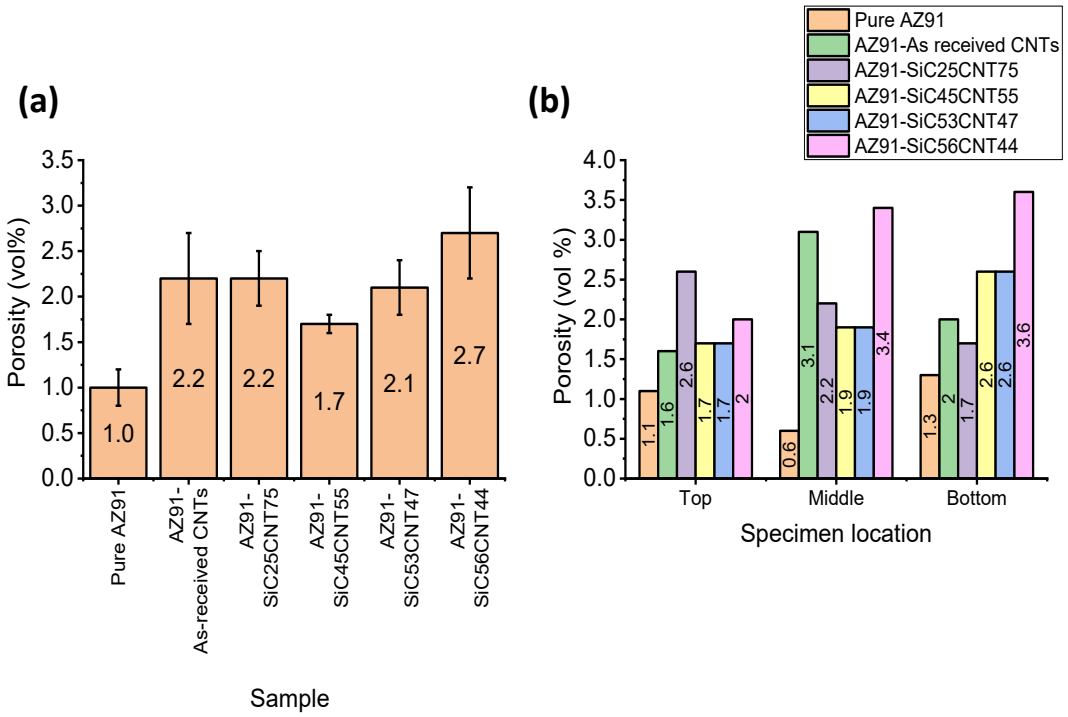


Figure 6.13. Porosity comparison between the as-cast pure AZ91 and AZ91 composites reinforced with as-received CNTs and SiC coated CNTs (a) by average and (b) by specimen location. A single measurement was performed for each specimen location.

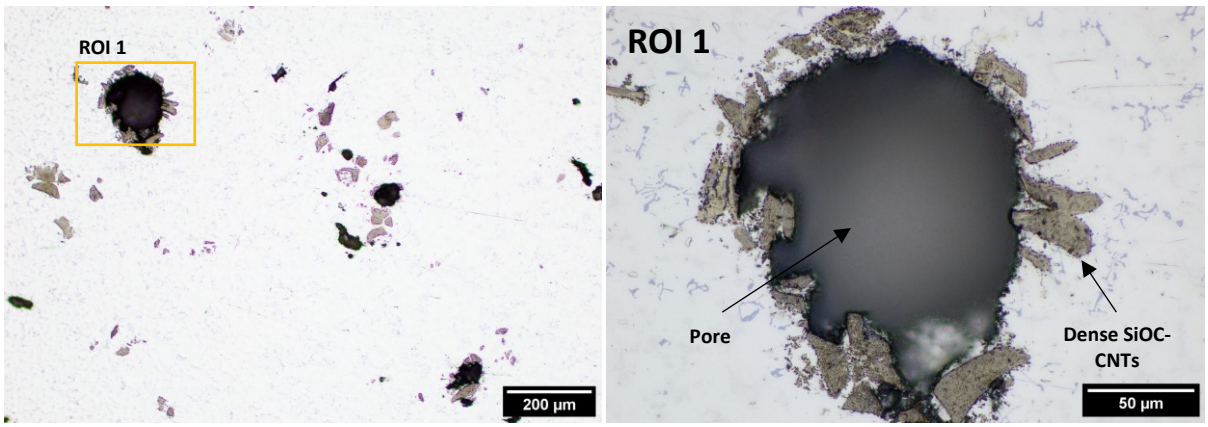


Figure 6.14. Optical micrographs showing the cross-section of AZ91 composites reinforced with SiC56CNT44 at a higher magnification.

Based on the results in this study and the previous sections, SiC45CNT55 was found to have the most suitable SiC coating concentration for further fabrication of AZ91-SiC coated CNTs composites at higher loading. At a lower SiC coating concentration of 25 wt%, the coated CNTs appeared largely as agglomerates despite of being capable to produce a considerable amount of individually dispersed CNTs via ultrasonication. However, the coating concentration was still too low to allow for a sufficient wetting of the CNTs by the AZ91 matrix. On the other hand, CNTs with higher SiC concentrations such as SiC53CNT47 and SiC56CNT44 were found to consist of dense SiOC-CNTs products which increases in amount as the coating increases. The presence of these dense particles was found to be undesirable as they could be easily aggregated in the melt which led to an ineffective wetting by the matrix.

6.3.2 Effect of CNTs loading on AZ91 composites properties

Pure AZ91 and AZ91 composites reinforced with as-received CNTs and SiC45CNT55 were fabricated as listed in Table 6.4 to investigate the effectiveness of SiC coating on improving the wettability and distribution of CNTs in AZ91 while increasing the CNTs loading. The pure AZ91 and AZ91-As received CNTs composites had been previously used for comparison with the AZ91-SiOC coated CNTs composites in Section 5.3.3. The AZ91 samples were fabricated via stir casting according to the procedure in Section 3.2.2 by stirring at 650 °C for 30 minutes. The CNTs samples were added to the melt via the Al parcel technique as described in Section 3.2.3 in a range of equivalent as-received CNTs loading from 0.1 to 1.0 wt%. Due to the presence of SiC coating, a different total nanoparticles loading was added to each AZ91-SiC45CNT55 composite in comparison to the AZ91-As received CNTs composite. For consistency, blank Al parcels had also been added to the pure AZ91 sample. One casting was produced for each sample for the microstructural and mechanical properties characterisations.

Similar to the study in Section 5.3.3, solution heat treatment and hot rolling were performed on the as-cast samples as described in Section 3.2.4 prior to sample characterisations to minimise the effect of porosity on the microstructure and mechanical properties of the samples. However, only the solution heat treatment was performed on the samples used for compression testing since hot rolling could not practically be done to produce the compression test coupons due to size limitation (see Section 3.3.13 for compression testing requirement). As a side note, the ageing heat treatment had not been performed on any of the samples in order to avoid the re-precipitation of the β-$Mg_{17}Al_{12}$ phases so that only the strengthening effect of the CNTs would be measured.

Table 6.4. Mg AZ91 samples fabricated to investigate the efficacy of SiC coating on improving the wettability and distribution of CNTs in the Mg matrix while increasing the CNTs loading.

Sample	Total nanoparticles loading (wt%)	Equivalent as-received CNTs loading (wt%)
Pure AZ91	0	0
AZ91-As received CNTs	0.10	0.1
	0.30	0.3
	0.50	0.5
	1.00	1.0
AZ91-SiC45CNT55	0.18	0.1
	0.55	0.3
	0.91	0.5
	1.82	1.0

Figure 6.15 shows the cross sections of the solution treated-hot rolled AZ91-SiC45CNT55 composites at a different coated CNTs loading. For comparison, the cross sections of pure AZ91 and AZ91-As received CNTs samples can be found in Figure 5.24 (a) to (e). Generally, each AZ91-SiC45CNT55 composite showed a low density of defects and no apparent effect from the increase in CNTs loading. Subsequently, the density and porosity of the solution treated-naturally aged and solution treated-hot rolled samples were also measured as shown in Table **6.5**. Theoretically, only a slight increase in the density of AZ91 composite was expected

from the addition of the nanoparticles. As shown in Figure 6.16, the increase in CNTs loading in both the AZ91-As received CNTs and AZ91-SiC45CNT55 composites had led to the increase in the porosity of the composites. It is also important to note that the porosity in the solution treated-naturally aged composites was remarkably reduced via hot rolling which would be desirable for the microstructural and mechanical properties characterisations.

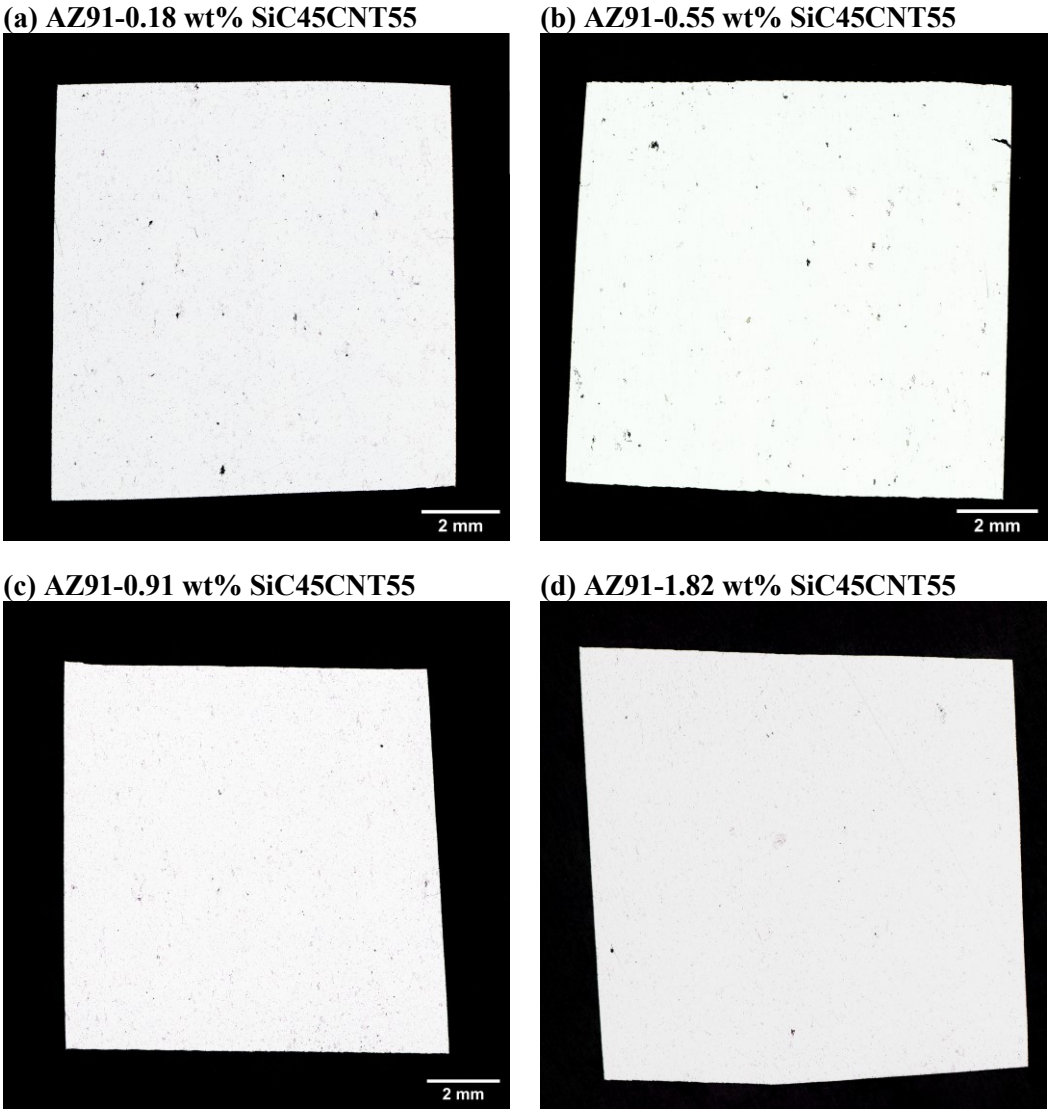


Figure 6.15. Optical micrographs showing the cross sections of solution treated-hot rolled AZ91 composites reinforced with SiC45CNT55 in a range of equivalent as received CNTs loading.

Table 6.5. Density and porosity results of pure AZ91 and AZ91 composites reinforced with as-received CNTs and SiC45CNT55 for the solution treated-naturally aged and solution treated-hot rolled samples.

The solution treated-hot rolled samples were used for all sample characterisations except for compression testing where the solution treated-naturally aged samples were used.

		Solution treated-naturally aged (used for compression testing)		**Solution treated-hot rolled** (used for grain size measurement, hardness and tensile testing)	
Sample	**Theoret. density (g/cm^3)**	**Measured density (g/cm^3)**	**Porosity (vol%)**	**Measured density (g/cm^3)**	**Porosity (vol%)**
Pure AZ91	1.81	1.79 ± 0.00	0.9 ± 0.1	1.81 ± 0.01	0.3 ± 0.3
AZ91-0.10 wt% As received CNTs	1.81	1.79 ± 0.00	1.4 ± 0.2	1.80 ± 0.00	0.5 ± 0.2
AZ91-0.30 wt% As received CNTs	1.81	1.78 ± 0.00	2.0 ± 0.2	1.78 ± 0.02	1.9 ± 1.3
AZ91-0.50 wt% As received CNTs	1.81	1.76 ± 0.00	2.8 ± 0.2	1.81 ± 0.00	0.2 ± 0.1
AZ91-1.00 wt% As received CNTs	1.83	1.77 ± 0.01	3.2 ± 0.4	1.80 ± 0.00	1.2 ± 0.1
AZ91-0.18 wt% SiC45CNT55	1.81	1.78 ± 0.00	1.8 ± 0.2	1.80 ± 0.00	0.8 ± 0.1
AZ91-0.55 wt% SiC45CNT55	1.81	1.79 ± 0.00	1.5 ± 0.1	1.80 ± 0.00	1.1 ± 0.1
AZ91-0.91 wt% SiC45CNT55	1.82	1.79 ± 0.01	1.9 ± 0.3	1.80 ± 0.00	1.4 ± 0.0
AZ91-1.82 wt% SiC45CNT55	1.83	1.76 ± 0.00	3.5 ± 0.2	1.80 ± 0.00	1.5 ± 0.1

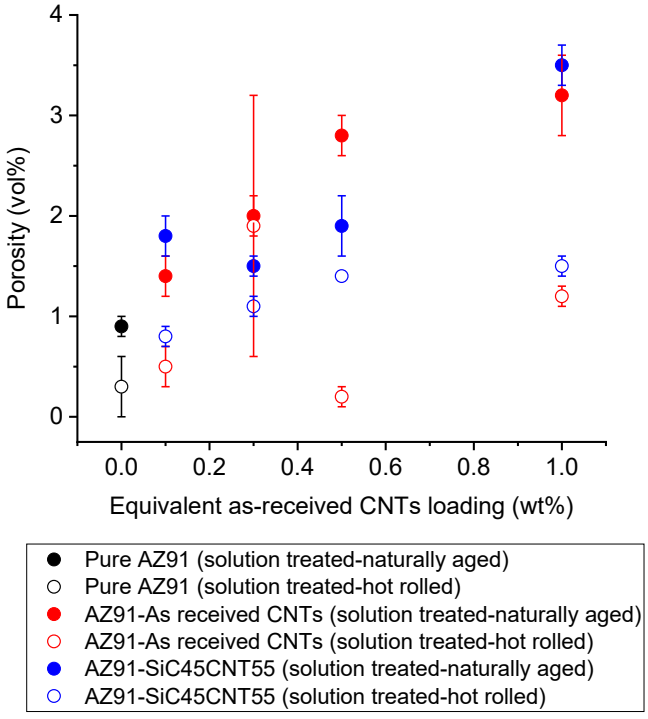


Figure 6.16. Scatter plot showing the porosity of pure AZ91 and AZ91 composites reinforced with as-received CNTs and SiC45CNT55 for the solution treated-naturally aged and solution treated-hot rolled samples.

Table 6.6. Grain size, hardness and tensile properties of solution treated-hot rolled pure AZ91 and AZ91 composites reinforced with as-received CNTs and SiC45CNT55.

Sample	Grain size (μm)	Hardness (HV3)	Young's modulus (GPa)	0.2% tensile yield strength (MPa)	Ultimate tensile strength (MPa)	Ductility (%)
Pure AZ91	37.5 ± 1.2	62.1 ± 2.3	14.8	98.7	248.2	5.8
AZ91-0.10 wt% As received CNTs	39.7 ± 0.7	63.2 ± 1.0	11.8	99.3	252.9	9.5
AZ91-0.30 wt% As received CNTs	36.7 ± 0.6	60.9 ± 0.4	Not measured due to sample defect			
AZ91-0.50 wt% As received CNTs	38.3 ± 0.7	61.6 ± 0.5	16.7; 15.5; 16.3	97.1; 94.8; 113.1	231.7; 250.3; 264.1	4.3; 6.7; 7.2
AZ91-1.00 wt% As received CNTs	34.9 ± 0.6	64.6 ± 0.4	Not measured due to sample defect			
AZ91-0.18 wt% SiC45CNT55	14.0 ± 0.4	65.7 ± 1.0	21.3; 18.1; 22.5	100.0; 115.9; 104.1	204.2; 218.0; 205.8	2.9; 3.8; 2.5
AZ91-0.55 wt% SiC45CNT55	17.6 ± 0.5	64.6 ± 0.5	Not measured due to sample defect			
AZ91-0.91 wt% SiC45CNT55	13.7 ± 0.4	65.8 ± 0.5	24.2; 25.6	84.5; 75.5	181.2; 238.1	2.3; 5.0
AZ91-1.82 wt% SiC45CNT55	12.9 ± 0.4	68.5 ± 0.5	Not measured due to sample defect			

Next, the grain size, hardness and tensile properties of the solution treated-hot rolled AZ91-SiC45CNT55 samples are shown in Table 6.6. As shown in Figure 6.17 and Figure 6.18 (a), the addition of SiC coated CNTs to the AZ91 matrix had led to a remarkable reduction in grain size by about 52-65% in comparison to the AZ91-As received CNTs composites. However, the grain size appeared to be only moderately affected by the increase in CNTs loading. On the other hand, the hardness of the AZ91-SiC45CNT55 composites was increased by only about 4-6 % in comparison to the AZ91-As received CNTs composites as shown in Figure 6.18 (b). In comparison to the AZ91-SiOC55CNT45 composites produced in Section 5.3.3, the AZ91-SiC45CNT55 composites exhibited slightly smaller grain size and lower hardness.

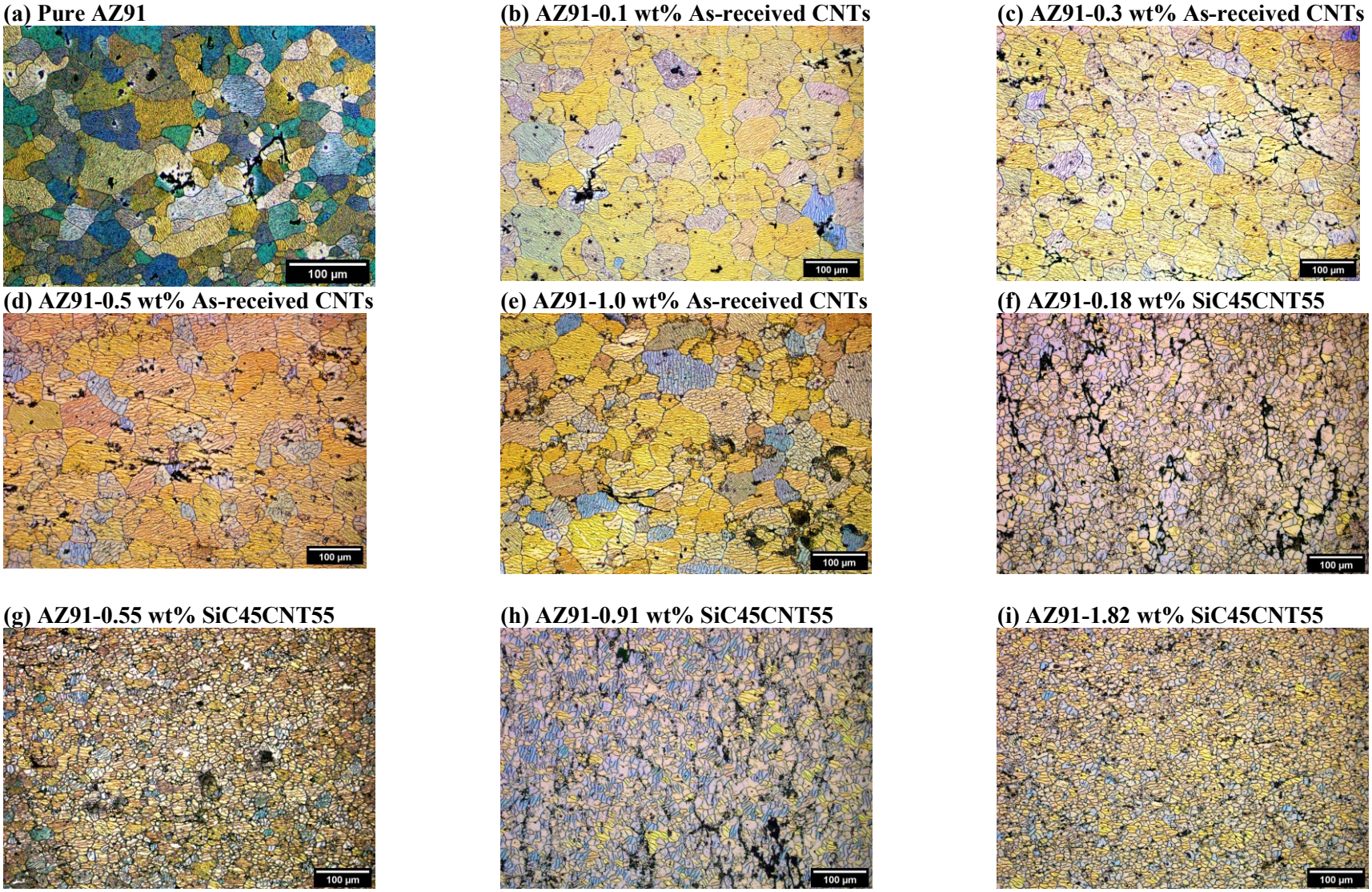


Figure 6.17. Optical micrographs showing the grain structures of solution treated-hot rolled (a) pure AZ91 and AZ91 composites reinforced with (b-e) as received CNTs and (f-i) SiC45CNT55 at various CNTs loadings.

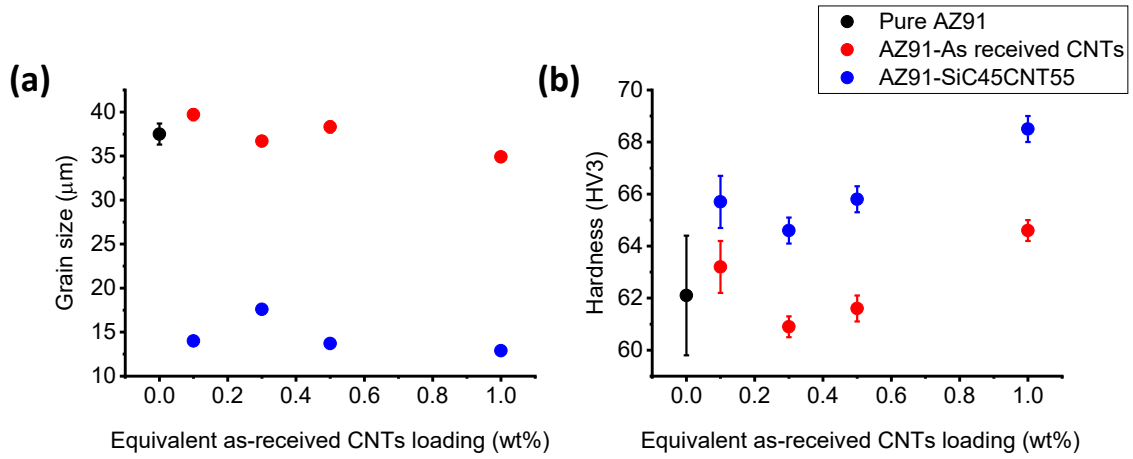


Figure 6.18. (a) Grain size and (b) hardness comparison between the pure AZ91 and AZ91 composites reinforced with as-received CNTs and SiC45CNT55.

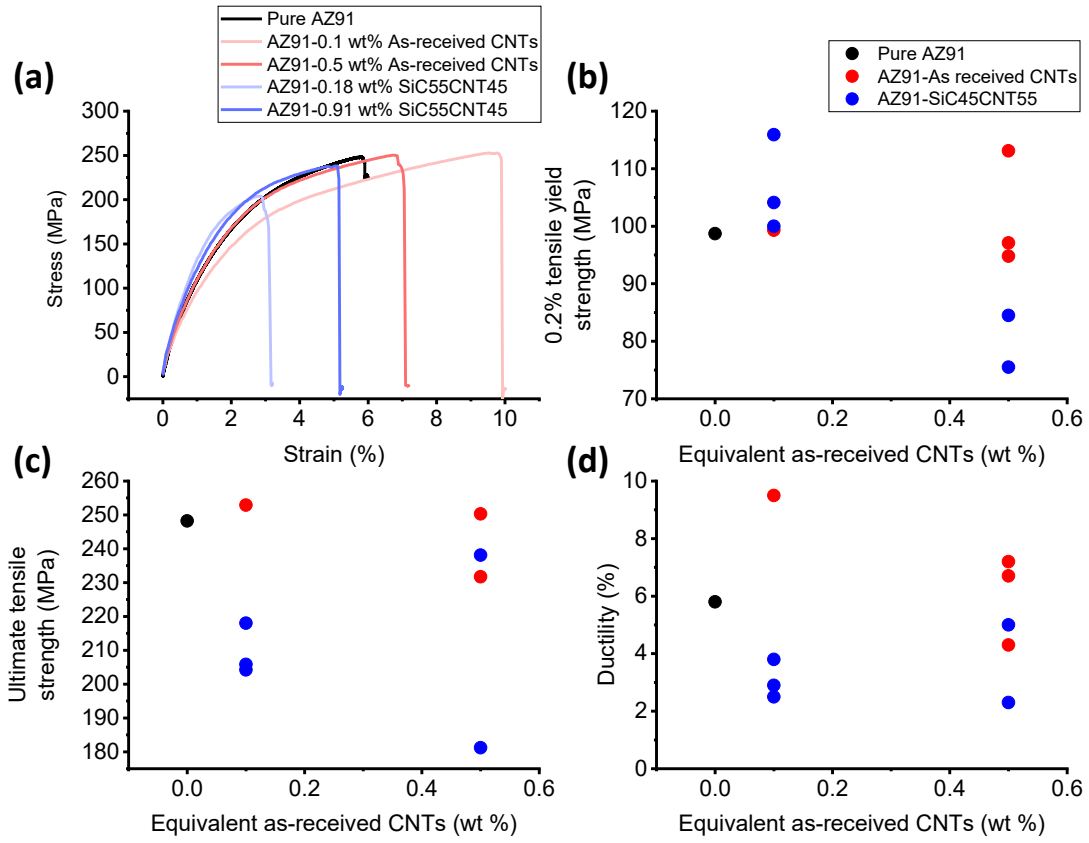


Figure 6.19. (a) Stress-strain curves, (b) 0.2% tensile yield strength, (c) ultimate tensile strength and (d) ductility of solution treated-hot rolled pure AZ91 and AZ91 composites reinforced with as-received CNTs and SiC45CNT55.

Next, the tensile properties of solution treated-hot rolled pure AZ91 and AZ91 composites reinforced with as-received CNTs and SiC45CNT55 are compared in Figure 6.19. As explained previously in Section 5.3.3, only a limited number of tensile specimens could be tested due to the defects caused by the hot rolling treatment on some of the specimens. Therefore, the tensile results in this study should also be treated as preliminary. Figure 6.19 (b) shows that the tensile yield strength of the AZ91-SiC45CNT55 composite was slightly higher than that of the AZ91-As received CNTs composite at the lowest loading (i.e. 0.1 wt%) but it was notably decreased when the SiC45CNT55 loading was increased to 0.5 wt%. On the other hand, the AZ91-SiC45CNT55 composite also exhibited lower ultimate tensile strength and ductility in comparison with the AZ91-As received CNTs composite as shown in Figure 6.19 (c) and (d). Finally, the Young's modulus of the AZ91-SiC45CNT55 composite was found to be higher than that of the pure AZ91 and AZ91-As received CNTs composite. Based on the grain structure of the composites in Figure 6.17, the presence of cracks in the AZ91-SiC45CNT55 composites could have probably explained for the poorer tensile properties of the composites. Therefore, a better quality of hot rolling specimens in a higher amount need to be produced in the future in order to obtain a more reliable tensile properties result.

Table 6.7. Compressive properties of solution treated-naturally aged pure AZ91 and AZ91 composites reinforced with as-received CNTs and SiC45CNT55.

Sample	Young's modulus (GPa)	0.2% compressive yield strength (MPa)	Ultimate compressive strength (MPa)	Compression at failure (%)
Pure AZ91	27.6 ± 1.8	97.6 ± 0.8	440.2 ± 1.3	20.1 ± 0.8
AZ91-0.10 wt% As received CNTs	32.0 ± 2.5	102.1 ± 4.1	446.3 ± 4.3	20.1 ± 0.7
AZ91-0.30 wt% As received CNTs	43.0 ± 5.3	85.7 ± 2.9	442.2 ± 7.7	20.2 ± 1.2
AZ91-0.50 wt% As received CNTs	29.7 ± 3.4	95.8 ± 3.9	429.1 ± 8.4	19.0 ± 1.0
AZ91-1.00 wt% As received CNTs	33.6 ± 4.2	92.2 ± 4.3	421.7 ± 13.3	19.4 ± 0.7
AZ91-0.18 wt% SiC45CNT55	32.7 ± 5.2	107.6 ± 4.3	447.2 ± 3.1	19.9 ± 0.5
AZ91-0.55 wt% SiC45CNT55	32.9 ± 3.8	105.0 ± 4.0	441.1 ± 4.9	18.6 ± 1.0
AZ91-0.91 wt% SiC45CNT55	28.5 ± 2.7	106.4 ± 3.9	438.8 ± 4.1	19.8 ± 0.8
AZ91-1.82 wt% SiC45CNT55	36.7 ± 7.4	111.7 ± 3.2	444.9 ± 4.3	17.8 ± 0.6

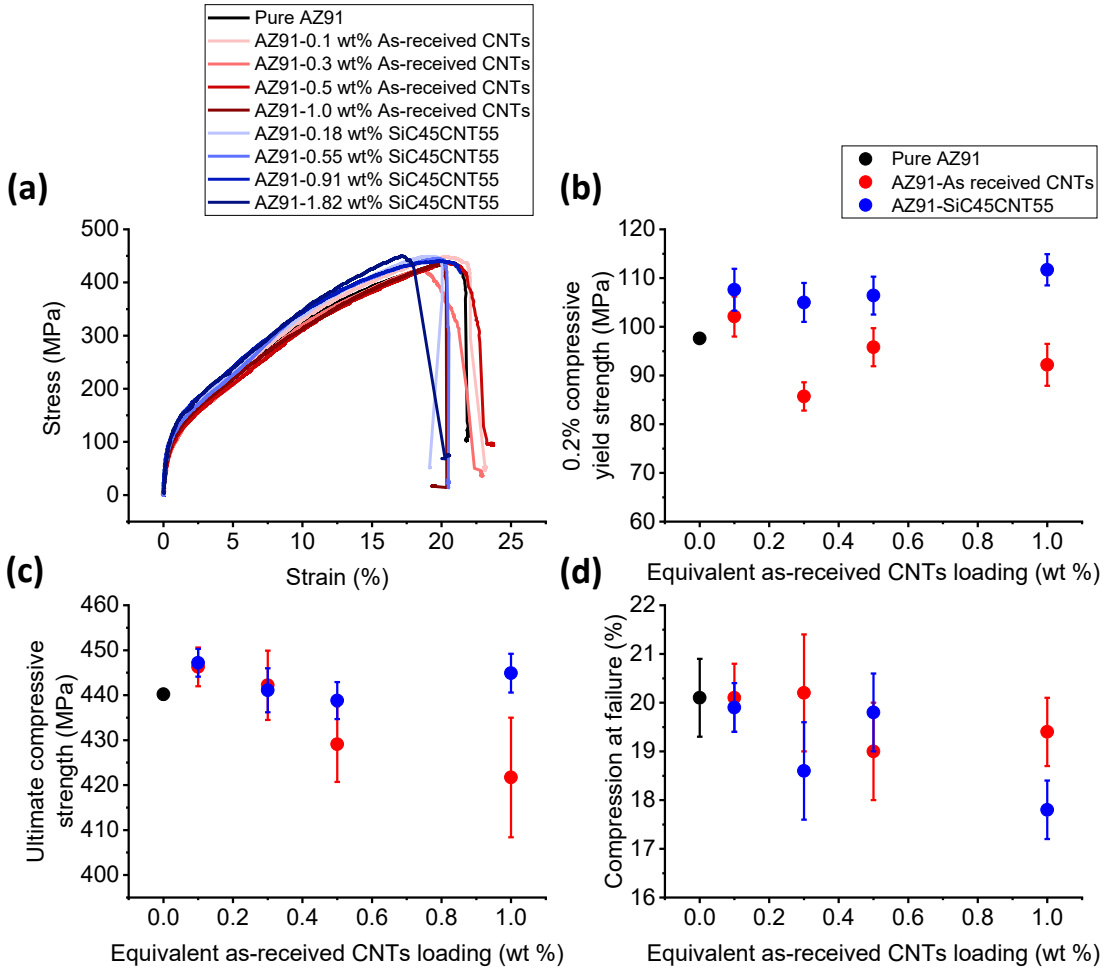


Figure 6.20. (a) Stress-strain curves, (b) 0.2% compressive yield strength, (c) ultimate compressive strength and (d) compression at failure of solution treated-naturally aged pure AZ91 and AZ91 composites reinforced with as-received CNTs and SiOC55CNT45.

Next, compression testing was performed on the solution treated-naturally aged samples and the results are presented in Table 6.7. As shown in Figure 6.20 (b), the yield strength of the AZ91-SiC45CNT55 composite was found to be higher than that of the AZ91-As received CNTs composite at each equivalent as-received CNTs loading. Furthermore, the increase in CNTs loading had also led to the increase in the yield strength of the AZ91-SiC45CNT55 composite whereas the opposite trend was observed for the AZ91-As received CNTs composite. On the other hand, Figure 6.20 (c) shows no improvement in the ultimate strength of the AZ91-SiC45CNT55 composite in comparison to the pure AZ91. However, the strength

of the AZ91-SiC45CNT55 composite did not appear to be affected by the increase in CNTs loading unlike the AZ91-As received CNTs composite which showed a notable reduction in strength as the CNTs loading was increased. As shown previously in Figure 5.31 (b), the decrease in the strength of the AZ91-As received CNTs composite could be strongly correlated to the increase in porosity as the CNTs loading was increased. On the contrary, as shown in Figure 6.21, the strength the AZ91-SiC45CNT55 composite was only moderately affected by the porosity in the sample. Next, the compression of failure of the AZ91-SiC45CNT55 composite was also found to decrease as the CNTs loading was increased as shown in Figure 6.20 (d). Finally, no obvious trend can be deduced from the Young's modulus of the composites.

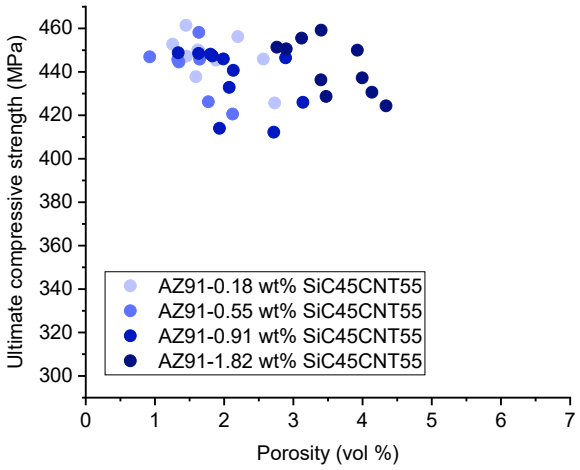


Figure 6.21. Scatter plot showing the relationship between porosity and ultimate compressive strength of the solution treated-naturally aged AZ91-SiC45CNT55.

The fracture surface of AZ91-SiC45CNT55 composite following the compression test was further investigated with SEM as shown in Figure 6.22. For comparison, the fracture surface of AZ91-As received CNTs composite can be found in Figure 5.32 (a) and (b). As shown in Figure 6.22 (a), coated CNTs agglomerates were frequently found within the pores of the AZ91-SiC45CNT55 composite unlike in the AZ91-As received CNTs composite where CNTs

were rarely found and only MgO was observed (see Figure 5.32 (a)). This observation seems to indicate that the aggregated coated CNTs agglomerates could not be effectively infiltrated by the matrix which led to the formation of porosity. Nevertheless, individual CNTs had been found embedded on the fracture surface as shown in Figure 6.22 (b) to (d) which highlights the potential of the coated CNTs to be successfully wetted by the matrix.

The addition of SiC coated CNTs was able to show a few improvements in the distribution and wettability of the CNTs therefore resulting in the improvement of the mechanical properties of the composites. The reduction in grain size and improvement in hardness observed in the AZ91-SiC45CNT55 composite in comparison to the AZ91-As received CNTs suggest that a higher distribution of CNTs in the AZ91 matrix could be achieved due to the presence of SiC coating. The improvement in the yield strength of AZ91-SiC45CNT55 composite as the CNTs loading was increased could also be attributed to the SiC coating as evident from the coated CNTs found on the fracture surface of the composite which led to the strengthening of the composite to occur via load transfer. However, although the SiC coated CNTs were much better wetted by the AZ91 matrix than the as-received CNTs, the presence of coated CNTs agglomerates would ultimately lead to an ineffective wetting by the matrix due to the difficulty of the melt to infiltrate through the CNTs network. Consequently, this behaviour would lead to the formation of pores as seen on the fracture surfaces which were likely to become sources for crack initiation therefore resulting in the lack of improvement in ultimate strength and the decrease in compression at failure.

A few similarities and differences could be found from the fabrication of AZ91-SiC45CNT55 composites in this chapter and the AZ91-SiOC55CNT45 composites in the previous chapter. Firstly, the presence of either SiOC or SiC coating was able to improve the wettability of CNTs

by the AZ91 matrix as it was immediately observed during casting where the SiOC55CNT45 and SiC45CNT55 could be fully incorporated in the melt while the as-received CNTs were rejected by the melt. The addition of SiOC55CNT45 and SiC45CNT55 had also led to a notable grain refinement in the AZ91 matrix and increase in hardness in comparison to the pure AZ91 and AZ91-As received CNTs composites. These findings can be attributed to the improvement in the wettability and distribution of CNTs due to the coating. Furthermore, the AZ91-SiC45CNT55 composites had shown slightly smaller grain size (between 12.9 to 14.0 μm) and lower hardness (between 64.6 to 68.5 HV3) than the AZ91-SiOC55CNT45 composites (14.3-24.2 μm for grain size and 68.5-72.6 HV3 for hardness). Further investigation needs to be carried out in the future, for example by analysing the microstructure of the naturally aged-hot rolled samples, to investigate the difference in the behaviour of the coated CNTs with the matrix. Then, the improvement in the yield strength was observed in both composites as the CNTs loading was increased. On the other hand, the yield strength of the AZ91-As received CNTs was found to deteriorate with the increase in the CNTs loading. Coupled with the observation of the wetted CNTs found on the fracture surface of the composites, the improvement in the yield strength of the composites can be attributed to the successful interfacial bonding between the coated CNTs and the AZ91 matrix which allows for stress transfer to occur. However, the presence of agglomerates in the SiOC55CNT45 and SiC45CNT55 samples had led to the formation of porosity in the composites therefore resulting in the deterioration of the ultimate strength and ductility of the composites as the CNTs loading was increased. Nevertheless, this finding indicates that further improvement to the AZ91 composites can still be achieved by improving the coating morphology of the CNTs and the distribution of the coated CNTs in the matrix.

The characterisation of the coating morphology in the SiOC55CNT45 and SiC45CNT55 samples shows that the SiOC and SiC coating tends to be formed over the CNTs agglomerates which could have probably contributed in the difficulty to disperse and distribute the CNTs homogeneously. Furthermore, while only SiOC coating was observed on the CNTs in the SiOC55CNT45 sample, the SiC45CNT55 sample was found to consist of several different morphologies such as the presence of dense SiOC-CNTs and SiC whiskers which disrupt the integrity of the SiC coated CNTs sample. Therefore, further considerations should be given to improve the quality of the SiC45CNT55 sample, for example by extending the duration of pyrolysis, so that only SiC coated CNTs would be produced. Otherwise, it is probably more desirable to focus on the fabrication of AZ91-SiOC coated CNTs composites since the production of the SiOC coated CNTs is more feasible due to the lower pyrolysis temperature and the SiOC coating can be sufficiently wetted by the matrix.

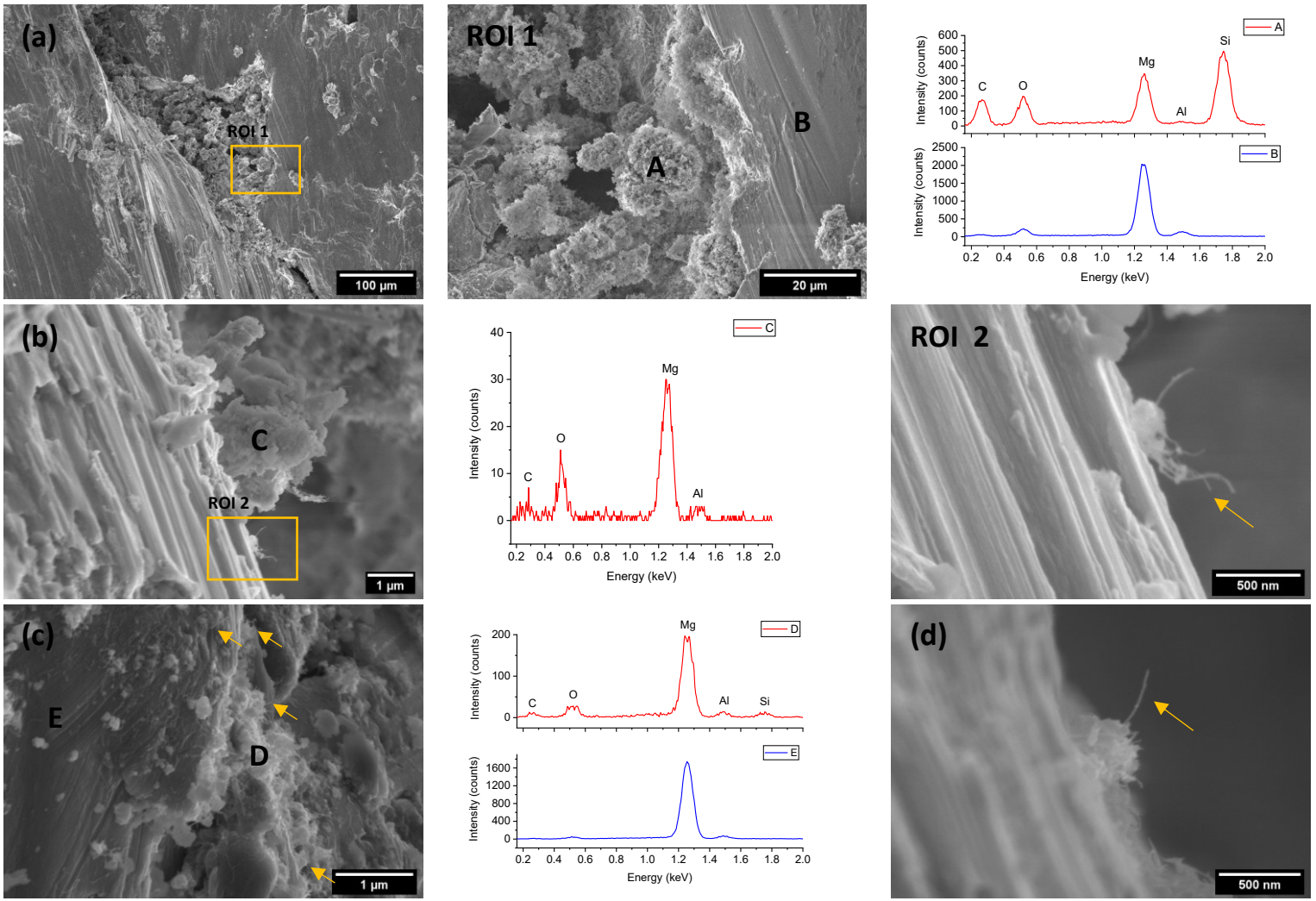


Figure 6.22. SEM images showing the fracture surface of AZ91 composites reinforced SiOC45CNT55 after compression test. Point EDX measurement was performed at the locations marked by the letters A-E in the SEM images. Individual CNTs found on the fracture surface are denoted by the yellow arrows.

6.4 Conclusions

SiC coated CNTs samples consisting of 24.8 to 58.3 wt% of SiC coating concentration were produced from the starting PMHS concentration of 10/1 to 50/1 PMHS/CNTs weight to weight ratio. Similar to the SiOC coated CNTs, the SiC coating was prone to form over the agglomerated CNTs network instead of the individual CNTs. Furthermore, the SiC coating precipitate appeared to grow in a cylindrical manner along the tangled CNTs as the coating concentration was increased. However, at the highest coating concentration of 56 wt%, a large amount of dense SiOC-CNTs products was observed in the sample such that only a small amount of SiC was detected from the XRD measurement which may indicate that the rate of conversion from SiOC to SiC was lowered as the coating concentration becomes larger. Next, the investigation of the SiC coated CNTs dispersions showed that the SiC coating can help to promote the debundling of the CNTs such that the size of the of the CNTs agglomerates could be considerably reduced as the coating concentration was increased. However, the dispersibility of CNTs with 53 wt% of coating concentration and above appeared to be worse than the dispersibility of the as-received CNTs due to the increased formation of the dense SiOC-CNTs products in the samples. The best dispersion was achieved for the SiC45CNT55 which showed relatively smaller agglomerate size than the as-received CNTs and the highest degree of individually dispersed CNTs across all samples.

Next, the effect of CNTs coating on the properties of the AZ91 composite was investigated. At the lowest SiC coating concentration of 25 wt%, the coated CNTs could not be sufficiently wetted by the matrix which had led to the CNTs being pushed out of the casting. On the other hand, at the highest coating concentration of 56 wt%, the porosity level in the composite was slightly increased due to the ineffective wetting of the dense SiOC-CNTs aggregates.

Therefore, based on the dispersion and composite studies, SiC45CNT55 was determined to have the most suitable SiC coating concentration among all the SiC coated CNTs samples. Finally, the investigation of the effect of CNTs loading on the properties of the AZ91 composites showed that a considerable grain refinement and improvement in hardness were observed in the AZ91-SiC45CNT55 composite in comparison to the AZ91-As received CNTs composite at each equivalent as-received CNTs loading suggesting that the distribution of CNTs in the matrix had been considerably improved due to the presence of SiC coating. Furthermore, the yield strength of the AZ91-SiC45CNT55 composite was also found to be notably higher than that of the AZ91-As received CNTs composite and increased with the increase in CNTs loading. The improvement in the yield strength of the AZ91-SiC45CNT55 composite was most likely attributed to the SiC coating which enable the CNTs to be wetted by the matrix. However, the presence of the coated CNTs agglomerates had led to the difficulty in the infiltration and wetting of the CNTs therefore resulting in the lack of improvement in the ultimate strength and the decrease in the compression at failure. The results from the investigation of the AZ91 composites reinforced with SiOC coated CNTs and SiC coated CNTs highlights the importance of the distribution of the CNTs which should be further optimised in future work so that further improvement can be achieved in the mechanical properties of the composites.

Chapter 7 : Conclusions and future work

In this thesis, a novel technique for coating either SiOC or SiC on the CNTs using a polysiloxane precursor was developed to enhance the properties of AZ91 composites by increasing the distribution of CNTs in the metal matrix and improving the wettability of the CNTs by the matrix.

Initially, the process for coating the CNTs with the polymethylhydrosiloxane (PMHS) precursor was developed. The curing and pyrolysis processes for transforming the PMHS to SiOC and SiC were established. A simple, catalyst-free curing procedure via the heat treatment in air was determined using the DSC analyses to achieve a 100% degree of cure of PMHS and a curing yield of 87.1 %. Next, the ceramisation of the crosslinked PMHS to SiOC and SiC was successfully performed via pyrolysis at 900 and 1500 °C, respectively, in Ar atmosphere to produce a ceramic yield of 64.9 ± 2.2 and 57.0 ± 1.9 %, respectively. The SiOC product was found to consist predominantly of SiOC and SiO_2 phases; meanwhile, the SiC product consisted of crystalline SiC dispersed with some SiO_2 phase. Subsequently, the application of PMHS as a precursor for SiOC or SiC coating on the CNTs was investigated through a preliminary production of SiOC coated CNTs. SiOC coated CNTs produced from a low range of starting PMHS concentration (i.e. 0.5/1 to 6/1 PMHS/CNTs w/w) was found to consist of a variety of coating morphologies. The deposition of SiOC coating on the CNTs agglomerate can be explained by the tendency of the polymer to adhere on the interconnected CNTs due to wicking effect; meanwhile, the formation of discontinuous SiOC coating on the individual

tubes was most likely due to the tendency of the liquid polymer to form clam-shell and barrel-type droplet on tubular structures. Finally, the investigation of the decomposition behaviour of crosslinked PMHS-CNTs during pyrolysis revealed that the PMHS-CNTs experienced an increased rate of decomposition which led to a substantial decrease in the resulting SiOC concentration. This behaviour can be explained by the catalytic effect of CNTs which accelerated the decomposition of the polymer during pyrolysis.

SiOC coated CNTs were then produced in a wider range of SiOC concentrations to investigate the effect of SiOC coating on the morphology and dispersibility of CNTs, and subsequently the properties of the AZ91 composites. At a low SiOC concentration of 22 wt%, only a small deposition of SiOC coating could be observed on the CNTs agglomerates meanwhile no coating was found on the individual tubes. Large CNTs agglomerates were predominantly observed in the dispersion of the coated CNTs, but the presence of coating seemed to have also increased the amount of individually dispersed CNTs. However, the coating concentration was found to be too low to achieve a desirable wetting by the AZ91 matrix as the addition of the coated CNTs had led to the rejection of the CNTs powder by the melt during casting and the increase in porosity in the composite. On the other hand, at a high SiOC concentration of 77 wt%, predominantly dense SiOC-CNTs products were observed in the sample. Consequently, this type of morphology caused the dispersibility of the CNTs to be reduced. Furthermore, the dense SiOC-CNTs products were found to be aggregated in the composite which then led to the increased formation of porosity due to inefficient wetting by the matrix. From these studies, the CNTs with 55 wt% of SiOC concentration (i.e. SiOC55CNT45) was determined to be suitable for further investigation in the fabrication of AZ91-SiOC coated CNTs composites. The addition of SiOC55CNT45 to the AZ91 matrix led to a notable grain refinement (by up to 62% in grain size reduction) and a higher hardness (by up to 17%) in comparison to the pure

AZ91 alloy which can be attributed to the increase in the distribution of CNTs in the matrix due to the presence of SiOC coating. The yield strength of the composite was also found to increase notably by 0.5 to 15 % relative to the pure AZ91 as the CNTs loading was increased from 0.22 to 2.22 wt%. This improvement was attributed to the successful wetting of individually coated CNTs in the metal matrix as evident from the fracture surface analysis. Meanwhile, the addition of the as-received CNTs had led to decrease of the yield strength of the composite by 12% due to a poor wetting of the CNTs by the matrix. However, the addition of the SiOC coated CNTs had also led to the decrease in the ultimate strength and compression at failure/ductility of the composite as the CNTs loading was increased. This behaviour had been attributed to the increase in the porosity of the composite as a result of the inefficient wetting of some agglomerated SiOC coated CNTs by the matrix. Therefore, further optimisation needs to be carried out in the future to diminish the presence of agglomerated CNTs in the coated CNTs samples and to improve the distribution of the coated CNTs in the melt during stir casting.

Finally, the types of morphologies formed in the production of SiC coated CNTs and their effects on the dispersibility of the CNTs and the properties of AZ91 matrix were investigated. At a low coating concentration of 25 wt%, a small amount of SiC was found to be precipitated on the CNTs agglomerate on a cylindrical manner meanwhile no coating layer had been observed on the individual CNTs. The coated CNTs, however, was found to be insufficient to promote the wetting of the CNTs by the AZ91 melt. On the other hand, at the coating concentration of 45 wt%, several types of morphologies could be found in the coated CNTs samples. Other than the SiC coating on the CNTs agglomerates, the sample was also found to consist of a slightly higher amount of SiC whiskers and a small amount of dense SiOC-CNTs products. At the coating concentration of 56 wt%, the coated CNTs sample was found to consist

predominantly of dense SiOC-CNTs products while the XRD measurement showed that only a small amount of SiC was detected in the sample. Consequently, the increased formation of dense SiOC-CNTs products had also led to the reduction in the dispersibility of the CNTs and an increased formation of porosity in the composite due to an ineffective wetting of the aggregates. Based on these findings, the coated CNTs with 45 wt% coating concentration (i.e. SiC45CNT55) was determined to be suitable for the subsequent composite fabrication study. Similar to the previous AZ91-SiOC55CNT45 composites, the addition of SiC45CNT55 was able to give a remarkable reduction in grain size (up to 66 %) and increase in hardness (by up to 10.3 %) in the composite in comparison the pure AZ91 alloy. The compressive yield strength of the composite was also improved between 10.2 to 14.4 % as the CNTs loading was increased from 0.18 to 1.82 % which was attributed to the coated CNTs that had been sufficiently wetted by the matrix. However, agglomeration of the coated CNTs had also seemed to cause a slight decrease in the ultimate compression strength and compression at failure as the CNTs loading was increased. Similar considerations as the SiOC coated CNTs should be applied in future work in order to achieve a better dispersion and distribution of the coated CNTs in the matrix which can potentially lead to a more effective strengthening of the matrix.

Even though SiOC coated CNTs and SiC coated CNTs had similar effects in the mechanical properties of the composites, the use of SiOC coated CNTs may offer several advantages in the fabrication of the AZ91 composites over the SiC coated CNTs based on the current results. Firstly, the production of the SiOC coated CNTs is a more feasible process since a much lower pyrolysis temperature can be used (i.e. 900 °C for SiOC coated CNTs vs. 1500 °C for SiC coated CNTs) therefore making it more attractive especially for large scale production. Furthermore, while only SiOC products was observed in the SiOC coated CNTs, the SiC coated CNTs consisted of several different morphologies including SiC whiskers and dense SiOC-

CNTs which challenges the integrity of the coating material. Finally, coating had not been observed on the individual CNTs in the SiC coated CNTs samples which can probably be due to the loss of coating material during the ceramisation process. On the contrary, individual CNTs in the SiOC coated CNTs was found to be coated with a discontinuous coating layer.

In comparison to the literature works, the effect of CNTs coating on the dispersibility and wettability of the CNTs, and the properties of the Mg composites had been more extensively studied in this work. Furthermore, a more careful research design had also been established by ensuring that the coating concentration was considered in the CNTs loading so that a more accurate comparison could be made between the AZ91-As received CNTs and AZ91-coated CNTs composites. Similar to this work, the deterioration of the composites at a higher CNTs loading had also been attributed to the agglomeration of the coated CNTs as reported in the literature works. However, it is unclear why agglomeration had been observed for their coated CNTs and what strategies can be applied to overcome the issue. Meanwhile, in this work, the agglomeration of the SiOC and SiC coated CNTs had been identified due to a combination of unoptimised coating on the CNTs because of the natural wetting behaviour of the polymer on the CNTs, and a lack of effective distribution of the coated CNTs in the metal melt. Therefore, several strategies are recommended for future work:

1. **Investigation of the effect of CNTs on the decomposition behaviour of the crosslinked PMHS**

   As described in Section 4.3.4, the increased rate of decomposition for crosslinked PMHS-CNTs during pyrolysis had led to a substantial reduction in the resulting SiOC concentration in the CNTs sample. Since the metal residue in the CNTs were postulated to catalyse the decomposition of PMHS, further studies should be done to confirm this hypothesis for example by using other commercial CNTs with lower metal residue [70] or

by the purification of the current as-received CNTs used [257]. Consequently, the investigation of this issue could probably lead to the improvement in the resulting coating concentration and therefore the coating morphology of the coated CNTs.

2. **Optimisation of PMHS coating on the CNTs**

   Due to the tendency of the polymer to adhere on the CNTs agglomerates, a better CNTs dispersion should be produced by optimising the sonication parameters to further promote the debundling of the CNTs agglomerates. Simultaneously, the mixing of PMHS with CNTs should also be improved from the current technique by sonicating the PMHS and CNTs together at an extended duration to allow the polymer to interact with the CNTs more effectively. Alternatively, surface treatment of the CNTs can also be considered prior to the mixing with the polysiloxane [258, 259] to promote the functionalisation of the polymer on the CNTs therefore producing a more homogeneous coating on the individual tubes.

3. **Optimisation of CNTs dispersion technique in the AZ91 melt**

   The current melt stirring process can be further optimised to ensure that the nanoparticles can be more homogeneously distributed in the CNTs for example by simply increasing the stirring duration of the melt. Alternatively, ultrasonic processing can also be applied in the future for a more enhanced dipersion and distribution of CNTs in the metal melt [99, 100, 102].

4. **Comparison with other reference materials**

   To further confirm for the strengthening of the composites due to the CNTs reinforcements, a few other reference materials could also be fabricated for example by only adding the SiOC or SiC particles in the AZ91 or by using SiOC/SiC coated carbon black as reinforcements.

Appendix

A.1 Temperature profile of tube furnace

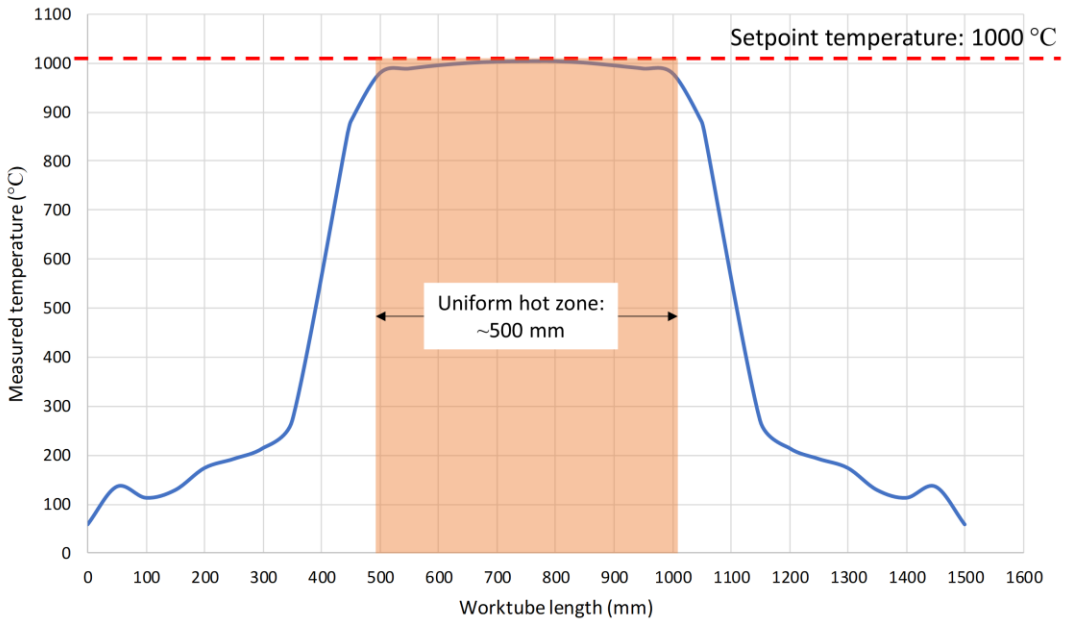


Figure A.1. Temperature profile inside the work tube (with insulation plugs fitted) as measured by an external thermocouple showing the uniform hot zone relative to the length of the work tube.

A.2 Crucible design

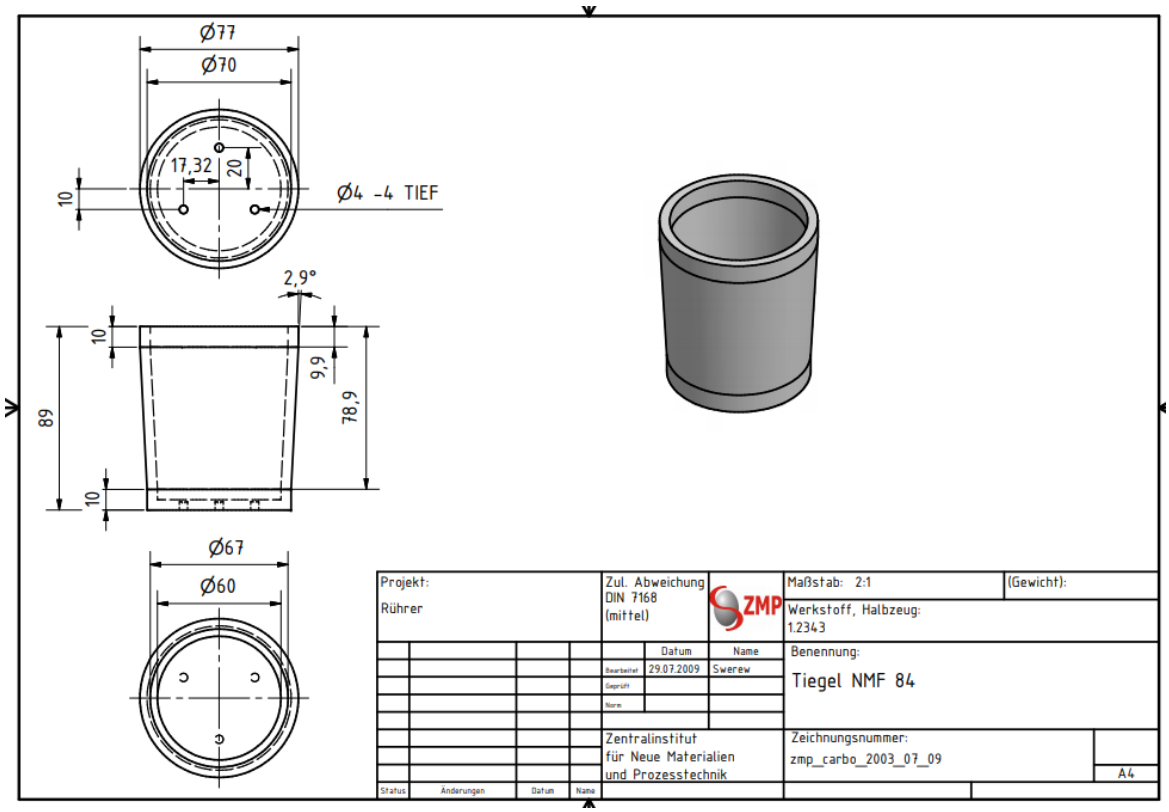


Figure A.2. Design of the H13 tool steel crucible used in the stir casting process.

A.3 Stirrer design

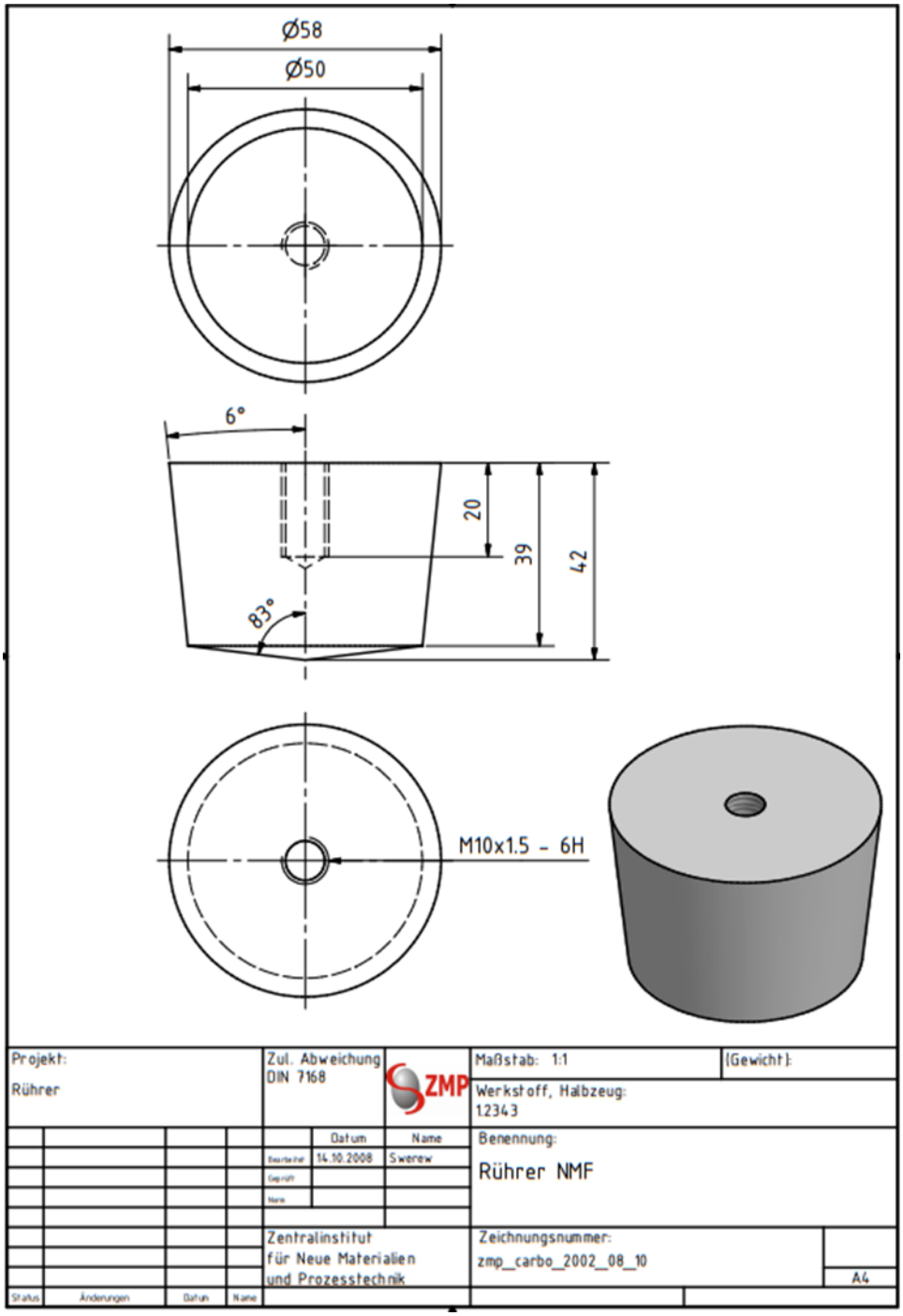


Figure A.3. Design of the S235 steel stirrer head used in the stir casting process.

A.4 Mould design

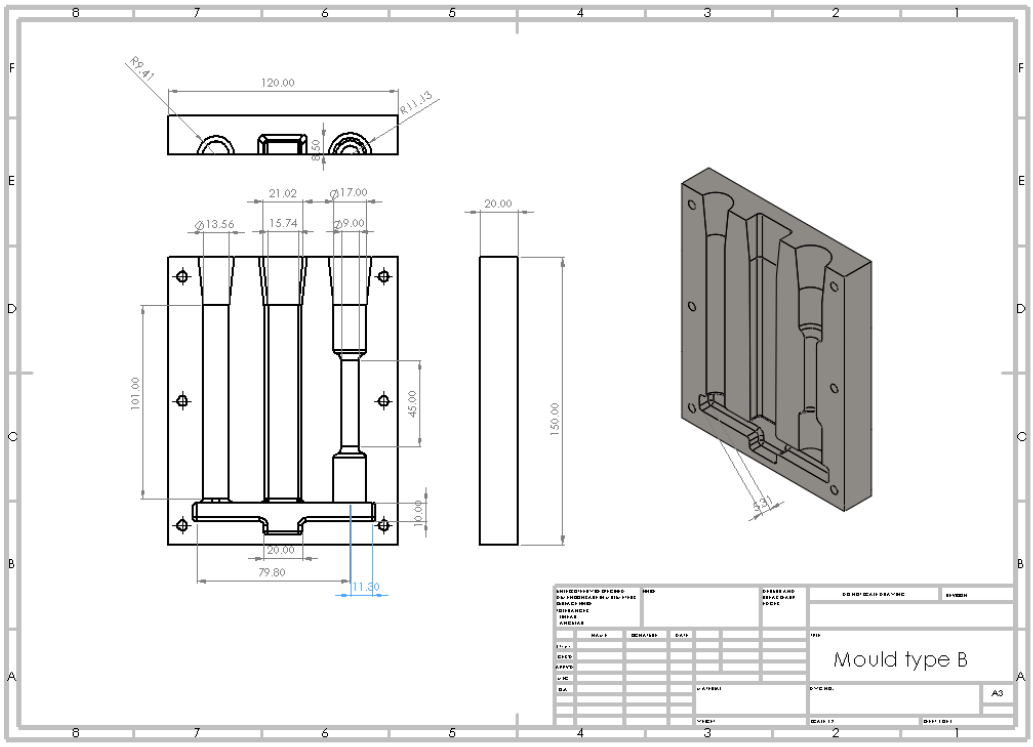


Figure A.4. Design of the permanent steel mould used in the stir casting process.

A.5 Al-Mg phase diagram

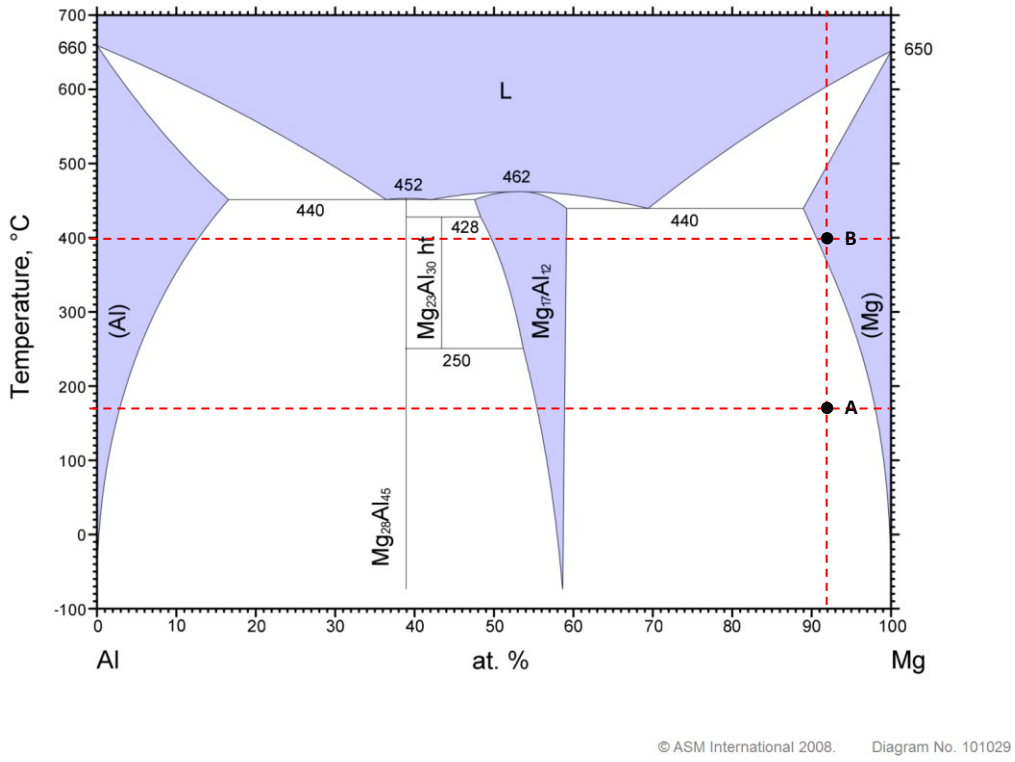


Figure A.5. Al-Mg phase diagram. The dotted line indicates the Mg-Al composition of the Mg AZ91 alloy used in this work. A and B points mark the temperatures typically used for the ageing and solution heat treatments, respectively. Image reproduced from [260].

A.6 Tensile test specimen configuration

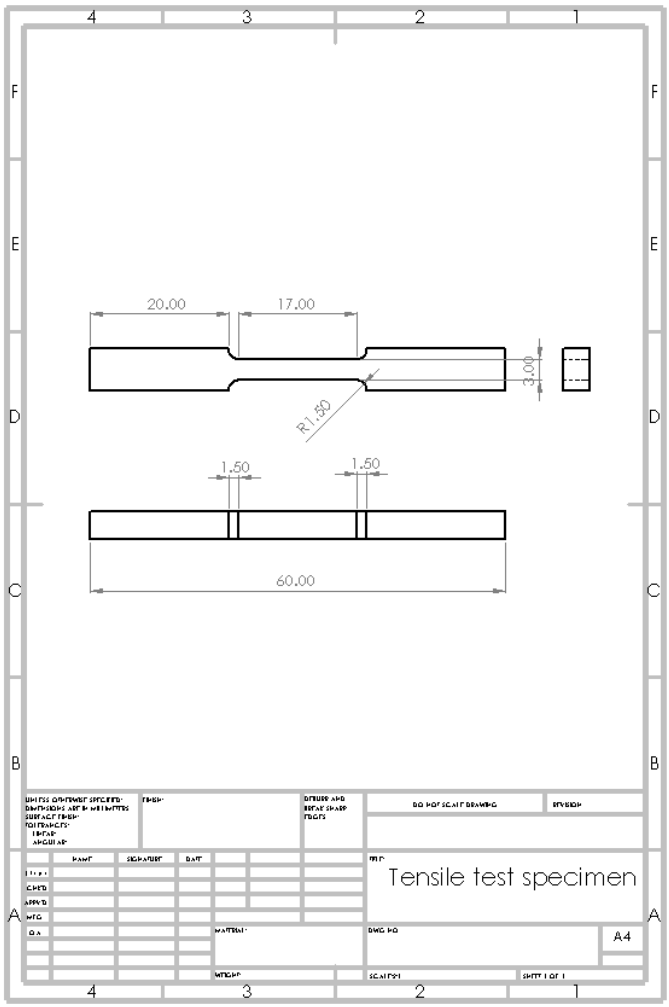


Figure A.6. Configuration of tensile test specimen.

A.7 Determination of optimum curing temperature(s) and duration

Step 1: Heat treatment of PMHS in air at 160 °C for t min. Note: this temperature was selected based on the onset temperature of the first exothermic peak in the DSC measurement of as-received PMHS in air as shown in Figure A.7.

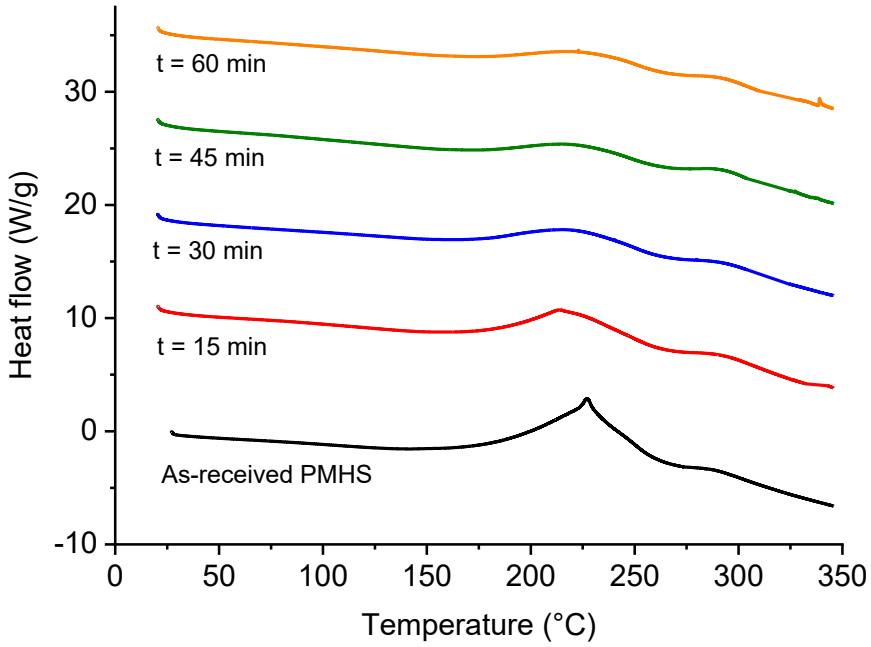


Figure A.7. DSC curves of PMHS samples which had been subjected to a heat treatment in air at 160 °C for t min.

Table A.1. Degree of cure measurement of PMHS based on Figure A.7 after heat treatment in air at 160 °C for t min. The maximum curing time and the new onset temperature of the remaining exothermic peak are highlighted in bold.

t (min)	Onset temperature (°C)	Heat of reaction, H_S (J/g)	Degree of cure (%)
15	171.5	996.6	32.8
30	168.0	738.8	50.2
45	**172.2**	**503.4**	**66.0**
60	173.0	509.79	65.6

Result: The maximum degree of cure (i.e. 66%) was obtained after heating the polymer at 160 °C for 45 min. The heating was continued at the new onset temperature of the remaining exothermic peak (i.e. 170 °C) in the next step to obtain a higher degree of cure.

Step 2: Heat treatment of PMHS in air at 160 °C for 45 min and 170 °C for t min

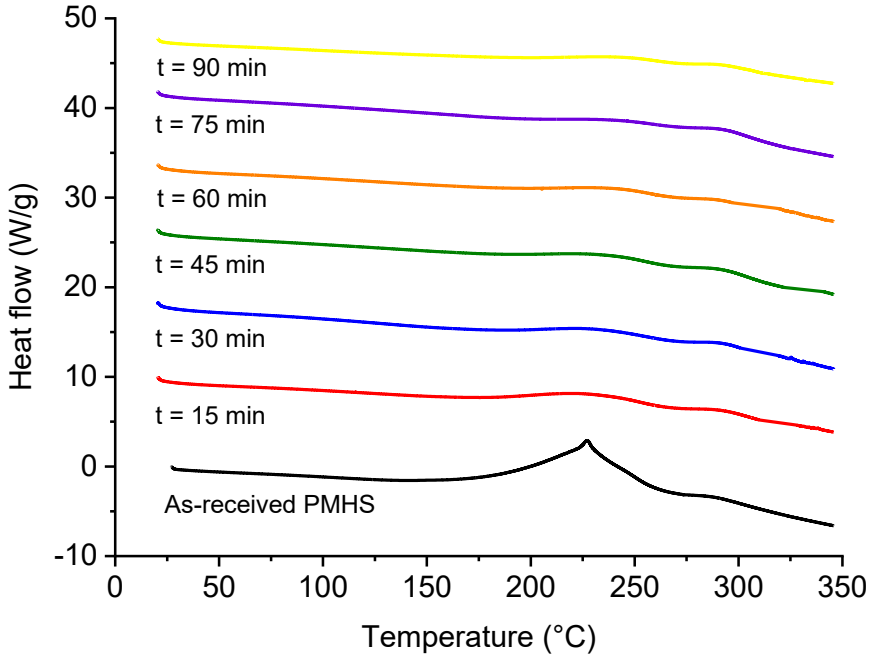


Figure A.8. DSC curves of PMHS samples which had been subjected to a heat treatment in air at 160 °C for 45 min and 170 °C for t min.

Table A.2. Degree of cure measurement of PMHS based on Figure A.8 after heat treatment in air at 160 °C for 45 min and 170 °C for t min. The maximum curing time and the new onset temperature of the remaining exothermic peak are highlighted in bold.

t (min)	**Onset temperature (°C)**	**Heat of reaction, H_S (J/g)**	**Degree of cure (%)**
15	174.5	448.7	69.7
30	176.7	292.2	80.3
45	177.0	345.3	76.7
60	187.8	208.8	85.9
75	**197.8**	**192.0**	**87.0**
90	194.1	187.7	87.3

Result: The maximum degree of cure (i.e. 87%) was obtained after heating the polymer at 160 °C for 45 min and 170 °C for 75 min. The heating was continued at the new onset temperature of the remaining exothermic peak (i.e. 190 °C) in the next step to obtain a higher degree of cure.

Step 3: Heat treatment of PMHS in air at 160 °C for 45 min, 170 °C for 75 min and 190 °C for t min

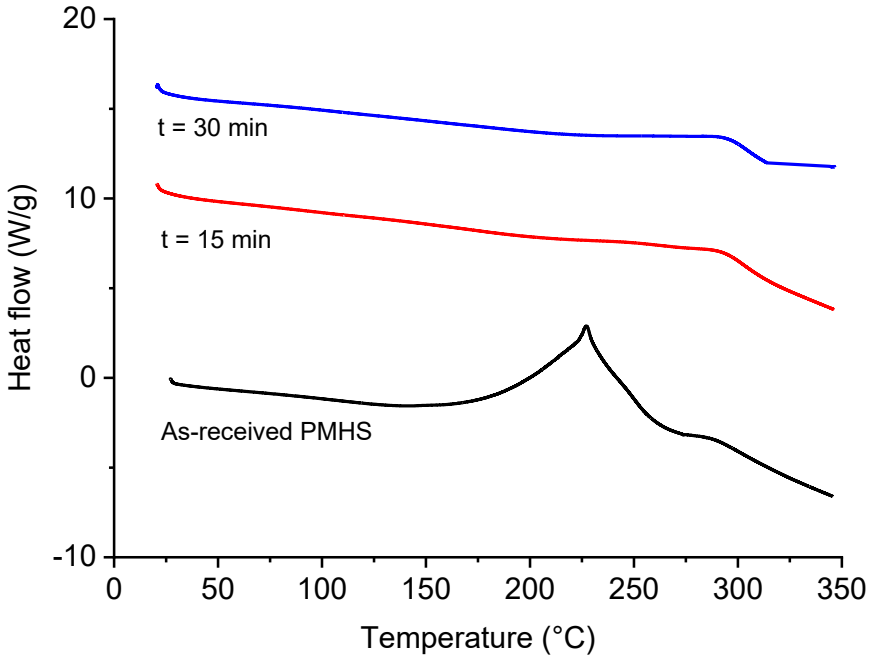


Figure A.9. DSC curves of PMHS samples which had been subjected to a heat treatment in air at 160 °C for 45 min, 170 °C for 75 min and 190 °C for t min.

Table A.3. Degree of cure measurement of PMHS based on Figure A.9 after heat treatment in air at 160 °C for 45 min, 170 °C for 75 min and 190 °C for t min. The maximum curing time and the new onset temperature of the remaining exothermic peak are highlighted in bold.

t (min)	Onset temperature (°C)	Heat of reaction, H_S (J/g)	Degree of cure (%)
15	218.7	86.3	94.2
30	**213.7**	**70.4**	**95.3**

Result: The maximum degree of cure (i.e. 95%) was obtained after heating the polymer at 160 °C for 45 min, 170 °C for 75 min and 190 °C for 30 min. The heating was continued at the new onset temperature of the remaining exothermic peak (i.e. 210 °C) in the next step to obtain a higher degree of cure.

Step 4: Heat treatment of PMHS in air at 160 °C for 45 min, 170 °C for 75 min, 190 °C for 30 min and 210 °C for t min

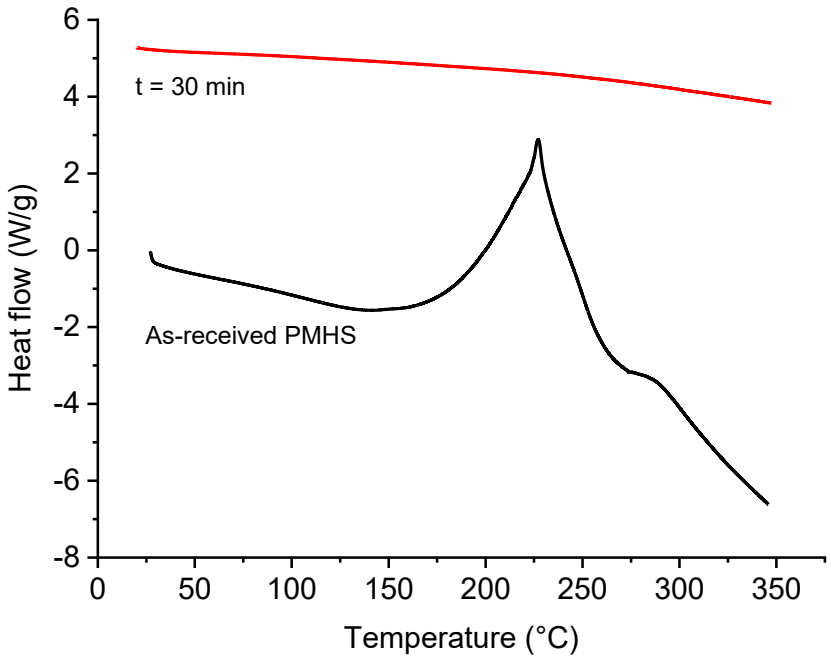


Figure A.10. DSC curves of PMHS samples which had been subjected to a heat treatment in air at 160 °C for 45 min, 170 °C for 75 min, 190 °C for 30 min and 210 °C for t min.

Table A.4. Degree of cure measurement of PMHS based on Figure A.10 after heat treatment in air at 160 °C for 45 min, 170 °C for 75 min, 190 °C for 30 min and 210 °C for t min The maximum curing time is highlighted in bold.

t (min)	Onset temperature (°C)	Heat of reaction, H_S (J/g)	Degree of cure (%)
30	**-**	**0**	**100**

Result: 100% degree of cure was obtained after heating the polymer at 160 °C for 45 min, 170 °C for 75 min, 190 °C for 30 min and 210 °C for 30 min. No remaining exothermic peaks was observed which indicates that a complete curing has been achieved.

A.8 Strategies to improve the ceramic yield of PMHS-CNTs samples

The established procedure for the production of SiOC and SiC coated CNTs is described in Section 3.2.1.1. The table below describes the modifications applied to the established procedure to improve the ceramic yield of PMHS-CNTs as discussed in Section 4.3.4.

Table A.5. Modifications of established SiOC and SiC coated CNTs produced to improve the ceramic yield of PMHS-CNTs samples.

Strategy	Curing procedure	Pyrolysis procedure
Closed crucible pyrolysis	As the established curing procedure	As the established pyrolysis procedure but with each crucible covered with a lid
Longer curing	Heat treatment in air at a heating rate of 5 °C/min from room temperature to 160 °C for 2 hr, 170 °C for 3 hr min, 190 °C for 1 hr and 210 °C for 1 hr, then cooling down to room temperature.	As the established pyrolysis procedure
Longer curing + increased Ar flow	Heat treatment in air at a heating rate of 5 °C/min from room temperature to 160 °C for 2 hr, 170 °C for 3 hr min, 190 °C for 1 hr and 210 °C for 1 hr, then cooling down to room temperature.	As the established pyrolysis procedure but at an Ar flow rate of 1.5 L/min
Lower pyrolysis heating rate	As the established curing procedure	As the established pyrolysis procedure but at a heating rate of 1 °C/min

References

[1] T. Hottle, C. Caffrey, J. McDonald, and R. Dodder, "Critical factors affecting life cycle assessments of material choice for vehicle mass reduction," *Transportation Research Part D: Transport and Environment,* vol. 56, pp. 241-257, 2017.

[2] R. S. Sims R., F. Creutzig, X. Cruz-Núñez, M. D'Agosto, D. Dimitriu, M. J. Figueroa Meza, L. Fulton, S. Kobayashi, O. Lah, A. McKinnon, P. Newman, M. Ouyang, J. J. Schauer, D. Sperling, and G. Tiwari, "Transport," *Climate Change 2014: Mitigation of Climate Change. Contribution of Working Group III to the Fifth Assessment Report of the Intergovernmental Panel on Climate Change,* 2014.

[3] A. Milovanoff, H. C. Kim, R. De Kleine, T. J. Wallington, I. D. Posen, and H. L. MacLean, "A Dynamic Fleet Model of U.S Light-Duty Vehicle Lightweighting and Associated Greenhouse Gas Emissions from 2016 to 2050," *Environmental Science & Technology,* vol. 53, no. 4, pp. 2199-2208, 2019/02/19 2019, doi: 10.1021/acs.est.8b04249.

[4] H. Helms and J. Krack, "Energy savings by light-weighting 2016 Update," International Aluminium Institute supported by European Aluminium, Heidelberg, Germany, 2016.

[5] E. Ordoukhanian and A. M. Madni, "Blended Wing Body Architecting and Design: Current Status and Future Prospects," *Procedia Computer Science,* vol. 28, pp. 619-625, 2014/01/01/ 2014, doi: https://doi.org/10.1016/j.procs.2014.03.075.

[6] M. Marino and R. Sabatini, "Advanced lightweight aircraft design configurations for green operations," presented at the Proceedings of the Practical Responses to Climate Change 2014, Barton, Australia, 2014.

[7] C. Blawert, N. Hort, and K. U. Kainer, "Automotive applications of magnesium and its alloys," (in English), *T Indian I Metals,* vol. 57, no. 4, pp. 397-408, Aug 2004. [Online]. Available: <Go to ISI>://WOS:000224580100009.

[8] T. Xu, Y. Yang, X. Peng, J. Song, and F. Pan, "Overview of advancement and development trend on magnesium alloy," *J Magnes Alloy,* vol. 7, no. 3, pp. 536-544, 2019/09/01/ 2019, doi: https://doi.org/10.1016/j.jma.2019.08.001.

[9] Y. Yang, X. Xiong, J. Chen, X. Peng, D. Chen, and F. Pan, "Research advances in magnesium and magnesium alloys worldwide in 2020," *J Magnes Alloy,* vol. 9, no. 3, pp. 705-747, 2021/05/15/ 2021, doi: https://doi.org/10.1016/j.jma.2021.04.001.

[10] M. Gupta and W. L. E. Wong, "Magnesium-based nanocomposites: Lightweight materials of the future," (in English), *Materials Characterization,* vol. 105, pp. 30-46, Jul 2015, doi: 10.1016/j.matchar.2015.04.015.

[11] M. K. Kulekci, "Magnesium and its alloys applications in automotive industry," (in English), *Int J Adv Manuf Tech,* vol. 39, no. 9-10, pp. 851-865, Nov 2008, doi: 10.1007/s00170-007-1279-2.

[12] A. A. Luo, "Magnesium casting technology for structural applications," *J Magnes Alloy,* vol. 1, no. 1, pp. 2-22, 2013/03/01/ 2013, doi: https://doi.org/10.1016/j.jma.2013.02.002.

[13] B. L. Mordike and T. Ebert, "Magnesium: Properties — applications — potential," *Materials Science and Engineering: A,* vol. 302, no. 1, pp. 37-45, 2001/04/15/ 2001, doi: https://doi.org/10.1016/S0921-5093(00)01351-4.

[14] M. K. Kulekci, "Magnesium and its alloys applications in automotive industry," *The International Journal of Advanced Manufacturing Technology,* vol. 39, no. 9-10, pp. 851-865, 2007, doi: 10.1007/s00170-007-1279-2.

[15] W. J. Joost and P. E. Krajewski, "Towards magnesium alloys for high-volume automotive applications," *Scripta Mater,* vol. 128, pp. 107-112, 2017/02/01/ 2017, doi: https://doi.org/10.1016/j.scriptamat.2016.07.035.

[16] A. Dey and K. M. Pandey, "MAGNESIUM METAL MATRIX COMPOSITES - A REVIEW," (in English), *Rev Adv Mater Sci,* Review vol. 42, no. 1, pp. 58-67, 2015. [Online]. Available: <Go to ISI>://WOS:000360110800007.

[17] H. Z. Ye and X. Y. Liu, "Review of recent studies in magnesium matrix composites," (in English), *Journal of Materials Science,* vol. 39, no. 20, pp. 6153-6171, Oct 15 2004, doi: Doi 10.1023/B:Jmsc.0000043583.47148.31.

[18] S. C. Tjong, "Recent progress in the development and properties of novel metal matrix nanocomposites reinforced with carbon nanotubes and graphene nanosheets," *Materials Science and Engineering: R: Reports,* vol. 74, no. 10, pp. 281-350, 2013, doi: 10.1016/j.mser.2013.08.001.

[19] R. K. Abu Al-Rub, A. I. Ashour, and B. M. Tyson, "On the aspect ratio effect of multi-walled carbon nanotube reinforcements on the mechanical properties of cementitious nanocomposites," *Construction and Building Materials,* vol. 35, pp. 647-655, 2012/10/01/ 2012, doi: https://doi.org/10.1016/j.conbuildmat.2012.04.086.

[20] J.-P. Salvetat *et al.*, "Elastic Modulus of Ordered and Disordered Multiwalled Carbon Nanotubes," *Adv Mater,* https://doi.org/10.1002/(SICI)1521-4095(199902)11:2<161::AID-ADMA161>3.0.CO;2-J vol. 11, no. 2, pp. 161-165, 1999/02/01 1999, doi: https://doi.org/10.1002/(SICI)1521-4095(199902)11:2<161::AID-ADMA161>3.0.CO;2-J.

[21] M. M. J. Treacy, T. W. Ebbesen, and J. M. Gibson, "Exceptionally high Young's modulus observed for individual carbon nanotubes," (in English), *Nature,* vol. 381, no. 6584, pp. 678-680, Jun 20 1996, doi: DOI 10.1038/381678a0.

[22] M. F. Yu, O. Lourie, M. J. Dyer, K. Moloni, T. F. Kelly, and R. S. Ruoff, "Strength and breaking mechanism of multiwalled carbon nanotubes under tensile load," (in English), *Science,* vol. 287, no. 5453, pp. 637-640, Jan 28 2000, doi: DOI 10.1126/science.287.5453.637.

[23] M.-F. Yu, B. S. Files, S. Arepalli, and R. S. Ruoff, "Tensile Loading of Ropes of Single Wall Carbon Nanotubes and their Mechanical Properties," *Physical Review Letters,* vol. 84, no. 24, pp. 5552-5555, 06/12/ 2000, doi: 10.1103/PhysRevLett.84.5552.

[24] E. W. Wong, P. E. Sheehan, and C. M. Lieber, "Nanobeam Mechanics: Elasticity, Strength, and Toughness of Nanorods and Nanotubes," *Science,* vol. 277, no. 5334, pp. 1971-1975, 1997/09/26 1997, doi: 10.1126/science.277.5334.1971.

[25] J.-P. Salvetat *et al.*, "Elastic and Shear Moduli of Single-Walled Carbon Nanotube Ropes," *Physical Review Letters,* vol. 82, no. 5, pp. 944-947, 02/01/ 1999, doi: 10.1103/PhysRevLett.82.944.

[26] B. G. Demczyk *et al.*, "Direct mechanical measurement of the tensile strength and elastic modulus of multiwalled carbon nanotubes," (in English), *Mat Sci Eng a-Struct,* vol. 334, no. 1-2, pp. 173-178, Sep 1 2002, doi: Pii S0921-5093(01)01807-X

Doi 10.1016/S0921-5093(01)01807-X.

[27] H. C. Kim and T. J. Wallington, "Life-Cycle Energy and Greenhouse Gas Emission Benefits of Lightweighting in Automobiles: Review and Harmonization," *Environmental Science & Technology,* vol. 47, no. 12, pp. 6089-6097, 2013/06/18 2013, doi: 10.1021/es3042115.

[28] F. E. Sato and T. Nakata, "Energy Consumption Analysis for Vehicle Production through a Material Flow Approach," *Energies*, vol. 13, no. 9, doi: 10.3390/en13092396.

[29] F. Czerwinski, "Current Trends in Automotive Lightweighting Strategies and Materials," *Materials*, vol. 14, no. 21, doi: 10.3390/ma14216631.

[30] D. Miracle, "Lightweighting and the Future of Aerospace Metals," in *Light Weighting for Defense, Aerospace, and Transportation*, A. A. Gokhale, N. E. Prasad, and B. Basu Eds. Singapore: Springer Singapore, 2019, pp. 27-38.

[31] W. Zhu, H. Fu, F. Li, X. Ji, Y. Li, and F. Bai, "Optimization of CFRP drilling process: a review," *The International Journal of Advanced Manufacturing Technology,* vol. 123, no. 5, pp. 1403-1432, 2022/11/01 2022, doi: 10.1007/s00170-022-10112-7.

[32] L. Zhu, N. Li, and P. R. N. Childs, "Light-weighting in aerospace component and system design," *Propulsion and Power Research,* vol. 7, no. 2, pp. 103-119, 2018/06/01/ 2018, doi: https://doi.org/10.1016/j.jppr.2018.04.001.

[33] I. Ostrovsky and Y. Henn, "Present state and future of magnesium application in aerospace industry," in *New challenges in aeronautics*, Moscow, Russia, 2007.

[34] V. V. Ramalingam, P. Ramasamy, M. D. Kovukkal, and G. Myilsamy, "Research and Development in Magnesium Alloys for Industrial and Biomedical Applications: A Review," *Met Mater-Int,* vol. 26, no. 4, pp. 409-430, 2020/04/01 2020, doi: 10.1007/s12540-019-00346-8.

[35] S. R. Agnew and Ö. Duygulu, "Plastic anisotropy and the role of non-basal slip in magnesium alloy AZ31B," *International Journal of Plasticity,* vol. 21, no. 6, pp. 1161-1193, 2005/06/01/ 2005, doi: https://doi.org/10.1016/j.ijplas.2004.05.018.

[36] S. Housh, B. Mikucki, and A. Stevenson, "Properties of Magnesium Alloys " in *Properties and Selection: Nonferrous Alloys and Special-Purpose Materials*: ASM International, 1990.

[37] J. H. Jackson, P. D. Frost, A. C. Loonam, L. W. Eastwood, and C. H. Lorig, "Magnesium-lithium base alloys—preparation, fabrication, and general characteristics," *JOM,* vol. 1, no. 2, pp. 149-168, 1949/02/01 1949, doi: 10.1007/BF03398089.

[38] H. E. Friedrich and B. L. Mordike, *Magnesium Technology*. Springer Berlin, Heidelberg, 2005.

[39] S. Housh, B. Mikucki, and A. Stevenson, "Selection and Application of Magnesium and Magnesium Alloys," in *Properties and Selection: Nonferrous Alloys and Special-Purpose Materials*: ASM International, 1990.

[40] D. Bairagi and S. Mandal, "A comprehensive review on biocompatible Mg-based alloys as temporary orthopaedic implants: Current status, challenges, and future prospects," *J Magnes Alloy,* vol. 10, no. 3, pp. 627-669, 2022/03/01/ 2022, doi: https://doi.org/10.1016/j.jma.2021.09.005.

[41] L. Liu, X. Chen, and F. Pan, "A review on electromagnetic shielding magnesium alloys," *J Magnes Alloy,* vol. 9, no. 6, pp. 1906-1921, 2021/11/15/ 2021, doi: https://doi.org/10.1016/j.jma.2021.10.001.

[42] B. A. Shaw, "Corrosion Resistance of Magnesium Alloys," *vol. 13A*, *Corrosion: Fundamentals, Testing, and Protection*: ASM International, 2003, p. 0. [Online]. Available: https://doi.org/10.31399/asm.hb.v13a.a0003675

[43] G. Song, "Recent Progress in Corrosion and Protection of Magnesium Alloys," *Adv Eng Mater,* https://doi.org/10.1002/adem.200500013 vol. 7, no. 7, pp. 563-586, 2005/07/01 2005, doi: https://doi.org/10.1002/adem.200500013.

[44] *Standard Guide for Development and Use of a Galvanic Series for Predicting Galvanic Corrosion Performance*, A. International, PA, United States, 2021.

[45] A. A. Luo, "Magnesium: Current and potential automotive applications," *JOM,* vol. 54, no. 2, pp. 42-48, 2002/02/01 2002, doi: 10.1007/BF02701073.

[46] K. Savage, "Magnesium and Magnesium Alloys," *vol. 15*, *Casting*: ASM International, 2008, p. 0. [Online]. Available: https://doi.org/10.31399/asm.hb.v15.a0005334

[47] S. G. Lee, G. R. Patel, A. M. Gokhale, A. Sreeranganathan, and M. F. Horstemeyer, "Quantitative fractographic analysis of variability in the tensile ductility of high-pressure die-cast AE44 Mg-alloy," *Materials Science and Engineering: A,* vol. 427, no. 1, pp. 255-262, 2006/07/15/ 2006, doi: https://doi.org/10.1016/j.msea.2006.04.108.

[48] J. Zhang *et al.*, "Microstructures, tensile properties and corrosion behavior of die-cast Mg–4Al-based alloys containing La and/or Ce," *Materials Science and Engineering: A,* vol. 489, no. 1, pp. 113-119, 2008/08/20/ 2008, doi: https://doi.org/10.1016/j.msea.2007.12.024.

[49] E. Aghion, B. Bronfin, and D. Eliezer, "The role of the magnesium industry in protecting the environment," (in English), *J Mater Process Tech,* vol. 117, no. 3, pp. 381-385, Nov 23 2001, doi: Doi 10.1016/S0924-0136(01)00779-8.

[50] F. Khomamizadeh, B. Nami, and S. Khoshkhooei, "Effect of rare-earth element additions on high-temperature mechanical properties of AZ91 magnesium alloy," *Metallurgical and Materials Transactions A,* vol. 36, no. 12, pp. 3489-3494, 2005/12/01 2005, doi: 10.1007/s11661-005-0022-6.

[51] D. Wenwen, S. Yangshan, M. Xuegang, X. Feng, Z. Min, and W. Dengyun, "Microstructure and mechanical properties of Mg–Al based alloy with calcium and rare earth additions," *Materials Science and Engineering: A,* vol. 356, no. 1, pp. 1-7, 2003/09/15/ 2003, doi: https://doi.org/10.1016/S0921-5093(02)00551-8.

[52] Y. Lü, Q. Wang, X. Zeng, W. Ding, C. Zhai, and Y. Zhu, "Effects of rare earths on the microstructure, properties and fracture behavior of Mg–Al alloys," *Materials Science and Engineering: A,* vol. 278, no. 1, pp. 66-76, 2000/02/15/ 2000, doi: https://doi.org/10.1016/S0921-5093(99)00604-8.

[53] Y. Huang, Q. Ouyang, D. Zhang, J. Zhu, R. Li, and H. Yu, "Carbon Materials Reinforced Aluminum Composites: A Review," *Acta Metallurgica Sinica (English Letters),* vol. 27, no. 5, pp. 775-786, 2014, doi: 10.1007/s40195-014-0160-1.

[54] D. E. Alman, "Properties of Metal-Matrix Composites," *vol. 21*, *Composites*: ASM International, 2001, p. 0. [Online]. Available: https://doi.org/10.31399/asm.hb.v21.a0003448

[55] D. J. Lloyd, "Particle reinforced aluminium and magnesium matrix composites," *International Materials Reviews,* vol. 39, no. 1, pp. 1-23, 2013, doi: 10.1179/imr.1994.39.1.1.

[56] P. Puspitasari, M. I. N. Sasongko, Sukarni, P. Murdanto, and Wahono, "Mechanical properties of Al-Si alloy with nanoreinforced manganese oxide by stir casting method," *AIP Conference Proceedings,* vol. 2120, no. 1, p. 050003, 2019/07/03 2019, doi: 10.1063/1.5115679.

[57] E. Orowan, "Zur Kristallplastizitt. III," *Zeitschrift fr Physik,* vol. 89, no. 9-10, pp. 634-659, 1934, doi: 10.1007/bf01341480.

[58] Q. Li, A. Viereckl, C. A. Rottmair, and R. F. Singer, "Improved processing of carbon nanotube/magnesium alloy composites," *Composites Science and Technology,* vol. 69, no. 7-8, pp. 1193-1199, 2009, doi: 10.1016/j.compscitech.2009.02.020.

[59] H. L. Cox, "The elasticity and strength of paper and other fibrous materials," *British Journal of Applied Physics,* vol. 3, no. 3, pp. 72-79, 1952, doi: 10.1088/0508-3443/3/3/302.

[60] H. J. Ryu, S. I. Cha, and S. H. Hong, "Generalized shear-lag model for load transfer in SiC/Al metal-matrix composites," (in English), *J Mater Res,* vol. 18, no. 12, pp. 2851-2858, Dec 2003, doi: Doi 10.1557/Jmr.2003.0398.

[61] R. J. Arsenault and N. Shi, "Dislocation Generation Due to Differences between the Coefficients of Thermal-Expansion," (in English), *Mater Sci Eng,* vol. 81, no. 1-2, pp. 175-187, Aug 1986, doi: Doi 10.1016/0025-5416(86)90261-2.

[62] N. Hansen, "Effect of Grain-Size and Strain on Tensile Flow-Stress of Aluminum at Room-Temperature," (in English), *Acta Metall Mater,* vol. 25, no. 8, pp. 863-869, 1977, doi: Doi 10.1016/0001-6160(77)90171-7.

[63] M. Taya, Arsenault, R. J *Metal Matrix Composites: Thermomechanical behavior*, First Edition ed. Pergamon Press, 1989.

[64] G. Q. Han, Z. H. Wang, R. Liu, S. B. Li, X. Du, and W. B. Du, "Synthesis of CNT-reinforced AZ31 magnesium alloy composites with uniformly distributed CNTs," (in English), *Mat Sci Eng a-Struct,* vol. 628, pp. 350-357, Mar 25 2015, doi: 10.1016/j.msea.2015.01.039.

[65] N. Moelans, B. Blanpain, and P. Wollants, "Pinning effect of second-phase particles on grain growth in polycrystalline films studied by 3-D phase field simulations," *Acta Materialia,* vol. 55, no. 6, pp. 2173-2182, 2007/04/01/ 2007, doi: https://doi.org/10.1016/j.actamat.2006.11.018.

[66] W. D. Callister, *Fundamentals of materials science and engineering : an integrated approach*, 3rd ed. Hoboken, N.J: Wiley, 2007.

[67] D. Fan, L.-Q. Chen, and S.-P. P. Chen, "Numerical Simulation of Zener Pinning with Growing Second-Phase Particles," *J Am Ceram Soc,* https://doi.org/10.1111/j.1151-2916.1998.tb02370.x vol. 81, no. 3, pp. 526-532, 1998/03/01 1998, doi: https://doi.org/10.1111/j.1151-2916.1998.tb02370.x.

[68] P. Jackson *et al.*, "Bioaccumulation and ecotoxicity of carbon nanotubes," *Chemistry Central Journal,* vol. 7, no. 1, p. 154, 2013/09/13 2013, doi: 10.1186/1752-153X-7-154.

[69] S. Iijima, "Helical Microtubules of Graphitic Carbon," (in English), *Nature,* vol. 354, no. 6348, pp. 56-58, Nov 7 1991, doi: DOI 10.1038/354056a0.

[70] C. M. White, R. Banks, I. Hamerton, and J. F. Watts, "Characterisation of commercially CVD grown multi-walled carbon nanotubes for paint applications," (in English), *Prog Org Coat,* vol. 90, pp. 44-53, Jan 2016, doi: 10.1016/j.porgcoat.2015.09.020.

[71] A. Eatemadi *et al.*, "Carbon nanotubes: properties, synthesis, purification, and medical applications," *Nanoscale Research Letters,* vol. 9, no. 1, p. 393, 2014/08/13 2014, doi: 10.1186/1556-276X-9-393.

[72] J. M. Schnorr and T. M. Swager, "Emerging Applications of Carbon Nanotubes," *Chemistry of Materials,* vol. 23, no. 3, pp. 646-657, 2011/02/08 2011, doi: 10.1021/cm102406h.

[73] A. Szabó, C. Perri, A. Csató, G. Giordano, D. Vuono, and J. B. Nagy, "Synthesis Methods of Carbon Nanotubes and Related Materials," *Materials*, vol. 3, no. 5, pp. 3092-3140doi: 10.3390/ma3053092.

[74] E. Ganesh, "Single walled and multi walled carbon nanotube structure, synthesis and applications," *International Journal of Innovative Technology and Exploring Engineering,* vol. 2, no. 4, pp. 311-320, 2013.

[75] R. Syed Awais, U. Zahid, M. Hafiz Tariq, M. Abdul Mannan, S. Mudassira, and A. Waseem, "Synthesis and Purification of Carbon Nanotubes," in *Carbon Nanotubes*, G. Prasanta Kumar, D. Kunal, and R. Arti Dinkarrao Eds. Rijeka: IntechOpen, 2021, p. Ch. 3.

[76] A. Krishnan, E. Dujardin, T. W. Ebbesen, P. N. Yianilos, and M. M. J. Treacy, "Young's modulus of single-walled nanotubes," *Physical Review B,* vol. 58, no. 20, pp. 14013-14019, 11/15/ 1998, doi: 10.1103/PhysRevB.58.14013.

[77] P. Poncharal, Z. L. Wang, D. Ugarte, and W. A. de Heer, "Electrostatic deflections and electromechanical resonances of carbon nanotubes," (in English), *Science,* vol. 283, no. 5407, pp. 1513-1516, Mar 5 1999, doi: DOI 10.1126/science.283.5407.1513.

[78] A. H. Barber, R. Andrews, L. S. Schadler, and H. D. Wagner, "On the tensile strength distribution of multiwalled carbon nanotubes," *Appl Phys Lett,* vol. 87, no. 20, p. 203106, 2005/11/14 2005, doi: 10.1063/1.2130713.

[79] M. Fujii *et al.*, "Measuring the Thermal Conductivity of a Single Carbon Nanotube," *Physical Review Letters,* vol. 95, no. 6, p. 065502, 08/02/ 2005, doi: 10.1103/PhysRevLett.95.065502.

[80] D. Markcoons, "Melt processing and characterisation of lightweight metal composites reinforced by nanocarbon," MPhil, Department of Aeronautics, University College London, London, UK, 2020.

[81] Y. Shimizu *et al.*, "Multi-walled carbon nanotube-reinforced magnesium alloy composites," (in English), *Scripta Mater,* vol. 58, no. 4, pp. 267-270, Feb 2008, doi: 10.1016/j.scriptamat.2007.10.014.

[82] C. S. Goh, J. Wei, L. C. Lee, and M. Gupta, "Development of novel carbon nanotube reinforced magnesium nanocomposites using the powder metallurgy technique," (in English), *Nanotechnology,* vol. 17, no. 1, pp. 7-12, Jan 14 2006, doi: 10.1088/0957-4484/17/1/002.

[83] A. Peigney, C. Laurent, E. Flahaut, R. R. Bacsa, and A. Rousset, "Specific surface area of carbon nanotubes and bundles of carbon nanotubes," (in English), *Carbon,* Article vol. 39, no. 4, pp. 507-514, 2001, doi: 10.1016/s0008-6223(00)00155-x.

[84] F. H. Gojny, M. H. G. Wichmann, U. Kopke, B. Fiedler, and K. Schulte, "Carbon nanotube-reinforced epoxy-compo sites: enhanced stiffness and fracture toughness at low nanotube content," (in English), *Composites Science and Technology,* vol. 64, no. 15, pp. 2363-2371, Nov 2004, doi: 10.1016/j.compscitech.2004.04.002.

[85] S. Cranford, H. M. Yao, C. Ortiz, and M. J. Buehler, "A single degree of freedom 'lollipop' model for carbon nanotube bundle formation," (in English), *Journal of the Mechanics and Physics of Solids,* vol. 58, no. 3, pp. 409-427, Mar 2010, doi: 10.1016/j.jmps.2009.11.002.

[86] P. M. Ajayan and F. Banhart, "Strong bundles," (in English), *Nat Mater,* vol. 3, no. 3, pp. 135-136, Mar 2004, doi: 10.1038/nmat1078.

[87] C. S. Goh, J. Wei, L. C. Lee, and A. Gupta, "Simultaneous enhancement in strength and ductility by reinforcing magnesium with carbon nanotubes," (in English), *Mat Sci Eng a-Struct,* vol. 423, no. 1-2, pp. 153-156, May 15 2006, doi: 10.1016/j.msea.2005.10.071.

[88] X. S. Zeng, G. H. Zhou, Q. A. Xu, Y. J. Xiong, C. Luo, and J. C. Wu, "A new technique for dispersion of carbon nanotube in a metal melt," (in English), *Mat Sci Eng a-Struct,* vol. 527, no. 20, pp. 5335-5340, Jul 25 2010, doi: 10.1016/j.msea.2010.05.005.

[89] J. Hou, W. Du, G. Parande, M. Gupta, and S. Li, "Significantly enhancing the strength + ductility combination of Mg-9Al alloy using multi-walled carbon nanotubes," *J Alloy Compd,* vol. 790, pp. 974-982, 2019/06/25/ 2019, doi: https://doi.org/10.1016/j.jallcom.2019.03.243.

[90] Y. Xiang *et al.*, "Achieving ultra-high strengthening and toughening efficiency in carbon nanotubes/magnesium composites via constructing micro-nano layered structure," *Composites Part A: Applied Science and Manufacturing,* vol. 119, pp. 225-234, 2019/04/01/ 2019, doi: https://doi.org/10.1016/j.compositesa.2019.02.006.

[91] J.-z. Liao, M.-J. Tan, and I. Sridhar, "Spark plasma sintered multi-wall carbon nanotube reinforced aluminum matrix composites," *Mater Design,* vol. 31, pp. S96-S100, 2010/06/01/ 2010, doi: https://doi.org/10.1016/j.matdes.2009.10.022.

[92] H. Hashim, M. S. Salleh, and M. Z. Omar, "Homogenous dispersion and interfacial bonding of carbon nanotube reinforced with aluminum matrix composite: A review," (in English), *Rev Adv Mater Sci,* vol. 58, no. 1, pp. 295-303, Apr 2019, doi: 10.1515/rams-2019-0035.

[93] S. K. Thakur, G. T. Kwee, and M. Gupta, "Development and characterization of magnesium composites containing nano-sized silicon carbide and carbon nanotubes as hybrid reinforcements," (in English),

Journal of Materials Science, vol. 42, no. 24, pp. 10040-10046, Dec 2007, doi: 10.1007/s10853-007-2004-0.

[94] E. Carreno-Morelli *et al.*, "Carbon nanotube/magnesium composites," (in English), *Phys Status Solidi A,* vol. 201, no. 8, pp. R53-R55, Jun 2004, doi: 10.1002/passa.200409045.

[95] Q. H. Yuan, D. M. Fu, X. S. Zeng, and Y. Liu, "Fabrication of carbon nanotube reinforced AZ91D composite with superior mechanical properties," (in English), *Transactions of Nonferrous Metals Society of China,* vol. 27, no. 8, pp. 1716-1724, Aug 2017, doi: 10.1016/S1003-6326(17)60194-8.

[96] H. L. Shi *et al.*, "A Novel Melt Processing for Mg Matrix Composites Reinforced by Multiwalled Carbon Nanotubes," *J Mater Sci Technol,* vol. 32, no. 12, pp. 1303-1308, 2016/12/01/ 2016, doi: https://doi.org/10.1016/j.jmst.2016.05.014.

[97] N. Darsono, D. H. Yoon, and J. Y. Kim, "Milling and dispersion of multi-walled carbon nanotubes in texanol," (in English), *Appl Surf Sci,* vol. 254, no. 11, pp. 3412-3419, Mar 30 2008, doi: 10.1016/j.apsusc.2007.11.028.

[98] D. Poirier, R. Gauvin, and R. A. L. Drew, "Structural characterization of a mechanically milled carbon nanotube/aluminum mixture," (in English), *Compos Part a-Appl S,* vol. 40, no. 9, pp. 1482-1489, Sep 2009, doi: 10.1016/j.compositesa.2009.05.025.

[99] F.-Z. Zhao, X.-H. Feng, and Y.-S. Yang, "Microstructure and Mechanical Properties of CNT-Reinforced AZ91D Composites Fabricated by Ultrasonic Processing," *Acta Metallurgica Sinica (English Letters),* vol. 29, no. 7, pp. 652-660, 2016/07/01 2016, doi: 10.1007/s40195-016-0438-6.

[100] C. D. Li *et al.*, "Distribution and integrity of carbon nanotubes in carbon nanotube/magnesium composites," *J Alloy Compd,* vol. 612, pp. 330-336, 2014/11/05/ 2014, doi: https://doi.org/10.1016/j.jallcom.2014.05.153.

[101] H. Fukuda, K. Kondoh, J. Umeda, and B. Fugetsu, "Fabrication of magnesium based composites reinforced with carbon nanotubes having superior mechanical properties," (in English), *Mater Chem Phys,* Article vol. 127, no. 3, pp. 451-458, Jun 2011, doi: 10.1016/j.matchemphys.2011.02.036.

[102] S. Liu, F. Gao, Q. Zhang, X. Zhu, and W. Li, "Fabrication of carbon nanotubes reinforced AZ91D composites by ultrasonic processing," (in English), *Transactions of Nonferrous Metals Society of China,* Article|Proceedings Paper vol. 20, no. 7, pp. 1222-1227, JUL 2010 2010, doi: 10.1016/s1003-6326(09)60282-x.

[103] J. N. Coleman, U. Khan, W. J. Blau, and Y. K. Gun'ko, "Small but strong: A review of the mechanical properties of carbon nanotube-polymer composites," (in English), *Carbon,* vol. 44, no. 9, pp. 1624-1652, Aug 2006, doi: 10.1016/j.carbon.2006.02.038.

[104] R. G. Coltters, "Thermodynamics of Binary Metallic Carbides - a Review," (in English), *Mater Sci Eng,* vol. 76, no. 1-2, pp. 1-50, Dec 1985, doi: Doi 10.1016/0025-5416(85)90078-3.

[105] E. Dujardin, T. W. Ebbesen, H. Hiura, and K. Tanigaki, "Capillarity and Wetting of Carbon Nanotubes," *Science,* vol. 265, no. 5180, pp. 1850-1852, 1994/09/23 1994, doi: 10.1126/science.265.5180.1850.

[106] H. Uozumi *et al.*, "Fabrication process of carbon nanotube/light metal matrix composites by squeeze casting," (in English), *Mat Sci Eng a-Struct,* vol. 495, no. 1-2, pp. 282-287, Nov 15 2008, doi: 10.1016/j.msea.2007.11.088.

[107] N. Shinozaki, J. Morita, and K. Wasai, "Wetting of graphite by molten magnesium," *Journal of Japan Institute of Light Metals,* vol. 55, no. 7, pp. 310-314, 2005, doi: 10.2464/jilm.55.310.

[108] Y. Q. Yao *et al.*, "Nickel Formation on Graphite Sheet Surface for Improving Wettability with Magnesium Alloy," (in English), *Mater Trans,* vol. 56, no. 10, pp. 83-87, Oct 2015, doi: 10.2320/matertrans.MAW201506.

[109] A. M. Nasiri, M. Y. Lee, D. C. Weckman, and Y. Zhou, "Effects of Interfacial Lattice Mismatching on Wetting of Ni-Plated Steel by Magnesium," *Metallurgical and Materials Transactions A,* vol. 45, no. 12, pp. 5749-5766, 2014/11/01 2014, doi: 10.1007/s11661-014-2514-8.

[110] T. W. Ebbesen, H. Hiura, M. E. Bisher, M. M. J. Treacy, J. L. Shreeve-Keyer, and R. C. Haushalter, "Decoration of carbon nanotubes," *Adv Mater,* https://doi.org/10.1002/adma.19960080212 vol. 8, no. 2, pp. 155-157, 1996/02/01 1996, doi: https://doi.org/10.1002/adma.19960080212.

[111] L. M. Ang, T. S. A. Hor, G. Q. Xu, C. H. Tung, S. P. Zhao, and J. L. S. Wang, "Decoration of activated carbon nanotubes with copper and nickel," *Carbon,* vol. 38, no. 3, pp. 363-372, 2000/01/01/ 2000, doi: https://doi.org/10.1016/S0008-6223(99)00112-8.

[112] B. C. Satishkumar, M. V. Erasmus, A. Govindaraj, and C. N. R. Rao, "The decoration of carbon nanotubes by metal nanoparticles," *Journal of Physics D: Applied Physics,* vol. 29, no. 12, p. 3173, 1996/12/14 1996, doi: 10.1088/0022-3727/29/12/037.

[113] J. H. Liang *et al.*, "Influence of Ni-CNTs additions on the microstructure and mechanical properties of extruded Mg-9Al alloy," (in English), *Mat Sci Eng a-Struct,* vol. 678, pp. 101-109, Dec 15 2016, doi: 10.1016/j.msea.2016.09.089.

[114] F.-P. Du, H. Tang, and D.-Y. Huang, "Thermal Conductivity of Epoxy Resin Reinforced with Magnesium Oxide Coated Multiwalled Carbon Nanotubes," *International Journal of Polymer Science,* vol. 2013, p. 541823, 2013/09/03 2013, doi: 10.1155/2013/541823.

[115] K. Kondoh, H. Fukuda, J. Umeda, H. Imai, B. Fugetsu, and M. Endo, "Microstructural and mechanical analysis of carbon nanotube reinforced magnesium alloy powder composites," *Materials Science and Engineering: A,* vol. 527, no. 16, pp. 4103-4108, 2010/06/25/ 2010, doi: https://doi.org/10.1016/j.msea.2010.03.049.

[116] Y. Wang, Z. Fan, X. Zhou, and G. E. Thompson, "Characterisation of magnesium oxide and its interface with α-Mg in Mg–Al-based alloys," *Philosophical Magazine Letters,* vol. 91, no. 8, pp. 516-529, 2011/08/01 2011, doi: 10.1080/09500839.2011.591744.

[117] Y. Park, K. Cho, I. Park, and Y. Park, "Fabrication and mechanical properties of magnesium matrix composite reinforced with Si coated carbon nanotubes," (in English), *Procedia Engineer,* vol. 10, pp. 1446-1450, 2011, doi: 10.1016/j.proeng.2011.04.240.

[118] L. Wu, R. Wu, L. Hou, J. Zhang, J. Sun, and M. Zhang, "Microstructure and Mechanical Properties of CNT-Reinforced AZ31 Matrix Composites Prepared Using Hot-Press Sintering," *J Mater Eng Perform,* vol. 26, no. 11, pp. 5495-5500, 2017/11/01 2017, doi: 10.1007/s11665-017-2971-5.

[119] Q.-h. Yuan *et al.*, "Microstructure and mechanical properties of AZ91 alloy reinforced by carbon nanotubes coated with MgO," *Carbon,* vol. 96, pp. 843-855, 2016/01/01/ 2016, doi: https://doi.org/10.1016/j.carbon.2015.10.018.

[120] J. H. Liang, H. J. Li, X. J. Hu, J. F. Wei, and L. H. Qi, "Fabrication of Ni-coated carbon nanotubes reinforced magnesium matrix composites," (in English), *Int Conf Manip Manu,* pp. 299-302, 2013. [Online]. Available: <Go to ISI>://WOS:000350808700062.

[121] M. H. Nai, J. Wei, and M. Gupta, "Interface tailoring to enhance mechanical properties of carbon nanotube reinforced magnesium composites," *Mater Design,* vol. 60, pp. 490-495, 2014/08/01/ 2014, doi: https://doi.org/10.1016/j.matdes.2014.04.011.

[122] G. Han *et al.*, "Compelling mechanical properties of carbon nanotubes reinforced pure magnesium composite by effective interface bonding of Mg2Ni," *J Alloy Compd,* vol. 727, pp. 963-969, 2017/12/15/ 2017, doi: https://doi.org/10.1016/j.jallcom.2017.08.133.

[123] Q. H. Yuan *et al.*, "Microstructure and mechanical properties of Mg-4.0Zn alloy reinforced by NiO-coated CNTs," (in English), *J Mater Sci Technol,* vol. 33, no. 5, pp. 452-460, May 2017, doi: 10.1016/j.jmst.2016.07.022.

[124] H. Dieringa, "Properties of magnesium alloys reinforced with nanoparticles and carbon nanotubes: a review," (in English), *Journal of Materials Science,* vol. 46, no. 2, pp. 289-306, Jan 2011, doi: 10.1007/s10853-010-5010-6.

[125] G. Cao, H. Konishi, and X. Li, "Mechanical properties and microstructure of SiC-reinforced Mg-(2,4)Al-1Si nanocomposites fabricated by ultrasonic cavitation based solidification processing," *Materials Science and Engineering: A,* vol. 486, no. 1, pp. 357-362, 2008/07/15/ 2008, doi: https://doi.org/10.1016/j.msea.2007.09.054.

[126] K. B. Nie, X. J. Wang, X. S. Hu, L. Xu, K. Wu, and M. Y. Zheng, "Microstructure and mechanical properties of SiC nanoparticles reinforced magnesium matrix composites fabricated by ultrasonic vibration," (in English), *Mat Sci Eng a-Struct,* vol. 528, no. 15, pp. 5278-5282, Jun 15 2011, doi: 10.1016/j.msea.2011.03.061.

[127] K. B. Nie, X. J. Wang, K. Wu, X. S. Hu, M. Y. Zheng, and L. Xu, "Microstructure and tensile properties of micro-SiC particles reinforced magnesium matrix composites produced by semisolid stirring assisted ultrasonic vibration," *Materials Science and Engineering: A,* vol. 528, no. 29, pp. 8709-8714, 2011/11/15/ 2011, doi: https://doi.org/10.1016/j.msea.2011.08.035.

[128] K. B. Nie, K. K. Deng, F. J. Xu, X. J. Wang, and K. Wu, "Development of microstructure in submicron particles reinforced magnesium matrix composite processed by room temperature deformation," *Mater Chem Phys,* vol. 149-150, pp. 21-26, 2015/01/15/ 2015, doi: https://doi.org/10.1016/j.matchemphys.2014.11.011.

[129] T. Epicier, F. Bosselet, and J. C. Viala, "Microstructure of interfaces between a magnesium matrix and preoxidized silicon carbide particles," *Interface Science,* vol. 1, pp. 213–221, 1994, doi: https://doi.org/10.1007/BF00198148.

[130] L. X. Shi, P. Shen, D. Zhang, and Q. C. Jiang, "Wetting and evaporation behaviors of molten Mg-Al alloy drops on partially oxidized alpha-SiC substrates," (in English), *Mater Chem Phys,* vol. 130, no. 3, pp. 1125-1133, Nov 1 2011, doi: 10.1016/j.matchemphys.2011.08.051.

[131] S. Yajima, J. Hayashi, and M. Omori, "CONTINUOUS SILICON CARBIDE FIBER OF HIGH TENSILE STRENGTH," *Chemistry Letters,* vol. 4, no. 9, pp. 931-934, 1975/09/05 1975, doi: 10.1246/cl.1975.931.

[132] S. Yajima, K. Okamura, J. Hayashi, and M. Omori, "Synthesis of Continuous Sic Fibers with High Tensile Strength," *J Am Ceram Soc,* https://doi.org/10.1111/j.1151-2916.1976.tb10975.x vol. 59, no. 7-8, pp. 324-327, 1976/07/01 1976, doi: https://doi.org/10.1111/j.1151-2916.1976.tb10975.x.

[133] G. Barroso, Q. Li, R. K. Bordia, and G. Motz, "Polymeric and ceramic silicon-based coatings – a review," *Journal of Materials Chemistry A,* 10.1039/C8TA09054H vol. 7, no. 5, pp. 1936-1963, 2019, doi: 10.1039/C8TA09054H.

[134] B. V. Manoj Kumar and Y.-W. Kim, "Processing of polysiloxane-derived porous ceramics: a review," *Science and Technology of Advanced Materials,* vol. 11, no. 4, p. 044303, 2010/09/10 2010, doi: 10.1088/1468-6996/11/4/044303.

[135] P. Greil, "Processing of silicon nitride ceramics," *Materials Science and Engineering: A,* vol. 109, pp. 27-35, 1989/03/01/ 1989, doi: https://doi.org/10.1016/0921-5093(89)90561-3.

[136] H. Tanaka, "Silicon carbide powder and sintered materials," *Journal of the Ceramic Society of Japan,* vol. 119, no. 1387, pp. 218-233, 2011, doi: 10.2109/jcersj2.119.218.

[137] P. D. Ceramics, "Theory and Applications, ed. P. Colombo, GD Soraru, R. Riedel and A. Kleebe," ed: DEStech Publications, Inc, 2009.

[138] K. H. Stern, *Metallurgical and ceramic protective coatings*. Springer Science & Business Media, 1996.

[139] P. Colombo, G. Mera, R. Riedel, and G. D. Sorarù, "Polymer-Derived Ceramics: 40 Years of Research and Innovation in Advanced Ceramics," *J Am Ceram Soc,* https://doi.org/10.1111/j.1551-2916.2010.03876.x vol. 93, no. 7, pp. 1805-1837, 2010/07/01 2010, doi: https://doi.org/10.1111/j.1551-2916.2010.03876.x.

[140] K. J. Wynne and R. W. Rice, "CERAMICS VIA POLYMER PYROLYSIS," (in English), *Annu. Rev. Mater. Sci.,* Review vol. 14, pp. 297-334, 1984, doi: 10.1146/annurev.ms.14.080184.001501.

[141] S. Kumar, R. Rajasekhar, G. C. Nayak, and C. K. Das, "Polycarbosilane-derived silicon carbide-functionalized multi-walled carbon nanotubes and influence on the polyethersulfone nanocomposites," (in English), *J Compos Mater,* Article vol. 45, no. 21, pp. 2225-2236, Oct 2011, doi: 10.1177/0021998311401077.

[142] G. Yamamoto *et al.*, "Polycarbosilane-derived SiC/single-walled carbon nanotube nanocomposites," (in English), *Nanotechnology,* vol. 18, no. 14, Apr 11 2007, doi: Artn 145614

10.1088/0957-4484/18/14/145614.

[143] R. K. Gupta, R. Mishra, K. Mukhopadhyay, R. K. Tiwari, A. Ranjan, and A. K. Saxena, "A New Technique for Coating Silicon Carbide Onto Carbon Nanotubes Using a Polycarbosilane Precursor," (in English), *Silicon-Neth,* vol. 1, no. 2, pp. 125-129, Apr 2009, doi: 10.1007/s12633-009-9016-0.

[144] R. Li, Y. Qing, J. Zhao, and S. Huang, "SiC-Coated Carbon Nanotubes with Enhanced Oxidation Resistance and Stable Dielectric Properties," *Materials,* vol. 14, p. 2770, 2021.

[145] K. P. So *et al.*, "SiC formation on carbon nanotube surface for improving wettability with aluminum," *Composites Science and Technology,* vol. 74, pp. 6-13, 2013/01/24/ 2013, doi: https://doi.org/10.1016/j.compscitech.2012.09.014.

[146] Y. Ji, Y. Y. Huang, A. R. Tajbakhsh, and E. M. Terentjev, "Polysiloxane Surfactants for the Dispersion of Carbon Nanotubes in Nonpolar Organic Solvents," *Langmuir,* vol. 25, no. 20, pp. 12325-12331, 2009/10/20 2009, doi: 10.1021/la901622c.

[147] J. H. Kim *et al.*, "Simple and cost-effective method of highly conductive and elastic carbon nanotube/polydimethylsiloxane composite for wearable electronics," *Sci Rep-Uk,* vol. 8, no. 1, p. 1375, 2018/01/22 2018, doi: 10.1038/s41598-017-18209-w.

[148] G. D. Sorar, R. Campostrini, S. Maurina, and F. Babonneau, "Gel Precursor to Silicon Oxycarbide Glasses with Ultrahigh Ceramic Yield," *J Am Ceram Soc,* https://doi.org/10.1111/j.1151-2916.1997.tb02933.x vol. 80, no. 4, pp. 999-1004, 1997/04/01 1997, doi: https://doi.org/10.1111/j.1151-2916.1997.tb02933.x.

[149] G. D. Sorarù, E. Dallapiccola, and G. D'Andrea, "Mechanical Characterization of Sol–Gel-Derived Silicon Oxycarbide Glasses," *J Am Ceram Soc,* https://doi.org/10.1111/j.1151-2916.1996.tb08939.x vol. 79, no. 8, pp. 2074-2080, 1996/08/01 1996, doi: https://doi.org/10.1111/j.1151-2916.1996.tb08939.x.

[150] M. Esfehanian, R. Oberacker, T. Fett, and M. J. Hoffmann, "Development of Dense Filler-Free Polymer-Derived SiOC Ceramics by Field-Assisted Sintering," *J Am Ceram Soc,* https://doi.org/10.1111/j.1551-2916.2008.02730.x vol. 91, no. 11, pp. 3803-3805, 2008/11/01 2008, doi: https://doi.org/10.1111/j.1551-2916.2008.02730.x.

[151] G. D. Sorarù, S. Modena, E. Guadagnino, P. Colombo, J. Egan, and C. Pantano, "Chemical Durability of Silicon Oxycarbide Glasses," *J Am Ceram Soc,* https://doi.org/10.1111/j.1151-2916.2002.tb00308.x vol. 85, no. 6, pp. 1529-1536, 2002/06/01 2002, doi: https://doi.org/10.1111/j.1151-2916.2002.tb00308.x.

[152] J. Latournerie, P. Dempsey, D. Hourlier-Bahloul, and J.-P. Bonnet, "Silicon Oxycarbide Glasses: Part 1—Thermochemical Stability," *J Am Ceram Soc,* https://doi.org/10.1111/j.1551-2916.2005.00869.x vol. 89, no. 5, pp. 1485-1491, 2006/05/01 2006, doi: https://doi.org/10.1111/j.1551-2916.2005.00869.x.

[153] E. Ionescu, H.-J. Kleebe, and R. Riedel, "Silicon-containing polymer-derived ceramic nanocomposites (PDC-NCs): preparative approaches and properties," *Chem Soc Rev,* 10.1039/C2CS15319J vol. 41, no. 15, pp. 5032-5052, 2012, doi: 10.1039/C2CS15319J.

[154] M. Y. Wong, A. F. Schneider, G. Lu, Y. Chen, and M. A. Brook, "Autoxidation: catalyst-free route to silicone rubbers by crosslinking Si–H functional groups," *Green Chemistry,* 10.1039/C9GC03026C vol. 21, no. 23, pp. 6483-6490, 2019, doi: 10.1039/C9GC03026C.

[155] R. Kalfat, F. Babonneau, N. Gharbi, and H. Zarrouk, "29Si MAS NMR investigation of the pyrolysis process of cross-linked polysiloxanes prepared from polymethylhydrosiloxane," *J Mater Chem,* 10.1039/JM9960601673 vol. 6, no. 10, pp. 1673-1678, 1996, doi: 10.1039/JM9960601673.

[156] X. Yang, P. Jiang, F. Sun, L. Yang, and X. Fan, "A pyrolysis heating rate based pressureless method for preparing dense and crack-free polymer-derived silicon oxycarbide bulk ceramics," *Ceram Int,* vol. 46, no. 8, Part A, pp. 10392-10399, 2020/06/01/ 2020, doi: https://doi.org/10.1016/j.ceramint.2020.01.037.

[157] M. Handke, M. Sitarz, and E. Długoń, "Amorphous SiCxOy coatings from ladder-like polysilsesquioxanes," *Journal of Molecular Structure,* vol. 993, no. 1, pp. 193-197, 2011/05/03/ 2011, doi: https://doi.org/10.1016/j.molstruc.2010.12.017.

[158] C. Carlomagno, G. Speranza, P. Aswath, G. D. Sorarù, C. Migliaresi, and D. Maniglio, "Breath figures decorated silica-based ceramic surfaces with tunable geometry from UV cross-linkable polysiloxane precursor," *Journal of the European Ceramic Society,* vol. 38, no. 4, pp. 1320-1326, 2018/04/01/ 2018, doi: https://doi.org/10.1016/j.jeurceramsoc.2017.10.005.

[159] K. Bawane, D. Erb, and K. Lu, "Carbon content and pyrolysis atmosphere effects on phase development in SiOC systems," *Journal of the European Ceramic Society,* vol. 39, no. 9, pp. 2846-2854, 2019/08/01/ 2019, doi: https://doi.org/10.1016/j.jeurceramsoc.2019.03.032.

[160] G. A. Danko, R. Silberglitt, P. Colombo, E. Pippel, and J. Woltersdorf, "Comparison of Microwave Hybrid and Conventional Heating of Preceramic Polymers to Form Silicon Carbide and Silicon Oxycarbide Ceramics," *J Am Ceram Soc,* https://doi.org/10.1111/j.1151-2916.2000.tb01440.x vol. 83, no. 7, pp. 1617-1625, 2000/07/01 2000, doi: https://doi.org/10.1111/j.1151-2916.2000.tb01440.x.

[161] V. Belot, R. J. P. Corriu, D. Leclercq, P. H. Mutin, and A. Vioux, "Thermal redistribution reactions in crosslinked polysiloxanes," *Journal of Polymer Science Part A: Polymer Chemistry,* https://doi.org/10.1002/pola.1992.080300413 vol. 30, no. 4, pp. 613-623, 1992/03/30 1992, doi: https://doi.org/10.1002/pola.1992.080300413.

[162] V. Belot, R. J. P. Corriu, D. Leclercq, P. H. Mutin, and A. Vioux, "Thermal reactions occurring during pyrolysis of crosslinked polysiloxane gels, precursors to silicon oxycarbide glasses," *Journal of Non-Crystalline Solids,* vol. 147-148, pp. 52-55, 1992/01/01/ 1992, doi: https://doi.org/10.1016/S0022-3093(05)80592-7.

[163] L. Duan and Q. Ma, "Effect of pyrolysis temperature on the pore structure evolution of polysiloxane-derived ceramics," *Ceram Int,* vol. 38, no. 4, pp. 2667-2671, 2012/05/01/ 2012, doi: https://doi.org/10.1016/j.ceramint.2011.11.033.

[164] G. D. Sorarù, L. Kundanati, B. Santhosh, and N. Pugno, "Influence of free carbon on the Young's modulus and hardness of polymer-derived silicon oxycarbide glasses," *J Am Ceram Soc,* https://doi.org/10.1111/jace.16131 vol. 102, no. 3, pp. 907-913, 2019/03/01 2019, doi: https://doi.org/10.1111/jace.16131.

[165] P. Dibandjo, S. Diré, F. Babonneau, and G. D. Soraru, "Influence of the polymer architecture on the high temperature behavior of SiCO glasses: A comparison between linear- and cyclic-derived precursors," *Journal of Non-Crystalline Solids,* vol. 356, no. 3, pp. 132-140, 2010/02/01/ 2010, doi: https://doi.org/10.1016/j.jnoncrysol.2009.10.006.

[166] M. C. Wang, L. J. Yang, C. D. Yu, and C. B. Xu, "Liquid poly(silylacetylene)siloxane resin as a novel precursor of silicon carbide and silicon oxycarbide ceramics," (in English), *Ceram Int,* Article vol. 38, no. 3, pp. 2449-2454, Apr 2012, doi: 10.1016/j.ceramint.2011.11.012.

[167] P. V. W. Sasikumar *et al.*, "Polymer derived silicon oxycarbide ceramic monoliths: Microstructure development and associated materials properties," *Ceram Int,* vol. 44, no. 17, pp. 20961-20967, 2018/12/01/ 2018, doi: https://doi.org/10.1016/j.ceramint.2018.08.102.

[168] S. Nedunchezhian, R. Sujith, and R. Kumar, "Processing and characterization of polymer precursor derived silicon oxycarbide ceramic foams and compacts," (in English), *J Adv Ceram,* vol. 2, no. 4, pp. 318-324, Dec 2013, doi: 10.1007/s40145-013-0078-5.

[169] D. Su *et al.*, "Pyrolytic transformation of liquid precursors to shaped bulk ceramics," *Journal of the European Ceramic Society,* vol. 30, no. 6, pp. 1503-1511, 2010/04/01/ 2010, doi: https://doi.org/10.1016/j.jeurceramsoc.2009.11.015.

[170] B. F. Sousa, I. V. P. Yoshida, J. L. Ferrari, and M. A. Schiavon, "Silicon oxycarbide glasses derived from polymeric networks with different molecular architecture prepared by hydrosilylation reaction," *Journal of Materials Science,* vol. 48, no. 5, pp. 1911-1919, 2013/03/01 2013, doi: 10.1007/s10853-012-6955-4.

[171] S. Vry, M. Roumanie, R. Laucournet, and G. Bernard-Granger, "Transmission Electron Microscopy Investigations on a Polysiloxane Preceramic Polymer Pyrolyzed at High Temperature in Argon," *Ceramics*, vol. 3, no. 4, pp. 421-427doi: 10.3390/ceramics3040035.

[172] "CHAPTER 2 - Catalytic Aspects of Hydrosilylation," in *Comprehensive Handbook on Hydrosilylation*, B. Marciniec Ed. Amsterdam: Pergamon, 1992, pp. 8-98.

[173] J. Cervantes, R. Zárraga, and C. Salazar-Hernández, "Organotin catalysts in organosilicon chemistry," *Applied Organometallic Chemistry,* https://doi.org/10.1002/aoc.2832 vol. 26, no. 4, pp. 157-163, 2012/04/01 2012, doi: https://doi.org/10.1002/aoc.2832.

[174] S. J. Clarson and J. A. Semlyen, *Siloxane polymers* (Polymer science and technology series (Englewood Cliffs, N.J.)). Englewood Cliffs, N.J.: Prentice Hall (in eng), 1993.

[175] J. C. Pivin, P. Colombo, and M. Tonidandel, "Ion Irradiation of Preceramic Polymer Thin Films," *J Am Ceram Soc,* https://doi.org/10.1111/j.1151-2916.1996.tb08021.x vol. 79, no. 7, pp. 1967-1970, 1996/07/01 1996, doi: https://doi.org/10.1111/j.1151-2916.1996.tb08021.x.

[176] K. Okamura and T. Seguchi, "Application of radiation curing in the preparation of polycarbosilane-derived SiC fibers," *Journal of Inorganic and Organometallic Polymers,* vol. 2, no. 1, pp. 171-179, 1992/03/01 1992, doi: 10.1007/BF00696544.

[177] K. E. Gonsalves, P. R. Strutt, T. D. Xiao, and P. G. Klemens, "Synthesis of Si(C, N) nanoparticles by rapid laser polycondensation/crosslinking reactions of an organosilazane precursor," *Journal of Materials Science,* vol. 27, no. 12, pp. 3231-3238, 1992/06/01 1992, doi: 10.1007/BF01116018.

[178] B. Du *et al.*, "Preparation and structural evolution of SiOC preceramic aerogel during high-temperature treatment," *Ceram Int,* vol. 44, no. 1, pp. 563-570, 2018/01/01/ 2018, doi: https://doi.org/10.1016/j.ceramint.2017.09.212.

[179] M. A. Schiavon, S. U. A. Redondo, S. R. O. Pina, and I. V. P. Yoshida, "Investigation on kinetics of thermal decomposition in polysiloxane networks used as precursors of silicon oxycarbide glasses," *Journal of Non-Crystalline Solids,* vol. 304, no. 1, pp. 92-100, 2002/06/01/ 2002, doi: https://doi.org/10.1016/S0022-3093(02)01009-8.

[180] P. H. Mutin, "Control of the Composition and Structure of Silicon Oxycarbide and Oxynitride Glasses Derived from Polysiloxane Precursors," *Journal of Sol-Gel Science and Technology,* vol. 14, no. 1, pp. 27-38, 1999/03/01 1999, doi: 10.1023/A:1008769913083.

[181] J. L. Plawsky, F. Wang, and W. N. Gill, "Kinetic model for the pyrolysis of polysiloxane polymers to ceramic composites," *AIChE Journal,* https://doi.org/10.1002/aic.690481021 vol. 48, no. 10, pp. 2315-2323, 2002/10/01 2002, doi: https://doi.org/10.1002/aic.690481021.

[182] D. Baskaran, J. W. Mays, and M. S. Bratcher, "Noncovalent and Nonspecific Molecular Interactions of Polymers with Multiwalled Carbon Nanotubes," *Chemistry of Materials,* vol. 17, no. 13, pp. 3389-3397, 2005/06/01 2005, doi: 10.1021/cm047866e.

[183] A. Beigbeder *et al.*, "CH-π Interactions as the Driving Force for Silicone-Based Nanocomposites with Exceptional Properties," *Adv Mater,* https://doi.org/10.1002/adma.200701497 vol. 20, no. 5, pp. 1003-1007, 2008/03/05 2008, doi: https://doi.org/10.1002/adma.200701497.

[184] J. D. Jovanovic, M. N. Govedarica, P. R. Dvornic, and I. G. Popovic, "The thermogravimetric analysis of some polysiloxanes," *Polymer Degradation and Stability,* vol. 61, no. 1, pp. 87-93, 1998/01/01/ 1998, doi: https://doi.org/10.1016/S0141-3910(97)00135-3.

[185] *Standard Practice for Heat Treatment of Magnesium Alloys*, B661-12, West Conshohocken, Philadelphia, USA, Dec 2020.

[186] B. Stuart, *Infrared spectroscopy : fundamentals and applications*. Chichester: John Wiley, 2004.

[187] S. R. Sandler, *Polymer synthesis and characterization : a laboratory manual*. San Diego ;: Academic, 1998.

[188] B. Koh, J. B. Park, X. Hou, and W. Cheng, "Comparative Dispersion Studies of Single-Walled Carbon Nanotubes in Aqueous Solution," *The Journal of Physical Chemistry B,* vol. 115, no. 11, pp. 2627-2633, 2011/03/24 2011, doi: 10.1021/jp110376h.

[189] J. Yu, N. Grossiord, C. E. Koning, and J. Loos, "Controlling the dispersion of multi-wall carbon nanotubes in aqueous surfactant solution," *Carbon,* vol. 45, no. 3, pp. 618-623, 2007/03/01/ 2007, doi: https://doi.org/10.1016/j.carbon.2006.10.010.

[190] O. V. Kharissova, B. I. Kharisov, and E. G. de Casas Ortiz, "Dispersion of carbon nanotubes in water and non-aqueous solvents," *Rsc Adv,* 10.1039/C3RA43852J vol. 3, no. 47, pp. 24812-24852, 2013, doi: 10.1039/C3RA43852J.

[191] J. L. Bahr, E. T. Mickelson, M. J. Bronikowski, R. E. Smalley, and J. M. Tour, "Dissolution of small diameter single-wall carbon nanotubes in organic solvents?," *Chemical Communications,* 10.1039/B008042J no. 2, pp. 193-194, 2001, doi: 10.1039/B008042J.

[192] R. Haggenmueller *et al.*, "Comparison of the Quality of Aqueous Dispersions of Single Wall Carbon Nanotubes Using Surfactants and Biomolecules," *Langmuir,* vol. 24, no. 9, pp. 5070-5078, 2008/05/01 2008, doi: 10.1021/la703008r.

[193] A. Elkordy, Ed. *Applications of Calorimetry in a Wide Context - Differential Scanning Calorimetry, Isothermal Titration Calorimetry and Microcalorimetry* (Applications of calorimetry in a wide context. IntechOpen, 2013. [Online]. Available: https://www.intechopen.com/books/2519

[194] M. D. A. Saldaña and S. I. Martínez-Monteagudo, "Oxidative Stability of Fats and Oils Measured by Differential Scanning Calorimetry for Food and Industrial Applications," in *Applications of Calorimetry in a Wide Context*, E. Amal Ali Ed. Rijeka: IntechOpen, 2013, p. Ch. 19.

[195] *Plastics. Epoxy resins. Determination of degree of crosslinking of crosslinked epoxy resins by differential scanning calorimetry*, BS ISO 14322:2012, B. S. Institution, Switzerland, 2012.

[196] A. X. H. Yong, "Improved Methods for the Thermal Analysis of Cure in Polymer Composites," Engineering Doctorate in Micro- and Nano- Materials and Technologies, University of Surrey, 2017.

[197] S. Ebnesajjad, "Chapter 4 - Surface and Material Characterization Techniques," in *Surface Treatment of Materials for Adhesive Bonding (Second Edition)*, S. Ebnesajjad Ed. Oxford: William Andrew Publishing, 2014, pp. 39-75.

[198] J. Goldstein, *Scanning electron microscopy and x-ray microanalysis*, Fourth edition. ed. New York, NY: Springer Science+Business Media, LLC, 2018.

[199] N. Erdman and D. C. Bell, "Scanning Electron and Ion Microscopy of Nanostructures," in *Nanocharacterisation (2)*: The Royal Society of Chemistry, 2015, pp. 300-350.

[200] P. J. Goodhew, F. J. Humphreys, and R. Beanland, *Electron microscopy and analysis*, 3rd ed. London: Taylor & Francis, 2000.

[201] P. W. Hawkes and J. C. H. Spence, Eds. *Springer Handbook of Microscopy* (Springer Handbooks). Switzerland: Springer Cham, 2019, pp. XXXII, 1543.

[202] A. B. Spierings, M. Schneider, and R. Eggenberger, "Comparison of density measurement techniques for additive manufactured metallic parts," *Rapid prototyping journal,* vol. 17, no. 5, pp. 380-386, 2011, doi: 10.1108/13552541111156504.

[203] A. Maltais, D. Dube, M. Fiset, G. Laroche, and S. Turgeon, "Improvements in the metallography of as-cast AZ91 alloy," (in English), *Materials Characterization,* vol. 52, no. 2, pp. 103-119, May 2004, doi: 10.1016/j.matchar.2004.04.002.

[204] A. Maltais, D. Dubé, F. Roy, and M. Fiset, "Optical anisotropy of a color-etched AZ91 magnesium alloy," *Materials Characterization,* vol. 54, no. 4, pp. 315-326, 2005/05/01/ 2005, doi: https://doi.org/10.1016/j.matchar.2004.04.011.

[205] *Standard Test Methods for Determining Average Grain Size*, E112-13, Philadelphia, USA, 2021.

[206] *Standard Test Methods for Determining Average Grain Size Using Semiautomatic and Automatic Image Analysis*, E1382-97, Philadelphia, USA, 2015.

[207] C. L. Bancroft, C. H. Cáceres, and J. R. Griffiths, "On The Relation between Hardness and Yield Strength in a Sand Cast AZ91 Alloy," in *Magnesium Technology 2000*, 2000, pp. 291-294.

[208] *Standard Test Methods for Vickers Hardness and Knoop Hardness of Metallic Materials*, E92-17, Philadelphia, USA, 2017.

[209] L. Samuels, "Microindentations in Metals," presented at the Microindentation Techniques in Materials Science and Engineering, 1985.

[210] *Standard Test Methods for Tension Testing of Metallic Materials*, E8/E8M-22, Philadelphia, USA, 2022.

[211] *Standard Terminology Relating to Methods of Mechanical Testing*, E6-15, Philadelphia, USA, 2015.

[212] *Standard Test Methods for Tension Testing Wrought and Cast Aluminium- and Magnesium- Alloy Products*, B557-15, Philadelphia, USA, 2015.

[213] *Standard Test Methods of Compression Testing of Metallic Materials at Room Temperature*, E9-09, Philadelphia, USA, 2009.

[214] *Atlast of stress-strain curves*, 2nd ed. Materials Park, Ohio, USA: ASM International, 2002.

[215] H. A. Kuhn, "Uniaxial Compression Testing," *vol. 8*, *Mechanical Testing and Evaluation*: ASM International, 2000, p. 0. [Online]. Available: https://doi.org/10.31399/asm.hb.v08.a0003265

[216] J. Homeny, G. G. Nelson, and S. H. Risbud, "Oxycarbide Glasses in the Mg-Al-Si-O-C System," *J Am Ceram Soc,* https://doi.org/10.1111/j.1151-2916.1988.tb05058.x vol. 71, no. 5, pp. 386-390, 1988/05/01 1988, doi: https://doi.org/10.1111/j.1151-2916.1988.tb05058.x.

[217] T. Gumula and S. Blazewicz, "Thermal conversion of carbon fibres/polysiloxane composites to carbon fibres/ceramic composites," (in English), *Ceram Int,* Article vol. 39, no. 4, pp. 3795-3802, May 2013, doi: 10.1016/j.ceramint.2012.10.219.

[218] W. Duan, X. Yin, Q. Li, X. Liu, L. Cheng, and L. Zhang, "Synthesis and microwave absorption properties of SiC nanowires reinforced SiOC ceramic," *Journal of the European Ceramic Society,* vol. 34, no. 2, pp. 257-266, 2014/02/01/ 2014, doi: https://doi.org/10.1016/j.jeurceramsoc.2013.08.029.

[219] D. Suttor, T. Erny, P. Greil, H. Goedecke, and T. Haug, "Fiber-Reinforced Ceramic-Matrix Composites with a Polysiloxane/Boron-Derived Matrix," *J Am Ceram Soc,* https://doi.org/10.1111/j.1151-2916.1997.tb03058.x vol. 80, no. 7, pp. 1831-1840, 1997/07/01 1997, doi: https://doi.org/10.1111/j.1151-2916.1997.tb03058.x.

[220] M. A. Schiavon, E. Radovanovic, and I. V. P. Yoshida, "Microstructural characterisation of monolithic ceramic matrix composites from polysiloxane and SiC powder," *Powder Technology,* vol. 123, no. 2, pp. 232-241, 2002/03/11/ 2002, doi: https://doi.org/10.1016/S0032-5910(01)00461-2.

[221] Y. Morisada and Y. Miyamoto, "SiC-coated carbon nanotubes and their application as reinforcements for cemented carbides," *Materials Science and Engineering: A,* vol. 381, no. 1, pp. 57-61, 2004/09/15/ 2004, doi: https://doi.org/10.1016/j.msea.2004.03.055.

[222] D. Bahloul-Hourlier, J. Latournerie, and P. Dempsey, "Reaction pathways during the thermal conversion of polysiloxane precursors into oxycarbide ceramics," *Journal of the European Ceramic Society,* vol. 25, no. 7, pp. 979-985, 2005/05/01/ 2005, doi: https://doi.org/10.1016/j.jeurceramsoc.2004.05.012.

[223] J. H. Walther, R. Jaffe, T. Halicioglu, and P. Koumoutsakos, "Carbon Nanotubes in Water: Structural Characteristics and Energetics," *The Journal of Physical Chemistry B,* vol. 105, no. 41, pp. 9980-9987, 2001/10/01 2001, doi: 10.1021/jp011344u.

[224] A. Alexiadis and S. Kassinos, "Molecular Simulation of Water in Carbon Nanotubes," *Chem. Rev.,* vol. 108, no. 12, pp. 5014-5034, 2008/12/10 2008, doi: 10.1021/cr078140f.

[225] A. P. Evseev *et al.*, "MWCNT-based surfaces with tunable wettability obtained by He+ ion irradiation," *Surfaces and Interfaces,* vol. 23, p. 100955, 2021/04/01/ 2021, doi: https://doi.org/10.1016/j.surfin.2021.100955.

[226] B. A. Kakade and V. K. Pillai, "Tuning the Wetting Properties of Multiwalled Carbon Nanotubes by Surface Functionalization," *The Journal of Physical Chemistry C,* vol. 112, no. 9, pp. 3183-3186, 2008/03/01 2008, doi: 10.1021/jp711657f.

[227] E. Dujardin, T. W. Ebbesen, A. Krishnan, and M. M. J. Treacy, "Wetting of single shell carbon nanotubes," (in English), *Adv Mater,* vol. 10, no. 17, pp. 1472-1475, Dec 1 1998, doi: Doi 10.1002/(Sici)1521-4095(199812)10:17<1472::Aid-Adma1472>3.0.Co;2-R.

[228] V. F. Arini, U. Fauziah, D. G. Auliya, S. Setiadji, Fitrilawati, and Risdiana, "Synthesis of low viscosity of polymethylhydrosiloxane using monomer of dichloromethylsilane," *Journal of Physics: Conference Series,* vol. 2165, no. 1, p. 012041, 2022/01/01 2022, doi: 10.1088/1742-6596/2165/1/012041.

[229] G. Sun, Z. Liu, and G. Chen, "DISPERSION OF PRISTINE MULTI-WALLED CARBON NANOTUBES IN COMMON ORGANIC SOLVENTS," *Nano,* vol. 05, no. 02, pp. 103-109, 2010/04/01 2010, doi: 10.1142/S1793292010001986.

[230] J. N. Lee, C. Park, and G. M. Whitesides, "Solvent Compatibility of Poly(dimethylsiloxane)-Based Microfluidic Devices," *Analytical Chemistry,* vol. 75, no. 23, pp. 6544-6554, 2003/12/01 2003, doi: 10.1021/ac0346712.

[231] S. Bekou and D. Mattia, "Wetting of nanotubes," *Current Opinion in Colloid & Interface Science,* vol. 16, no. 4, pp. 259-265, 2011/08/01/ 2011, doi: https://doi.org/10.1016/j.cocis.2011.01.009.

[232] M. Q. Tran, J. T. Cabral, M. S. P. Shaffer, and A. Bismarck, "Direct Measurement of the Wetting Behavior of Individual Carbon Nanotubes by Polymer Melts: The Key to Carbon Nanotube−Polymer Composites," *Nano Letters,* vol. 8, no. 9, pp. 2744-2750, 2008/09/10 2008, doi: 10.1021/nl801209g.

[233] S. C. Roh, E. Y. Choi, Y. S. Choi, and C. K. Kim, "Characterization of the surface energies of functionalized multi-walled carbon nanotubes and their interfacial adhesion energies with various polymers," *Polymer,* vol. 55, no. 6, pp. 1527-1536, 2014/03/24/ 2014, doi: https://doi.org/10.1016/j.polymer.2014.02.015.

[234] G. McHale, M. I. Newton, and B. J. Carroll, "The Shape and Stability of Small Liquid Drops on Fibers," *Oil & Gas Science and Technology - Rev. IFP,* 10.2516/ogst:2001006 vol. 56, no. 1, pp. 47-54, // 2001. [Online]. Available: https://doi.org/10.2516/ogst:2001006.

[235] A. V. Neimark, "Thermodynamic equilibrium and stability of liquid films and droplets on fibers," *Journal of Adhesion Science and Technology,* vol. 13, no. 10, pp. 1137-1154, 1999/01/01 1999, doi: 10.1163/156856199X00839.

[236] B. J. Carroll, "Physical aspects of detergency," *Colloids and Surfaces A: Physicochemical and Engineering Aspects,* vol. 74, no. 2, pp. 131-167, 1993/07/23/ 1993, doi: https://doi.org/10.1016/0927-7757(93)80262-D.

[237] Q. Li, S. Nasiri, S. Feng, G. Yang, and E. Spiecker. (2018). Surface decorated carbon nanotube reinforced magnesium AZ91 composites.

[238] X. Gu *et al.*, "Covalently functionalized carbon nanotube supported Pd nanoparticles for catalytic reduction of 4-nitrophenol," *Nanoscale,* 10.1039/C4NR00826J vol. 6, no. 12, pp. 6609-6616, 2014, doi: 10.1039/C4NR00826J.

[239] L. S. K. Pang, J. D. Saxby, and S. P. Chatfield, "Thermogravimetric Analysis of Carbon Nanotubes and Nanoparticles," (in English), *J Phys Chem-Us,* vol. 97, no. 27, pp. 6941-6942, Jul 8 1993, doi: DOI 10.1021/j100129a001.

[240] S. A. Visser, C. E. Hewitt, and T. D. Binga, "Stability of filled poly(dimethylsiloxane) and poly(diphenylsiloxane-co-dimethylsiloxane) elastomers to cyclic stress at elevated temperature," *Journal of Polymer Science Part B: Polymer Physics,* https://doi.org/10.1002/(SICI)1099-0488(19960715)34:9<1679::AID-POLB17>3.0.CO;2-4 vol. 34, no. 9, pp. 1679-1689, 1996/07/15 1996, doi: https://doi.org/10.1002/(SICI)1099-0488(19960715)34:9<1679::AID-POLB17>3.0.CO;2-4.

[241] G. Deshpande and M. E. Rezac, "Kinetic aspects of the thermal degradation of poly(dimethyl siloxane) and poly(dimethyl diphenyl siloxane)," *Polymer Degradation and Stability,* vol. 76, no. 1, pp. 17-24, 2002/01/01/ 2002, doi: https://doi.org/10.1016/S0141-3910(01)00261-0.

[242] Z.-M. Qin, P.-C. Wang, R. Yang, and H.-B. Chen, "Fast pyrolysis of silicones at low temperatures catalyzed by anatase titanium dioxide," *Polymer Degradation and Stability,* vol. 182, p. 109387, 2020/12/01/ 2020, doi: https://doi.org/10.1016/j.polymdegradstab.2020.109387.

[243] Z. Li, K.-s. Moon, Z. Lin, Y. Yao, S. Wilkins, and C. P. Wong, "Carbon nanotubes inhibit the free-radical cross-linking of siloxane polymers," *Journal of Applied Polymer Science,* https://doi.org/10.1002/app.40355 vol. 131, no. 12, 2014/06/15 2014, doi: https://doi.org/10.1002/app.40355.

[244] A. C. M. Yang, "Filler-induced softening effect in thermally aged polydimethylsiloxane elastomers," *Polymer,* vol. 35, no. 15, pp. 3206-3211, 1994/07/01/ 1994, doi: https://doi.org/10.1016/0032-3861(94)90123-6.

[245] J. Campbell, *Castings the new metallurgy of cast metals*, 2nd ed. Burlington, Mass: Butterworth Heinemann, 2003.

[246] Q. Han, "Shrinkage Porosity and Gas Porosity," *vol. 15*, *Casting*: ASM International, 2008, p. 0. [Online]. Available: https://doi.org/10.31399/asm.hb.v15.a0005222

[247] A. Majeed, Y. Zhang, J. Lv, T. Peng, Z. Atta, and A. Ahmed, "Investigation of T4 and T6 heat treatment influences on relative density and porosity of AlSi10Mg alloy components manufactured by SLM," *Computers & Industrial Engineering,* vol. 139, p. 106194, 2020/01/01/ 2020, doi: https://doi.org/10.1016/j.cie.2019.106194.

[248] A. R. Jones, B. Ralph, and N. Hansen, "Subgrain Coalescence and the Nucleation of Recrystallization at Grain Boundaries in Aluminium," *Proceedings of the Royal Society of London. Series A, Mathematical and Physical Sciences,* vol. 368, no. 1734, pp. 345-357, 1979. [Online]. Available: http://www.jstor.org/stable/79873.

[249] P. R. Rios, F. Siciliano Jr, H. R. Z. Sandim, R. L. Plaut, and A. F. Padilha, "Nucleation and growth during recrystallization," *Materials Research,* vol. 8, pp. 225-238, 2005.

[250] C. Y. Park and D. Y. Yang, "A study of void crushing in large forgings I: Bonding mechanism and estimation model for bonding efficiency," *J Mater Process Tech,* vol. 57, no. 1, pp. 129-140, 1996/02/01/ 1996, doi: https://doi.org/10.1016/0924-0136(95)02055-1.

[251] Q. Ma, B. Li, W. R. Whittington, A. L. Oppedal, P. T. Wang, and M. F. Horstemeyer, "Texture evolution during dynamic recrystallization in a magnesium alloy at 450°C," *Acta Materialia,* vol. 67, pp. 102-115, 2014/04/01/ 2014, doi: https://doi.org/10.1016/j.actamat.2013.12.025.

[252] B. Alili, H. Azzeddine, K. Abib, and D. Bradai, "Texture evolution in AZ91 alloy after hot rolling and annealing," *Transactions of Nonferrous Metals Society of China,* vol. 23, no. 8, pp. 2215-2221, 2013/08/01/ 2013, doi: https://doi.org/10.1016/S1003-6326(13)62720-X.

[253] L. Zheng, H. Nie, W. Liang, H. Wang, and Y. Wang, "Effect of pre-homogenizing treatment on microstructure and mechanical properties of hot-rolled AZ91 magnesium alloys," *J Magnes Alloy,* vol. 4, no. 2, pp. 115-122, 2016/06/01/ 2016, doi: https://doi.org/10.1016/j.jma.2016.04.002.

[254] C. H. Wörner and P. M. Hazzledine, "Grain growth stagnation by inclusions or pores," *JOM,* vol. 44, no. 9, pp. 16-20, 1992/09/01 1992, doi: 10.1007/BF03222320.

[255] N. A. Rawashdeh, W. Khraisat, and H. Borgstrom, "Pinning Effect of Pores on Grain Growth in Sintered Steel," *JORDAN JOURNAL OF MECHANICAL AND INDUSTRIAL ENGINEERING,* vol. 11, no. 2, pp. 73-78, APR 2017.

[256] Z. Ryu, J. Zheng, M. Wang, and B. Zhang, "Synthesis and characterization of silicon carbide whiskers," *Carbon,* vol. 39, no. 12, pp. 1929-1930, 2001/10/01/ 2001, doi: https://doi.org/10.1016/S0008-6223(01)00153-1.

[257] P.-X. Hou, C. Liu, and H.-M. Cheng, "Purification of carbon nanotubes," *Carbon,* vol. 46, no. 15, pp. 2003-2025, 2008/12/01/ 2008, doi: https://doi.org/10.1016/j.carbon.2008.09.009.

[258] M. Wang, B. Li, J. Wang, and P. Bai, "Preparation and properties of polysiloxane grafting multi-walled carbon nanotubes/polycarbonate nanocomposites," *Polymers for Advanced Technologies,* https://doi.org/10.1002/pat.1665 vol. 22, no. 12, pp. 1738-1746, 2011/12/01 2011, doi: https://doi.org/10.1002/pat.1665.

[259] B. Li and J. Zhang, "Polysiloxane/multiwalled carbon nanotubes nanocomposites and their applications as ultrastable, healable and superhydrophobic coatings," *Carbon,* vol. 93, pp. 648-658, 2015/11/01/ 2015, doi: https://doi.org/10.1016/j.carbon.2015.05.103.

[260] Y. Zhong, M. Yang, and Z.-K. Liu, "Contribution of first-principles energetics to Al–Mg thermodynamic modeling," *Calphad,* vol. 29, no. 4, pp. 303-311, 2005/12/01/ 2005, doi: https://doi.org/10.1016/j.calphad.2005.08.004.